Synthesis and Characterization of Molybdenum Carbide(s) for Electrocatalytic Applications

A

Thesis

Submitted for partial fulfillment of the requirements for the award of

Doctor of Philosophy

THAPAR INSTITUTE
OF ENGINEERING & TECHNOLOGY
(Deemed to be University)

By

Rameez Ahmad Mir
(Registration No. 901412020)

Under the supervision of

Dr. O. P. Pandey
Senior Professor and Head
School of Physics & Materials Science
Thapar Institute of Engineering & Technology, Patiala
Punjab-147004
July, 2019

Dedicated to

MIR LIYAQAT

Will always remain alive in my heart

Declaration

This is to certify that the thesis entitled **"Synthesis and Characterization of Molybdenum Carbide(s) for Electrocatalytic Applications"** being submitted by **Rameez Ahmad Mir** in the fulfilment of the requirement for the award of the degree of DOCTOR OF PHILOSOPHY in the School of Physics and Materials Science (SPMS), Thapar Institute of Engineering and Technology (TIET), Patiala Punjab is an authentic record of candidate's own work carried out by him under my supervision and guidance. The matter presented in the thesis has not been in part or full to any other University or Institute for the award of any other degree.

Dr. O. P. Pandey

Senior Professor and Head
School of Physics and materials Science
Thapar Institute of Engineering and Technology

Table of contents

Comparative study of C-Mo_2C and C/N-Mo_2C

Synthesis of Mo_2C@C/N using plastic waste

Conclusions and future scope

Acknowledgement

It is my pleasure to express thanks and gratitude to every individual who supported me during my journey since I started the thesis work and finally reached the destination.

I would like to express my deep and sincere gratitude to my supervisor **Dr. O. P. Pandey**, Senior Professor and Head, School of Physics and Materials Science (SPMS), Thapar Institute of Engineering and Technology (TIET), Patiala Punjab for giving me an opportunity to carry out the research work under his supervision. I am thankful to him for providing invaluable, creative and scholarly guidance throughout the journey without whom the work would not have been crowned with success. His vitality, vision, motivation and integrity has inspired me a lot.

I express my thanks to **Doctoral Committee** members **Dr. Kulvir Singh**, **Dr. S. D Tiwari** and **Dr. Amjad Ali**, Head School of Chemistry and Bio-Chemistry (SCBC), TIET Patiala for the encouragement, suggestions and fruitful discussions. I extend my gratitude to all faculty members of the SPMS who supported and encouraged me especially **Dr. Puneet Sharma**, **Dr. B.N Chudasama**, **Dr. B. C. Mohanty** and **Dr. Chandini Khurana**. I specially offer my thanks to **Dr. L. K Brar** for the discussions and help regarding the thesis work. I also express thanks to **Dr. H. Bhunia**, Head Chemical Engineering Department, TIET for the kind support during the initial stage of my research work.

I sincerely express my gratitude to **Dr. Gurbinder Kaur** for the suggestions, fruitful discussions, moral support and guidance to improve the working skills both in analysis and presentation. The constructive criticisms and the working atmosphere she always created has inspired me during my thesis work. I am grateful to **Dr. Anup Thakur,** Associate Professor, Department of Applied Physics, Punjabi University-Patiala for the valuable time and suggestions in carrying the Rietveld refinement analysis. He always encouraged and helped me whenever I approached him. I would like to take this opportunity to express my special thanks to **Dr. Gourav Singla** for introducing me to the fields of carbides, autoclave synthesis and electro catalysis. His suggestions and help during initial stage of my work inspired me to work hard.

I would also like to thank **Purshottam Singh**, **Mr. Jant Singh**, **Mr. Lal Ji**, **Mr. S. P. Verma**, **Mr. Indermani Mishra**, **Mrs. Neelam Sadana**, and **Mr. Pardeep Singla** for their help at various stages.

I am thankful to my seniors **Dr. Suresh Kumar**, **Dr. Paramjot Jha**, **Dr. Mani Mahajan**, **Dr. Manish Mittal and Mrs. Suninderjeet** for the suggestions and valuable help. I am grateful to **Dr.**

Akshay Kumar, Assistant Professor, SGGSWU and **Dr. Rabia Pandit**, Assitant Professor NIT, Hamirpur for their valuable help. I am thankful to my colleagues and my lab mates **Piyush Sharma, Aayush Gupta, Ruby Priya, Shivani Singla, Sanjay Upadhay, Raveena and Puneet** for their company during my research work. My special thanks to **Aayush Gupta** and **Piyush Sharma** for their kind support from initial stage of work. The support of **Piyush Sharma** during the thesis work is highly acknowledged.

To carry this work a happy cheerful atmosphere created by my friends **Chhavi Pahwa, Ishita sharma** and **Piyush Sharma** is always appreciable. I am especially thankful to **Ishita Sharma** for the kind and moral support she always provided to me during the stay. She supported and encouraged me during the bad times. I express my deep gratitude to **Gurwinder Kaur** for the joyful company during my work. The kind support of **Gurwinder Kaur** in thesis formatting is highly acknowledged. I express my thanks to **Megha Jain (Research Scholar)** Punjabi University, **Ishfaq Shah** and **MuZaif Dar** for their help whenever required. Shah and Dar always encouraged and supported me to finish the work in the best possible way. A special thanks to **Dr. Rayees Ahmad Rather** for the fruitful discussions and suggestions regarding hydrogen production study. I am also thankful to **Shahid Bhat** (TIET) and **Rayees Thakur** (Research Scholar) MNIT, Jaipur for their kind help.

I would like to extend my thanks to **Mr. Ghanshyam Morya**, **Mr. Pradeep** and **Mr. Mukesh Aggarwal** at SAI labs, TIET for their continues support for material characterizations. I take an opportunity to express my gratitude to **Dr. Vasant Sathe**, UGC-DAE Indore for Raman analysis. I am thankful to AIRF JNU for TEM/HRTEM and Raman spectroscopy, SAIF PU for XRD and FESEM and **D. D. Pal**, IIT Kanpur for XPS. I express deep gratitude to **Surbhi Sharma** and **Dr. Sumen Basu**, SCBC for BET analysis.

In the ocean of words, I find no pretentious gems to express my heartfelt gratitude to my Father, **Ab. Rashid Mir**, Mother, **Jawhar Rashid** who instead of their many serious concerns supported me for the higher education, with spring of inspiration and sacrifices since I saw the light on this earth. Both of them not only been a fathomless ocean of knowledge and wisdom to me but most of all, their love, intellectual answers, words of care and hands of blessing influenced and enriched me a lot.

Words fail to express my gratitude from the depth of my heart for my loving brothers and loving sister and all family members who provided me relentless encouragement, prayers, pure love, an unmatched affection that made this work to reach its destination. Thanks to cheerful support from **Mubarak Bhat**, who gave me the strength to live my life to fullest even through difficult times.

Above all, I bow down before **Almighty Allah** to express my deepest sense of gratitude to **His Blessings, Peace & Mercy** for providing me an opportunity of exploring the texture of His beauties at substructure level.

Rameez Ahmad Mir

List of Publications

From Ph.D work

1. **Rameez Ahmad Mir**, Piyush Sharma, Om. Prakash. Pandey, *Structural and thermal studies of carbon coated Mo_2C synthesized via insitu single step reduction-carburization*" **Scientific Reports** 2017, 7, 3518.
2. **Rameez Ahmad Mir**, Om Praksh Pandey "*Influence of graphitic/amorphous coated carbon on HER activity of low temperature synthesized β-Mo_2C@C nanocomposites*" Chemical Engineering Journal, 2018, 348, 1037-1048.
3. **Rameez Ahmad Mir** and O. P. Pandey "Waste plastic derived carbon supported Mo_2C composite catalysts for hydrogen production and energy storage applications" Journal of Cleaner Production, 2019, 218, 644-655.
4. **Rameez Ahmad Mir**, Gurbinder Kaur and O. P. Pandey, "*Facile process to utilize carbonaceous waste as carbon source for synthesis of low cost electrocatalyst for green energy production and supercapacitors*" (Under review).
5. **Rameez Ahmad Mir** and O. P. Pandey "*An ecofriendly route to synthesize C-Mo_2C and C/N-Mo_2C utilizing waste polyethene for efficient HER activity and high performance supercapacitors*" (Under review).

Other than Ph.D work

1. H.K. Sidana, **Rameez Ahmad Mir** and Om. Prakash Pandey, *Synthesis of molybdenum nitride (Mo_2N) nanoflakes via in-situ reduction-nitridation*, **Journal of Alloys and Compounds**, 2018, 736, 255-265.
2. Rupinderjeet Bains, Piyush Sharma, **Rameez Ahmad Mir**, Suninder Jeet, Gurbinder Kaur, Om Prakash Pandey "*Influence of CuO/MgO ratio on the gene expression, cytocompatibilty, and antibacterial/anticancerous/analgesic drug loading kinetics for (15-x) CuO-xMgO-10P2O5-60SiO2-10CaO-5ZnO (2.5≤ x≤ 12.5) mesoporous bioactive glasses*", 2018, **Journal of Bio Medical Research A** 106, 2116-2130.
3. Navpreet Kaur, **Rameez Ahmad Mir**, O. P. Pandey "*Electrochemical and optical studies of facile synthesized molybdenum disulphide (MoS_2) nano structures*" **Journal of Alloys and Compounds**, 2019, 782, 119-131.
4. Kajal Rajrana, Aayush Gupta, **Rameez Ahmad Mir** and O. P. Pandey, "*Facile sono-chemical*

synthesis of nanocrystalline MnO_2 for catalytic and capacitive applications" **Physica B: Condensed Matter**, 2019, 564, 179-185.

5. M Burhanuz Zaman, **Rameez Ahmad Mir** and Rajaram Poolla, "*Growth and Properties of Solvothermally derived highly crystalline Cu_2ZnSnS_4 nanoparticles for Photocatalytic and Electrocatalytic applications*" **International Journal of Hydrogen Energy** (Accepted).
6. **Rameez Ahmad Mir,** Shivani Singla and O. P. Pandey, "*Conversion of plastic waste to hetero carbon structures for electrochemical applications*" (Under review).
7. Navpreet Kaur, **Rameez Ahmad Mir** and O. P. Pandey, "*A novel study on soft ferromagnetic nature of nano molybdenum sulphide (MoS_2)"* (under review).
8. Shweta Chalotra, **Rameez Ahmad Mir**, Gurbinder Kaur and O. P pandey "*Oxygen deficient V_2O_3: A suitable electrocatlyts for HER and EDLC applications*", (Under review).
9. Gurbinder Kaur, **Rameez Ahmad Mir**, Piyush Sharma, Vishal Kumar, Kulvir Singh, Om Prakash Pandey, "*X-Ray Photoelectron spectroscopy and high resolution TEM studies of glass composites*" (submitted).
10. **Rameez Ahmad Mir,** Navpreet Kaur, and O. P. Pandey "Mo_2C/MoS_2 composite: An efficient and stable electrocatalyst for HER" (Under Preparation).

List of Papers presented in Conferences (National/International)

1. **Rameez Ahmad Mir**, Aayush Gupta, O. P. Pandey, S*tudy on reduction-carburization of* MoO_3 *to nano* Mo_2C, Proc.of the Intl. Conf. on Nanotechnology for Better Living, 2016, 3, 149 (doi:10.3850/978-981-09-7519-7-nbl16-rps-149).
2. **Rameez Ahmad Mir**, Aayush Gupta, O. P. Pandey *Study on reduction of* MoO_3 *to* Mo_2C *via carburization,* **2nd National conference on "Microscopy of Academy of Microscopy Science and Technology (AMST)"** 2016, Thapar university, Patiala (**Poster presentation**).
3. **Rameez Ahmad Mir**, Aayush Gupta, O. P. Pandey, *Electrochemical studies of carbon coated molybdenum carbide* (Mo_2C) *nano powders synthesized via Solvothermal route*, **"International conference on Advances in nanomaterials and nanotechnology (ICANN) 2016"** Jamia Millia Islamia New Delhi, 4 & 5 November 2016 (**Poster presentation).**
4. **Rameez Ahmad Mir**, O. P. Pandey, *Structural and morphological studies of Mo2C synthesized via reduction-carburization route at low temperature*, International conference on **"Role of microscopy and allied techniques in the development of functional and nano materials (ICMAMN)"**, Fakir Mohan University, Balasore, Odhisa 25-27, November, 2016 (**Oral presentation**).
5. **Rameez Ahmad Mir "Materials Research Society of India Symposium MRSI 2017 Advanced Materials for Healthcare, Clean Energy and Sustainability" & 28th Annual General Meeting of MRSI,** IIT Bombay, February 13-15, 2017 (Attended).
6. Harneet kaur, **Rameez Ahmad Mir**, O. P. Pandey, *Optimization of process parameters for in-situ synthesis of molybdenum nitride* (Mo_2N) *Nano powders* **"National Symposium on Materials for Advanced Technologies (MAT 2017)"** DIT University, Dehradun, February 20-21st, 2017 (**Poster presentation**).
7. Aayush Gupta, **Rameez Ahmad Mir** and **O.P. Pandey**, *Synthesis and photo-catalytic behavior of NbC/C nanocomposite*, **9th International Symposium on Group Five Elements held at Vivanta by Taj,** New Delhi on November 22-24th, 2017 (Poster presentation).
8. Navpreet Kaur, **Rameez Ahmad Mir and** O. P. Pandey, "*Synthesis of the molybdenum disulphide* (MOS_2) *for electro catalytic applications"* **National Conference on "Advanced Materials and Devices for Futuristic Applications" (AMDFA 2018),** Chandigarh University, Chandigarh 19-20 May, 2018.

9. **Rameez Ahmad Mir**, O. P. Pandey "*Influence of carbon on electrochemical behavior of nanomolybdenum carbide (*Mo_2C*)*" **2nd International Conference On Energy Harvesting, Storage, And Transfer (EHST'18)**, Niagara Falls, Canada 7-9 June 2018.
10. **Rameez Ahmad Mir**, O. P. Pandey "*Influence of nature of carbon support over nano* Mo_2C *on HER activity and storage capacity*" **ISERD –403rd International Conference on Recent Innovations in Engineering and Technology (ICRIET)**, 28-29 June, Toronto, Canada.
11. **Rameez Ahmad Mir,** Navpreet Kaur and O. P. Pandey, "Mo_2C/MoS_2 *nanocomposite: Highly efficient elctrocatalyst for hydrogen generation and capacitor applications* "**International Conference on Environmental and Biomedical Nanotechnology (ICEBN-2018)",** JNU-New Delhi, 14-15 September 2018 (Poster presentation).
12. **Rameez Ahmad Mir,** Gurbinder Kaur and O. P. Pandey**,** *Facile process to utilize carbonaceous waste as carbon source for synthesis of low cost electrocatalyst for green energy production and supercapcitors*, **"International conference on Materials for Energy Applications (ICMA)",** S. S Jain Subodh P. G. (Autonomous) College, Jaipur, 6-8 December, 2018. (Oral presentation).
13. Navpreet Kaur, **Rameez Ahmad Mir** and O. P. Pandey, *A novel study on soft ferromagnetic nature of nano molybdenum sulphide (MoS2)*, **"Joint MMM Conference",** Wardman Park Marriott in Washington, D.C, January 14-18, 2019 (Oral Presentation).
14. **Rameez Ahmad Mir,** O. P. Pandey, *Utilization of carbonaceous waste to synthesize carbon based materials for green energy production and high performance capacitors*, **"International conference on advanced materials (ICAM-2019)"**, Jamia Millia Islamia, New Delhi 6-7, March 2019, (Poster presentation).

List of Tables

Chapter 1

Page No.

Introduction

Chapter 2

Literature review

Chapter 4

Synthesis of nano Mo_2C using polypropylene

Chapter 5

Synthesis of nano Mo_2C using plastic waste

Chapter 6

Comparative study of C-Mo_2C and C/N-Mo_2C

Chapter 7

Synthesis of Mo_2C@C/N using waste plastic

Chapter 8

Conclusions and Future scope

List of Figures

Page No.

Chapter 1

Introduction

Chapter 2

Literature review

Chapter 3

Experimental Details

Chapter 4

Synthesis of nano Mo$_2$C using polypropylene

Chapter 5

Synthesis of nano Mo_2C using plastic waste

Chapter 6

Comparative study of C-Mo_2C and C/N-Mo_2C

Chapter 7

Synthesis of Mo_2C@C/N using waste plastic

Preface

The increasing demand for energy with the limited supply of resources of fossil fuels have led to the development of new materials for energy production from natural or renewable sources. The production of hydrogen by hydrogen evolution reaction (HER) through electrochemical water splitting can provide a clean and renewable energy resource. The high-performance electrocatalysts are required in order to increase the efficiency of water splitting to promote the HER. Various efforts have been made in last few decades for the development of low cost electrocatalysts for HER. Among the noble-metal free catalysts, molybdenum carbide (Mo_2C) is the fascinating candidate for electrocatalysis because of its low cost, high chemical stability and structural similarity to Pt group metals. Carbon support in various forms enhances the HER and electrochemical double layer capacitance (EDLC) performance.

In the present work carbon supported nano Mo_2C has been synthesized using different molybdenum and carbon sources. The electrochemical HER activity and EDLC performance of the synthesized products has been studied in detail. The effect of synthesis parameters and the corresponding features of the synthesized products, which also affect the electrochemical properties has been studied. Based on work done the entire study is presented in 8 chapters.

Chapter 1 presents the current status of hydrogen production through HER using different techniques like photocatalysis and electrocatalysis. In both the processes, the role of catalyst for efficient HER activity has been described in this chapter. The important parameters affecting the HER activity has also been highlighted. The limitations of various developed catalysts has been discussed to improve the performance of developed materials. The basic introduction of transition metal carbides (TMCs) along with their applications is presented. A detailed discussion of Mo_2C has been done considering its nature of bonding and phase transitions (α- Mo_2C, β- Mo_2C and γ-MoC). The reason to achieve better catalyst resembling to platinum (Pt) is given. It also pave a path to replace Pt an efficient electrocatalyt in HER. The role of various carbon support on HER activity and EDLC performance has been elaborated. Moreover, the need of carbon supported nano scaled Mo_2C for such specific applications are also highlighted.

Chapter 2 describes the details of literature for the synthesis of Mo_2C. Different properties of the synthesized product is also given in detail. The effect of synthesis parameters on the phase transition, composition of Mo_xC_y and their electrochemical properties has been highlighted.

Moreover, utilization of non-biodegradable wastes carbon source to obtain Mo_2C has also been discussed. Based on literature, their limitations pertaining to synthesis of developed materials and lack of stability of the product phase in the reported results, the work plan for this thesis is also proposed.

Chapter 3 presents the methodology adopted for synthesis of nano Mo_2C. It also includes the characterization of the synthesized products, which has been obtained using different molybdenum and carbon sources. The brief description of characterizations techniques (XRD, FESEM/TEM, Raman spectroscopy, XPS, and BET) are also been presented in this chapter. The method adopted for electrode fabrication to study the electrochemical activity has been included in this chapter. The importance of the method adopted for synthesis using analytical grade polypropylene and carbonaceous wastes (waste plastics and polyethene) and their electrochemical performance has been described in the subsequent chapters.

Chapter 4 describes a brief introduction of need of hydrogen as green and renewable energy source. It also represents the importance of Mo_2C as low cost elctrocatalysts for HER and EDLC applications. The optimization of synthesis parameters (reaction temperature, time and amount of initial carbon content) using analytical grade polypropylene as carbon source is done to obtain nano Mo_2C. The effect of temperature and holding time on the formation of β-Mo_2C@C has been discussed in detail. Features observed in FESEM and TEM analysis of the synthesized β-Mo_2C@C has been analyzed critically. TEM/HRTEM results revealed the formation of carbon supported nano β-Mo_2C@C. Moreover, Raman spectroscopy and XPS were carried out to understand the nature of carbon network and elemental composition on the surface of optimized samples. The detailed synthesis mechanism associated with pure phase formation has been presented in this chapter. The electrochemical activity of the synthesized products having variation in synthesis temperature and time has been tested in acidic medium. The obtained results are compared with the reported data in literature. The effect of scan rate on cyclic voltammetry (CV) analysis to obtain EDLC has been presented. The potential dependent electrochemical impedance spectroscopy (EIS) plots supporting HER activity has been presented at the end of this chapter.

Chapter 5 describes the synthesis of Mo_2C/C composite utilizing used pipette tip (waste plastic) as carbon source. The environmental issues caused by the disposal of these plastic wastes and the limitations of recycling/reuse has been addressed. In this chapter, reaction parameters have been optimized to obtain pure phase Mo_2C encapsulated in carbon matrix (Mo_2C/C).The effect of initial amount of carbon content on pure phase formation and the amount of residual surface carbon in the synthesized product has been discussed in detail. The pure phase (Mo_2C/C) synthesized under different experimental conditions has been characterized for structural, morphological and surface characteristic by XRD, Raman spectroscopy, FESEM, TEM/HRTEM, XPS, BET and TGA. The dependence on amount of carbon source along with the reaction temperature on the surface characteristics (specific surface area) has been studied. The amount of carbon present in Mo_2C/C determined by TGA varying with respect to initial amount of carbon source plays imperative role in protecting the carbide particles from oxidation and firmly contributes to the electrochemical activity. The effect of initial carbon content and its influence on nature of residual surface carbon over Mo_2C on HER activity and EDLC has been elaborated.

In order to increase the electrochemical efficiency of the carbon coated Mo_2C, incorporation of nitrogen (N) was done. The brief description regarding the role of nitrogen (N) in carbon matrix over Mo_2C for enhancing electrochemical performance has been described in **Chapter 6**. The comparative study C-Mo_2C and C/N-Mo_2C utilizing waste polyethene as carbon source has been presented in this chapter. In this chapter reaction temperature and time have been optimized to obtain pure phase C-Mo_2C and C/N-Mo_2C in an autoclave. The MoO_3 and ammonium hepta molybdate tetra hydrate (AHM) were used as Mo source and N/Mo source for the synthesis of C-Mo_2C and C/N-Mo_2C composites. The presence of N in the carbon matrix over Mo_2C has been confirmed by XPS and STEM. The comparative electrochemical study (HER activity and EDLC performance) of C-Mo_2C and C/N-Mo_2C has been done to highlight the role of N encapsulation in the carbon matrix supported over Mo_2C.

Chapter 7 presents formation of Mo_2C@C/N using waste plastics as carbon source. The nature of hydrocarbons present in the carbon source affect the pure phase formation of Mo_2C (Mo_2C@C/N). The role of processing parameters (temperature, time and carbon source) on pure phase formation has been described in detail. The HER activity and EDLC performance of Mo_2C@C/N synthesized under different synthesis conditions has been described.

Chapter 8 concludes and summarizes the entire work of the present study. The work done shows the prominent role of synthesis parameters on formation of Mo_2C. The nature of carbon coating on the surface of the carbide depends on the synthesis parameters, which influence the electrocatalytic activity and efficiency. The importance of using waste carbonaceous species as carbon source and incorporation of nitrogen in the supported carbon matrix over Mo_2C on HER activity and EDLC performance has been summarized. Suggestion for the future work is also given at the end of the chapter.

Chapter 1

Introduction

Overview

In this chapter the environmental issues and the energy crisis caused due to overuse of diminishing fossil fuels is introduced. The need of new renewable and non-carbon emission energy sources, importance of hydrogen (H_2) as clean and efficient energy generated via hydrogen evolution reaction (HER) through electrochemical water splitting is discussed. The demand of efficient energy storage devices (supercapacitors) on the basis of storage mechanism and stability has been described. The role of efficient elctrocatalyst for HER has been highlighted. The requirement of low-cost efficient and durable electrocatalysts for HER to replace the costly platinum (Pt) electrocatalysts is introduced. The importance of nano transition metal carbides (TMCs) especially molybdenum carbide (Mo_2C) as electrocatalysts and electrode in terms of similarity to electronic structure of Pt has been discussed in detail. The different ways to improve the electrocatalytic performance of nano Mo_2C on the basis of synthesis, size, shape and carbon support in different forms is discussed. The importance of in-situ developed carbon over Mo_2C has been highlighted. To improve the HER, the importance of non-noble metal substituents as supportive/coated carbon matrix is discussed.

1.1 Introduction

The energy crisis and environmental degradation are the most critical issues prevailing in the society. For the sustainable development of society, these issues need to be addressed properly. Research groups around the globe are engaged to address these prevailing issues and has become an interesting research topic in the present era. With increasing population and modern industrialization, the need of energy is expected to rise from 18 TW (2013) to 24-26 TW (2040) under new policies and current scenarios. The corresponding rise in carbon dioxide (CO_2) emission is expected to increase from 32 (2013) to 37-44 (2040) as per the reports of international energy agency (IEA) [1]. The overuse of fossil fuels exhausting poisonous gases are intensifying air pollution and global warming [2]. The demand for the alternate renewable and green source of energy to conquer the issues caused due to diminishing fossil fuels is the matter of urgency. Different energy sources like wind, hydrothermal electricity and solar energy have also been studied and implemented [3]. The universal stock of water, CO_2 and nitrogen in earth's atmosphere can be converted to valuable energy via electrochemical processes. Among all sources, the hydrogen (H_2) produced via water splitting is considered as the most efficient and the green energy resource [4,5]. The production of hydrogen via hydrogen evolution reaction (HER) through water splitting is the most sustainable and environment friendly method. The photocatalytic and electrochemical water splitting pathways are most favoring pathways for sustainable hydrogen production [6–10] . The schematic representation of electrochemical and photocatalytic water splitting is shown in Fig. 1.1 (a-b) below:

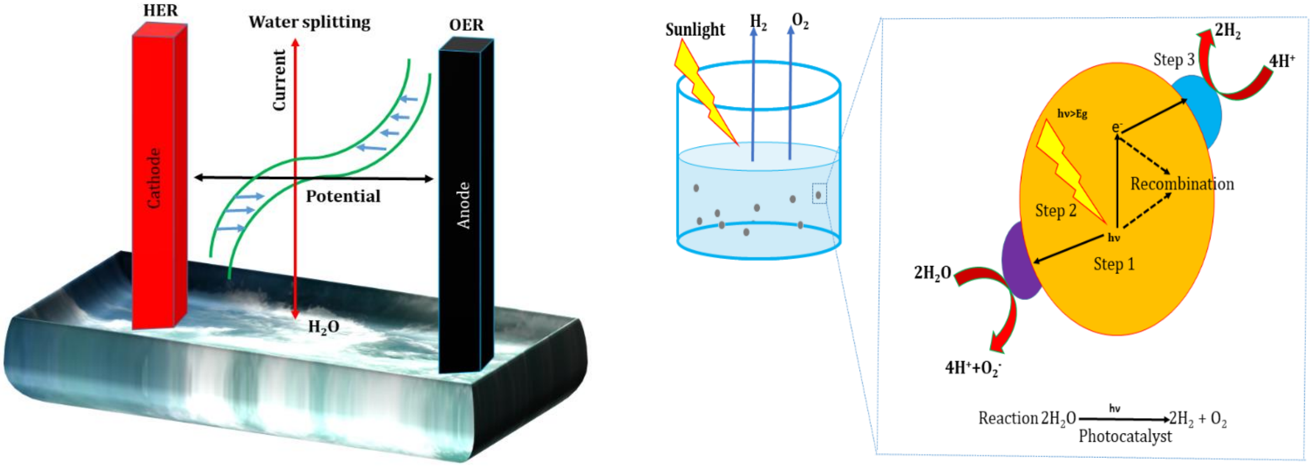

$$\text{Reaction } 2H_2O \xrightarrow[\text{Photocatalyst}]{h\nu} 2H_2 + O_2$$

Figure 1.1: Pictorial representation of water splitting (a) Electrocatalysis and (b) Photocatalysis.

However, both of these processes shown in Fig. 1.1 (a-b) require highly active and efficient non-noble metal catalysts to make the HER through water splitting efficient and economical. The selection and development of suitable catalyst is important to increase the production of hydrogen through HER with low outer source utilization, like low band gap materials for photocatalytic and low overpotential for electrochemical water splitting [11,12].

1.1.1 Electrochemical water splitting

Electrocatalysis is also known as electrochemical activation is the process, which usually involves interfacial oxidative or reductive reconstitution [13–15]. The electrochemical HER also called elctrocatalysis of water molecules has attracted great attention to produce H_2 as a sustainable energy source. The electrochemical HER is the auspicious approach for hydrogen production through water splitting due to its high energy efficiency and the cornerstone of exploring the mechanism responsible for it. It consists of two half-reactions hydrogen and oxygen evolution at cathode and anode, respectively as shown in Fig. 1.2.

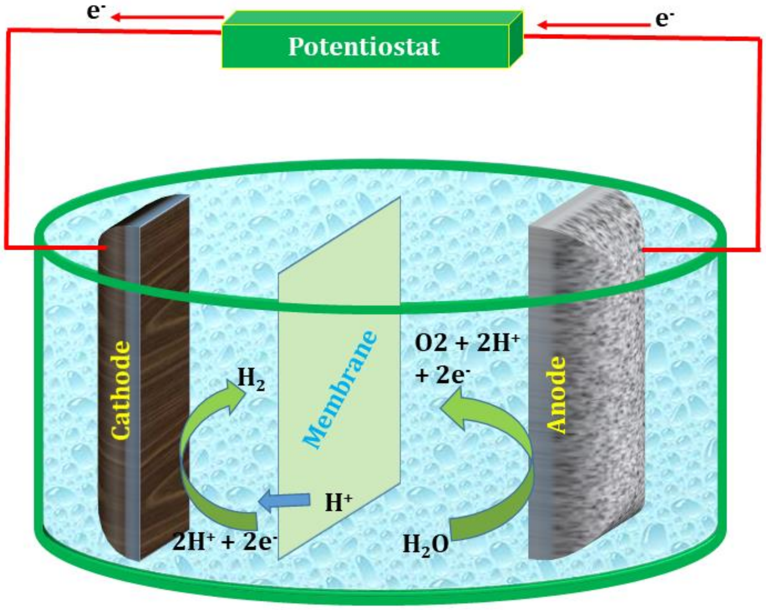

Figure 1.2: Schematic representation of electrocatalysis of water.

The main requirement of this method is the highly active electrocatalyst that reduce the overpotential, increases adsorption/desorption kinetics of H^+ ion and enhance HER performance. The HER reaction $(HER; 2H^+ + 2e^- \rightarrow H_2)$ is the cathodic process in electrochemical water splitting as shown in Fig. 1.1 and 1.2. The HER reaction is two electron transfer reaction and takes place either of the following steps [12,13,16].

$$Volmer\ step: H_3O^+ + S + e^- \rightarrow SHads + H_2O \quad (adsorption) \qquad (1.1)$$

$$Heyrovsky\ step: H_3O^+ + SHads + e^- \rightarrow H_2 + S + H_2O \quad (desorption) \qquad (1.2)$$

$$Tafel\ step: SHads + SHads \rightarrow 2S + H_2 \quad (desorption) \qquad (1.3)$$

The activity depends on the nature of the medium and the electrocatalyst involved in the reaction, which is defined by the difference in peak current and potential (Fig. 1.1). Till date, platinum (Pt) is the most efficient and durable catalyst for HER because it requires negligible over potential to achieve better reaction rates in acidic medium [17,18]. The high cost and low abundance hinder its commercial use. To increase the efficiency and commercialization of the HER process for hydrogen production as fuel, the development and search of noble metal-free electrocatalysts are in high demand. The synthesis of nanostructured noble metal free catalysts will enhance HER activity and efficiency. The designing of new electrocatalyst materials for the HER and understanding of the surface structures and properties that govern HER activity and stability is need of the day.

1.2 Electric double layer capacitor (EDLC, C_{dl})

With the increase in clean, sustainable and renewable energy demands, developing efficient energy storage devices has become an essential task for the global communities of science and technology. Among various energy storage technologies, like batteries and fuel cells, electrochemical supercapacitors (ESs) are the most important and efficient candidates [19–21]. In comparison to conventional capacitors, ECs particularly, *supercapacitors*, *ultracapacitors*, or *electrochemical double-layer capacitors* (EDLCs) relatively store higher energy in smaller dimensions [19,22,23]. In 1957, the very first ES was patented by Howard Becker, using a porous carbon electrode and sulfuric acid (H_2SO_4) as its electrolyte, forming an electric double layer system [24]. The charges stored in EDLCs reside within the electric double layer at the electrode/electrolyte interface. In certain cases rapid reversible oxidation and reduction reaction occurs on the surface of electrode, such capacitors are called Pseudocapacitors [25–27]. EDLCs achieve longer cycle life during continuous charging/discharging, whereas pseudocapacitors have cycling issues.

The supercapacitors (EDLCs) are the promising candidates to replace traditional batteries and conventional capacitors because of inertness towards chemical changes [28,29]. Due to their fast discharging and charging characteristics, uninterruptable backup and instant supply of power, the industrial demand of these materials is increasing. In the present era, the demand of supercapacitors for hybrid electric vehicles (HEV) in public transportation has reenergized their interest. Two energy storage mechanisms are responsible for energy storage in supercapacitors, depending on the material of the electrode. EDLCs store charges inside the porous structures of electrodes without any redox reaction [30]. Pseudocapacitive supercapacitor, mainly consisting of conducting polymers, transitional metal oxides and nitrides, accumulate charge through, reversible redox reactions with the electrode material. The less thermodynamic stability in the charged state results in self-discharging mechanism and Faradaic decomposition of the solution, if the charged potential may transcend the thermodynamic limitation of the electrolyte [19]. EDLCs are primarily made of carbonaceous materials, because of their porous structures and high inertness to redox reactions in an electrolyte. However, the metal oxides (pseudocapcitors) undergo many oxidation reactions at specific potentials, leading to increased capacitance [19]. In certain cases, carbon supplements are incorporated within the electrode material to improve its conductivity. The search for new low cost carbon based electrode materials are of high industrial demand having both high efficiency, energy density and stability.

1.3 Progress and limitations in electrocatalyt design and fabrication

Some of the common requirements for selecting the appropriate electrocatalyst for HER and electrode materials for capcitors are given in Table 1.1.

Table 1.1: Essential requirement for HER electrocatalyst and ES electrode [19, 27]

HER	Electrode
1. Large surface to volume ratio.	1. High porosity and surface area.
2. High surface coordination of corner and edge atoms.	2. Good wettability.
3. Unique electronic properties.	3. Higher electrical conductivity.
4. The decrease in the size of nanoparticles, increase the number of edges and corner sites.	4. Specific morphology (particle dimensions/distributions).
5. Low agglomeration.	5. Long cycle stability (>100 cycles).
6. High resistance to acidic/basic corrosion.	6. Stable over a wide operational potential range.

Two strategies usually govern the HER activity of the electrocatalyst and performance of the electrode materials. These are mutually exclusive but can be addressed simultaneously.

(1) Improving the number of active sites (through increased catalyst loading or improving catalyst structuring by exposing maximum active sites).

(2) Increasing the intrinsic activity of active sites (intercalation, alloy, adsorbates on the surface and core-shell).

Increasing intrinsic activity enhances the activity rather than the catalyst loading which causes issues in transport phenomena. The requirement of less catalyst loading in the improved intrinsic activity electrocatalyst material reduces the cost also, which is the basic requirement for commercial scale applications. To improve the new electrocatalytic properties, the deliberate tailoring of size of the nanoparticles, their surface and shape is desirable. The present goal of nanocatalysis technology is to develop and design the nanoparticles with controlled size, shape, surface and spatial properties. The support and capping of different species on the catalytic materials to exploit surface sites are emerging rapidly for practical purposes. The fabrication of the nanomaterials still faces certain challenges like;

- Preparation of controlled nanoscale dimensions.
- Prevention of intrinsic aggregation.
- Preparation of multi component phases with uniform composition.

The propensity of poisoning is the main issue in sustaining the high activity of catalysts especially in energy systems like fuel cells, water splitting, etc. [32]. The multi component (in terms of compound or support) catalysts have shown low poisoning property [33,34]. The interdisciplinary idea of design and fabrication of new nanocatalysts at this stage is taking the advantage of nanotechnology. In addition to size, the synthesis parameters affect the activity of the catalyst [18,35–37]. The synthesis of the cost effective catalysts will economically impact multi-billion chemical industries implying on synthetic processes. This will also benefit in other social areas like energy materials, including oil, and gas. The requirement of new strategies to manipulate nanoscale materials with higher precision is the prevailing challenge.

Depending on the catalytic materials and applications, numerous methods have been reported. The traditional methods are co-precipitation, deposition-precipitation, ion-exchange, impregnation etc. [38–42]. Surface capping approach to synthesize catalyst has recently attained great attention [43]. To enhance the stability against agglomeration, the surface engineering overcomes the issues of traditional methods in controlling size, shape and surface properties.

Core-shell structures prevent the issue of aggregation, but enhance the stability [44]. At the same time it has disadvantage of blocking of certain active sites. The catalytic activity of a supported species is defined by its contact structure, supper selection and particle size. The contact structure plays vital role because the perimeter interface acts as active sites around the host surface. The electronic conductivity and the interfacial reactivity of the supported catalysts need to be emphasized. It usually depends on the particle size of core and length of the linker chain. The noble metal catalysts supported by different species have shown efficient results. Researchers all over the globe are engaged to develop non-noble metal catalysts having similar efficiency and durability to Pt., so that the water splitting phenomena can be commercialized [45,46]. The change in the electronic structure of metal catalyst by incorporation of other species collectively account for their enhanced activity.

Till date, different materials including non-noble metal electrocatalysts and electrode materials have been synthesized and fabricated like chalcogenides, carbides, metal oxides and different metallic/non-metallic alloys [6,16,47–55]. The metallic species of sulphides, carbides, phosphides and nitrides have shown promising applications to replace costly noble metal electrocatalysts in HER [50,56–58]. Among them, the transition metal carbides (TMCs) being the carbon species are the efficient and durable electrocatalysts [59]. The schematic representation of these species is shown in Fig. 1.3.

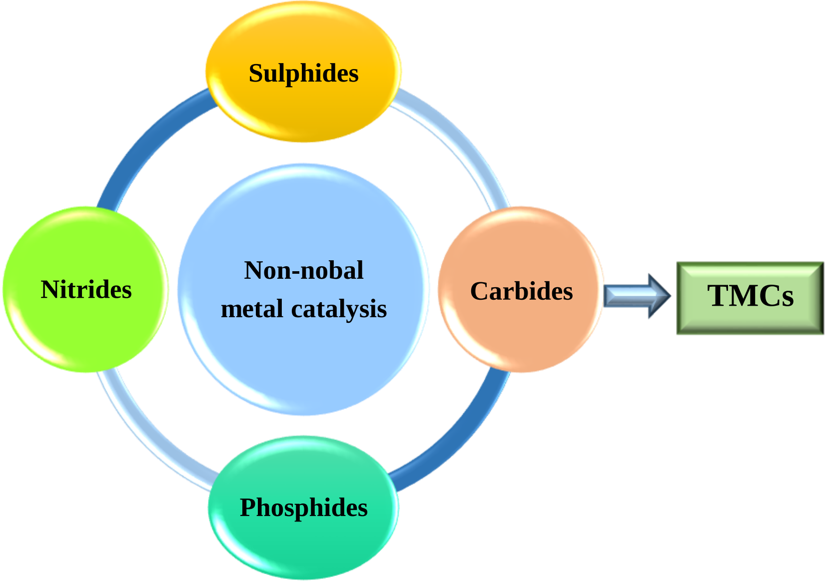

Figure 1.3: Pictorial representation of different electrocatalyst species.

1.4 Transition metal carbides (TMCs): Properties and applications

Carbides are the most inter-dispensable compounds composed of carbon and metal having different electronegativity. The metal carbides of early transition metals are called transition metal carbides (TMCS). They are also termed as *refractory carbides* corresponding to their high melting points (>1800 °C) [60,61] . The high degree of chemical stability is also an important criterion for refractory materials. Their unique physiochemical properties, high hardness and resistance to corrosion makes them widely useful for various industrial applications like drill bits, machine parts and high temperature applications [60,62–64]. Three general characteristics play an important role in the formation of carbides like, the electronegativity difference between carbon and the other element, the size of the respective atoms, and the bonding nature of these atoms [65]. These compounds have been classified on the basis of nature of bond between carbon and the other metal. The elements of group IV, V and VI form an important class TMCs called interstitial carbides [60]. They have a large electronegativity difference between the element and carbon. The size of carbon atom being smaller than the metal atom allows carbon to nest in the interstices of the metal lattice (hence the name interstitial). The bonding is partly covalent and ionic, but mostly metallic, which signifies why the interstitial carbides closely resemble metals. The stoichiometry is an important criteria for various applications of the carbides and it depends on the site occupancy of the carbon atom at all available interstitial sites. Hägg in 1931, formulated a criteria for interstitial structures referred as 'Hägg's structure' and observed that 9 early transitions metals are fit for these criteria in terms of size and site availability which are as follows [60]:

Table 1.2: TMCs of group IV, V and VI [60].

Group (IV)	**Group (V)**	**Group (VI)**
Titanium (Ti) **TiC_{1-x} (fcc)**	**Vanadium (V)** **V_2C (hcp), VC (fcc)**	**Chromium (Cr)** **$Cr_{23}C_6$ (hcp), Cr_3C_2 (hex)**
Zirconium (Zr) **ZrC_{1-x} (fcc)**	**Niobium (Nb)** **Nb_2C (hcp), NbC (fcc)**	**Molybdenum (Mo)** **Mo_2C (hex), MoC (hex)**
Hafnium (Hf) **HfC_{1-x} (fcc)**	**Tantalum (Ta)** **Ta_2C (hcp), TaC**	**Tungsten (W)** **W_2C (hcp), WC (hex)**

Carbon form compounds with all transition metals (TMs) excluding the last elements of 2nd and 3rd row. The ratio of the atomic radii of the elemental components $r = R_c/R_M$, where ‘R_c’ is the radius of nonmetal atom and ‘R_M’ is the radius of metal atom respectively. It determines the appropriateness of a system to form interstitial structures [60]. If the value of “*r*” is less than 0.59, the transition metals form common structures like face centered cubic (fcc), hexagonal close packing (hcp) and simple hexagonal (hex), with non-metals placed at interstitial sites of octahedral and cubic geometry [66]. However, if the ‘*r*’ is greater than 0.59 the metallic arrangement disturbs to accommodate the larger non-metal atoms and retain metal-metal interactions [60]. The main compositions and crystal structures of interstitial carbides are summarized in Table 1.2. and the corresponding characteristics of each group are summarized in Table 1.3 [60,65].

Table 1.3: Phases and crystal structures of interstitial carbides [60].

(C is carbon and M is transition metal)

Group IV	**Group V**	**Group VI**
• Lowest C/M atomic radii ratio • The composition is M-C with C atoms in all octahedral sites • fcc structure • Structure of host metal is either hcp/bcc	• Intermediate C/M atomic radii ratio • The major composition is M_2C composition (stable phase) with C atoms occupying half the octahedral sites • hcp and fcc structures • Host metal has structure: bcc	• Highest C/M atomic radii ratio • Several compositions • fcc, hcp, and hexagonal structures • Host metal has only one structure: bcc

The TMCs are also used as a catalyst for various reactions because of their exceptional chemical behavior. The various applications of TMCs are shown in Fig.1.4. TMCs show characteristics of both ceramics and metals due to the presence of only metal-carbon and metal-metal bonds. The first report of Levi and Boudart [50,67] regarding the platinum (Pt) like electronic structure of TMCs especially group VI elements (Mo and W) widens their scope for various catalytic applications like hydrodesulphurization (HDS) [68], fuel cells [69], hydrogenation [70], water gas shift (WGS) [71], carbon dioxide (CO_2) reduction [72] and hydrogen evolution reaction (HER) for water splitting [73–75]etc.

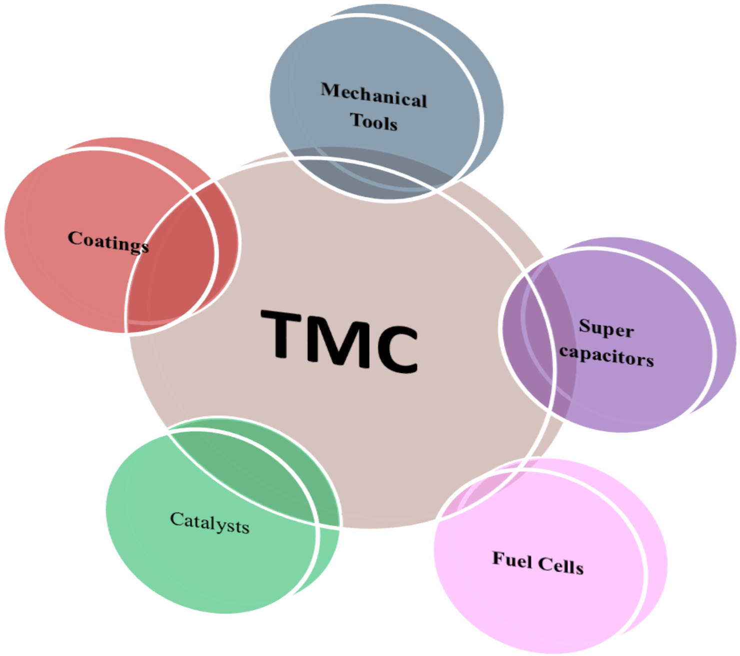

Figure 1.4: Schematic representation of applications of TMCs.

1.4.1 Molybdenum carbide properties and applications

Among TMCs, molybdenum carbide is mostly studied and promising candidate for such applications exhibiting high chemical stability, thermal stability, hardness, surface activity and moreover, its catalytic activity is similar to noble metals. To increase the mechanical strength, stiffness, wear and corrosion resistance of high temperature steels, super alloys and cast iron, molybdenum carbide are widely used as alloying element [76]. Molybdenum carbide belongs to interstitial carbides, group VI of the periodic table. The physical and mechanical properties of molybdenum carbide are given in table Table 1.4. The incorporation of C in the atomic lattice of Mo increases the lattice parameter. It also leads to an increase in Mo-Mo distance and contraction of d-band. Mo-Mo interaction is mostly metallic and the partially filled d orbital electrons of the TM results in some covalent contribution [60,66]. The carbide bond is ionic due to the transfer of electrons from metal to carbon and the covalent contribution arises due to bonding between d-state of Mo and p-state of C. The d-electron density states of Mo after incorporation of C in lattice becomes higher near the Fermi level and resembles to Pt. Higher the amount of C in Mo lattice, the more will Pt. like behavior of molybdenum carbide [77]. The high abundance, low cost and more similarity to Pt. or noble metals makes molybdenum carbide a promising potential candidate for the replacement of these costly metals.

Table 1.4: Properties of molybdenum carbide [60,62]

S. No	Property	Value
1.	Electronic configuration	[Kr]$4d^5 5s^1$
2.	Coordination number	6
3.	valance states	+2, +4 and +6
4.	Space group	P63/mmc
5.	Density	9.06 g/cm^3
6.	Melting point	2520 °C
7.	Molecular Mass	203.9
8.	Thermal conductivity	21.5 W/m-K
9.	Electrical resistivity	21.5 W/m-K
10.	Thermal expansion	7.9×10^{-6} /ºC

This also increases the industrial demand of the product material. The higher electrocatalytic activity and stability exhibited by commercial molybdenum carbide (β-Mo_2C) particles opens a new and wide area for their efficient utilization. Wan *et al.* [78] observed the HER activity of the four different phases in order of α-MoC_{1-x} < η-MoC < γ-MoC < β-Mo_2C. The higher HER activity of β-Mo_2C has also been observed in various well reported results. However, required parameters to get pure phase and the corresponding structural parameters for HER activity of molybdenum carbide particles is critical issue. The phase formation and crystallinity depends on the nature, amount of carbon source and other reaction parameters.

1.4.2 Molybdenum-Carbon (Mo-C) system

The different phase of molybdenum carbide has been identified with two phases of Mo_2C where carbon occupy the octahedral sites. The phase change occurs due to topotactic and order/disorder transformation of the interstitial carbon atom. The effect of temperature and composition on phase formation Mo-C carbides is shown in Fig. 1.5. The phases obtained in Mo-C system are α-Mo_2C (orthorhombic), β-Mo_2C (Hexagonal), η-MoC_{1-x} (Hexagonal), δ-MoC_{1-x} (Cubic), γ-MoC (Hexagonal), γ`-MoC_{1-x} (Hexagonal). Only Mo_2C and MoC are thermally stable phases. The topotactic transformation from cubic to hexagonal was also observed depending upon the nature of reaction gases and Mo source. The more rich carbon phase MoC is formed as an intermediate phase and transforms to Mo_2C and carbon at higher temperatures.

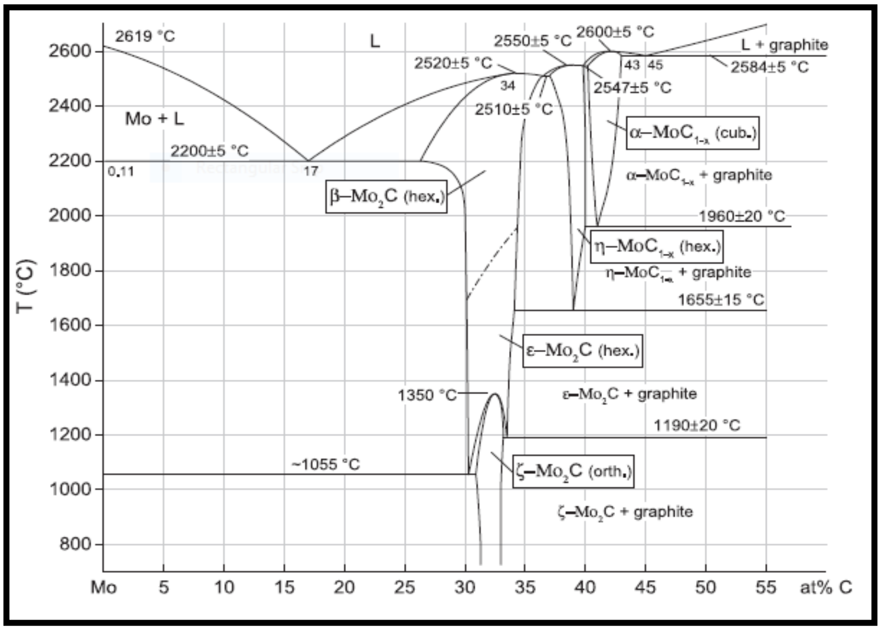

Figure 1.5: Phase diagram of Mo-C system [79–81].

The density functional theory (DFT) also reveals the transformation of metastable to stable phase with respect to temperature [82]. In certain cases γ`-MoC_{1-x} is formed due to combination of MoC and Mo_2C phases, usually stable at low temperatures. The variation in homogeneity of the substiometric phases is in accordance with the stabilizing and destabilizing of the electronic states when vacancies are introduced. It also confirms the higher stability of β-Mo_2C as compared to orthorhombic phase. The catalytic transformation of MoO_3 in presence of CH_4/H_2/CO to more thermally stable β-Mo_2C is an effective method.

1.4.3 Nano molybdenum carbide (Mo_2C)

The optimization of structural, morphological and surface features of the Mo_2C at nano scale is being actively pursued. In case of molybdenum carbide, the crystal phase developed during synthesis plays an important role for electrocatalytic HER activity, β-Mo_2C being the most suitable one [83]. The enhanced specific surface area in nano dimensions improve the catalytic activity, but the pore size and distribution affects the stability. The performance of EDLCs depend on the pore size and distribution. Along with the efficiency, the stability for longer duration is essential for commercial scale applications. Particle size influences the reaction pathway, which shows an increase in ability of catalyst. The structure and crystallite size of carbides is mainly dependent on temperature, type and concentration of carbon source [36,84]. The nano structured molybdenum carbide is considered as promising candidate for HER because of low cost, chemically stable and high similarity to platinum based catalyst [85]. The construction of various nanostructures e.g., nanooctahedrons, nanowires (NWs), nanoparticles (NPs) improved the HER activity because of enhanced exposure of active surfaces of molybdenum carbide [85–87]. Due to localized agglomeration of overlapped structures, the particle size increases. The precise control on size, morphology and crystal structure during synthesis is necessary for broad study of catalytic activity of molybdenum carbide. The molybdenum carbide NPs enclosed by supportive catalyst showed enhanced HER activity in acidic medium with very low over potential and higher stability during operation for longer time [14]. Carbon deposition and morphology shows a dependency on holding time and temperature. It has strong dependency on the nature and amount of initial carbon source. The support of carbon over Mo_2C in various forms like CNTs, graphene, porous carbon not only protect it from corrosion, but also increases the active sites and improves the HER performance [85,88,89]. It not only hinders the surface corrosion, but also due to its conductive nature the efficiency is also improved. In certain cases the catalytic activity of molybdenum carbide improved by introducing other elements, which may adjust the electronic sites in a sensible way [17,18]. To improve the charge transfer rate and active sites, the introduction of metal–free elements like nitrogen (N), phosphor (P) and sulphur (S) within the carbon matrix improves HER activity [73,90–92]. The synergistic effect of N incorporation in the less resistance network of C encapsulating Mo_2C further shortens the electronic path and enhances the electrochemical activity. The improved electrochemical HER activity of the carbon (C) or nitrogen doped carbon (C/N) support over Mo_2C has broaden the application for energy storage devices like electric double layer, pseudo and super capacitors depending on the interaction of the material surface with electrolyte ions [93–97].

The advances and progress in the synthesis of nano Mo_2C and its HER and EDLC behavior is discussed in next chapter.

References

1 M. W. Thring, *Electronics and Power*, 2010, **23**, 329.
2 H. B. Gray, *Nature Chemistry*, 2009, **1**, 112–112.
3 M. Z. Jacobson, *Energy and Environmental Science*, 2009, **2**, 148–173.
4 J. A. Turner, *Science*, 2004, **305**, 972–974.
5 I. P. Jain, *International Journal of Hydrogen Energy*, 2009, **34**, 7368–7378.
6 R. A. Rather, S. Singh and B. Pal, *Applied Catalysis B: Environmental*, 2017, **213**, 9–17.
7 N. S. Alhajri, D. H. Anjum and K. Takanabe, *Journal of Materials Chemistry A*, 2014, **2**, 10548–10556.
8 N. S. Alhajri, H. Yoshida, D. H. Anjum and A. T. Garcia-esparza, *Journal of Materials Chemistry*, 2013, **1**, 12606–12616.
9 K. Ojha, S. Saha, S. Banerjee and A. K. Ganguli, *ACS Applied Materials and Interfaces*, 2017, **9**, 19455–19461.
10 K. Ojha, M. Sharma, H. Kolev and A. K. Ganguli, *Catalysis Science and Technology*, 2017, **7**, 668–676.
11 R. A. Rather, D. Pooja, P. Kumar, S. Singh and B. Pal, *Journal of Cleaner Production*, 2018, **175**, 394–401.
12 Y. Zheng, Y. Jiao, M. Jaroniec and S. Z. Qiao, *Angewandte Chemie - International Edition*, 2015, **54**, 52–65.
13 A. J. Bard and L. R. Faulkner, *Electrochemical Methods Fundamentals and Applications*, 2015, vol. 8.
14 C. G. Zoski, *Handbook of Electrochemistry*, Elsevier, New Mexico USA, First., 2007.
15 M. Zeng and Y. Li, *Journal of Materials Chemistry A*, 2015, **3**, 14942–14962.
16 X. Li, X. Hao, A. Abudula and G. Guan, *Journal of Materials Chemistry A*, 2016, **4**, 11973–12000.
17 W. Zhou, J. Jia, J. Lu, L. Yang, D. Hou, G. Li and S. Chen, *Nano Energy*, 2016, **28**, 29–43.
18 X. Zou and Y. Zhang, *Chemical Society reviews*, 2015, **44**, 5148–80.
19 B. K. Kim, S. Sy, A. Yu and J. Zhang, *Handbook of Clean Energy Systems*, 2014, 1–25.
20 G. Kaur, D. Homa, K. Singh, O. P. Pandey, B. Scott and G. Pickrell, *Journal of Power Sources*, 2013, **242**, 305–313.
21 Y. Su and I. Zhitomirsky, *Applied Energy*, 2015, **153**, 48–55.
22 A. Allagui, T. J. Freeborn, A. S. Elwakil and B. J. Maundy, *Scientific Reports*, 2016, **6**, 1–8.
23 S. Sampath, D. D. Sarma and A. K. Shukla, *ACS Energy Letters*, 2016, **1**, 1162–1164.
24 B. Howard, *United states patent Office*.
25 Y. Wang, Y. Song and Y. Xia, *Chemical Society Reviews*, 2016, **45**, 5925–5950.
26 Z. S. Iro, C. Subramani and S. S. Dash, *International Journal of Electrochemical Science*, 2016, **11**, 10628–10643.
27 J. Li, Q. M. Yang and I. Zhitomirsky, *Nanoscale Research Letters*, 2010, **5**, 512–517.
28 W. Chen, R. B. Rakhi, L. Hu, X. Xie, Y. Cui and H. N. Alshareef, *Nano Letters*, 2011, **11**, 5165–5172.
29 A. Yu, V. Chabot and J. Zhang, *Electrochemical Supercapacitors for Energy Storage and Delivery*, CRC Press Taylor and Francis Group, 2018.
30 T. Thomberg, A. Jänes and E. Lust, *Electrochimica Acta*, 2010, **55**, 3138–3143.
31 J. Regalbuto, *Catalyst Preparation: Science and Engineering*, CRC Press Taylor and

Francis Group, Broken Sound Parkway NW, Suite 300 Boca Raton, FL 33487-2742, 2007, vol. 2007.
32 H. Wei, Q. Xi, X. Chen, D. Guo, F. Ding, Z. Yang, S. Wang, J. Li and S. Huang, *Advanced Science*, 2018, **5**, 1–7.
33 B. Šljukic, D. M. F. Santos, M. Vujkovic, L. Amaral, R. P. Rocha, C. A. C. Sequeira and J. L. Figueiredo, *ChemSusChem*, 2016, **9**, 1200–1208.
34 K. Zhang, C. Li, Y. Zhao, X. Yu and Y. Chen, *Physical chemistry chemical physics*, 2015, **17**, 16609–14.
35 M. Behrens and M. Armbrüster, *Catalysis for Alternative Energy Generation*, Springer New York Heidelberg Dordrecht London, NEw York, ISBN 978-1., 2012.
36 T. Mo, J. Xu, Y. Yang and Y. Li, *Catalysis Today*, 2016, **261**, 101–115.
37 A. Gupta and O. P. Pandey, *Solar Energy*, 2018, **163**, 167–176.
38 S. V. P. Vattikuti, C. Byon, C. V. Reddy, J. Shim and B. Venkatesh, *Applied Physics A: Materials Science and Processing*, 2015, **119**, 813–823.
39 I. J. Hsu, Y. C. Kimmel, X. Jiang, B. G. Willis and J. G. Chen, *Chemical Communications*, 2012, **48**, 1063–1065.
40 M. Wang, P. Ju, Y. Zhao, J. Li, X. Han and Z. Hao, *New Journal of Chemistry*, 2018, **42**, 910–917.
41 J. Min, K. Wang, J. Liu, Y. Yao, W. Wang, L. Yang, R. Zhang and M. Lei, *Journal of Power Sources*, 2017, **363**, 392–403.
42 A. Malathi and J. Madhavan, *Journal of Nano Research*, 2017, **48**, 49–61.
43 C. H. Kuo, L. K. Lamontagne, C. N. Brodsky, L. Y. Chou, J. Zhuang, B. T. Sneed, M. K. Sheehan and C. K. Tsung, *ChemSusChem*, 2013, **6**, 1993–2000.
44 S. J. Kim, D. H. Shin, Y. S. Choi, H. Rho, M. Park, B. J. Moon, Y. Kim, S. K. Lee, D. S. Lee, T. W. Kim, S. H. Lee, K. S. Kim, B. H. Hong and S. Bae, *ACS Nano*, 2018, **12**, 2803–2808.
45 R. Michalsky, Y. J. Zhang and A. A. Peterson, *ACS Catalysis*, 2014, **4**, 1274–1278.
46 H. Yuan, L. Kong, T. Li and Q. Zhang, *Chinese Chemical Letters*, 2017, **28**, 2180–2194.
47 R. M. Silva, B. S. Noremberg, N. H. Marins, J. Milne, I. Zhitomirsky and N. L. V. Carreño, *Journal of Materials Research*, 2019, **34**, 592–599.
48 I. Wiesel, R. Popovitz-Biro and R. Tenne, *Nanoscale*, 2013, **5**, 1499.
49 K. Ojha, S. Saha, S. Banerjee and A. K. Ganguli, *ACS Applied Materials and Interfaces*, 2017, **9**, 19455–19461.
50 S. Meyer, A. V. Nikiforov, I. M. Petrushina, K. Köhler, E. Christensen, J. O. Jensen and N. J. Bjerrum, *International Journal of Hydrogen Energy*, 2015, **40**, 2905–2911.
51 R. A. Rather, S. Singh and B. Pal, *Journal of Catalysis*, 2017, **346**, 1–9.
52 B. Huang, Y. Liu and Z. Xie, *Journal of Materials Chemistry A*, 2017, **5**, 23481–23488.
53 Y. C. Kimmel, D. V. Esposito, R. W. Birkmire and J. G. Chen, *International Journal of Hydrogen Energy*, 2012, **37**, 3019–3024.
54 J. K. Huang, J. Pu, C. L. Hsu, M. H. Chiu, Z. Y. Juang, Y. H. Chang, W. H. Chang, Y. Iwasa, T. Takenobu and L. J. Li, *ACS Nano*, 2014, **8**, 923–930.
55 D. Mukherjee, P. Muthu Austeria and S. Sampath, *ACS Applied Energy Materials*, 2018, **1**, 220–231.
56 Z. Yang, D. Gao, J. Zhang, Q. Xu, S. Shi, K. Tao and D. Xue, *Nanoscale*, 2015, **7**, 650–658.
57 K. An and X. Xu, *Electrochimica Acta*, 2019, **293**, 348–355.

58 D. J. Weber, M. Janssen and M. Oezaslan, *Journal of The Electrochemical Society*, 2019, **166**, F66–F73.

59 Y. Liu, T. G. Kelly, J. G. Chen and W. E. Mustain, *ACS Catalysis*, 2013, **3**, 1184–1194.

60 H. Pierson, *Noyes Publications, new Jersey U.S.A*.

61 T. V. Kosolapova, *Carbides:Properties, Production, and Applications*, Plenum Press, NewYork, ist., 1971.

62 G. V. Samsonov, *Refractory Carbides*, Plenum Publishing Corporation, NEw York, 1970.

63 J. Sun, Tawei; Gary R. Pickrell and Jeese J. Brown, *Journal of American Ceramic Society*, 1994, **77**, 3209–3214.

64 G. R. Pickrell, T. Sun and J. J. Brown, *Fuel Processing Technology*, 1995, **44**, 213–236.

65 S. T. Omaya, 1996.

66 H. H. Hwu and J. G. Chen, *Chemical Reviews*, 2005, **105**, 185–212.

67 R. B. Levy and M. Boudart, *Science*, 1973, **181**, 547–549.

68 X. H. Wang, H. L. Hao, M. H. Zhang, W. Li and K. Y. Tao, *Journal of Solid State Chemistry*, 2006, **179**, 538–543.

69 H. Zhong, H. Zhang, G. Liu, Y. Liang, J. Hu and B. Yi, *Electrochemistry Communications*, 2006, **8**, 707–712.

70 C. Liu, M. Lin, D. Jiang, K. Fang and Y. Sun, *Catalysis Letters*, 2014, **144**, 567–573.

71 J. Patt, D. J. Moon, C. Phillips and L. Thompson, *Catalysis Letters*, 2000, **65**, 193–195.

72 M. D. Porosoff, X. Yang, J. A. Boscoboinik and J. G. Chen, *Angewandte Chemie - International Edition*, 2014, **53**, 6705–6709.

73 Y. Liu, B. Huang, X. Hu and Z. Xie, *International Journal of Hydrogen Energy*, 2019, **44**, 3702–3710.

74 Y. N. Regmi, G. R. Waetzig, K. D. Duffee, S. M. Schmuecker, J. M. Thode and B. M. Leonard, *Journal of Materials Chemistry A*, 2015, **3**, 10085–10091.

75 J. Dong, Y. Shi, C. Huang, Q. Wu, T. Zeng and W. Yao, *Applied Catalysis B: Environmental*, 2019, **243**, 27–35.

76 E. J. Pavlina, J. G. Speer and C. J. Van Tyne, *Scripta Materialia*, 2012, **66**, 243–246.

77 J. S. Choi, G. Bugli and G. Djéga-Mariadassou, *Journal of Catalysis*, 2000, **193**, 238–247.

78 C. Wan, Y. N. Regmi and B. M. Leonard, *Angewandte Chemie - International Edition*, 2014, **53**, 6407–6410.

79 H. W. Hugosson, O. Eriksson, L. Nordström, U. Jansson, L. Fast, a Delin, J. M. Wills and B. Johansson, *Journal of Applied Physics*, 1999, **86**, 3758–3767.

80 B. Predel, *B-Ba – C-Zr*, 2006, 1–4.

81 S. Eroglu and H. I. Bakan, *Key Engineering Materials*, 2009, **264**–**268**, 121–124.

82 M. Cao, C. Gao, T. Meng, P. Yang and W. Guo, *Chemistry – An Asian Journal*, 2019, asia.201900312.

83 S. Jing, L. Zhang, L. Luo, J. Lu, S. Yin, P. K. Shen and P. Tsiakaras, *Applied Catalysis B: Environmental*, 2018, **224**, 533–540.

84 A. Gupta, G. Singla and O. P. Pandey, *Ceramics International*, 2016, **42**, 13024–13034.

85 H. Bin Wu, B. Y. Xia, L. Yu, X. Y. Yu and X. W. Lou, *Nature Communications*, 2015, **6**, 1–17.

86 Q. Gao, C. Zhang, S. Xie, W. Hua, Y. Zhang, N. Ren, H. Xu and Y. Tang, *Chemistry of Materials*, 2009, **21**, 5560–5562.

87 R. Li, S. Wang, W. Wang and M. Cao, *Physical Chemistry Chemical Physics*, 2015, **17**, 24803–24809.

88 M. Pang, L. Ding, C. Li and C. Liang, *Studies in Surface Science and Catalysis*, 2010, **175**, 275–278.

89 J. Sen Li, Y. Wang, C. H. Liu, S. L. Li, Y. G. Wang, L. Z. Dong, Z. H. Dai, Y. F. Li and Y. Q. Lan, *Nature Communications*, 2016, **7**, 11204.

90 X. J. Yang, X. J. Feng, H. Q. Tan, H. Y. Zang, X. L. Wang, Y. H. Wang, E. B. Wang and Y. G. Li, *Journal of Materials Chemistry A*, 2016, **4**, 3947–3954.

91 Z. Shi, K. Nie, Z. J. Shao, B. Gao, H. Lin, H. Zhang, B. Liu, Y. Wang, Y. Zhang, X. Sun, X. M. Cao, P. Hu, Q. Gao and Y. Tang, *Energy and Environmental Science*, 2017, **10**, 1262–1271.

92 Z. Wu, M. Song, Z. Zhang, J. Wang and X. Liu, *Journal of Colloid and Interface Science*, 2019, **536**, 638–645.

93 C. Zhan, Y. Zhang, P. T. Cummings and D. E. Jiang, *Physical Chemistry Chemical Physics*, 2016, **18**, 4668–4674.

94 R. R. Li, S. G. Wang, W. Wang and M. H. Cao, *Physical Chemistry Chemical Physics*, 2015, **17**, 24803–24809.

95 R. Chen, I. K. Puri and I. Zhitomirsky, *Ceramics International*, 2018, **44**, 18007–18015.

96 C. J. Wallar, R. Poon and I. Zhitomirsky, *Journal of The Electrochemical Society*, 2017, **164**, A3620–A3627.

97 C. Wallar, D. Luo, R. Poon and I. Zhitomirsky, *Journal of Materials Science*, 2017, **52**, 3687–3696.

Chapter 2

Literature review

Overview

In this chapter the work done in the field of synthesis and characterization of different phases of nano molybdenum carbide is presented. The role of synthesis parameters on formation of pure nano crystalline Mo_2C and its stability has been discussed. The features associated with nano Mo_2C influencing electrochemical properties is discussed in detail. Apart from this, the influence of different forms of carbon support in nano composites $C@Mo_2C$ and occupancy of different metals/non-metals influencing HER and EDLC has been described in detail. Based on literature gap, the objectives of the present work has been formulated.

2.1 Literature review

The synthesis of nano Mo_2C having higher crystallinity and surface area are important for electrocatalytic applications. In order to achieve it different synthesis methods have been proposed where synthesis parameters like temperature, pressure and time play an important role for obtaining pure phase. Apart from synthesis parameters, the starting materials, their nature, amount of different carbon source and the catalyst used to get final product are also vital for pure phase formation. These not only affect the phase purity of the product, but also plays a vital role on stability and efficiency of the product during its application. Moreover, the economical factor for the synthesis of such product (Mo_2C) is also important for its end use. At present many research groups around the globe are working on the synthesis of Mo_2C for different applications especially the electrochemical reactions. The most common molybdenum source used for the synthesis of Mo_2C are molybdenum (Mo) metal powder, molybdenum oxide (MoO_3), ammonium molybdate ($(NH_4)_6 Mo_7O_{24}$). However, there are other precursors but are rarely reported. For the synthesis of Mo_2C different synthesis procedures have been adopted that include temperature programed reaction (TPR), direct carburization using Mo and C and many other chemical synthesis routes. The schematic representation of the synthesis methods adopted so far are shown in Fig. 2.1. In all these methods, the role of carburizing agent is important. In this chapter a brief discussion on the work done in the area of synthesis of nano Mo_2C and its electrochemical application has been described.

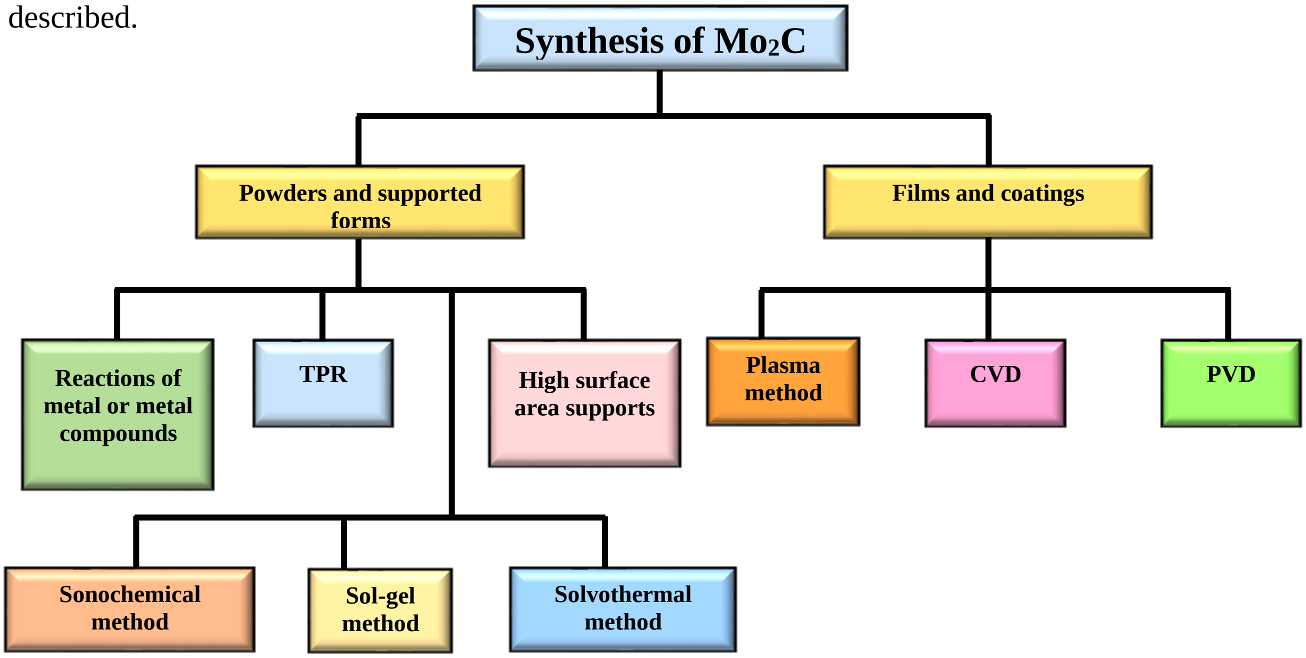

Figure 2.1: Pictorial representation of different synthesis methods.

2.2 Synthesis of nano Mo_2C

2.2.1 Direct carburization and Temperature programmed reaction (TPR)

The traditional methods to synthesize Mo_2C at higher temperature (>1000 °C) include direct carburization method of molybdenum oxide (MoO_3) and Mo metal. The obtained materials were of high particle sizes and low specific surface area. **Covington *et al.*** [1] synthesized powders of two molybdenum carbides (Mo_2C and MoC_{1-x}) by TPR method in temperature range 950-1050 °C. Mo_2C and MoC_{1-x} were prepared by reacting MoO_3 with fixed molar ratio of CH_4/H_2 and carbon monoxide (CO)/H_2 gas mixtures, respectively. **Xiao *et al.*** [2] explored the effect of various carburizing agents on preparation of molybdenum carbide prepared by temperature programmed reaction (TPR) at 800 °C. The mixtures of methane and hydrogen, ethane and hydrogen, butane and hydrogen were used as carburizing gases and the results confirmed that the choice of hydrocarbons significantly affect the structure and texture of synthesized product. Particle size reduces with increase in chain length of hydrocarbons. The temperature and pressure generated further affects the transformation from oxycarbide to carbide phase. Using methane as carbon source gives rise to hexagonal phase of carbide, whereas using butane as carbon source results in face centered cubic (fcc) phase of carbide. Using ethane as carbon source resulted the carbides with mixed phase composition with hexagonal as predominant one. **Choi *et al.*** [3] studied the reduction and carburization of molybdic acid under the atmosphere of CH_4/H_2 through temperature-programmed carburization. The results reveal the transformation of molybdic acid to Mo_4O_{11}, MoO_2, and Mo metal, which readily carburized to hexagonal Mo_2C. The degree of carburization affects both the number and the quality of sites. **Nelson and Wagner** [4] synthesized orthorhombic molybdenum carbide by alkalide reduction at temperatures (>575 ºC) having a broader size distribution (3.0 to 50 nm). These methods seem simple, but different type of gases are utilized for synthesis, which makes the product costly.

2.2.2 Thermochemical synthesis

In this process thermally activated chemical reactions take place between molybdenum source and the solid carbon species when mixed together. In this regard, **Yang *et al.*** [5] observed the effect carbon source on particle size and surface area of the synthesized product. Nano crystallites of Mo_2C were synthesized by reacting molybdenum chloride ($MoCl_5$) with graphite and CNT as carbon sources in presence of metallic Na. They observed that the particle size is reduced whereas surface area is increased while using CNT as carbon source. **Wang *et al.*** [6] synthesized β-Mo_2C

by reacting mixed salt precursor of $(NH_4)_4(HMT)_2Mo_7O_{24}4H_2O$ (Mo-HMT) and HMT (hexamethylenetetramine) in Argon atmosphere at 700 °C. **Redyy *et al.*** [7] synthesized Mo_2C (β-Mo_2C and α-Mo_2C) thermochemically at 1000 °C and investigated their structural stability. The concentration of C in Mo lattice was higher than equilibrium C-level in β-Mo_2C than α-Mo_2C. The high agglomeration of particles was observed in case of α-Mo_2C. The reaction kinetics of C diffusion in Mo was higher for the formation of β-Mo_2C. In this method, the requirement of the inert atmosphere is necessary to avoid the oxygen diffusion at higher synthesis temperatures.

2.2.3 Mechano-chemical, microwave and sono-chemical synthesis

Mechano-chemical synthesis is a top-down approach used to produce uniform and smaller size materials from mixture of starting precursors. The particles so obtained are usually of uniform size and shape exhibiting narrow range of size distribution. Microwave is a powerful tool to synthesize materials in less time due to fast heating of reaction mixtures. In Sono-chemical synthesis the reaction time reduces from several hours to only a few minutes inside the chamber. The physical phenomena of acoustic cavitation in which, the formation, growth, and implosive collapse of bubbles lead to the chemical and physical affects during sono-chemical synthesis. A very different mechanism of action make it powerful tool for material synthesis including graphene, crystallization of metals, metal oxides and carbide catalysts. **Xia *et al.*** [8] synthesized and studied the structural/thermal stability of Mo_2C and Mo_3C_2, respectively. Different molar concentrations of graphite were used as carbon source and MoO_3 as molybdenum source in presence of aluminum (Al). Mechanically induced self-propagating reaction (MSR) facilitate the transformation from MoO_3 to Mo_2C. **Vallance *et al.*** [9] illustrated a smaller time scale, microwave (MW) assisted method to synthesize Mo_2C from MoO_3 and Mo. The pure Mo_2C was prepared in less time frame using high power MW system. **Hoseinpur *et al.*** [10] used microwave assisted combustion method to synthesize hexagonal Mo_2C nano crystallites by zincothermic reduction. MoO_3 and amorphous carbon (commercial) was used as Mo and C source, respectively. **Hyeon *et al.*** [11] synthesized FCC nano molybdenum carbide by sono-chemical decomposition of molybdenum hexacarbonyl. The aggregated Mo_2C crystals of 2 nm size obtained were highly active catalyst for dehydrogenation. In mechano-chemical synthesis although the particle size is smaller and uniform, but the phase purity having strong dependence on synthesis temperature and carbon composition remained an unresolved issue. However, the other two synthesis methods are suitable for lab scale production rather than producing the materials in bulk.

2.2.4 Chemical vapor deposition (CVD) method

CVD also called chemical vapor reaction (CVR) method is usually used to deposit the films over the heated substrate and also for a protective coating by chemical reaction of gaseous phase species within a reactor. Different coating layers are generated where the nucleation occurs on the substrate when gaseous phase species are transported through the reactor. The precursors can be solid or liquid, but within the CVD chamber they react in gaseous form. **Lu *et al.*** [12] prepared different molybdenum carbides like MoC_{1-x}, MoC_{1-x}, and Mo_2C by mixture of $MoCl_5/H_2/C_2H_4$ at 800 °C. The study also investigated the effect of H_2 on phase formation, composition and morphology. Same group also studied the effect of various synthesis parameters on the nano crystallinity of the synthesized phase [13]. **Eroglu *et al.*** [14] showed that deposition of Mo_2C film by CVD using MoO_3 is better as compared to those produced by $MoCl_5$, because of their narrow range of depositions. However, physical vapor deposition (PVD) is a way of producing metal-based coatings by generation of partially ionized metal vapors. These vapors react with certain gases inside chamber and form a thin film on the substrate with a specified composition. The commonly used PVD methods are sputtering and cathodic arc. **Weigert *et al.*** [15] employed PVD route for the synthesis of molybdenum carbide by depositing molybdenum on carbon foam substrate. The heating of coated films in vacuum promotes the interaction of molybdenum with carbon foam to produce molybdenum carbide. The Mo-C/foam samples show the promising potential applications in electro catalysis as stable elctrocatalyts. These methods are useful for depositing films, which require specific techniques for the synthesis. However, the morphology is uncontrolled. After the reports of **Vrubel and Hu** [16] regarding the potential applications of commercial Mo_2C as efficient catalyst for HER in both acidic and alkaline electrolyte, the synthesis of Mo_2C became an interesting research area. To improve the efficiency and stability of Mo_2C several modification have been done to control the size and shape of particles for better efficiency and stability.

2.2.5 Chemical synthesis (solid solution route)

This method is mostly preferred for shape and size controlled synthesis, which is essential for enhancing the catalytic activity. The synthesis is carried in two or more steps: (1) a mixture of Mo salt and carbon source are mixed in water for polymerization or forming a complex in presence of some reducing agent or surfactant. The prepared solution is then dried to remove some water content and the obtained product is then carburized either in some inert atmosphere or in an autoclave to get the final product. **Stux *et al.*** [17] synthesized molybdenum carbide and nickel-molybdenum carbide by Pechini process (Sol-gel method). For it the mixture of precursor (metal acetate) with citric acid and ethylene glycol are heated under H_2 atmosphere with precursor solution being carbon source itself. Molybdenum carbide was prepared by heating precursor solution upto 850 °C. Using nickel and molybdenum precursors, molybdenum carbide was synthesized at 700 °C and nickel-molybdenum carbide at 800-900 ºC. **Dong *et al.*** [18] modified the technique for the synthesis of Mo_2C catalyst for H_2 production by mixing $((NH_4)_6Mo_7O_{24}4H_2O)$ and aniline in flask containing 40 ml deionized water and retaining the pH at 4 using hydrochloric acid (HCl). The solution was kept at 50 °C for 4 hours after that it was washed with water and ethanol. Finally the obtained powder was dried overnight in vacuum at 60 °C. The product was then heated in argon (Ar) atmosphere for different temperatures (675 and 775 °C) to get the modified Mo_2C. The obtained products were utilized for HER activity. These studies show that the chemical methods have many advantages over other processes like wide temperature range in between 500 to 1000 °C, effective way to control morphology, size reduction, and uniform carburization. However, the multi-step and longtime process utilizing large energy during processes hinders their commercial application.

For enhanced activity and stability of electrocatalyst, currently the research is focused on developing hybrid systems like $C@Mo_2C$ where nature of carbon plays important role. Moreover, doping of metal/non-metal in $C@Mo_2C$ helps to achieve enhanced activity. Overall goal of the entire work is to synthesize such composites to enhance HER and energy storage capacity of the synthesized product. Different researchers have adopted various methods to synthesize Mo_2C based catalysts for HER activity. **Weidman *et al*.**[19] synthesized Mo_2C and WC by direct carburzation of Mo and W foils and studied their electrochemical stability in different pH like acidic, basic and neutral. The Mo_2C shows little less stability than WC in acidic medium. To improve the stability **Kelly *et al.*** [20] synthesized Mo_2C through TPR and deposited monolayer (ML) of Pd through PVD. The ML deposition of Pd over Mo_2C demonstrated higher activity and stability. The summary of the work done so far for the synthesis of Mo_2C, $C@Mo_2C$ is presented in Table 2.1.

Apart from this extensive progress is has been made to enhance the energy storage capacity of the materials, which possess higher charging capacity and exhibit charging-discharging stability for longer duration. In this case carbon structures and carbon supported materials exhibit the exceptional performances [21,22]. The carbon strautres derived from waste have also shown promising application for supercapacitors [23]. TMC supported by carbon also have high potential applications for EDLCs and supercapacitors in both acidic and basic mediums [24,25]. The EDLC or super capacitor performances of the reported results are also tabulated in Table 2.2. as reading reference to compare the work done in present investigation.

Table 2.1: Synthesis of Mo_2C and C supported Mo_2C for HER applications.

Sample	Author	Year	Synthesis method	Carbon support	Morphology	Size (nm)	Surface area (m^2/g)	Tafel slope ($mVdec^{-1}$)	Reference
β-Mo_2C	Wan *et al.*	2014	Chemical route	-	Nanospheres	120	90.42	-	26
Np-Mo_2C NWs	Liao *et al.*	2014	Chemical pyrolysis	-	Nano wires	10-15	67.6	60	27
Mo_2C NWs **Mo_2C NS**	Ge *et al.*	2014	Chemical route	-	Nano wires (NW) Nano sheets (NS)	30-60		55.8 64.5	28
MoC_x nanooctahedrons	Wu *et al.*	2014	Chemical route (MOF)	-	nanooctahedrons		147	53	29
Mo_2C	Xiao *et al.*	2014	Chemical route	-	Nano rods	3.4	52	45	30
Mo_2C/CNT	Alhajri *et al.*	2014	Microwave	Graphitic carbon	spherical	3-20	308	110-235	31
Mo_2C/GCSs	Cui *et al.*	2014	Solid state raection	Graphene sheets	Nanoparticles	5-23	-	62.6	32
MoC-G **Mo_2C-G**	He *et al.*	2015	In-situ synthesis	Graphene	Nanoparticles	2.5 5		88 116	33

Mo_2C-RGO **Mo_2C**	Pan *et al.*	2014	Hydrothermal + Carburization	RGO	Amorphous	10	-	57.3 76.7	34
Mo_2C/CXG **Mo_2C/CNT**	Sljukic *et al.*	2015	Chemical route + wet impregnation	Carbon nano tubes (CNT) Carbon xerogel (CXG)	Nanoparticles	10-60	410 182	251 261	35
MCNs@carbon **MoDCA-5** **MoDCA-2**	Ma *et al.*	2015	One-step protocol synthesis (chemical route)	Graphene shells	Nanoparticles	3 nm	70	64 41	36
Mo_2C	Meyer *et al.*	2015	Oxidation-carburization	-	Layered structure	-	-	-	37
β-Mo_2C	Tang *et al.*	2015	Calcination-reduction	-	Nanoparticles	100	120	55	38
Mo_2C/CC **C-Mo_2C** **P-Mo_2C**	Fan *et al.*	2015	Chemical route	Carbon cloth (CC)	Nanoparticles	20-100	-	124 168 128	39

Mo_2C	Zhang *et al.*	2015	Chemical route	Porous amorphous carbon	Tubular shape	3-20	-	57.5-74	40
Mo_2C-C-15 (OER)	Luo *et al.*	2016	CVD	Carbon spheres	York-shell spheres		119	72.2-86.7	41
Mo_2C/C	Mu *et al.*	2016	Solid state reaction	Graphitic carbon	Nanoparticles	8-15	259	52	42
Mo2C/GNS	Shen and Gong	2016	Carburization process	graphite nano sheets	Nanoparticles	26	162	42-58	43
Mo_2C	Ojha *et al.*	2016	Chemical complexation + carburization	graphene	Nano rods	-	-	67-101	44
Mo_2C-9h **Mo_2C-12h**	Tang *et al.*	2016	Chemical route	-	Particles	100 300	0.101 0.008	55	45
Mo_2C@NPC **Mo_2C@NPC/NPRGO**	Li *et al.*	2016	Chemical route	Reduced graphene oxide (RGO)	Nanoparticles			126.4 33.6	46
β-Mo_2C/C	Qamar *et al.*	2016	MOF + carburization	Mesoporous carbon	Spherical	20-40		63.6	47
2D Mo_2C	Geng *et al.*	2017	CVD	Graphene	Stacked layers	-	-	73	48

MoC@NPC **Mo$_2$C@NPC**	Ji *et al.*	2017	Chemical route	Carbon matrix	Nanoparticles	10 10-15		75.3-118 52.5-62.1	49
MoC/C **MoC@C**	Lv *et al.*	2017	Chemical route	Layered carbon	Solid spheres Cavity induced spheres	3.9 3.5	23.57 149.4	63.6 93.3	50
Mo2C/C	Yang *et al.*	2018	Polymerization + carburization	Carbon sheets	Hollow nanospheres	<10	91.6	75	51
β-Mo$_2$C	Xing *et al.*	2019	Chemical route	Carbon matrix	Nanoparticles	5-30	334.7	66.5-188.8	52
MoC$_x$@SWCNTs	Cui *et al.*	2019	Chemical route	Single wall (SW) CNTs (SWCNTs)	Nanoparticles	1-4	467	115	53

Table 2.2: Synthesis of metal and non-metal doped C supported Mo_2C and other Mo_2C composites for HER.

Sample	Author	Year	Synthesis method	Carbon support	Morphology	Size (nm)	Surface area (m^2/g)	Tafel slope ($mVdec^{-1}$)	Reference
Mo_2C-WC	Xiao *et al.*	2015	Hydrothermal/ carburization	Layered carbon	nanowires		44	56	54
MoS_x@Mo_2C	Tang *et al.*	2015	Chemical route	Sulphur decorated	Lamellar structures	-	-	44-52	55
MoC_x@C-1 **MoC_x-2**	Yang *et al.*	2016	Hydrothermal/ carburization	N-doped graphene No coating	Core shell Nanoparticles	5-50 2-10	- -	56 93	56
Mo_2C@N-CNFs	Wu *et al.*	2016	Chemical route	N-doped carbon nano fiber (N-CNF)	Nanoparticles	<5	81.98	70	57
Ag/Mo_2C/CNTs	Li et al.	2016	Chemical route	Ag doped CNTs	Nano wires	50	10.5		58
MoS_2/Mo_2C	Zhao *et al.*	2017	Hydrothermal/ carburization	-	Nano sheets	9 nm thick	-	53-63	59

P-Mo_2C@CNWs	Shi *et al.*	2017	Chemical route	Graphite	Nano wires	120	-	50-59	60
Mo_2C-TiO_2	Yue *et al.*	2017	Hydrothermal	C+TiO_2	Nanoparticles	10	105	-	61
α-MoC **β-Mo_2C**	Lin *et al.*	2017	Oxidation + carburization	Pt	-	-	-	-	62
Mo_2C@2D-NPCs	Lu *et al.*	2017	Polymerization + Carburization	N doped carbon nano sheets	Nanoparticles	-	110.2	46	63
α-Mo_2C	Garcia *et al.*	2017	Carbothermal	-	Nanoparticles	20	-	61	64
2D Mo_2C/C lamellas	Peng *et al.*	2017	Chemical route	Graphitic carbon lamellas	Nanoparticles	3-4	290.3		65
Mo_2C/CTSSs	Xu *et al.*	2018	Chemical route	Tube-sheet carbon	Tubular structure	2-10	117	54-59	66
Mo_2C	Jing et al.	2018	Chemical route	N-doped Carbon	Nanobelt	-		51.3	67
Mo_2C@NC	Li *et al.*	2018	High temperature pyrolysis	N-doped Carbon	Nano flakes	2-3	240.2	45-63	68

Mo2C/G-NCS	Wei *at al.*	2018	Spray drying + annealing	N-doped porous Carbon spheres	Nanoparticles	4.5- 6	-	39 80	69
β-Mo_2C **Fe-Mo_2C** **Co-Mo_2C** **Ni-Mo_2C** **Cu- Mo_2C** **Ag- Mo_2C** **Pt- Mo_2C**	Chen *et al.*	2018	Organic-inorganic precursor carburization		Random morphology Wire likes shape	3-10	20.7 3.2 9.7 15.3 14.9 14.3 48.3	124 132 89 81 84 55 32	70
MoS_2/Mo_2C	Luo *et al.*	2019	Hydrothermal + CVD	C/MoS_2	Microspheres	1.16 (µm)		43	71
Mo_2C@C@Pt	Chi *et al.*	2019	Carburization + Reduction	C & Pt	Nanospheres	90	128.4	28	72
Mo_2C/CNT	Song *et al.*	2019	Chemical route	N doped Carbon	Nanoparticles	-	149-205	81-86	73
MoC-MoP/BCNC NFs	Chen *et al.*	2019	Chemical route	N doped CNFs	Nanoparticles	3.8	-	58	74
Mo_2C	An and Xu	2019	Chemical route	N doped 3D porous	Nanoparticles	4-6	-	88	75

				carbon					
β-Mo$_2$C/N, P	Tan *et al.*	2019	Chemical route	N, P co-doped Carbon	Nanoparticles	-	9.83	672.55.3	76
N-Mo$_x$C@C HSs	Xiong *et al.*	2019	CVR	N doped carbon sheet	Nanosheet	50	99.9-109.6	60-94	77
Mo$_2$C@C	Liu *et al.*	2019	Hydrothermal route	N doped Carbon	sheet	5-8 (µm)	-	53-55	78
Co/β-Mo$_2$C	Ouyang *et al.*	2019	Chemical route	N doped Carbon	Nanoparticles	21.4	-	170	79

Along with HER, the different methods and modifications were done to enhance the supercapacitor/EDLC performance of the supported Mo$_2$C species. Certain research groups study the bifunctional (HER and EDLC) application of supported Mo$_2$C at the same time, in this regard some reports are similar as given in (Table 2.1 and 2.2). But the support of carbon, non-metal or metal doped carbon over Mo$_2$C enhances the EDLC performance. The heterojunction/interface of Mo$_2$C and C not only improve efficiency but also enhance the stability. The advances in the synthesis of EDLCs in the recent years is given in Table 2.3 below:

Table 2.3: Synthesis of carbon, nitrogen supported carbon coated Mo_2C for EDLC applications.

Sample	Author	Year	Synthesis method	Carbon support	Morphology	Size (nm)/ Surface area (m^2/g)	EDLC ($mFcm^{-2}$)	Reference
Mo_2C/CXG **Mo_2C/CNT**	Sljukic *et al.*	2015	Chemical route + wet impregnation	Carbon nano tubes (CNT) Carbon xerogel (CXG)	Nanoparticles	10-60/410 182	Ratio 2.3	35
MCNs@carbon **MoDCA-5** **MoDCA-2**	Ma *et al.*	2015	One-step protocol synthesis (chemical route)	Graphene shells	Nanoparticles	3/14&70	22.3 2.5	36
Mo_2C/C	Mu *et al.*	2016	Solid state reaction	Graphitic carbon	Nanoparticles	8-15/259	38.6	42
Mo_2C@NPC **Mo_2C@NPC/NPRGO**	Li *et al.*	2016	Chemical route	Reduced graphene oxide (RGO)	Nanoparticles	-	0.092 17.9	46

MoC_x@C-1 **MoC_x-2**	Yang *et al.*	2016	Hydrothermal/ carburization	N-doped graphene No coating	Core shell Nanoparticles	5-50/- 2-10/-	Higher lower	56
MoS_2/Mo_2C	Zhao *et al.*	2017	Hydrothermal/ carburization	-	Nano sheets	9 nm thick	51-158	59
Mo_2C@NC	Li *et al.*	2018	High temperature pyrolysis	N-doped Carbon	Nano flakes	2-3/240.2	18.0	68
Mo_2C@C@Pt	Chi *et al.*	2019	Carburization + Reduction	C & Pt	Nanospheres	90/128.6	3.8	72
MoC-MoP/BCNC NFs	Chen *et al.*	2019	Chemical route	N doped CNFs	Nanoparticles	3.8	70.8	74
Mo_2C@3DNMC	An and Xu	2019	Chemical route	N doped 3D porous carbon	Nanoparticles	4-6	11.56	75
β-Mo_2C/N, P	Tan *et al.*	2019	Chemical route	N, P co-doped Carbon	Nanoparticles	-/9.83	1.57-2.22	76
N-Mo_xC@C HSs	Xiong *et al.*	2019	CVR	N doped carbon sheet	Nanosheet	50/ 99.9-109.6	0.8-2.8	77

Mo_2C@C	Liu *et al.*	2019	Hydrothermal route	N doped Carbon	sheet	5-8 (µm)	20.29-45.28	78
Co/β-Mo_2C	Ouyang *et al.*	2019	Chemical route	N doped Carbon	Nanoparticles	21.4	0.7-2.1	79
Mo_2C	Morishita *et al.*	2007	Solution + carburization	Carbon coated	Nanoparticles	5-200/350	50 Fg^{-1}	80
(Mo_2C) CDC	Leis *et al.*	2010	Carburization + Chlorination	Coated carbon	-	-/ 1472-2121	83-130 Fg^{-1}	81
C(Mo_2C)	Thomberg *et al.*	2010	High temperature decomposition	-	-	-/ 163-1855	35-143 Fg^{-1}	25
CDC-Mo2C	Eskusson *et al.*	2011	Commercial (Sigma Aldrich)	Amorphous + graphitic	Porous structures	10-100/ 1855	supercapacitors	82
C(Mo_2C)	Kruusma *et al.*	2014	-	Carbon	In-situ with XPS	-	EDLC	83

2.3 Gaps in study

The literature review reveals that different efforts have been made to enhance the HER activity and EDLC performance of the Mo_2C elctrocatalyst. The carbon support in different forms (graphene, RGO, CNSs, CNTs, graphitic and amorphous) enhances the HER activity to the greater extent. The doping of metal and non-metal elements has given enhanced HER results. The synthesis of these Mo_2C carbon supported species is multistep, time and energy consuming. The simple in-situ reduction-carburization inside the autoclave will provide fine nano powders at relatively lower temperatures, because the pressure generated inside the autoclave will contribute positively during the synthesis. The HER and EDLC activity is dependent on the type and amount of carbon source used along with the reaction parameters like temperature, time and source of precursor. The role of supported carbon has been discussed in detail, but the information regarding the in-situ developed supported carbon over Mo_2C on HER activity and EDLC performance has not been explored much. Different carbon and nitrogen sources are required for the synthesis of C-Mo_2C and C/N-Mo_2C, respectively. Although the chemical route synthesis is advantageous than other methods, but the long time synthesis, high energy consumption during synthesis and multistep processing limits the applicability of the route for laboratory tests rather than commercial use. The autoclave synthesis method is useful for bulk production in lesser time. The study by **Chen *et al.*** [84] have shown the possibility of such in-situ reduction and carburization of Mo source to get Mo_2C. In their study they have taken metallic magnesium (Mg) powder with molybdenum trioxide (MoO_3) and potassium acetate (CH_3COOK) in an autoclave. Heating the mixture at 600 °C could lead to formation of Mo_2C. However, they have not tried with other carbon sources. Moreover, the reaction kinetics as well as the synthesis parameters, which control the size, stoichiometry and also the phase formation of molybdenum carbide by this route has not been investigated. To make the HER and EDLCs useful commercially, the synthesis of low cost electrocatalysts and electrode materials is essential. At the same time the method of synthesis method should be simple, eco-friendly and low energy consumption. The autoclave synthesis is one of the most simple and highly environmental friendly. To the best of our knowledge, none of the research groups has utilized the nitrogen (N) present in AHM as the in-situ non-metal substituted catalyst support in carbon matrix over Mo_2C. The in-situ developed carbon support over Mo_2C and N incorporated in carbon matrix over Mo_2C has not been explored. The use of the low cost precursor will enable this process cost effective and of industrial importance. Non-biodegradable waste carbon sources like (waste polyethene and waste plastic) have not used for such synthesis. The use of these waste not only reduces the cost but also addresses the environmental issues caused due to these wastes. In order to overcome this problem, various thermochemical recycling processes viz thermo-catalytic, pyrolysis, incineration, gasification, pyrolysis-reforming strategies have been adopted to convert waste plastics into transport fuel grade hydrocarbons [85–88]. However, the zero emission of the toxic gases in the thermo chemical conversion of plastic wastes to fuel is still an unresolved and critical issue. The high production of tar, and carbonaceous gases emission during their decomposition again create environmental problems. Moreover, some amount of these non-biodegradable wastes are landfilled; again problematic to the human health. Recently the generation of H_2 and carbon nano tubes (CNTs) from waste plastics have been reported, where the role of metal catalyst used during processing has been highlighted [89]. To increase the efficiency of the H_2 production from waste plastics the search of suitable and stable catalyst is still prevailing. The CNTs are the useful catalyst and catalyst support materials in various energy production and storage devices.

The goal of the present study is to synthesize Mo_2C electrocatalyts for HER and EDLC in a specially designed autoclave using analytical grade hydrocarbons and non-biodegradable waste as carbon source. The use of these wastes as carbon source (rich in C and H) via autoclave synthesis will be highly economical and eco-friendly. The optimization of the reaction conditions and effect of different kind waste carbon on phase formation and electrocatalytic activities will be explored. The effect of N incorporation in C matrix over Mo_2C developed inside the autoclave on HER activity and EDLC performance will also be explored. Based on the gaps in study, the following objectives have been framed:

2.4 Objectives

- Synthesis of molybdenum carbide nanopowders by using different carbon sources and molybdenum precursors.
- To optimize the synthesis parameters for pure phase Mo_2C nano powders.
- To study the electrochemical activity of synthesized nano powders.

The methodology opted for synthesis of molybdenum carbides, effect of processing parameters on phase formation is given in next chapters.

References

1 L. Covington, K. Munirathinam, A. Islam and K. Roberts, *Polish Journal of Chemical Technology*, 2012, **14**, 28–34.

2 T. Xiao, A. P. E. York, K. S. Coleman, J. B. Claridge, J. Sloan, J. Charnock and M. L. H. Green, *Journal of Materials Chemistry*, 2001, **11**, 3094–3098.

3 J. S. Choi, G. Bugli and G. Djéga-Mariadassou, *Journal of Catalysis*, 2000, **193**, 238–247.

4 J. A. Nelson and M. J. Wagner, *Chemistry of Materials*, 2002, **14**, 1639–1642.

5 Z. Yang, P. Cai, L. Shi, Y. Gu, L. Chen and Y. Qian, *Journal of Solid State Chemistry*, 2006, **179**, 29–32.

6 H. M. Wang, X. H. Wang, M. H. Zhang, X. Y. Du, W. Li and K. Y. Tao, *Chemistry of Materials*, 2007, **19**, 1801–1807.

7 K. M. Reddy, T. N. Rao, J. Revathi and J. Joardar, *Journal of Alloys and Compounds*, 2010, **494**, 386–391.

8 Z. P. Xia, Y. Q. Shen, J. J. Shen and Z. Q. Li, *Journal of Alloys and Compounds*, 2008, **453**, 185–190.

9 S. R. Vallance, S. Kingman and D. H. Gregory, *Chemical Communications*, 2007, 742–744.

10 A. Hoseinpur, M. Sh. Bafghi, J. Vahdati Khaki, M. Jalaly and M. Sakaki, *International Journal of Refractory Metals and Hard Materials*, 2015, **50**, 191–196.

11 T. Hyeon, M. Fang and K. S. Suslick, *Journal of the American Chemical Society*, 1996, **118**, 5492–5493.

12 J. Lu, H. Hugosson, O. Eriksson, L. Nordström and U. Jansson, *Thin Solid Films*, 2000, **370**, 203–212.

13 J. U. Lu and U. Jansson, *Thin Solid Films*, 2001, **396**, 53–61.

14 S. Eroglu and H. I. Bakan, *Key Engineering Materials*, 2009, **264**–**268**, 121–124.

15 E. C. Weigert, J. South, S. A. Rykov and J. G. Chen, *Catalysis Today*, 2005, **99**, 285–290.

16 H. Vrubel and X. Hu, *Angewandte Chemie - International Edition*, 2012, **51**, 12703–12706.

17 A. M. Stux, C. Laberty-Robert and K. E. Swider-Lyons, *Journal of Solid State Chemistry*, 2008, **181**, 2741–2747.

18 J. Dong, Y. Shi, C. Huang, Q. Wu, T. Zeng and W. Yao, *Applied Catalysis B: Environmental*, 2019, **243**, 27–35.

19 M. C. Weidman, D. V. Esposito, Y. C. Hsu and J. G. Chen, *Journal of Power Sources*, 2012, **202**, 11–17.

20 T. G. Kelly, S. T. Hunt, D. V. Esposito and J. G. Chen, *International Journal of Hydrogen Energy*, 2013, **38**, 5638–5644.

21 H. Raj and A. Sil, *Ionics*, 2018, **24**, 2543–2553.

22 M. Wahid, D. Puthusseri, Y. Gawli, N. Sharma and S. Ogale, *ChemSusChem*, 2018, **11**, 506–526.

23 M. Biswal, A. Banerjee, M. Deo and S. Ogale, *Energy and Environmental Science*, 2013, **6**, 1249–1259.

24 E. H. Ang, K. N. Dinh, X. Sun, Y. Huang, J. Yang, Z. Dong, X. Dong, W. Huang, Z. Wang, H. Zhang and Q. Yan, *Research*, 2019, **2019**, 1–14.

25 T. Thomberg, A. Jänes and E. Lust, *Electrochimica Acta*, 2010, **55**, 3138–3143.

26 C. Wan, Y. N. Regmi and B. M. Leonard, *Angewandte Chemie - International Edition*, 2014, **53**, 6407–6410.

27 L. Liao, S. Wang, J. Xiao, X. Bian, Y. Zhang, M. D. Scanlon, X. Hu, Y. Tang, B. Liu and H. H. Girault, *Energy and Environmental Science*, 2014, **7**, 387–392.

28 C. Ge, P. Jiang, W. Cui, Z. Pu, Z. Xing, A. M. Asiri, A. Y. Obaid, X. Sun and J. Tian, *Electrochimica Acta*, 2014, **134**, 182–186.

29 H. Bin Wu, B. Y. Xia, L. Yu, X. Y. Yu and X. W. Lou, *Nature Communications*, 2015, **6**, 1–17.

30 P. Xiao, Y. Yan, X. Ge, Z. Liu, J. Y. Wang and X. Wang, *Applied Catalysis B: Environmental*, 2014, **154–155**, 232–237.

31 N. S. Alhajri, D. H. Anjum and K. Takanabe, *Journal of Materials Chemistry A*, 2014, **2**, 10548–10556.

32 W. Cui, N. Cheng, Q. Liu, C. Ge, A. M. Asiri and X. Sun, *ACS Catalysis*, 2014, **4**, 2658–2661.

33 C. He and J. Tao, *Chemical Communications*, 2015, **51**, 8323–8325.

34 L. F. Pan, Y. H. Li, S. Yang, P. F. Liu, M. Q. Yu and H. G. Yang, *Chemical Communications*, 2014, **50**, 13135–13137.

35 B. Šljukić, M. Vujković, L. Amaral, D. M. F. Santos, R. P. Rocha, C. A. C. Sequeira and J. L. Figueiredo, *Journal of Materials Chemistry A*, 2015, **3**, 15505–15512.

36 R. Ma, Y. Zhou, Y. Chen, P. Li, Q. Liu and J. Wang, *Angewandte Chemie - International Edition*, 2015, **54**, 14723–14727.

37 S. Meyer, A. V. Nikiforov, I. M. Petrushina, K. Köhler, E. Christensen, J. O. Jensen and N. J. Bjerrum, *International Journal of Hydrogen Energy*, 2015, **40**, 2905–2911.

38 C. Tang, A. Sun, Y. Xu, Z. Wu and D. Wang, *Journal of Power Sources*, 2015, **296**, 18–22.

39 M. Fan, H. Chen, Y. Wu, L. L. Feng, Y. Liu, G. D. Li and X. Zou, *Journal of Materials Chemistry A*, 2015, **3**, 16320–16326.

40 K. Zhang, C. Li, Y. Zhao, X. Yu and Y. Chen, *Physical chemistry chemical physics*, 2015, **17**, 16609–14.

41 Y. Luo, Z. Wang, Y. Fu, C. Jin, Q. Wei and R. Yang, *Journal of Materials Chemistry A*, 2016, **4**, 12583–12590.

42 Y. Mu, Y. Zhang, L. Fang, L. Liu, H. Zhang and Y. Wang, *Electrochimica Acta*, 2016, **215**, 357–365.

43 Y. Shen and B. Gong, *Journal of The Electrochemical Society*, 2016, **163**, H1060–H1065.

44 K. Ojha, S. Saha, H. Kolev, B. Kumar and A. K. Ganguli, *Electrochimica Acta*, 2016, **193**, 268–274.

45 C. Tang, Z. Wu and D. Wang, *ChemCatChem*, 2016, **8**, 1961–1967.

46 J. Sen Li, Y. Wang, C. H. Liu, S. L. Li, Y. G. Wang, L. Z. Dong, Z. H. Dai, Y. F. Li and Y. Q. Lan, *Nature Communications*, 2016, **7**, 11204.

47 M. Qamar, A. Adam, B. Merzougui, A. Helal, O. Abdulhamid and M. N. Siddiqui, *Journal of Materials Chemistry A*, 2016, **4**, 16225–16232.

48 D. C. Geng, X. X. Zhao, Z. X. Chen, W. W. Sun, W. Fu, J. Y. Chen, W. Liu, W. Zhou and K. P. Loh, *Advanced Materials*, 2017, **29**, 1700072–1700080.

49 L. Ji, J. Wang, L. Guo and Z. Chen, *Journal of Materials Chemistry A*, 2017, **5**, 5178–5186.

50 C. Lv, Z. Huang, Q. Yang, G. Wei, Z. Chen, M. G. Humphrey and C. Zhang, *Journal of Materials Chemistry A*, 2017, **5**, 22805–22812.

51 Y. Yang, M. Luo, Y. Xing, S. Wang, W. Zhang, F. Lv, Y. Li, Y. Zhang, W. Wang and S. Guo, *Advanced Materials*, 2018, **30**, 1–8.

52 J. Xing, Y. Li, S. Guo, T. Jin, H. Li, Y. Wang and L. Jiao, *Electrochimica Acta*, 2019, **298**, 305–312.

53 T. Cui, J. Dong, X. Pan, T. Yu, Q. Fu and X. Bao, *Journal of Energy Chemistry*, 2019, **28**,

123–127.
54 P. Xiao, X. Ge, H. Wang, Z. Liu, A. Fisher and X. Wang, *Advanced Functional Materials*, 2015, **25**, 1520–1526.
55 C. Tang, W. Wang, A. Sun, C. Qi, D. Zhang, Z. Wu and D. Wang, *ACS Catalysis*, 2015, **5**, 6956–6963.
56 X. J. Yang, X. J. Feng, H. Q. Tan, H. Y. Zang, X. L. Wang, Y. H. Wang, E. B. Wang and Y. G. Li, *Journal of Materials Chemistry A*, 2016, **4**, 3947–3954.
57 Z.-Y. Wu, B.-C. Hu, P. Wu, H.-W. Liang, Z.-L. Yu, Y. Lin, Y.-R. Zheng, Z. Li and S.-H. Yu, *NPG Asia Materials*, 2016, **8**, 1–8.
58 X. Li, X. Ma, X. Du, J. Zheng, X. Hao, A. Abudula and G. Guan, *Physical Chemistry Chemical Physics*, 2016, **18**, 32780–32785.
59 Z. Zhao, F. Qin, S. Kasiraju, L. Xie, K. Alam and S. Chen, *ACS Catalysis*, 2017, **7**, 7312–7318.
60 Z. Shi, K. Nie, Z. J. Shao, B. Gao, H. Lin, H. Zhang, B. Liu, Y. Wang, Y. Zhang, X. Sun, X. M. Cao, P. Hu, Q. Gao and Y. Tang, *Energy and Environmental Science*, 2017, **10**, 1262–1271.
61 X. Yue, S. Yi, R. Wang, Z. Zhang and S. Qiu, *Journal of Materials Chemistry A*, 2017, **5**, 10591–10598.
62 L. Lin, W. Zhou, R. Gao, S. Yao, X. Zhang, W. Xu, S. Zheng, Z. Jiang, Q. Yu, Y. W. Li, C. Shi, X. D. Wen and D. Ma, *Nature*, 2017, **544**, 80–83.
63 C. Lu, D. Tranca, J. Zhang, F. RodrÍguez Hernández, Y. Su, X. Zhuang, F. Zhang, G. Seifert and X. Feng, *ACS Nano*, 2017, **11**, 3933–3942.
64 G. García, M. Roca-Ayats, O. Guillén-Villafuerte, J. L. Rodríguez, M. C. Arévalo and E. Pastor, *Journal of Electroanalytical Chemistry*, 2017, 793, 235–241.
65 L. Peng, Y. Nie, L. Zhang, R. Xiang, J. Wang, H. Chen, K. Chen and Z. Wei, *ChemCatChem*, 2017, **9**, 1588–1593.
66 Z. Xu, G. Zhang, C. Lu, H. Tian, X. Xi, R. Liu and D. Wu, *Journal of Materials Chemistry A*, 2018, **6**, 18833–18838.
67 S. Jing, L. Zhang, L. Luo, J. Lu, S. Yin, P. K. Shen and P. Tsiakaras, *Applied Catalysis B: Environmental*, 2018, **224**, 533–540.
68 J. Li, C. Zhou, J. Mu, E. C. Yang and X. J. Zhao, *RSC Advances*, 2018, **8**, 17202–17208.
69 H. Wei, Q. Xi, X. Chen, D. Guo, F. Ding, Z. Yang, S. Wang, J. Li and S. Huang, *Advanced Science*, 2018, **5**, 1–7.
70 M. Chen, Y. Ma, Y. Zhou, C. Liu, Y. Qin, Y. Fang, G. Guan, X. Li, Z. Zhang and T. Wang, *Catalysts*, 2018, **8**, 294.
71 Y. Luo, L. Tang, U. Khan, Q. Yu, H. M. Cheng, X. Zou and B. Liu, *Nature Communications*, 2019, **10**, 1–9.
72 J. Q. Chi, J. Y. Xie, W. W. Zhang, B. Dong, J. F. Qin, X. Y. Zhang, J. H. Lin, Y. M. Chai and C. G. Liu, *ACS Applied Materials and Interfaces*, 2019, **11**, 4047–4056.
73 Y. J. Song, J. T. Ren, G. Yuan, Y. Yao, X. Liu and Z. Y. Yuan, *Journal of Energy Chemistry*, 2019, **38**, 68–77.
74 N. N. Chen, Q. Mo, L. He, X. Huang, L. Yang, J. Zeng and Q. Gao, *Electrochimica Acta*, 2019, **299**, 708–716.
75 K. An and X. Xu, *Electrochimica Acta*, 2019, **293**, 348–355.
76 J. Tan, X. He, F. Yin, X. Liang, B. Chen, G. Li and H. Yin, *Journal of Materials Science*, 2018, **54**, 4589–4600.

77 T. Xiong, J. Jia, Z. Wei, L. Zeng, Y. Deng, W. Zhou and S. Chen, *Chemical Engineering Journal*, 2019, **358**, 362–368.

78 Y. Liu, B. Huang, X. Hu and Z. Xie, *International Journal of Hydrogen Energy*, 2019, **44**, 3702–3710.

79 T. Ouyang, Y. Q. Ye, C. Y. Wu, K. Xiao and Z. Q. Liu, *Angewandte Chemie - International Edition*, 2019, **58**, 1–7.

80 T. Morishita, Y. Soneda, H. Hatori and M. Inagaki, *Electrochimica Acta*, 2007, **52**, 2478–2484.

81 J. Leis, M. Arulepp, M. Käärik and A. Perkson, *Carbon*, 2010, **48**, 4001–4008.

82 J. Eskusson, A. Jänes, A. Kikas, L. Matisen and E. Lust, *Journal of Power Sources*, 2011, **196**, 4109–4116.

83 E. L. Jaanus Kruusma, Arvo T˜onisoo, Rainer P¨arna, Ergo N˜ommiste, *Journal of The Electrochemical Society*, 2014, **161**, 1266–1277.

84 Y. Chen, H. Zhang, J. Zhang, J. Ma, H. Ye, G. Qian and Y. Ye, *Materials Sciences and Applications*, 2011, **2**, 1313–1316.

85 and D. A. A. Sharmina Begum, M. G. Rasul, *International Journal of Environmental and Ecological Engineering*, 2012, **6**, 74–80.

86 Y. Zhang, M. A. Nahil, C. Wu and P. T. Williams, *Environmental Technology*, 2017, **38**, 2889–2897.

87 A. Ramos, E. Monteiro, V. Silva and A. Rouboa, *Renewable and Sustainable Energy Reviews*, 2018, **81**, 380–398.

88 S. Ohnishi, M. Fujii, M. Ohata, I. Rokuta and T. Fujita, *Resources, Conservation and Recycling*, 2018, **128**, 394–405.

89 D. Yao, Y. Zhang, P. T. Williams, H. Yang and H. Chen, *Applied Catalysis B: Environmental*, 2018, **221**, 584–597.

Chapter 3

Experimental Details

Overview

The materials used and the methodology followed for the synthesis of the nano molybdenum carbide is presented in this chapter. The synthesized products were characterized for their structural, morphological and surface features by X-ray diffraction (XRD), Raman spectroscopy, Field emission scanning electron microscopy (FESEM), Transmission electron microscopy (TEM), High resolution TEM (HRTEM), Energy dispersive spectroscopy (EDS), X-ray photoelectron spectroscopy (XPS) and Brunauer-Emmett-Teller (BET) analysis. Moreover, for structural optimization, the theoretical models used have been also presented. The details of the electrochemical analysis (HER activity and EDLC performance) and the procedure adopted for the fabrication of working electrode have also been included in the present chapter.

3.1 Synthesis of nano Mo_2C

3.1.1 Precursors

For the synthesis of nano Mo_2C particles, molybdenum trioxide (MoO_3, 99.99 %, Loaba Chemie), ammonium heptamolybdate tetrahydrate (AHM, $(NH_4)_6Mo_7O_{24}4H_2O$, SD Fine Chemicals, 99.9%), polypropylene (Haldia Petro Chemicals), Magnesium (Mg, 99%, SD Fine Chemicals), HCl (99% S.D. Fine Chemicals) were used. Waste plastic (Pipette tips), waste polyethene as carbon source were used in required quantity after proper washing and drying.

3.1.2 Methodology

The synthesis nano Mo_2C in the present work was carried out in a specially designed autoclave via reduction-carburization route [1–3]. For its synthesis, the required quantity of ingredeints MoO_3, Mg and polypropylene were first mixed with the help of agate-mortar. The above mixture was put in the autoclave. The autoclave was sealed properly and put in a furnace at room temperature. The temperature of the furnace was raised from room temperature to desired temperature in between 600 ºC to 800 ºC at constant heating rate of 5 ºC per minute and maintained at that particular temperature for different time durations. After that autoclave was allowed to cool to room temperature in the furnace and the product mixture was collected from the autoclave chamber. This product phase was washed with (1:1) diluted HCl to remove the MgO. After that the resultant powder was washed with distilled water many times to remove the HCl followed by vacuum drying at 120 ºC. The flow chart of the procedure adopted for the synthesis and the different characterization used are listed in Fig. 3.1. Finally the product phase was characterized and tested for its electrochemical properties. All these details have been presented in Fig. 3.1.

3.1.3 Molybdenum source

In the present work the Mo_2C was synthesized using two different low cost molybdenum sources MoO_3 and ammonium heptamolybdate tetrahydrate (AHM), respectively. The AHM acts both as molybdenum and nitrogen source, which provide a supportive substitute to get nitrogen incorporated Mo_2C for the enhanced electrochemical applications.

3.1.4 Reducing agent

Magnesium (Mg) was used as reducing agent, which forms MgO with the atmospheric oxygen present inside the autoclave to favor fast reduction and carburization of MoO_3 to form Mo_2C.

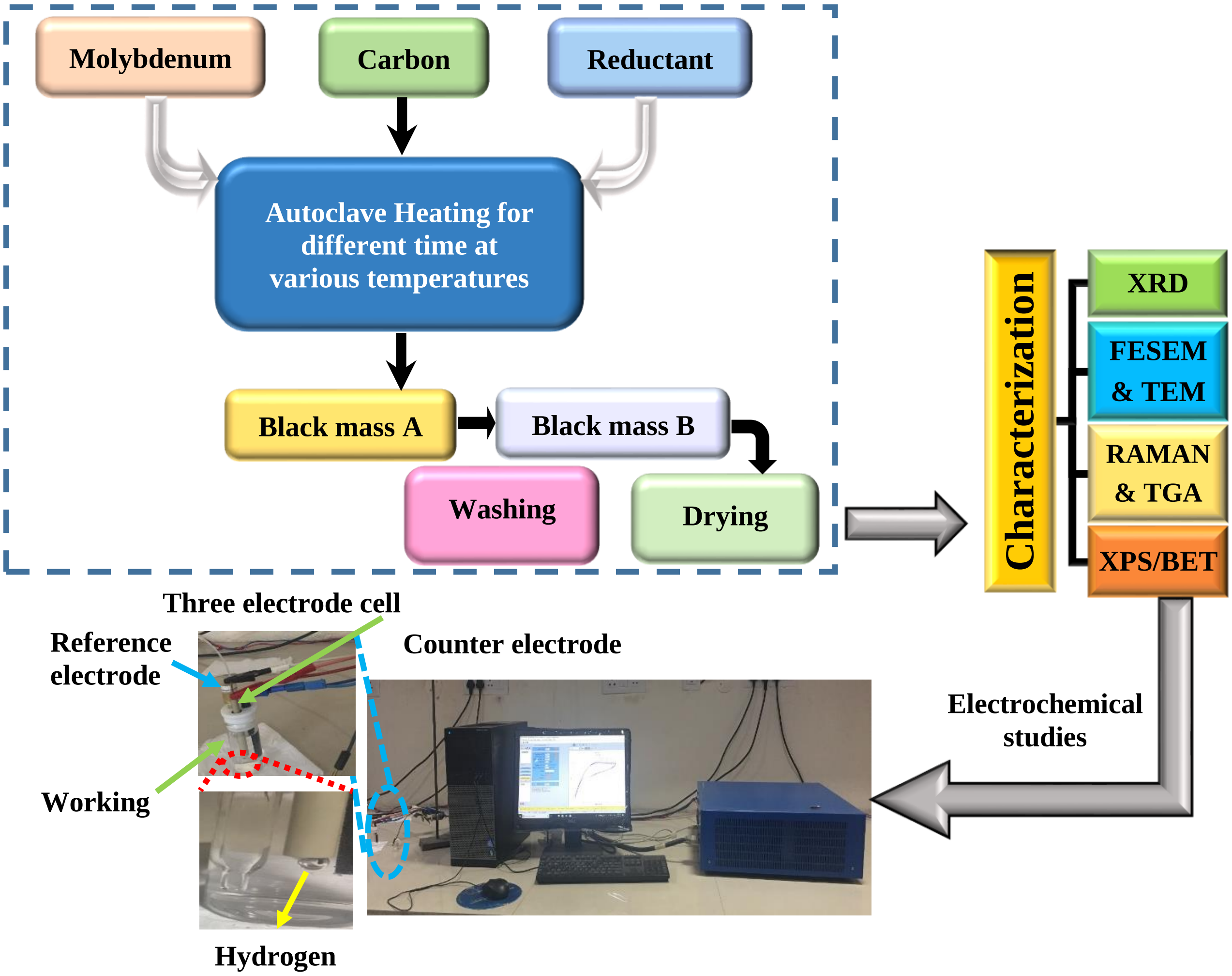

Figure 3.1: Schematic representation of synthesis of Mo_2C, characterization and EC setup for electrochemical study of product phases.

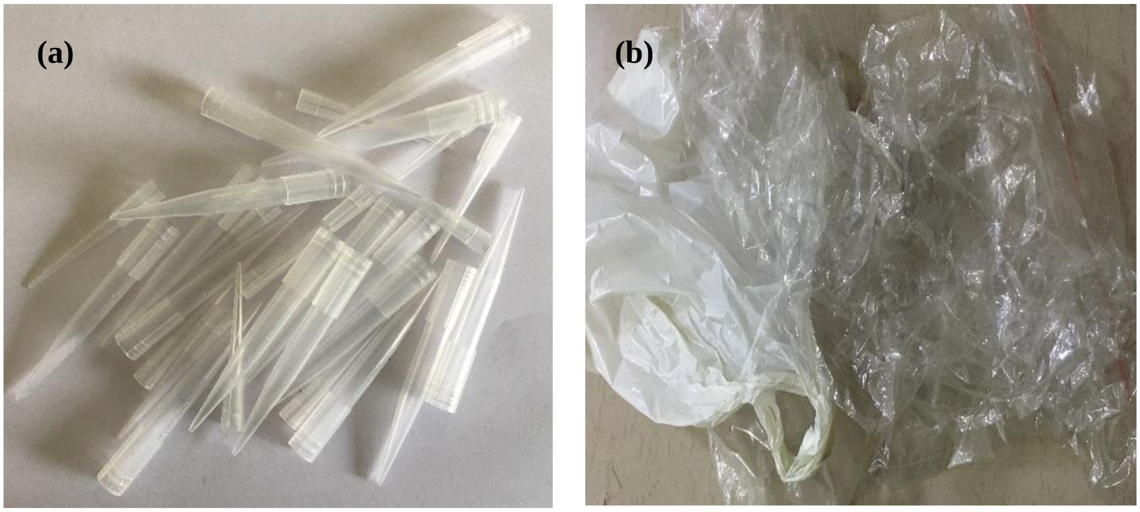

Figure 3.2: Carbon sources (a) used (waste) pipette tip and (b) waste polyethene.

3.1.5 Carbon sources

The two main categories of carbon sources have been used for the synthesis of Mo_2C. Firstly the analytical grade polypropylene was used as carbon source with MoO_3 to form Mo_2C in presence of reducing agent. Secondly the waste plastics (used pipette tip) as shown in Fig 3.2a, which is polypropylene based waste. Another carbonaceous waste (polyethene) was also used for the synthesis of Mo_2C as shown in Fig. 3.2b.

Both being rich in carbon and hydrogen favor the formation of Mo_2C at relatively low temperature. Moreover, their utilization also helps to address the environmental issue caused due to these wastes. The synthesis of Mo_2C depends on the chain length of hydrocarbons as reported by ***Xiao et. al*** [4]. The hydrocarbon chain and carbon content for pipette tip and polyethene is different, so this will also affect both the phase formation and morphology of the product phase.

3.2 Material characterization

Depending on the end applications, the synthesized products are analyzed by different techniques for structural, surface and morphological characteristics as represented in Fig 3.1.

3.2.1 X-ray diffraction (XRD)

The phase confirmation and the structural parameters of the synthesized samples were analyzed by XRD technique. The plot of intensity of scattered X-rays as a function of diffraction angle, expressed according to the Bragg's law is obtained. The synthesized samples were characterized by XRD using PANalytical X-Pert-Pro with CuKα radiation ($\lambda = 1.5406$ Å) attained from copper target using an inbuilt Ni filter. The X-ray powder diffraction data of all samples was collected at room temperature between $20° \leq 2\theta \leq 80°$ with a step size of 0.0130° (2θ). The ICDD data base (using X-Pert High Score Plus) was used for phase identification and further confirmation was done with the help of Rietveld refinement of the pure phase XRD patterns (using Full Prof Suite). The data was fitted via Rietveld refinement for hexagonal space group P63/mmc (194) and the crystal structure was confirmed from the fit. The Wyckoff positions used for Rietveld refinement of XRD data are 2(c) 1/3,2/3,1/4 ; 2/3,1/3,3/4 for Mo and 2(a) 0,0,0; 0,0,1/2 for C [5].

3.2.1.1 Crystallize and strain

The peak position, 2θ (Bragg Peaks) and full width half maxima $\beta_{observed}$ of peaks were calculated by X-ray line profile fitting technique using the Gaussian function. The breadth of the Bragg peaks combines both instrumental and sample dependent effects. The instrumental corrected broadening β_{hkl} corresponding to diffraction peak of Mo_2C was calculated using following relation [6,7]:

$$(\boldsymbol{\beta_{hkl}})^2 = [(\boldsymbol{\beta^2})_{\boldsymbol{Observed}} - (\boldsymbol{\beta^2})_{\boldsymbol{Instrumental}}] \qquad (\mathbf{3.1})$$

The crystallite size was calculated by using the common Scherrer criterion [8]:

$$\boldsymbol{D = \frac{k\lambda}{\beta_{hkl}Cos\theta} \Rightarrow cos\ \theta = \frac{k\lambda}{D}\left(\frac{1}{\beta_{hkl}}\right)} \qquad (\mathbf{3.2})$$

Where, k is shape factor, λ is wavelength of X-ray radiation, D is effective crystallite size in nanometers, β_{hkl} is peak width corrected for instrumental broadening as described in equation (1) and θ is Bragg angle.

The slope of the plot between $1/\beta_{hkl}$ on x-axis and cosθ on y-axis gives the crystallite size. The peak broadening in this case is attributed to crystallite size.

3.2.1.2 Williamson Hall analysis

Stokes and Wilson assigned a mathematical relation for peak broadening solely due to strain [9]. Williamson-Hall analysis was carried out by considering three models like Uniform deformation model (UDM), uniform stress deformation model (USDM) and uniform deformation energy density model (USEDM). Crystal imperfection and distortion constitute the strain broadening and the induced strain is given as follows:

$$\boldsymbol{\beta_{hkl} = 4\ \varepsilon\ tan} \qquad (\mathbf{3.3})$$

As Scherrer equation follows 1/cosθ dependency, the Williamson-Hall method varies with tanθ and allows the separation of diffracted beams when both crystallite size and strain are simultaneously involved. Even though β_{hkl} is combination of equation 2 and 3, Williamson Hall plot is used to separate the individual effects:

$$\boldsymbol{\beta_{hkl}cos\theta = \left(\frac{k\lambda}{D}\right) + (4\varepsilon\ sin\theta)} \qquad (\mathbf{3.4})$$

Equation 3.4 represents the uniform deformation model where strain was considered to be isotropic through whole crystal. The slope and intercept of graph plotted between 'β_{hkl} cosθ' as function of '4 sinθ', measures the magnitude of micro strain ε and crystallite size respectively. The positive value of strain confirms the compression in lattice. In many cases the strain homogeneity assumption and isotropy is not fulfilled, so uniform stress deformation model and uniform deformation energy density model come into consideration. The anisotropic nature of Young's modulus is considered by both the models, hence are more realistic routes [6,10]. In uniform deformation stress model, anisotropic micro strain ε is exhibited due to isotropic stress σ. The linear proportionality between stress and strain is given by Hook's law, $\sigma = \varepsilon E_{hkl}$. Considering this, Williamson-Hall equation has been formulated as:

$$\boldsymbol{\beta_{hkl} = \left(\frac{k\lambda}{D}\right) + \left(\frac{4\sigma\, sin\theta}{E_{hkl}}\right)} \qquad \mathbf{(3.5)}$$

Where $\boldsymbol{E_{hkl}}$ is Young modulus and for hexagonal crystal phases, it can be calculated by following relation [7,11]:

$$\boldsymbol{E_{hkl} = \left(h^2 + \frac{(h+2k)^2}{3} + \left(\frac{al}{c}\right)^2\right)^2 \times \left[S_{11}\left(h^2 + \frac{(h+2k)^2}{3}\right)^2 + S_{33}\left(\frac{al}{c}\right)^4 + (2S_{13} + S_{44})\left(\left(h^2 + \frac{(h+2k)^2}{3}\right)\left(\frac{al}{c}\right)^2\right)\right]^{-1}} \qquad \mathbf{(3.6)}$$

Where S_{11}, S_{13}, S_{33} and S_{44} are elastic compliances of Mo_2C having values of 2.4×10^{-3}, -0.68×10^{-3}, 2.56×10^{-3} and 7.353×10^{-3} GPa^{-1} respectively [11,12]. Plotting ($4\sin\theta / E_{hkl}$) on x-axis and ($\beta\cos\theta$) on y axis, the value of stress was calculated from slope of fitted line and crystallite size is extracted from intercept. The uniform deformation energy density model assumes isotropic energy density as a cause of anisotropic deformation within the crystal. The energy density u as function of strain for as system that follows Hook's law is given by $u = \varepsilon^2 E_{hkl}/2$. According to energy and strain relation, the uniform deformation energy model is given by following mathematical relation:

$$\boldsymbol{\beta_{hkl} = \left(\frac{k\lambda}{D}\right) + \left(4\, sin\theta\left(\frac{2u}{E_{hkl}}\right)^{\frac{1}{2}}\right)} \qquad \mathbf{(3.7)}$$

Plots drawn with $4\sin\theta\,(2u/E_{hkl})^{1/2}$ and $\beta_{hkl}\cos\theta$ on x-axis and y-axis respectively, the slope of the fitted line is used to estimate the value of energy density u whereas crystallite size D is estimated from intercept. The deformation stress and deformation energy density are related as $u = \sigma^2/E_{hkl}$.

3.2.2 Electron Microscopy

The morphological and microstructural features like shape, size and nature of carbon support of the synthesized powders was analyzed with field- emission scanning electron microscope (FE-SEM) (*Hitachi SU 8010*) and transmission electron microscope (*TEM) (JEOL 2100 F*) operating at 15 kV and 200 kV respectively. The phase confirmation was also done by high resolution TEM (HRTEM). The exact nature of carbon over Mo_2C was also confirmed by TEM and HRTEM. Moreover, the energy dispersive spectroscopy (EDS) of FESEM and TEM was done to confirm the elemental contribution. The distribution of elements were also confirmed by FESEM area mapping and scanning tunneling electron microscopy (STEM). The particle size distribution is calculated using the following criterion.

$$f(d) = \frac{1}{\sqrt{2\pi} d log\sigma_s} exp\left\{-\frac{(\log d_i - log\mu_s)^2}{2(\log\sigma_s)^2}\right\} \quad (3.8)$$

$$log\sigma_s = \sqrt{\frac{\sum(logd_i - log\mu_s)^2}{\sum n_i}} \quad (3.9)$$

$$log\mu_s = \frac{\sum d_i}{\sum n_i} \quad (3.10)$$

Where, $f(d)$ signifies the log-normal distribution, d_i particle diameter, n_i is the number of particles, μ_s is the mean diameter and σ_s is the standard deviation respectively.

3.2.3 Raman spectroscopy

The nature of carbon has strong dependence on HER activity and EDLC performance. The higher amount graphitization enhances the movement of electron due to its high conductivity. The formation of graphene structure were aslo confirmed by Raman spectroscopy performed in the range 500 to 2900 cm^{-1}. Raman spectroscopy using STR 500 Airix was done to determine the degree of graphitization at laser wavelength 532 nm.

3.2.4 Thermal analysis

The thermal stability of the synthesized samples was confirmed by performing thermogravimetric (TG) in air atmosphere at a heating rate of 5 ºC/min using TG (NETZSCH STA 449F3) TG/DTA and DTG (*Exstar TG/DTA 6300*). The amount of free carbon in the synthesized samples was also calculated depending on the end product formed during the thermal analysis.

3.3 Surface studies

3.3.1 X-ray photoelectron microscopy (XPS)

The surface chemical compositions and the valence states of the carbon coated/supported Mo_2C samples were analyzed by X-ray photoelectron spectroscopy (XPS). The measurements were carried out using XPS spectrometer (ESCA+) using Al-Kα radiation (1486.7 eV), operating at 15 kV and 15mA. The C1s peak ~284eV was selected as reference to calibrate the position of other peaks**.**

3.3.2 Nitrogen adsorption/desorption studies

The specific surface area (SSA) and the pore size and distribution are important characteristics for the HER activity and EDLC applications. The nitrogen sorption studies for surface analysis were conducted at 77K to determine Brunauer-Emmet-Teller (BET) surface area. The pore size and the pore volume was determined from Barret-Joyer-Halenda (BJH) plot using BEL-miniII Micro Trac

Corp. Pvt. Ltd (Tokyo, Japan). The sample was degassed to remove the adsorbed water and gas molecules at pretreatment temperature 80 °C.

3.4 Electrochemical activity

For different electrochemical applications, nano particles having enhanced active sites are preferred. In this work, nano molybdenum carbide (Mo_2C) synthesized at different synthesis conditions having variation in size and morphology is expected to possess efficient electrochemical HER activity through water splitting and supercapacitor (EDLC) performance. The carbon support over nano Mo_2C in different forms adherently influences the HER activity and EDLC performance. Some common techniques like cyclic voltammetry (CV), Linear sweep voltammetry (LSV), chronoamperometry (CA) and electrochemical impedance spectroscopy (EIS) were applied to study the electrochemical behavior (current-voltage) characteristics, HER activity, EDLC, stability and efficiency, respectively. It also determines the mechanism responsible for the HER activity. The shape of the CV curve determines the reversibility of the electrode material [13].

In the present work, the electrochemical studies has been done by standard three electrode setup (Bio-Logic SP 300) as shown in Fig. 3.2. The potential of the working electrode was measured with respect to the reference electrode (RE) such as reversible hydrogen electrode (RHE) as depicted in Fig 3.2. The high purity graphite rod and the reversible hydrogen electrode (RHE) were used as counter and reference electrode, respectively. The working electrode was fabricated manually using glassy carbon electrode (GCE) of surface area 0.07 cm^{-2}.

3.4.1 Electrode fabrication

The fabrication of the working electrode was done by dispersing 1 mg of the sample in 250 µl ethanol and 60 µl of the Nafion® solution was added to it. The solution was sonicated for 30 min and the slurry was prepared. One drop of solution (10 µl) was put on top surface of GCE and dried overnight.

3.4.2 Electrochemical measurements

The prepared working, reference and counter electrodes were put in the electrochemical cell containing 0.5M H_2SO_4 electrolyte solution for further measurements. The CV plotted in voltage window (-0.3 to 0.3 V) at 50 mVs^{-1} scan rate were done to remove contamination, activate surface of catalyst and stabilize the electrochemical currents before analysis. The linear sweep voltammetry (LSV) at scan rate 2 mVs^{-1} was performed in voltage range 0 to -0.3 V. The CV for

2000 cycles was performed at 100 mVs-1 scan rate in the voltage window -0.2 to 0.2 V to determine the stability of the elctrocatalyst. To elucidate further insight regarding the kinetics of HER, the electrochemical impedance spectroscopy (EIS) analysis was performed in range 100 kHz to 200 mHZ at potentials 10-550 mV in different intervals. The EDLC performance was determined by CV performed in the voltage window of 0.2 to 0.4V at multiple san rate 20-320 mVs^{-1}. The durability of electric double layer (EDLC) was analyzed by CV analysis performed for 1000 cycles in same voltage window at fix scan rate (100 mVs^{-1}). The Tafel slope and over potential are related according to the following criteria:

$$\boldsymbol{\eta = a + b\log j} \qquad (\mathbf{3.11})$$

Where '$\boldsymbol{\eta}$' is the overpotential (mV), '$\boldsymbol{b}$' is the Tafel slope (mVdec^{-1}) and is '$\boldsymbol{j}$'current density (mAcm^{-2}).

The Specific capacitance is estimated by the following formula [14]:

$$\boldsymbol{Specific\ capictance\ (Fg^{-1}) = \frac{C_{dl}}{m}} \qquad \mathbf{(3.12)}$$

Where C_{dl} or EDLC is calculated from the the plot of Δj (mAcm^{-2}) at fixed potential vs scan rate (mVs^{-1}) and m is mass of electrode.

References

1 A. Gupta, G. Singla and O. P. Pandey, *Ceramics International*, 2016, **42**, 13024–13034.
2 G. Singla, K. Singh and O. P. Pandey, *International Journal of Hydrogen Energy*, 2015, **40**, 5628–5637.
3 H. K. Sidana, R. A. Mir and O. P. Pandey, *Journal of Alloys and Compounds*, 2018, **736**, 255–265.
4 T. Xiao, A. P. E. York, K. S. Coleman, J. B. Claridge, J. Sloan, J. Charnock and M. L. H. Green, *Journal of Materials Chemistry*, 2001, **11**, 3094–3098.
5 E. Parthé and V. Sadogopan, *Acta Crystallographica*, 1963, **16**, 202–205.
6 A. Khorsand Zak, W. H. Abd. Majid, M. E. Abrishami and R. Yousefi, *Solid State Sciences*, 2011, **13**, 251–256.
7 G. Singla, K. Singh and O. P. Pandey, *Applied Physics A: Materials Science and Processing*, 2013, **113**, 237–242.
8 N. Kaur, R. A. Mir and O. P. Pandey, *Journal of Alloys and Compounds*, 2019, **782**, 119–131.
9 S. Vives, E. Gaffet and C. Meunier, *Materials Science and Engineering A*, 2004, **366**, 229–238.
10 Y. Rosenberg, V. S. Machavarian, A. Voronel, S. Garber, A. Rubshtein, A. I. Frenkel and E. A. Stern, *Journal of Physics: Condensed Matter*, 2000, **8081**, 8081–8088.
11 Y. Liu, Y. Jiang, R. Zhou, X. Liu and J. Feng, *Ceramics International*, 2015, **41**, 5239–5246.
12 J. M. Zhang, Y. Zhang, K. W. Xu and V. Ji, *Solid State Communications*, 2006, **139**, 87–91.
13 C. M. A. Brett and A. M. O. Brett, *Oxford University*, 1994, 359–360.
14 B. K. Kim, S. Sy, A. Yu and J. Zhang, *Handbook of Clean Energy Systems*, 2014, 1–25.

Chapter 4

Synthesis of nano Mo_2C using polypropylene

Overview

In this chapter, details of experimental conditions to get carbon coated molybdenum carbide (β-Mo_2C@C) has been optimized using polypropylene as carbon source. The products so obtained under each experimental conditions are characterized using different tools like XRD, FESEM, TEM/HRTEM, Raman spectroscopy, BET and XPS. The nature of carbon coating on the surface of nano Mo_2C (β-Mo_2C@C) plays vital role to extract HER activity and also the performance of these materials for EDLC applications. Moreover, crystallite size, lattice strain and pore size measured through XRD and BET surface area analyzer also plays an important role. Influence of all these parameters have been correlated and presented in this chapter with emphasis to enhance the HER activity and EDLC performance.

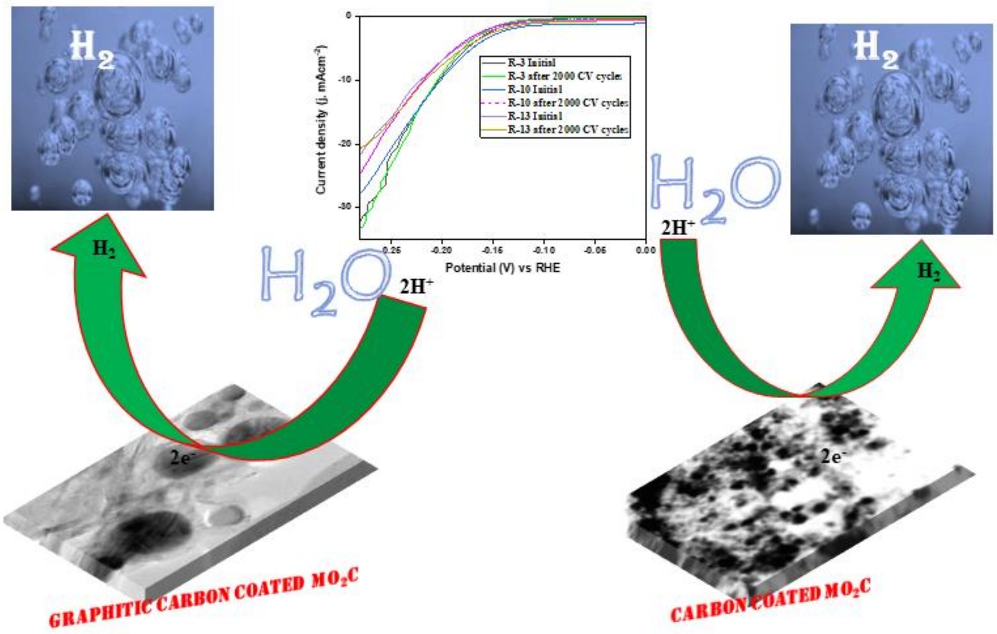

Schematic representation of H_2 evolution on the surface of Mo_2C

4.1 Introduction

The solemnity of environmental issues and the increasing demand for energy with the limited supply of resources of fossil fuels have led to the evolution of new materials for energy production from natural or renewable sources [1]. The production of hydrogen by HER through electrochemical water splitting can provide a clean and renewable energy resource [2]. The high-performance electrocatalysts are required in order to improve the efficiency of water splitting to promote the HER. Various efforts have been made in last few decades for the development of low cost electrocatalysts for HER [3–8]. Among the noble-metal free catalysts, molybdenum carbide (β-Mo_2C) is the fascinating candidate for electrocatalysis because of its low cost, high chemical stability and structural similarity to Pt group metals [9,10]. Carbon support in various forms enhances the HER and EDLC performance [10,11].

In the present work, the synthesis of β-Mo_2C@C in an autoclave at relatively low temperature has been described and discussed. Polypropylene, a low cost thermoplastic polymer utilized for the manufacturing of various plastic products, which ends as waste material is used as carbon source. The emission of carbonaceous gases during decomposition of polypropylene inside the autoclave serve as reaction gases and help in fast reduction-carburization of MoO_3 to form Mo_2C. The path described for synthesis of β-Mo_2C@C is low cost and environmentally friendly. The reaction parameters were optimized to obtain pure phase carbon coated Mo_2C. The HER activity of the as synthesized sample β-Mo_2C@C was investigated in acidic medium. The synthesized β-Mo_2C@C shows higher stability and improved electrocatalytic HER performance in the acidic medium than the bulk and supported non-noble metal materials [12,13]. It has been noticed that the graphitic surface carbon improves the charge transfer kinetics whereas amorphous carbon enhances the stability of the electrocatalyst.

4.2 Synthesis of nano Mo_2C

The synthesis of pure phase Mo_2C (β-Mo_2C@C) was carried out in autoclave using polypropylene as carbon source, MoO_3 and Mg as Mo and reducing agent, respectively. The methodology and experiment details are given in section 3.1 (Chapter 3). The other synthesis parameters are given in Table 4.1.

Table 4.1: Synthesis parameters and phases obtained

Sample Id	**Temperature (°C)**	**Time (h)**	**Heating Rate (°C/min)**	**Carbon source (g)**	**MoO_3 (g)**	**Mg (g)**	**Phases obtained**		**Crystallite size D (nm)**
							Major	**Minor**	
R-1	600	10	5	1	1.4394	3.5	MoO_3, Mo_4O_{11}		
R-2	700	10	5	1	1.4394	3.5	Mo_2C	C, Mo MoO_2	38.00
R-3	800	10	5	1	1.4394	3.5	Mo_2C	C	36.36
R-4	800	2	5	1	1.4394	3.5	Mo_2C	MoO_2, C	31.63
R-5	800	5	5	1	1.4394	3.5	Mo_2C	MoO_2, C	41.70
R-6	800	12	5	1	1.4394	3.5	Mo_2C	MoO_2, C	63.16
R-7	800	10	5	0.5	1.4394	3.5	Mo_2C	MoO_2, Mo, $Mo_{0.42}C_{0.58}$	73.0
R-8	800	10	5	0.75	1.4394	3.5	Mo_2C	MoO_2, Mo, $Mo_{0.42}C_{0.58}$	78.33
R-9	700	12	5	1	1.4394	3.5	Mo_2C	Mo	68.5
R-10	700	14	5	1	1.4394	3.5	Mo_2C	C	74.9
R-11	600	15	5	1	1.4394	3.5	MoC	-	8.0
R-12	600	17	5	1	1.4394	3.5	MoC	-	12.7
R-13	600	20	5	1	1.4394	3.5	Mo_2C	C	63.6

4.3 Results and discussion

4.3.1 X-ray diffraction (XRD)

Table 4.1 gives the details of reaction parameters and the major and minor phases obtained in the synthesized samples. The XRD pattern of sample (R-1) synthesized at 600 °C for 10 h reveals the presence of MoO_3 (ICDD reference -089-7112) and intermediate phase Mo_4O_{11} (ICDD reference -072-0447) as shown in Fig. 4.1a, indicating that the temperature is not adequate enough for the carbon diffusion and to reduce the MoO_3 to MoO_2 [14]. The reduction of MoO_3 to MoO_2 in presence of hydrogen and carbon proceed via formation of an intermediate phase Mo_4O_{11} [15,16].

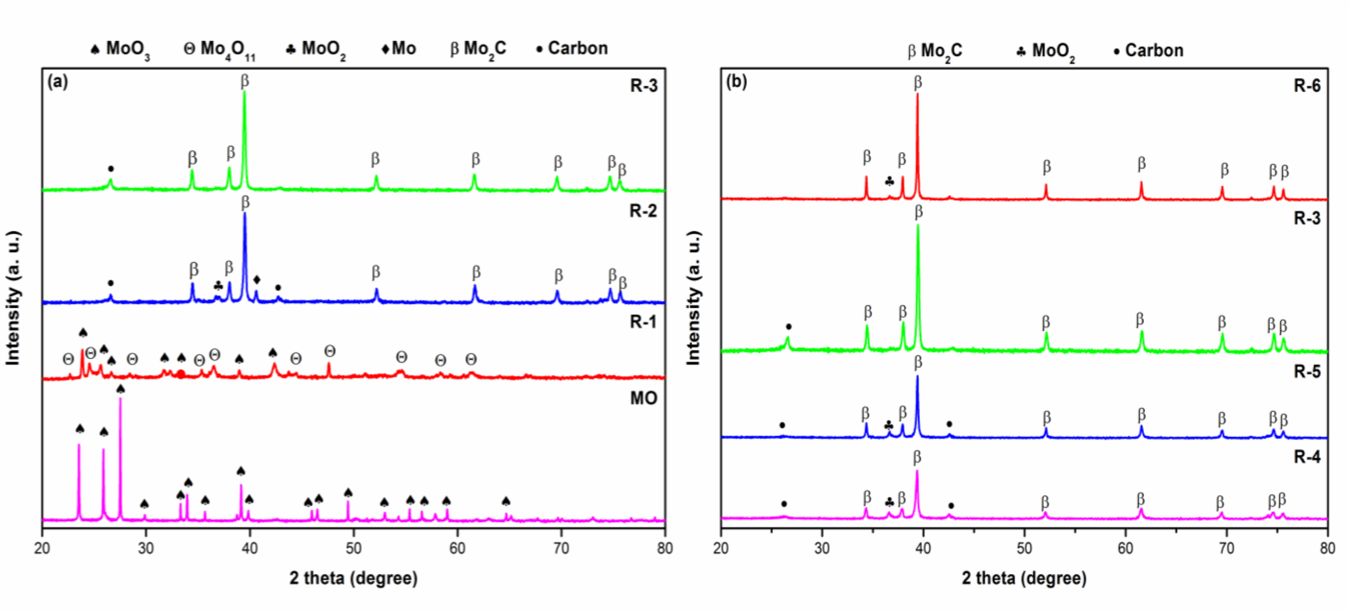

Figure 4.1: (a) XRD pattern of MO (MoO_3) and samples synthesized at different temperatures: 600 °C (R-1), 700 °C (R-2), 800 °C (R-3) with constant holding time of 10h. (b) XRD pattern of samples synthesized at 800 °C with different holding time: 2h (R-4), 5h (R-5), 10h (R-3) and 12h (R-6).

With increase in the temperature up to 700 °C (R-2), XRD pattern shows an increase in the peak intensity of Mo_2C (ICDD reference -035-0787) phase with decreasing minor phases (Table 4.1), indicating that the reaction temperature is still not sufficient for carbon diffusion to carburize the reduced oxide phase MoO_2 (ICDD reference -078-1070) and molybdenum (Mo) (ICDD reference -089-5156) to pure Mo_2C. The reduction-carburization of MoO_3 to Mo_2C proceeds via two steps as given in equations 4.1 and 4.2 [17,18].

$$MoO_3 \rightarrow MoO_2 \rightarrow Mo + Mo_2C \qquad (4.1)$$

$$MoO_3 \rightarrow MoO_2 \rightarrow Mo_2C \qquad (4.2)$$

R-2 sample shows the feasibility of reaction path as given in equation 4.1. Firstly, reduction of MoO_3 to MoO_2 followed by MoO_2 to Mo_2C. The reduction of MoO_2 to Mo_2C can occur through an intermediate product of metallic Mo as shown in equation 4.1. Sometimes reaction proceeds without formation of metallic phase depending on reaction conditions as given in equation 4.2 and is more favorable for endothermic solid state reactions. In the similar way, the conversion of MoO_3 to Mo_2C is accomplished at 800 °C (R-3). All peaks correspond to Mo_2C with no minor phase except single peak of excess carbon (ICDD reference -026-1076) as shown in Fig. 4.1a, confirming the sufficient diffusion of carbon in Mo lattice to form pure Mo_2C and the most favorable reaction path as given in equation 4.2. The peaks at 34.4, 37.9, 39.4, 52.2, 61.6, 74.7 and 75.6 correspond to (100), (002), (101), (102), (110), (103), (112) and (201) planes of hexagonal molybdenum carbide (β-Mo_2C) phase.

In order to reduce the soaking time for R-3 (800 °C, 10 h), experiments employing different soaking times have been optimized (Table 4.1). Figure 4.2b shows the XRD pattern of samples synthesized at 800 °C for different soaking times. R-4 and R-5 almost depict the similar XRD patterns, but the intensity of pure phase Mo_2C is enhanced in R-5 as compared to R-4 (Fig. 4.1b). The results confirm the enhancement in phase formation with respect to reaction time at a fixed temperature. The diffusion of carbon into MoO_{3-x} (x=0,1) increases with increase in the time. This confirms that the reaction time of 10 h at 800 °C is sufficient enough for reduction and carburization of MoO_3 to Mo_2C. It also shows the feasibility of most favorable reactions (equation 4.2) for solid-state reactions. Moreover, further increase in soaking time to 12 h in R-7 sample, the minor phase of MoO_2 appears because of decarburization and oxidation. At higher temperature, affinity of oxygen diffusion is more when the reaction time is sufficient enough for oxygen to diffuse into Mo_2C to favor reversible reaction [19–22]. The carburizing atmosphere inside the autoclave is very complex involving the interaction of numerous gases. The methane and other hydrocarbon gases like ethane, propane, ethylene and propylene etc. generated by decomposition of polypropylene may break into C and H_2 and facilitate the carburization more rapidly [23,24]. In contrast to this CO_2 and H_2O being byproducts of the decomposition reactions act as decarburizing agents. However, certain amount of CO_2 is tolerable at defined carburizing temperature, without causing decarburization action. Presence of CO_2 in small amount requires a high concentration of CO to balance the decarburization action [25,26]. The amount of initial carbon content adherently affects the Mo_2C phase formation. Figure 4.2 shows the phase formation with variation of carbon content from 0.5, 0.75 and 1 g, respectively.

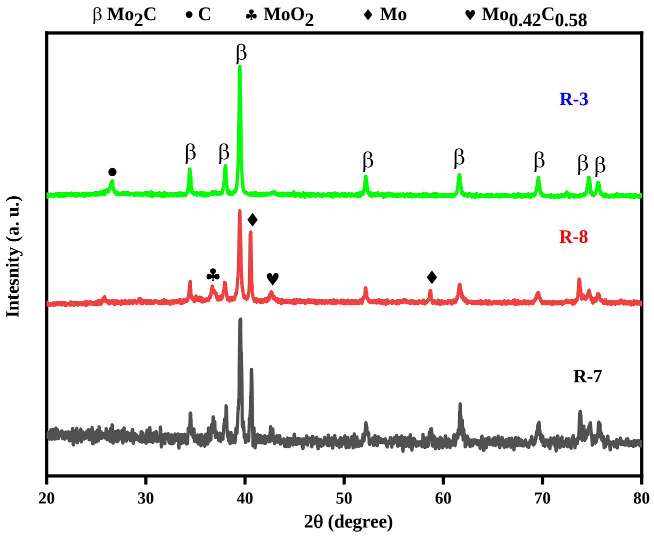

Figure 4.2: XRD pattern of samples synthesized at 800 °C for 10 h with different intial carbon concentrations: 0.5 g (R-7), 0.75 g (R-8) and 1 g (R-3).

The sample (R-7) reveals the formation of mixed phases with higher amount of Mo (Fig. 4.2), which depicts the enhanced carburization at 800 °C for 10 hours, but the amount of carbon is not sufficient enough to accomplish carburization. Increasing the amount of carburization 0.75 g (R-8), the intensity of oxide phase decreases (Fig. 4.2), but the intensity of Mo phase enhances. It corresponds to enhancement in reduction of MoO_2 to Mo, because the carburized gases are not optimum to favor formation of Mo_2C. The sample (R-3) shows the formation of pure phase Mo_2C where the carbon is optimum to favor both reduction and carburization of MoO_3.The peak at lower angle corresponding to carbon reveals formation of crystallized carbon along with Mo_2C. The certain amount of carbon deposition on the surface is necessary for carburization as described by Zhao *et. al* [27] for formation of Mo_2C using di methyl ether (DME) as carbon source. If the amount of carbon is further increased, it might inhibit transformation of MoO_3 to Mo_2C due to increase of pressure with respect to carbon and hydrogen inside the autoclave as revealed by Kumar *et. al* [28]. This may also enhance the amount of decarburizing gases inside the autoclave. Furthermore, the deposition of carbon (peak of carbon) as seen in R-3 XRD pattern should be optimum enough to favor carburization. The thick deposited layer might hinder the further diffusion of C in Mo lattice and impede the formation Mo_2C. In another set of experiments, the optimization was done to attain pure phase Mo_2C at relatively lower temperatures 600 and 700 °C, respectively. The synthesis conditions and obtained phases are given in Table 4.1. The typical X-ray diffraction pattern of sample synthesized at 600 °C for 15 hours (R-11) reveals the formation of intermediate mono molybdenum carbide (MoC) phase (ICDD reference -089-4305) as shown in Fig. 4.3a. The results show that the carburization of MoO_3 occurred with the increase in reaction time beyond 10 hours. Increasing the reaction time to 17 hours at 600 °C (R-12) does not make any change in product phase formation (Fig. 4.3a). Only MoC phase of higher intensity was observed. When the reaction time was further increased to 20 hours at 600 °C (R-13), the formation of the pure phase Mo_2C with impurity peak corresponding to hexagonal carbon was observed (Fig. 4.3a).

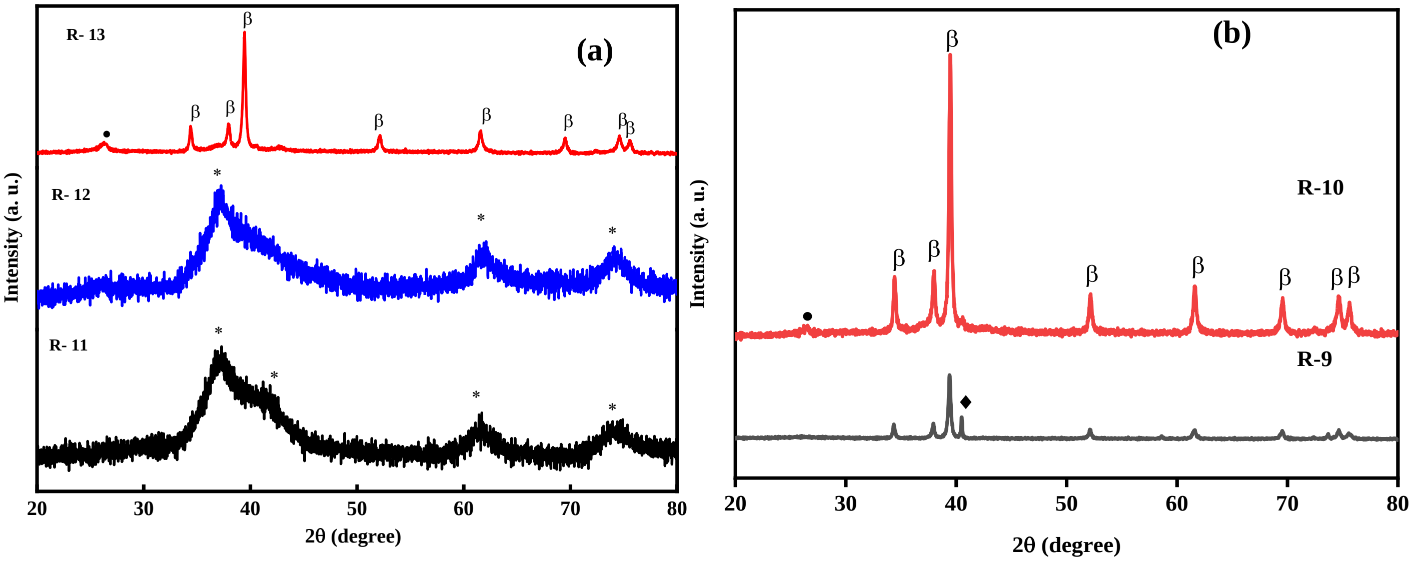

Figure 4.3: XRD pattern of sample synthesized at 600 °C (R-11, R-12 & R-13) and 700 °C (R-9 & R-10).

The reaction time of 12 hours at 700 °C (R-9) reveals the formation of Mo_2C along with impurity peak of Mo as shown in Fig. 4.3b. The results indicate that the reduction has completed at 700 °C for 12 hours, but reaction time is not sufficient enough to accomplish the complete carburization of reduced Mo to Mo_2C. Increasing the reaction time to 14 hours at 700 °C (R-10) has led to the formation of pure crystalline phase Mo_2C (Fig. 4.3b). These results indicate that pure β-Mo_2C can be obtained at relatively lower temperature via the in-situ reduction-carburization route in the autoclave. The additional peaks at 26.6 in R-10 having low intensity and the peaks at 26.6 and 42.8 in R-13 are attributed to hexagonal carbon. The reaction temperature and time enhances the reduction and carburization to form pure carbide phase [19,28–30]. The higher intensity peaks corresponding to Mo_2C in R-10 may be ascribed to more crystalline nature compared to R-13 [31].

The more crystalline nature of R-10 has been confirmed by lower full-width half maxima (FWHM) value as compared to R-13 as shown in Fig. 4.4a-b. The higher amount of carbon present in R-13 determined by the prominent peak at ~26.6 may correspond to unreacted carbon present on the surface at the lower reaction temperature. The increase in reaction time at lower temperature enhances the carburization of reduced oxide phase because the carbon atoms present on the surface needs to travel a longer distance to form pure phase Mo_2C [32].

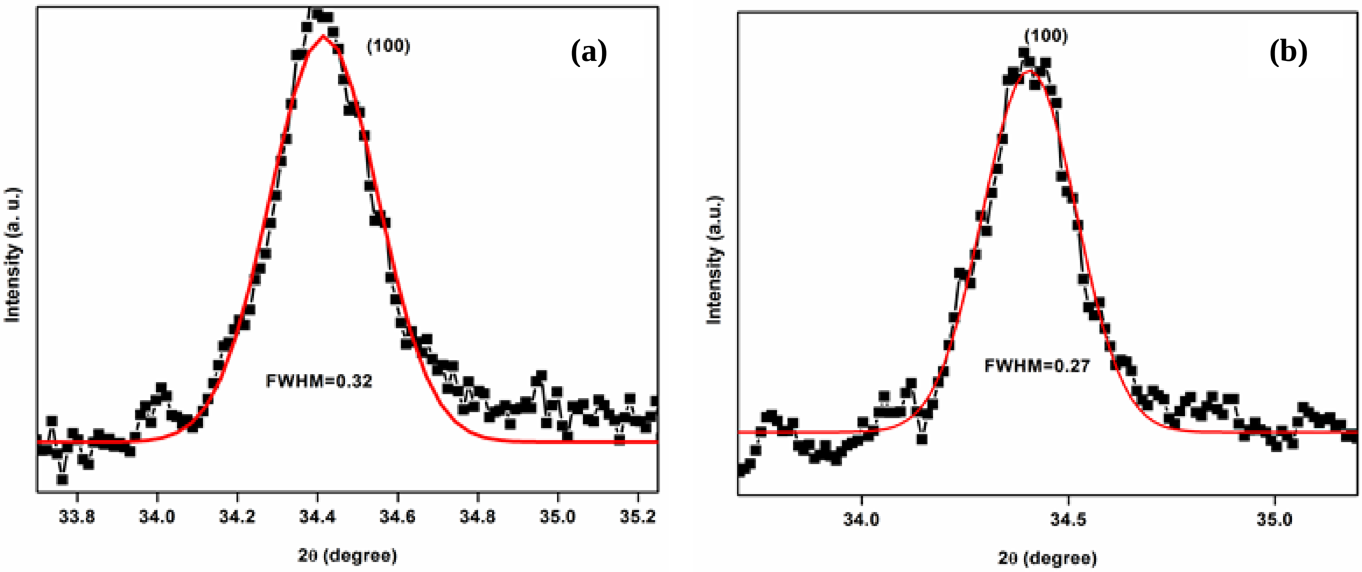

Figure 4.4: XRD peak of (100) plane showing FWHM of (a) R-13 and (b) R-10.

4.3.1.1 Rietveld refinement

The XRD results of samples R-3, R-10 and R-13 confirm the formation of pure phase Mo_2C. The data was fitted via Rietveld refinement for hexagonal space group P63/mmc (194) to confirm the crystal structure. Figure 4.5a-c shows the Rietveld refinement plots of the product phases. The Wyckoff positions used for Rietveld refinement of XRD data are 2(c) 1/3,2/3,1/4 ; 2/3,1/3,3/4 for Mo and 2(a) 0,0,0; 0,0,1/2 for C [33]. The χ^2 values obtained from the Rietveld refinement for R-3, R-9 and R-13 are 1.95, 1.93 and 2.1 respectively. The values of lattice parameters a, b and c as calculated from Rietveld refinement are a=b 3.007, c = 4.73; a= b = 3.016, c = 4.750 and a=b=3.013, c= 4.745 for R-3, R-9 and R-13, respectively.

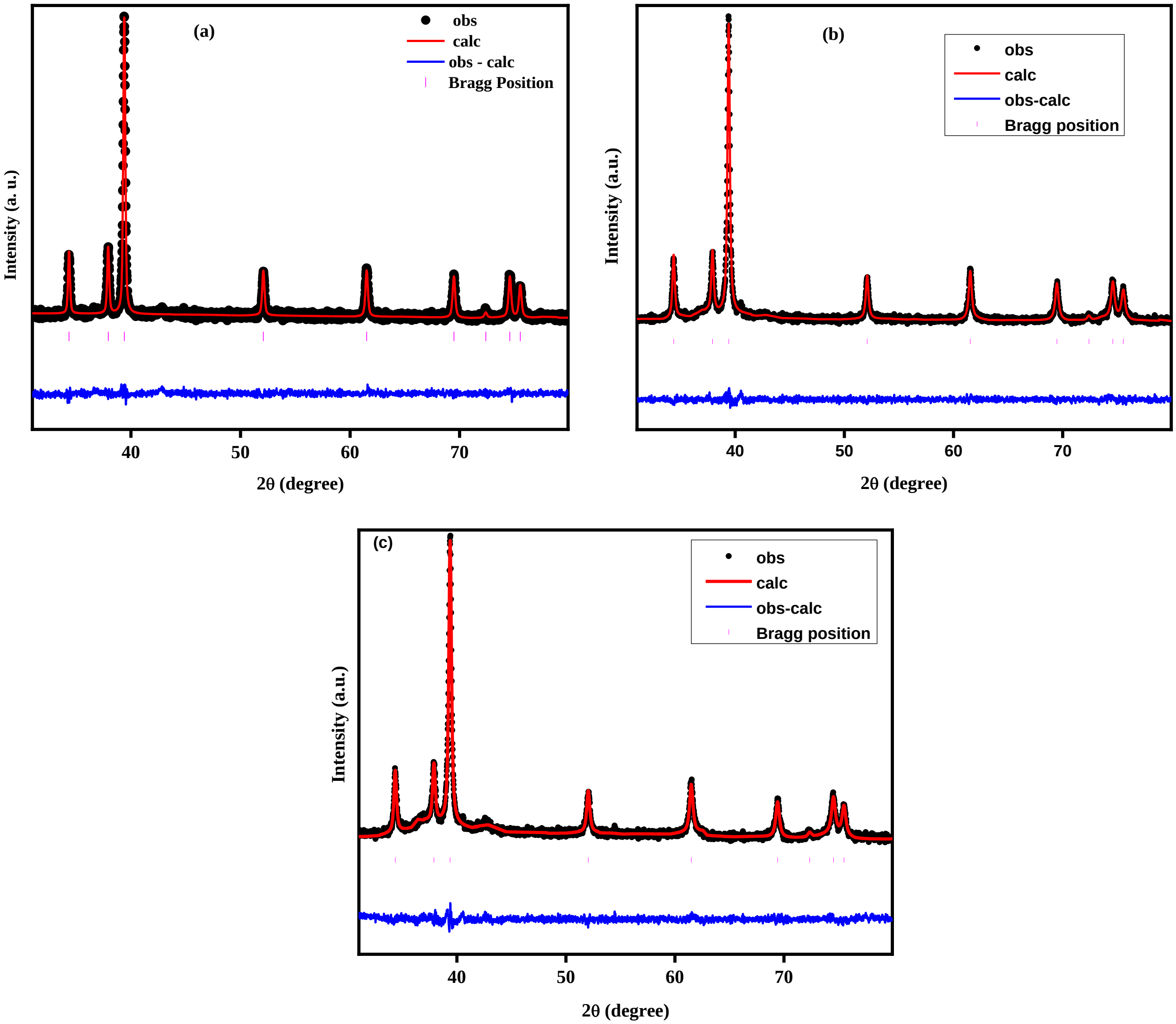

Figure 4.5: Rietveld refinement pattern of (a) R-3 (800 °C for 10 h), (b) R-10 (700 °C for 14 h) and R-13 (600 °C for 20 h).

4.3.1.2 Crystallite size and strain

The peak position, 2θ (Bragg Peaks) and full width half maxima $\beta_{observed}$ of peaks were calculated by X-ray line profile fitting technique using the Gaussian function and values obtained from the fit are more pragmatic. The result of curve fit for peak (100) is shown in Fig. 4.6a. The crystallite size is estimated from the commonly used method Scherrer criterion, the details of which is given in section 3.2.1.1. Scherrer plot of R-3 was drawn with 1/β on x-axis and cosθ on y-axis of and the corresponding values obtained for the synthesized samples are given in Table 4.1. By fitting the data, crystallite size D was calculated from slope of the fit line as shown in Fig. 4.6b. Peak broadening in above case is attributed coherently due to the crystallite size.

4.3.1.3 Williamson-Hall methods

Williamson-Hall analysis was carried out by considering three models, that is using Uniform deformation model (UDM) , uniform stress deformation model (USDM) and uniform deformation energy density model (USEDM) using equations 3.4 -3.7, already described in chapter 3.

Table 4.2: William-son Hall (W-H) analysis parameters of pure phase Mo_2C.

Sample Id	**UDM**		**USDM**			**USEDM**			
	D (nm)	**ϵ $\times10^{-3}$**	**D (nm)**	**ϵ $\times10^{-3}$**	**σ (GPa)**	**D (nm)**	**ϵ $\times10^{-3}$**	**σ (GPa)**	**U$\times10^{2}$ (KJm^{-3})**
R-3	47.32	0.59	45.76	0.53	0.21	46.68	0.56	0.22	0.61
R-10	47.3	1.25	45.6	1.18	0.46	46.68	0.87	0.34	2.92
R-13	37.13	1.18	35.5	1.08	0.42	36.5	0.82	0.32	2.53

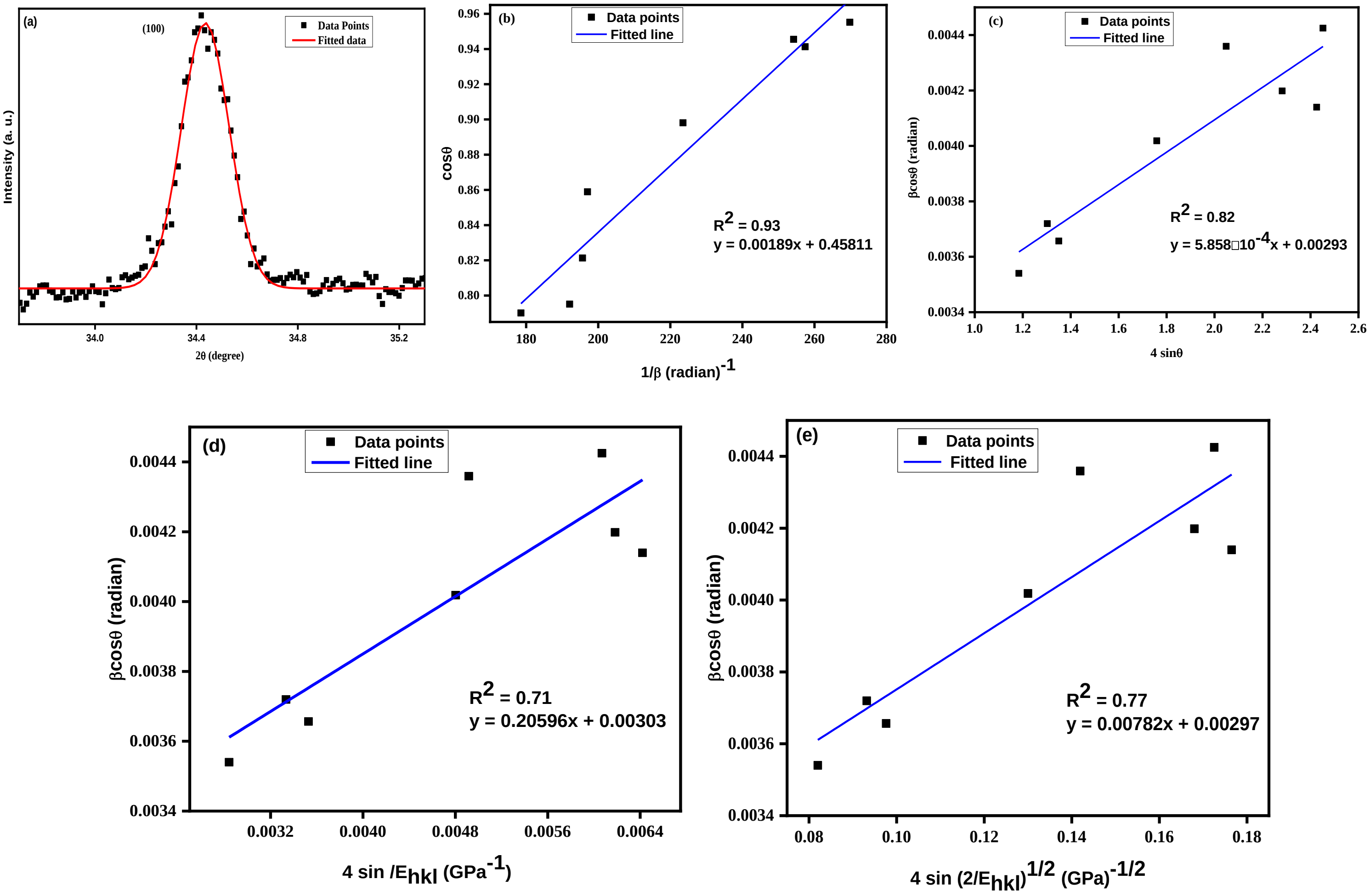

Figure 4.6: W-H analysis of (R-3 sample). (a) Gaussian fitted data, (c) Sherrer plot of sample, (d) UDM, (e) USDM and (f) USEDM model.

The slope and intercept of graph plotted between ‘β cosθ’ as function of ‘4 sinθ’, measures the magnitude of micro strain ε and crystallite size, respectively as shown in Fig. 4.6c. The positive value of strain confirms the compression in lattice. The UDM model in Fig. 4.6c proves to be more appropriate with less scattering of data away from the linear expression as compared to USDM and USEDM as shown in Fig. 4.6d-e, respectively. The decrement in the value of strain with rise in temperature has been observed and is listed in Table 4.2. The extra carbon present in the system, with a prominent peak ~26.6 in R-3 may result in less strain value as compared to R-10 and R-13 [32]. The presence of carbon hinders the further diffusion of carbon to attain a stable state of the system with low strain value. The increase in crystallite size from R-13 to R-10 is in accordance with the more crystalline nature of R-10, but the size decreases again with rise in temperature (800 °C), because of the lattice contraction at higher temperatures.

4.3.2 Raman spectroscopy

The degree of graphitization of the pure phase (β-Mo_2C@C)synthesized samples is determined by Raman spectra as shown in Fig. 4.7.

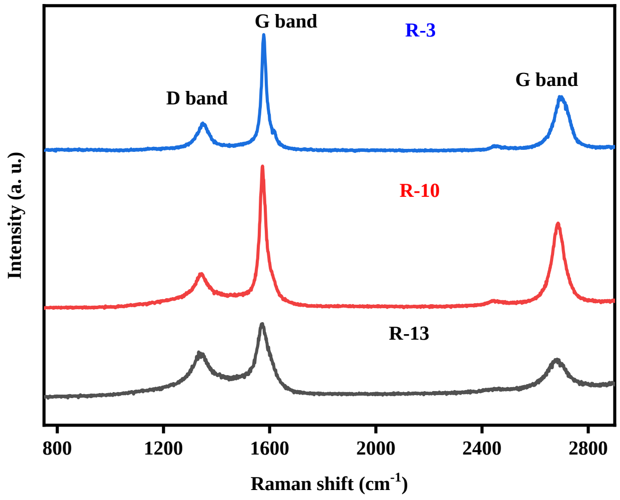

Figure 4.7: Raman spectra of R-3 (800 °C for 10 h), R-10 (700 °C for 14 h) and R-13 (600 °C for 20 h) samples.

The peak positions in Raman spectra located at ~1345, 1580 and 2690 cm^{-1} correspond to induced disordered D-band, G-band and the 2D band of crystalline graphite, respectively [34–36]. The results predict the existence of the ordered graphitic carbon in the synthesized samples. The decrease in the ratio of ID/IG 0.88 to 0.23 for R-13 and R-10 suggest the increase in graphitization of carbon with the increase in temperature [37]. The ratio of ID/IG (0.24) of R-3 is almost similar to R-10. Moreover, the increase in the intensity of 2D band in R-700/14 reveals that the crystalline graphitic carbon becomes more prominent and the widening of 2D peak in R-3 confirms that the number of graphite/graphene layers increases with temperature. The results indicate that R-13 contains more distorted or amorphous carbon in comparison to R-10 and R-3.

4.3.3 Microstructural Analysis

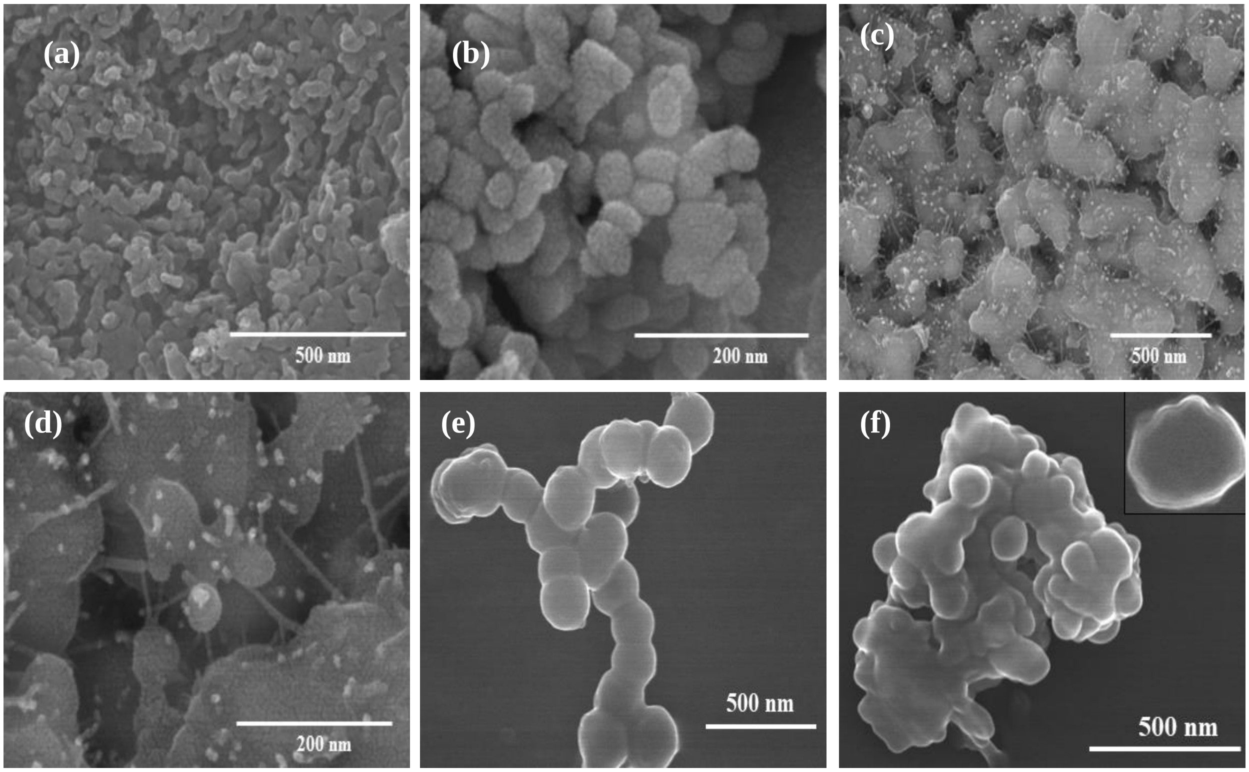

Figure 4.8: Field emission scanning electron microscope **(**FESEM) images of (a) & (b) of R-13 (c) & (d) of R-10 and (e) & (f) of R-3.

Figure 4.8 shows the FESEM micrographs of pure phase β-Mo_2C@C synthesized at 600, 700 and 800 °C, respectively. It clearly depicts that the particles have higher tendency to agglomerate and reveals an inhomogeneous size distribution. The FESEM micrographs in Fig. 4.8a-b) elucidate that particles are highly agglomerated and have nearly spherical morphology. The size uniformity of R-13 has been observed in the magnified image shown in Fig. 4.8b. The results reveal that R-10 consists of bigger particle size as compared to R-13 and are connected through a carbon network (Fig. 4.8c-d). Spherical to faceted morphology was observed in both R-10 and R-3 synthesized at relatively higher temperatures 700 and 800 °C, respectively.

The relatively higher temperature phase (R-3) shows smaller size particles (Fig. 4.8e-f) compared to R-10.

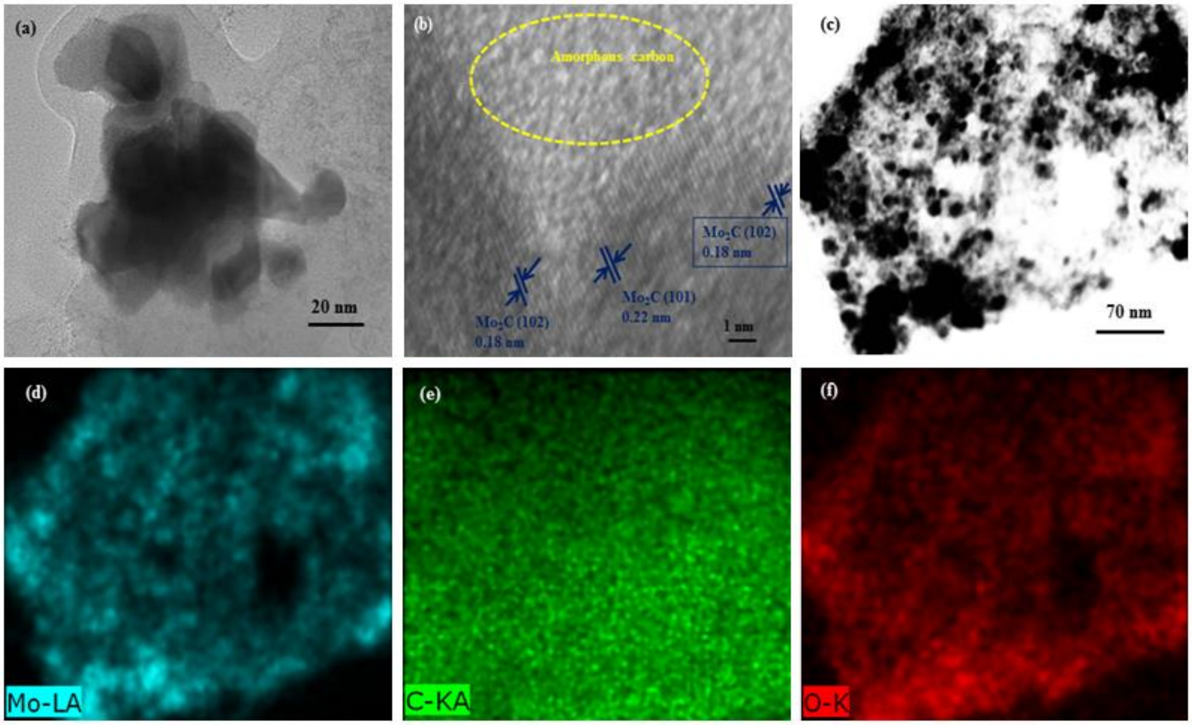

Figure 4.9: TEM micrographs of β-Mo_2C@C synthesized R-13 (600 °C for 20 h) (a) TEM (b) HRTEM and STEM images (c) survey β-Mo_2C@C, (d) Molybdenum (Mo), (e) Carbon (C) and (f) Oxygen (O).

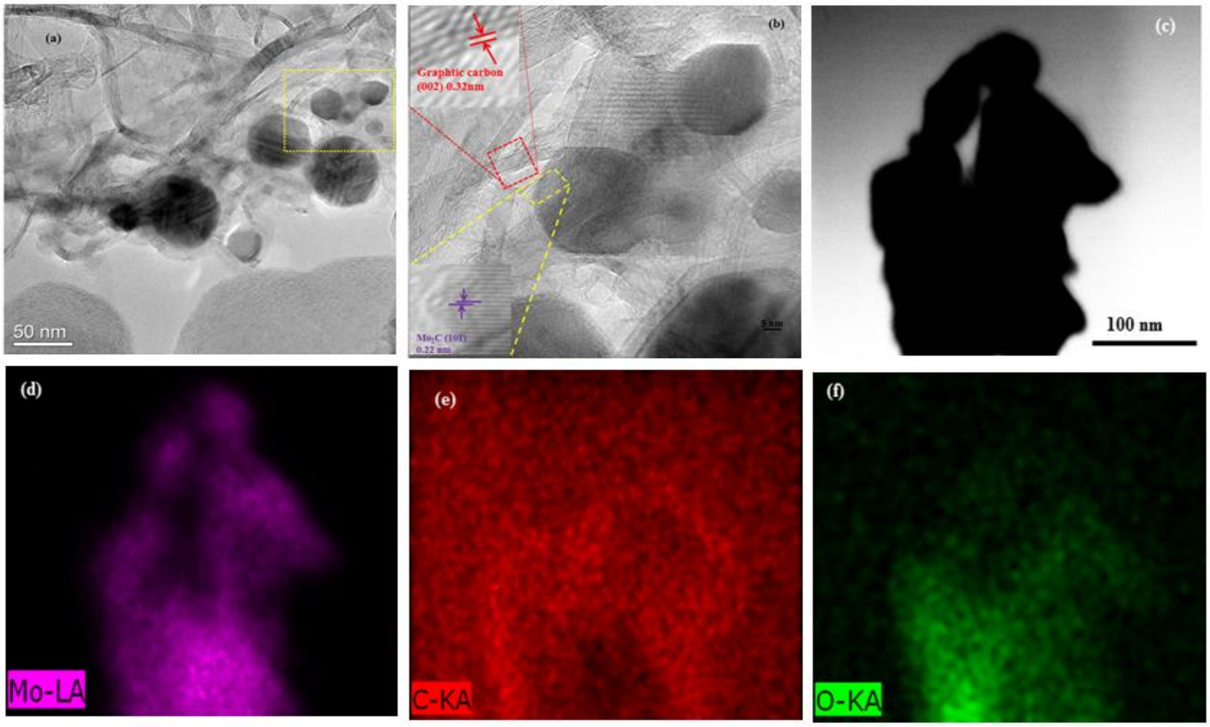

Figure 4.10: TEM micrographs of β-Mo_2C@C synthesized R-10 (700 °C for 14 h) (a) TEM (b) HRTEM and STEM images (c) survey β-Mo_2C@C, (d) Molybdenum (Mo), (e) Carbon (C) and (f) Oxygen (O).

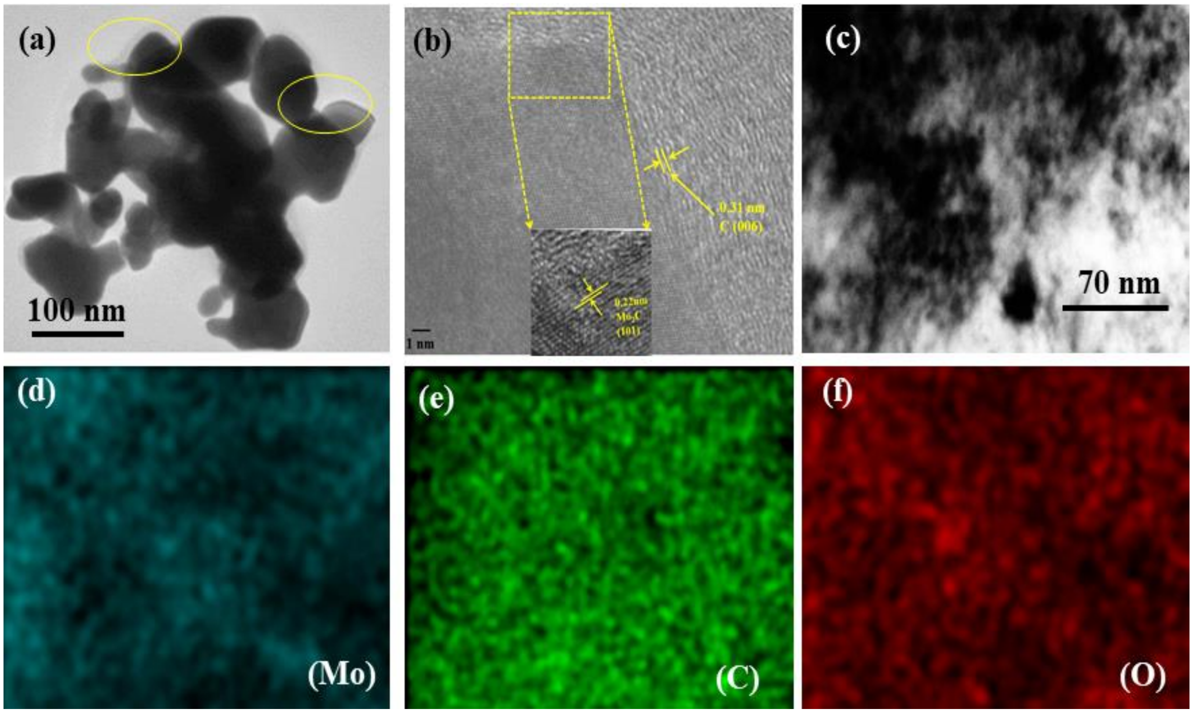

Figure 4.11: TEM micrographs of β-Mo_2C@C synthesized R-3 (800 °C for 10 h) (a) TEM (b) HRTEM and STEM images (c) survey β-Mo_2C@C, (d) Molybdenum (Mo), (e) Carbon (C) and (f) Oxygen (O).

To confirm further the shape, size of particles, nature of surface carbon and phase confirmation, TEM and HRTEM analysis was done as shown in Fig. 4.9 to 4.11. In case of R-13, the particles are encapsulated in thick carbon layers (Fig. 4.9a). The HRTEM micrograph of R-13 (Fig. 4.9b) reveals the presence of more amorphous carbon content. The lattice fringing 0.22 nm and 0.18 nm correspond to (101) and (102) plane of Mo_2C (-035-0787 ICDD pattern). The deposition of more amorphous carbon content in R-13 is in accordance with the relatively lower synthesis temperature**.** The carbon network observed in TEM (Fig. 4.10a) of R-10 consists of the graphitic carbon as shown in HRTEM (Fig. 4.10b). The inset in Fig.4.10b elucidates the lattice fringes of 0.22 nm corresponding to (101) plane of Mo_2C (ICDD reference pattern -035-0787). The coated and wrapped graphitic carbon encapsulating Mo_2C particles correspond to (002) plane having lattice fringes 0.32 nm in accordance with the d spacing of ICDD reference pattern -026-1076 and -001-0640. The HRTEM micrographs (Fig. 4.10b) reveals the graphitic sheets and tubules like growth morphology of carbon as observed by Iijima *et al.* [38] also**.** Figure 4.11a shows the TEM images of sample (R-3) synthesized at 800 °C for 10 h. The clear visibility of surface coating of particle confirms the presence of carbon (circled). The carbon coated Mo_2C particles are embedded in the carbon matrix and have tendency to agglomerate. The lattice fringes in the

HRTEM micrograph (Fig. 4.11b) correspond to inter planar distance (0.22 nm) of (101) plane of hexagonal Mo_2C (ICDD pattern 035-0787). The lattice fringes of outer layer correspond to graphitic carbon, which is thicker in R-3 compared to R-10 and R-13, respectively. The higher carbon content in R-3 and R-9 compared to R-13 is in accordance with Raman spectroscopy.

The EDS elemental mapping of STEM shown in Fig. 4.9 to 4.11(c-f) of R-13, R-10 and R-3 predicts the spatial distribution of Mo and C elements with exception of small amount of oxygen. The EDS elemental mapping (STEM) shows the more spatial distribution of Mo and C except for a lesser amount of oxygen present within the carbon matrix. However, the oxygen content in R-13 is more as compared to R-10 and R-3. The Mo and C are more uniformly distributed in R-13 than R-10 as shown in Fig. 4.9c-f. The individual elemental distribution of (R-13) Mo, C and O are given in Fig. 4.9d, Fig. 4.9e and Fig. 4.9f, respectively. The variation of oxygen content from case to core in the observed spectra indicate that the reduction-carburization of MoO_3 to Mo_2C occurs via formation of intermediate oxide and Mo metal. Figure 4.12a-c shows the wide particle size distribution as observed from TEM images. More than 100 particles from different areas/scans were measured and the particle size follows lognormal distribution as given in equation 3.8-3.11. The particle size calculated from TEM is comparable to that calculated from XRD (W-H) analysis. The results indicate that deviation in particle size using different models may be the consequence of agglomeration of particles. However, certain deviation in size using different methods may be due to the agglomeration of particles [19].

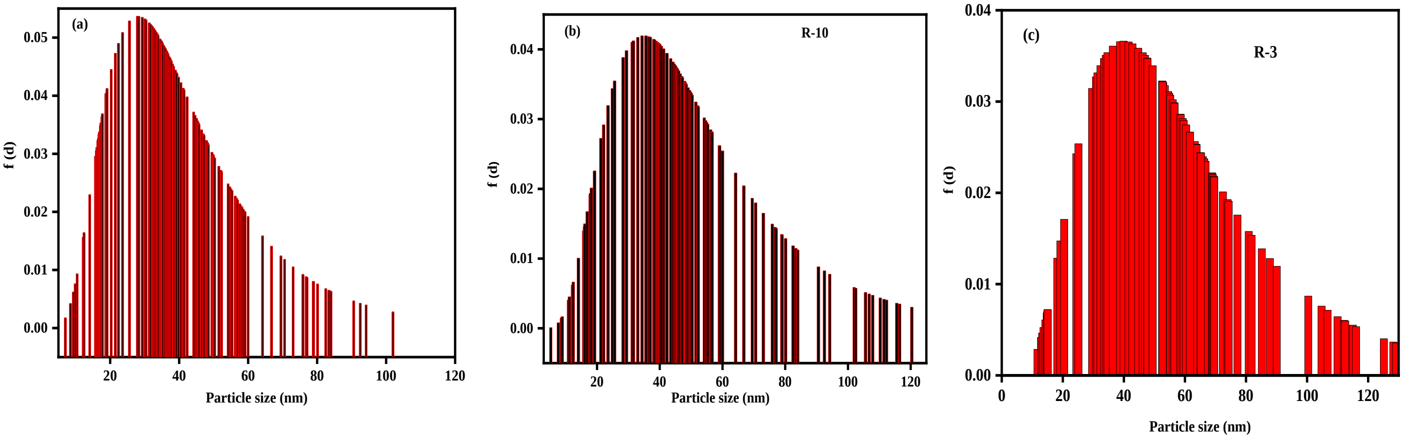

Figure 4.12: Particle size distribution from TEM analysis (a) R-13, (b) R-10 and (c) R-3.

4.3.4 Surface analysis

4.3.4.1 X-ray Photo electron spectroscopy (XPS)

The composition and surface chemical state of carburized products R-3, R-6, R-10 and R-13 samples were further identified by X-ray photoelectron spectroscopy. The full survey spectrum of R-3, R-6, R-10 and R-13 are shown in Fig. 4.13a-d, respectively. The survey spectrum shows the presence of five distinct peaks at 232.9, 284.8, 397.7 532.4 eV, which can be attributed to Mo3d, C1s, Mo3p, and O1s respectively [39]. By means of curve fitting, the distribution of molybdenum (Mo) species and the corresponding oxidation states were estimated.

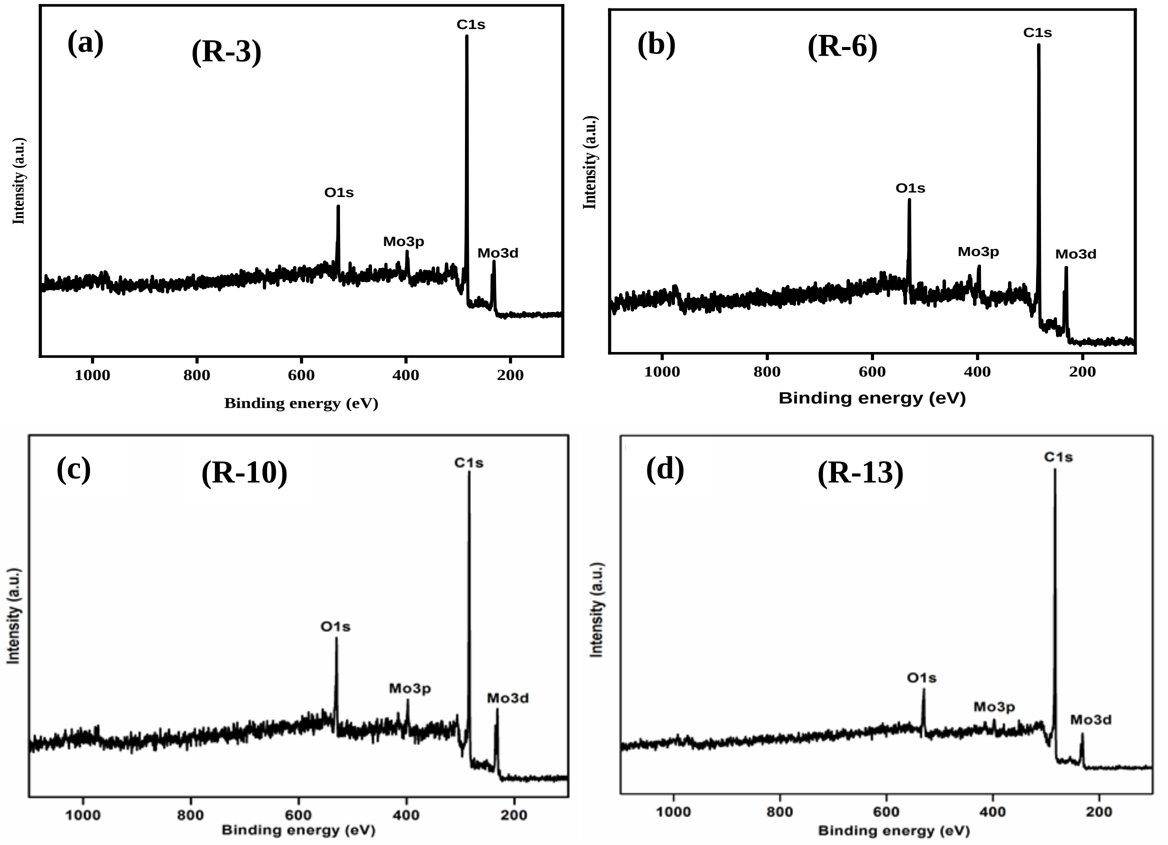

Figure 4.13: XPS survey spectrum of Mo_2C (a) R-3 (800 °C for 10 h), (b) R-6 (800 °C for 12 h), (c) R-10 (700 °C for 14 h) and (d) R-13 (600 °C for 20 h).

The high resolution (HR) spectrum of Mo3d (R-3) is shown in Fig. 4.14a. It reveals two peaks at 228.1 and 231.7 eV (Table 4.2) assigned to (Mo^{2+}) $Mo3d_{5/2}$ and $Mo3d_{3/2}$ respectively, originating from Mo_2C. In parallel, the two peaks (Table 4.3) attributed to (Mo^{6+}) $Mo3d_{5/2}$ and $Mo3d_{3/2}$, respectively were also observed [40]. This arise due to the surface oxidation of Mo_2C when exposed to air for prolonged duration [31,41].

Table 4.3: Peak positions of XPS analysis.

Sample Id	Mo3d						C1s		O1s		
	Mo_2C (2+)		Mo_2C (4+)		Mo_2C (6+)		Mo-C (ev)	C-C (ev)	Mo-O (ev)	C-O (ev)	C=O (ev)
	$Mo3d_{5/2}$ (ev)	$Mo3d_{3/2}$ (ev)	$Mo3d_{5/2}$ (ev)	$Mo3d_{3/2}$ (ev)	$Mo3d_{5/2}$ (ev)	$Mo3d_{3/2}$ (ev)					
R-3	228.1	231.7	-	-	232.4	235.4	284.1	285.4	530.2	531.1	532.4
R-6	228.1	231.3	229.3	232.7	232.4	235.5	284.0	284.7	530.2	531.1	532.4
R-10	228.1	231.8	-	232.4	232.2	235.5	284.2	285.1	530.2	531.1	-
R-13	228.1	231.8	-	232.6	232.1	235.4	284.2	285.1	530.2	531.1	-

The high resolution spectrum of Mo3d (R-6) as shown in Fig. 4.14b revealed that the double peaks assigned to (Mo^{2+}) Mo $3d_{5/2}$ and $Mo3d_{3/2}$ stemming from Mo_2C. The corresponding peak positions are given in Table 4.3. The double peaks (Table 4.3) as shown in insert of (Fig. 4.14b) are attributed to (Mo^{4+}) $Mo3d_{5/2}$ and $Mo3d_{3/2}$, respectively. Due to the surface oxidation of Mo_2C during XPS analysis, the peaks observed can be assigned to (Mo^{6+}) $Mo3d_{5/2}$ and $Mo3d_{3/2}$, respectively (Table 4.3) [41]. The surface oxidation during XPS measurements results in the formation of MoO_x mainly composed of MoO_2 and MoO_3. Additional peaks of Mo^{4+} were observed in R-6 sample, which correspond to MoO_2. The presence of MoO_2 in R-6 XPS spectrum of Mo3d is in accordance with the XRD results, which also show the presence of MoO_2 phase in sample. The presence of four distinct peaks for both R-10 and R-13 at positions 231.8, 282.4, 399.5 and 528.6 eV correspond to Mo3d, C1s, Mo3p, and O1s, respectively [42]. The high resolution (HR) spectra of Mo3d (R-10) is shown in Fig. 4.14c and the peak positions are tabulated in Table 4.3. The peaks attributed to (Mo^{2+}) $Mo3d_{5/2}$ and $Mo3d_{3/2,}$ respectively reveals the formation of Mo_2C. An additional peak assigned to (Mo^{4+}) Mo3d3/2 has originated from MoO_2 (Table 4.3). In addition to this, the peaks attributed to (Mo^{6+}) $Mo3d_{5/2}$ and $Mo3d_{3/2}$, respectively originate from surface oxidation [40]. However, the HR spectra of Mo3d (R-13) as shown in Fig. 4.14d confirms the presence of (Mo^{2+}) $Mo3d_{5/2}$ and $Mo3d_{3/2}$ stemming from Mo_2C at peak positions given in Table 4.3. In parallel, the peaks (Table 4.3) attributed to (Mo^{6+}) $Mo3d_{5/2}$ and $Mo3d_{3/2}$ of MoO_3, respectively are shown in Fig 4.14d. An additional peak at position (Table 4.3) attributed to (Mo^{4+}) $Mo3d_{3/2}$ (Fig 4.14d) originates from MoO_2. The superficial oxidation in the air might have resulted in the formation of these oxide species. However, the existence of MoO_2 may correspond to the presence of inherent oxide species within the carbon matrix.

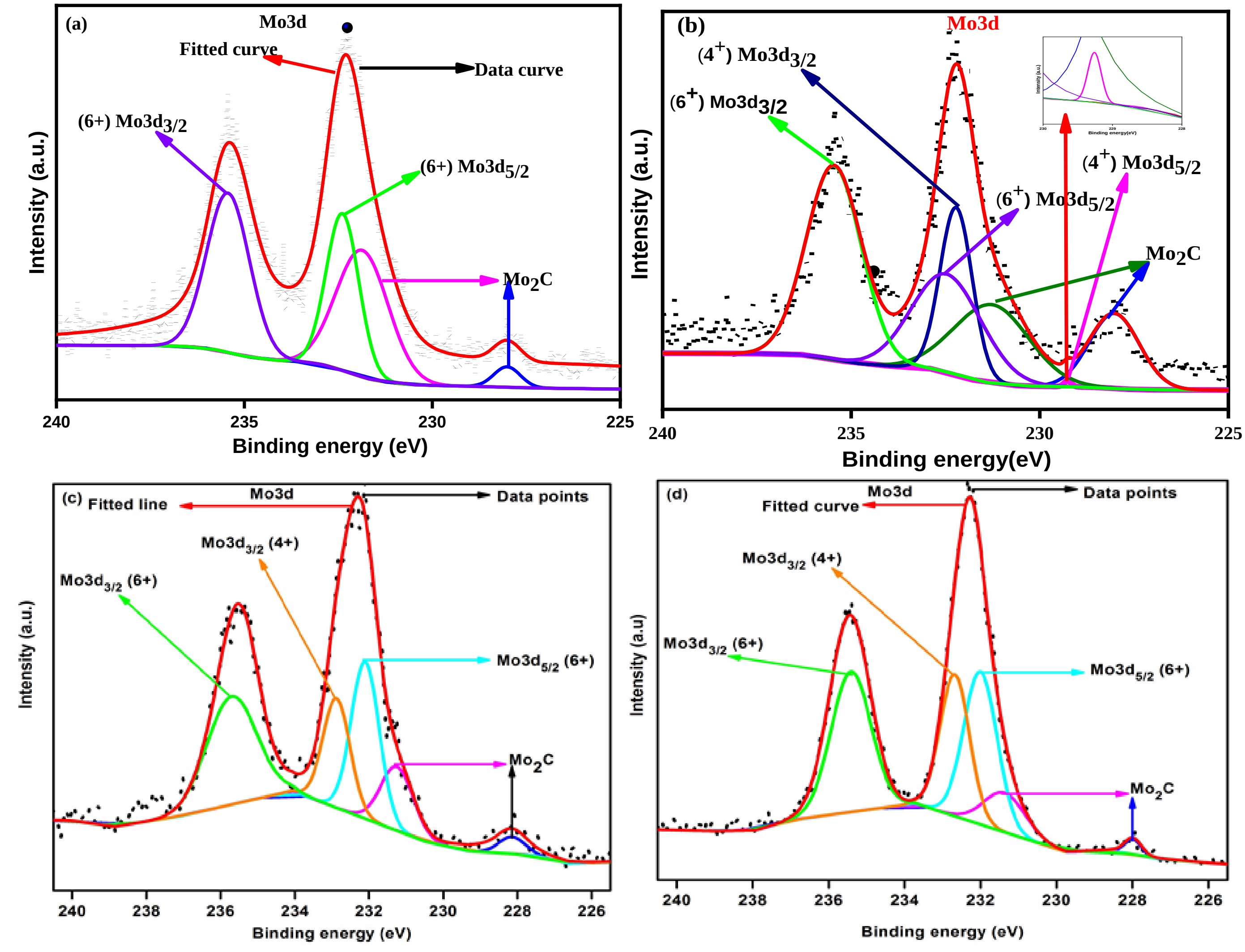

Figure 4.14: HR XPS spectrum of Mo3d (a) R-3 (800 °C for 10 h), (b) R-6 (800 °C for 12 h), (c) R-10 (700 °C for 14 h) and (d) R-13 (600 °C for 20 h).

Figure 4.15 shows high resolution spectrum of C1s for all the samples R-3 (Fig. 4.15a), R-6 (Fig. 4.15b), R-9 (Fig. 4.15c) and R-13 (Fig. 4.15d). Nearly similar pattern of peaks is exhibited by all the synthesized samples with the peaks corresponding to Mo-C and C-C and the peak positions are given in Table 4.3. The O1s spectra of the synthesized samples is shown in Fig. 4.16 for R-3 (Fig. 4.16a), R-6 (Fig. 4.1b), R-10 (Fig. 4.16c) and R-13 (Fig. 4.16d). The peaks of Mo-O and C-O, almost exhibit similar peak positions as given in Table 4.3. Moreover, the O1s spectrum of R-6 shows presence of three peaks after deconvolution. However, the peaks observed at 532.4 eV have originated from C=O [43]. The high intensity of C1s and O1s spectra in R-13 predicts the higher content of carbon and oxygen in comparison to R-10.

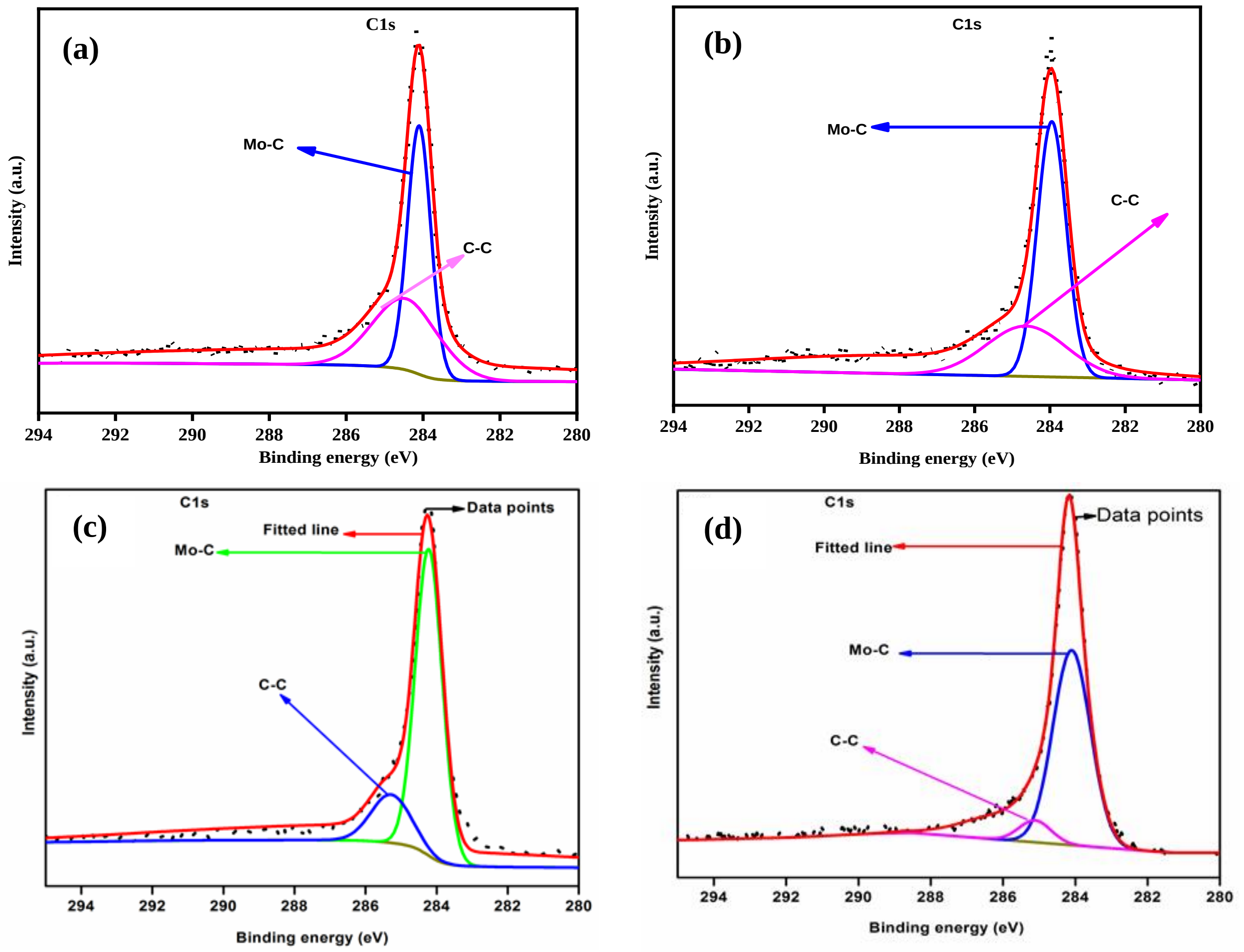

Figure 4.15: HR XPS spectrum of C1s (a) R-3, (b) R-6, (c) R-10 and (d) R-13.

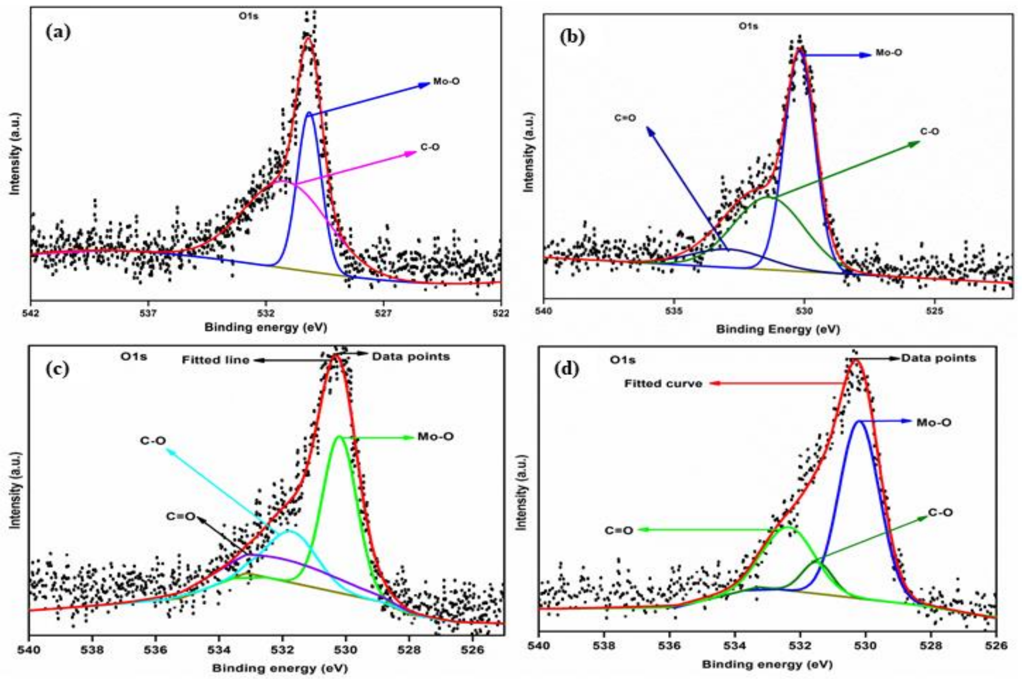

Figure 4.16: HR XPS spectrum of O1s (a) R-3, (b) R-6, (c) R-9 and (d) R-13.

4.3.4.2 Nitrogen adsorption/desorption (BET) analysis

The nitrogen sorption studies were performed to measure the Brunauer-Emmet-Teller (BET) specific surface area of the synthesized samples (β-Mo_2C@C) R-3, R-6, R-10 and R-13. The measured BET specific surface area of carbon coated Mo_2C (R-3 sample) is 15.7 m^2g^{-1} having mean pore size 33.04 nm and pore volume 0.13 cm^3g^{-1}, respectively. However, R-6 sample exhibits BET specific surface area 7.8 m^2g^{-1} along with the mean pore size of 39.33 nm and pore volume of 0.07 cm^3g^{-1}, respectively. The data showed that the surface area decreased with the increase in time at particular temperature corresponding to R-3 and R-6 samples, respectively. Moreover, the particle size increases with increase in the reaction time, which is in agreement with the crystallite size and is in tune with the values obtained with Scherrer equation in XRD pattern (Table 4.1). Figure 4.17 shows the adsorption isotherms of β-Mo_2C@C (R-3, R-6, R1-0 and R-13) samples. As compared to R-3 sample, the inclusion of oxide particle within the synthesized powder R-6 a decrease in the BET surface area and the pore volume is observed. However, the mean pore size increases [44]. The adsorption isotherms (Fig. 4.17) of all the samples demonstrate the characteristic of a type-II isotherm, as per IUPAC classification [45,46]. The isotherms observed in the present study shows characteristic of H-4 hysteresis [47]. This indicates that there is formation of complex structure with mesopores and micropores, for both the samples.

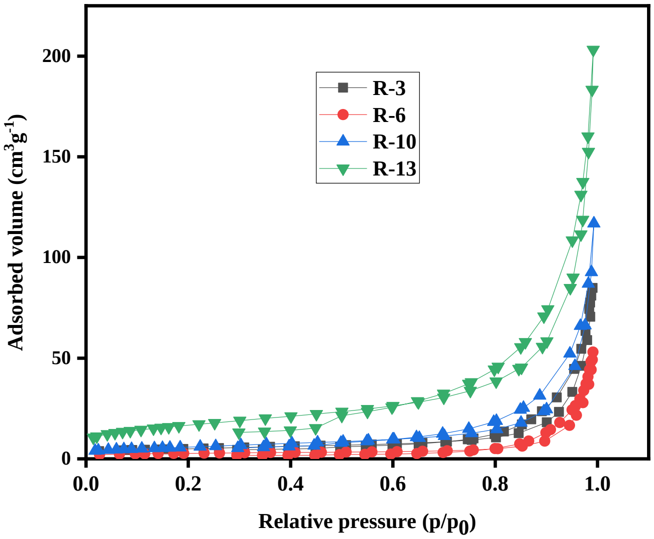

Figure 4.17: BET desorption isotherm of β-Mo_2C@C samples.

The measured BET specific surface area of R-10 is 20.9 m^2g^{-1} along with the mean pore size 14.4 nm and pore volume 0.16 cm^3g^{-1}, respectively. However, R-13 sample exhibits BET specific surface area 60.8 m^2g^{-1} along with the mean pore size of 15 nm similar to R-10 and total pore volume of 0.292 cm^3g^{-1}, respectively. The surface area decreases with the increase in temperature, which is in agreement with the crystallite size trend calculated using Scherrer equation from XRD pattern. The higher crystallite size as observed in R-10 sample with the increase in the reaction temperature apparently decreases the specific surface area [48,49]. Figure 4.17 also shows the adsorption/desorption isotherms and mean pore size distribution of R-10 and R-13 samples. The surface area of R-10 decreased as compared to R-13. This might be because of higher crystallite size and degree of graphitization of particle surface with the increase in temperature, as observed in Raman spectra [50]. The internal pore strain or pore rupture also results in the decrease in surface area as temperature is increased [6]. Moreover, the decrease in total pore volume may also result from agglomeration and sintering of particles with the rise in temperature. This indicates that there is formation of the complex structure with mesopores and micropores, associated with the agglomeration of particles in the final product.

4.3.5 Formation mechanism of Mo_2C

The formation of Mo_2C by reduction-carburization in an autoclave is multistep reduction and carburization process. Based on XRD pattern of all the synthesized samples followed by the microstructural analysis, the formation mechanism of Mo_2C (800 °C) has been predicted. Mg being highly reactive substance absorbs oxygen to form MgO, whereas polypropylene decomposes into the gaseous hydrocarbons inside the autoclave [23]. The generation of carburizing atmosphere inside autoclave is rather complex due to the interaction of various gases. Moreover, the exact nature of gases evolved during decomposition of polypropylene in closed autoclave cannot be determined. The MgO being highly reactive catalyst inside the autoclave reduces the gaseous compounds into carbon and hydrogen [29]. The carbon along with hydrogen inside the autoclave is in excess amount. It helps in reduction and as well as carburization. The lower reaction temperature of 600 ºC for 10 h reaction time reveals that only some reduction of MoO_3 to intermediate Mo_4O_{11} specie has taken place. The initial reduction of MoO_3 to Mo_4O_{11} in presence of Mg in carbon and hydrogen atmosphere follows a number of reaction paths, giving rise to different reaction products. Considering all the feasible reactions and their thermodynamic parameters for various stages of reduction and carburization, the most feasible reaction paths are as follows [51]:

$$4MoO_3 + Mg \rightarrow Mo_4O_{11} + MgO \qquad (4.3)$$

The heat of formation (ΔH) of the above reaction can be calculated using relations [52].

$$\Delta H = \Delta H_{298} + \int_{298}^{T} C_p \, dt \qquad (4\ .4)$$

$$C_p = a + b10^{-3}T + C10^{6}T^{-2} + d10^{-6}T^{2} \qquad (4.5)$$

Where ΔH is the heat of formation, ΔH_{298} is heat of formation at standard temperature and C_p is the heat capacity varying with temperature.

Variation of ΔH with temperature for the reduction of MoO_3 to Mo_4O_{11} for the most feasible with Mg as reducing agent (equation 4.3), having more negative ΔH variation with temperature is shown in Fig. 4.18a. The reaction has less feasibility with higher hydrocarbons as they readily decompose to H and C [24].

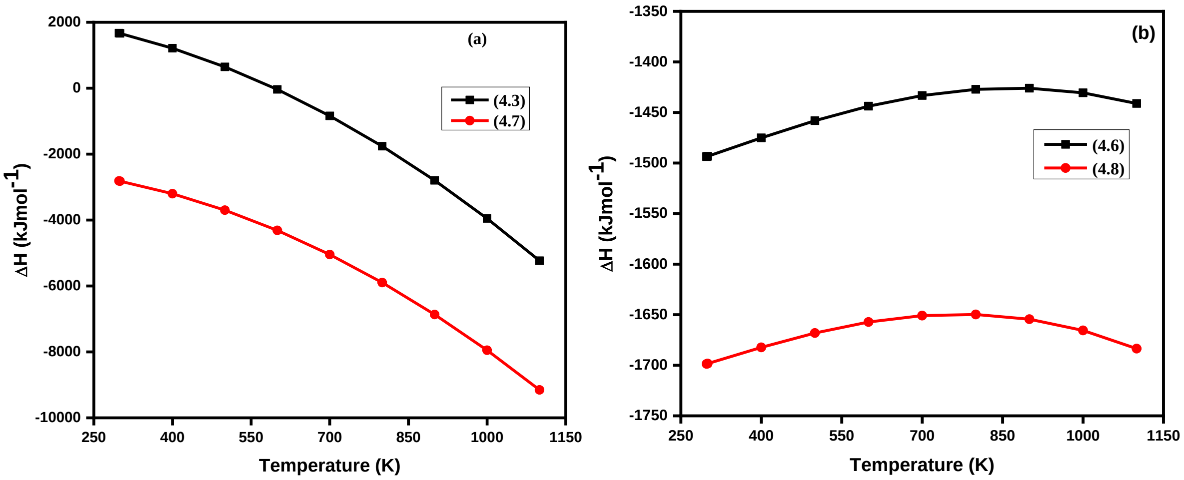

Figure 4.18: Variation of ΔH with temperature for best possible reactions for (a) reduction and (b) carburization.

The carbon encapsulates the oxide particles and the hydrogen being small in size penetrates along the grain boundaries and breaks the oxide particles into small constituents which facilitate the reaction in forward direction at faster rate. With the increase in temperature, the formation of Mo_2C seems to be feasible, the presence of Mo, MoO_2 and Mo_2C at 700 °C for 10 h holding reveals that the reduction- carburization proceeds in forward direction with increase in temperature. The reduction-carburization of MoO_3 to Mo_2C is multistep reduction process (equation 4.1 and 4.2). Considering the results obtained at 600 °C in hydrogen and carbon atmosphere, the reaction corresponding to reduction- carburization with C and H_2 (4.6) is most feasible and the reaction path is given as:

$MoO_3 + Mo_4O_{11} + 9C + 6H_2 \rightarrow 2Mo_2C + 1/2\ MoO_2 + 1/2Mo + 3CO + 4H_2O + 3CO_2 + CH_4$ (4.6)

The ΔH variation with temperature of above reaction is shown in (Fig. 4.18b) having negative ΔH at different temperatures and has shown a decreasing trend at higher temperatures predicting more feasibility of phase formation. Carbon being present in high concentration creates a thick coating around the produced Mo_2C phase as shown in schematic diagram Fig. 4.19.

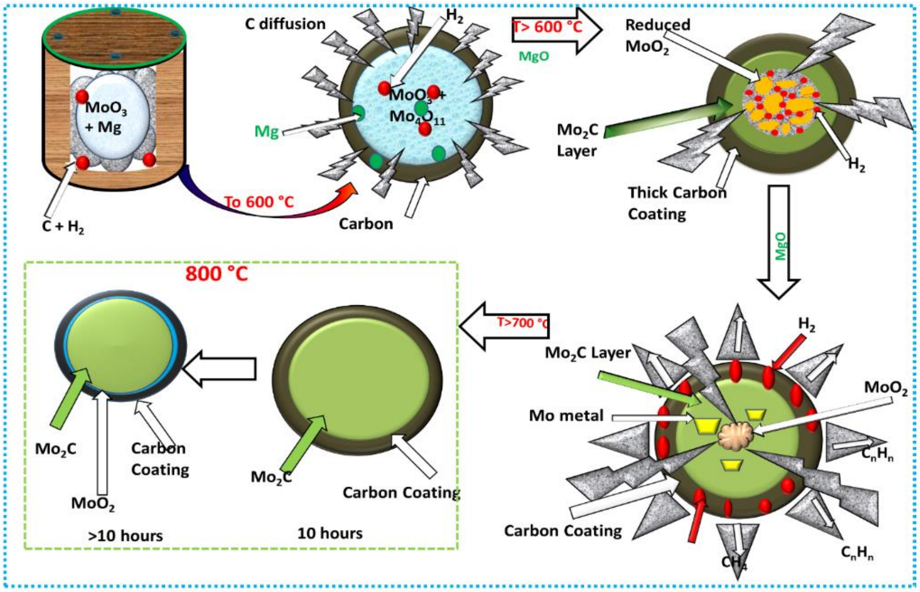

Figure 4.19: Schematic representation of transformation of MoO_3 to Mo_2C nano particles

High carbon concentration also facilitates the direct carburization of MoO_2 to Mo_2C with small amount of Mo metal present, which may be because of the enclosed Mo_2C layer in thick carbon coating that hinders further diffusion of carbon to thoroughly carburize the reduced oxide phase and Mo metal to form single phase Mo_2C. Certain authors suggested the low concentration of CO leads to the formation of metallic Mo, whereas, a high concentration of CO forms Mo_2C directly from MoO_2 [17,53]. So the presence of sufficient carbon atoms on the surface needs to travel longer distance to carburize the reduced oxides. Carbon deposit on carbides is higher at lower temperatures. Carburization process may involve other catalytic reactions as CO_2/H_2O, reforming of CH_4 to H_2 and CO and direct cracking of CH_4 to H_2. The decomposition of polypropylene enriches the C_nH_n gases, which react with CO_2 and H_2O to reduce their concentration and produce more amount of H_2, C and CO to enhance the reduction carburization reaction. The enrichment of CO and H_2 proceed via different path ways [54]. Hydrogen produced in reaction also facilitates the carburization reaction by removing excess carbon from the surface by forming hydrocarbon gases. The deposition, removal of carbon (by hydrogen) and carbon dissolution occur simultaneously during reaction process. In order to facilitate the carburization the increase in reaction temperature to 800 ºC for 10 h thoroughly reduce the MoO_3 and Mo_4O_{11} to MoO_2 and simultaneously carburize MoO_2 to Mo_2C and single phase Mo_2C is obtained with excess carbon residue present. The reduction of MoO_3 and Mo_4O_{11} to MoO_2 results via different reaction paths inside an autoclave in presence of H and C. The reaction (4.7) shows the feasible reaction path having Mg and H_2 as reducing agents as given below:

$$MoO_3 + Mo_4O_{11} + Mg + 3H_2 \rightarrow 5MoO_2 + 3H_2O + MgO \tag{4.7}$$

The ΔH versus T variation of above reaction is shown in Fig. 4.18a, having more negative ΔH variation with temperature. All the reactions proceed in presence of Mg as catalyst and favor the reduction of MoO_3 and MoO_2 at temperatures greater than 600 °C [55], which simultaneously get carburized to Mo_2C. The reaction temperature 800 °C and 10 h time seems to be sufficient to reduce and carburize the MoO_3 to single phase Mo_2C. Carburization reaction (equation 4.8) shows the more feasible reaction path given as:

$$MoO_3 + Mo_4O_{11} + 9H_2 + 10C \rightarrow 5/2Mo_2C + 4H_2O + 6CO + 1/2CH_4 + 8H_2O + C \tag{4.8}$$

The ΔH variation with temperature of above reaction as given in (Fig. 4.18b) shows the feasibility of reaction having low negative ΔH variation with temperature. The formation of Mo_2C considering the above reaction paths based on the thermodynamic parameters has been schematically represented in Fig. 4.19. Formation of larger amount of CO_2 and H_2O enhances the decarburization reaction. The reaction of surface carbon with CO inside an autoclave results in higher concentration of CO_2, which favors the diffusion of oxygen in Mo_2C at higher temperatures as has been schematically represented in Fig. 4.19. So, increasing the time upto 12 h shows the reversibility of reaction due to presence of large amount of the decarburizing agents CO_2 and H_2O as reaction by products.

4.3.6 Electrochemical activity

4.3.6.1 HER activity

The electrocatalytic HER activity of as synthesized samples were studied by linear sweep voltammetry (LSV). The LSV was performed in the voltage window 0 to -0.28 V at a scan rate 2 mVs^{-1}. The LSV plots of the samples synthesized at different temperature and time conditions is shown in Fig. 4.20. Among all the samples synthesized at different temperatures at fixed time (Fig. 4.20a), only sample (R-3-pure phase Mo_2C) shows maximum current density of 35 $mAcm^{-2}$. The impure phases R-1 and R-2 reveal the lower current densities of 10 and 15 $mAcm^{-2}$, respectively. The pure phase Mo_2C (β-Mo_2C@C)samples (R-13), (R-10) and (R-3) synthesized at 600, 700 and 800 °C, respectively reveal the current densities of 22, 27 and 35 $mAcm^{-2}$, respectively (Fig.

4.20b). The impure phase contained samples obtained at different conditions at 800 and 700 °C show lower current density values than pure phase sample as shown in Fig. 4.20c-d.

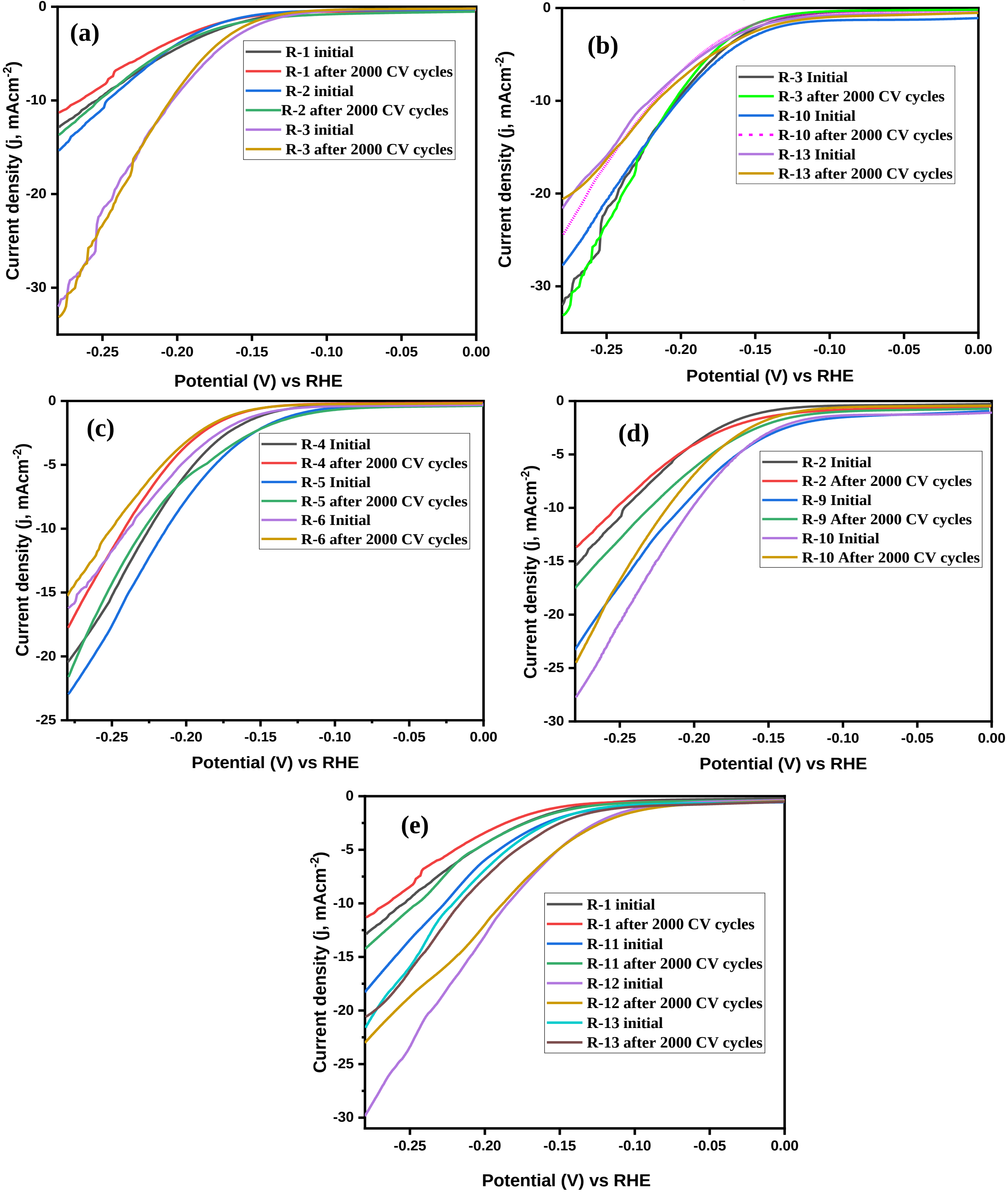

Figure 4.20: Polarization (LSV) plots of synthesized samples (a) variation in temperature, (b) pure phase β–Mo_2C@C, (c) variation of time at 800 °C, (d) variation of time at 700 °C and (e) variation of time at 600 °C.

The relatively higher temperature synthesized phase shows higher current density, which might be due to the result of enhanced crystallization of Mo_2C and surface carbon at higher temperatures. Only intermediate MoC phase (R-12) shown in Fig. 4.20e, reveals higher current density of 30.0 mAcm^{-2}, which is higher than pure phase Mo_2C samples (R-13) and (R-10). The high current density value of R-12 might be due to the lower crystallite size as calculated form XRD analysis. Moreover, the increase in reaction time favors the carburization process and crystallization of the product phase. This reveals the increment in value of current density with increase in reaction time. The incorporation of C in the Mo lattice provide a resemblance of its d-band structure with Pt and hence enhance the current density. It also favors the graphitization of surface carbon and hence enhances the charge transfer rate and increases the current density. The critical factor for HER catalysts is their long term stability.

To probe the stability of the synthesized electrocatalysts, cyclic voltammetry (CV) measurements were performed in voltage range 0.2 to -0.28 V for 2000 cycles at the scan rate of 100 mVS^{-1}. The polarization curve obtained after 2000 cycles are shown in Fig. 4.20a-e. The results depict the decrease in current density for impure phase incorporated samples (R-1 and R-2) as shown in Fig. 4.20a. The pure sample (R-3) predicts higher stability, showing negligible loss of current after 2000 CV cycles (Fig. 4.20a). Among the pure phase Mo_2C samples, only R-10 sample reveals lower stability in comparison to R-3 and R-13 as depicted in Fig 4.20b. The intermediate phases obtained at 800 °C for different time variations (Fig. 4.20c) destabilizes after 2000 CV cycles because of lower corrosion resistance of Mo and Mo oxide phases. The similar trend was observed for the samples synthesized at 700 °C (Fig. 4.20d). The current density of R-9 decreases by 24 % after 2000 cycles (Fig. 4.20d). This reveals that Mo_2C along with impurity phase Mo (R-2 and R-9) are not stable catalysts for HER. However, increasing the time at the same temperature leading to pure phase Mo_2C (R-10) further enhances the current density value to 27.9 mAcm^{-2} (Fig. 4.20 b and d). The long term stability of R-10 (Fig. 4.20b) depicts the decrease in the current density after 2000 CV cycles by 10 %. A different pattern was observed for samples synthesized at relatively lower temperature 600 °C (Fig. 4.20e). The intermediate MoC phase are not stable HER electrocatalyst for long term durability. Whereas samples synthesized at same temperature for higher holding time (20 hours) leading to Mo_2C phase (R-13) encapsulated in carbon matrix exhibits higher stability exhibiting similar polarization curve after 2000 cycles as shown Fig. 4.20 b and e. The pure phase Mo_2C (R-13) encapsulated in carbon coating, although having low current density value as compared to R-12 has higher stability with negligible loss of current after 2000 CV cycles. The lower current density of R-13 in comparison to R-12 might be consequence of bigger crystallite size. The R-10 having the low surface area as compared to R-13 shows enhanced current density value. The increase in current density is in agreement with the decrease in lattice strain from R-10 to R-13 (Table 4.2) [56,57]. The strained nano β–Mo_2C@C shows variation in d-band structures, which enhances the current density [57]. The more crystalline nature of R-10 and R-3 having more graphitic carbon on the surface in comparison to R-13 enhances the electron transfer rate and hence improves the HER activity [58]. The coated graphitic carbon residue on the surface of Mo_2C acts as the supporting matrix and enhances the electrical conductivity or charge transfer capacity of the electrocatalyst [37,59]. The low value of the current density of R-13 having the high surface area as compared to R-3 and R-10 might be because of the more carbon on the surface as determined by a prominent peak in XRD (graphitic and amorphous) and less graphitic carbon content as observed in Raman spectroscopy. The more amorphous carbon in R-13 has also been observed in TEM/HRTEM analysis and this deteriorates the catalytic performance of the electrocatalyst [37]. The porous carbon matrix support of β–Mo_2C@C particles prevents them from aggregation during reaction process and hence increases the stability [58]. However, R-13 having higher distorted carbon (amorphous) as compared to R-3 and R-10 might render an extra protection [41]. The Mo_2C phase embedded in the amorphous carbon matrix might not be performing actively due to extra protection of carbon resulting in decrease in current density with higher stability [60]. The high durability of the catalyst originated from the coupling between the surface carbon and enclosed Mo_2C particles. The tight binding of carbon support and Mo_2C particles occurring during in-situ synthesis also improves the durability of the catalyst [61]. Moreover, the presence of more oxygen content in R-13 within the carbon matrix as observed in STEM mapping results in enhancement of stability by creating a layer of oxide species, which inhibits further degradation of the active particle [62]. This also results in the decrease of current density because of low efficiency of these oxide phases towards HER.

The Tafel slope '$\boldsymbol{b}$' is an inherent property of the catalyst surface and is extracted from Tafel plot as shown in Fig. 4.21a-c. The value of '$\boldsymbol{b}$' determines the probable mechanism of HER on the surface of the catalyst [63]. The value of HER in acidic medium follows the following steps [64,65]:

$$M + H_3O^+ + e^- \leftrightarrow MH_{ads} + H_2O \qquad (Volmer\ step) \qquad (4.9)$$

$$MH_{ads} + H_3O^+ + e^- \leftrightarrow H_2 + M + H_2O \qquad (Heyrovsky\ step) \qquad (4.10)$$

$$MH_{ads} + MH_{ads} \leftrightarrow H_2 + 2M \qquad (Tafel\ step) \qquad (4.11)$$

Where 'M' is the active site and MH_{ads} denote the hydrogen absorbed on that site. The value of Tafel slope '$\boldsymbol{b}$' up to 120 mVdec^{-1} suggests that Volmer reaction (4.9) is rate determining step, otherwise, the value of b about 40 and 30 mVdec^{-1} is referred to Heyrovsky (4.10) and Tefel (4.11) reactions, respectively [58]. The Tafel plots of the synthesized samples is shown in Fig. 4.21 and the corresponding values of Tafel slope '$\boldsymbol{b}$' are given in the Table 4.4.

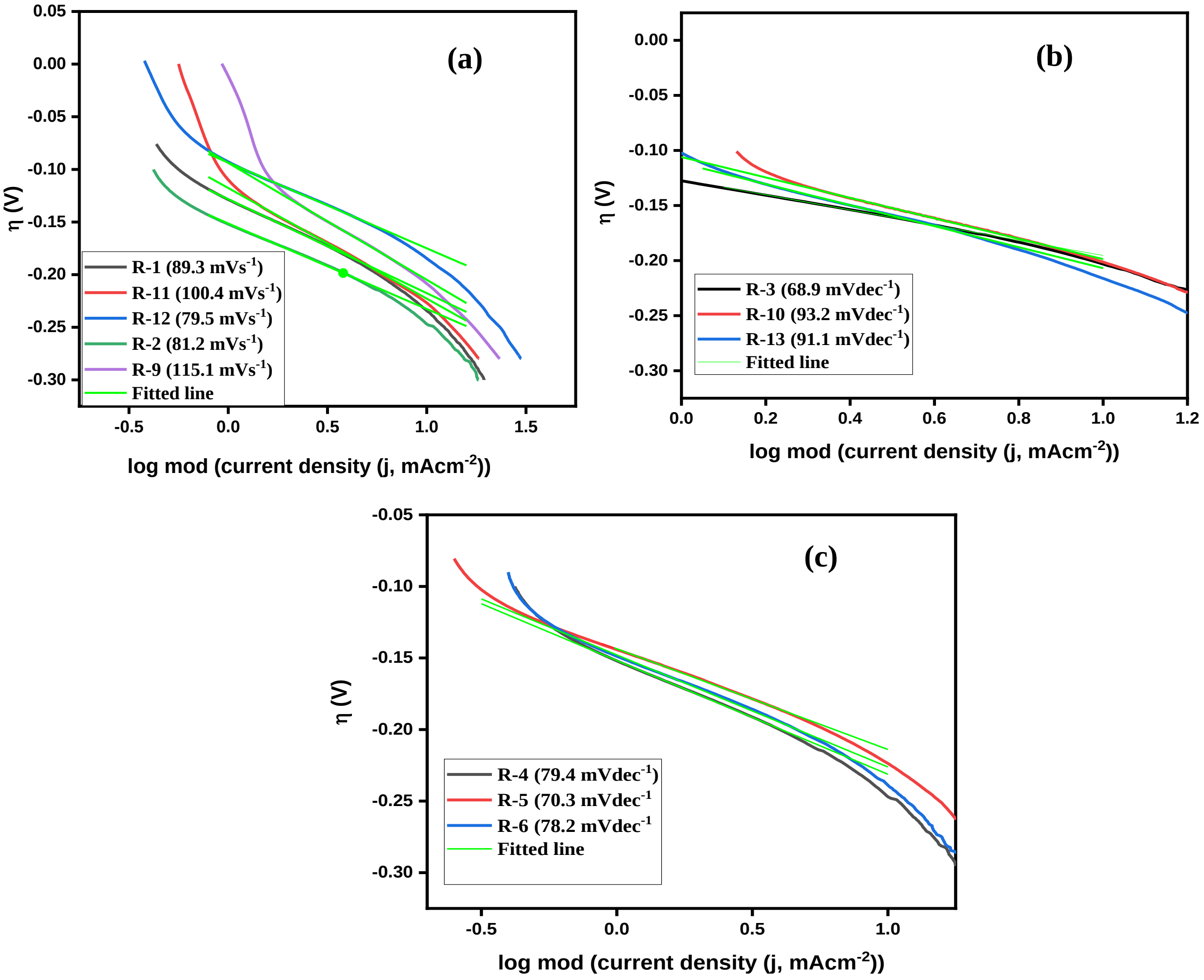

Figure 4.21: Tafel slope '$\boldsymbol{b}$' values of the synthesized samples (a) samples synthesized at 600 and 700 °C, (b) pure phase and (c) samples synthesized at 800 °C.

The relatively lower temperature (600 and 700 °C) synthesized samples containing some impure phases along with Mo_2C shows higher Tafel slope (Fig. 4.21a) compared to pure phase Mo_2C samples (Fig. 4.21b). The Tafel slope '$\boldsymbol{b}$' of MoC phase samples (R-11 and R-12) is 100.4 and 79.5 mVdec^{-1}, respectively.

Table 4.4: Eelectrochemical parameters of the synthesized samples having catalyst loading of $0.57 gcm^{-2}$.

Sample Id	Tafel slope '*b*' (mVs^{-1})	Overpotential (mV) at 10 $mAcm^{-2}$	EDLC (C_{dl}) ($mFcm^{-2}$)
R-1	**94.8**	**217.3**	**10.6**
R-2	**81.2**	**232.6**	**5.8**
R-3	**68.9**	**195.3**	**9.8**
R-4	**79.4**	**231.2**	**7.7**
R-5	**70.3**	**213.8**	**9.7**
R-6	**78.2**	**225.2**	**12.0**
R-9	**115.1**	**220.6**	**11.0**
R-10	**93.2**	**198.7**	**12.5**
R-11	**100.4**	**220.0**	**10.9**
R-12	**79.5**	**173.6**	**35.5**
R-13	**91.1**	**211.2**	**30.0**

However, the value of '***b***' (Fig. 4.21a) for impure phases R-2 and R-9 is higher than those synthesized at 600 °C. Moreover, the value of Tafel slope is lower for the samples synthesized at relatively higher temperature compared to 600 and 700 °C. The value of '***b***' (Fig. 4.21b) for R-3, R-10 and R-13 (β–Mo_2C@C) is 68.9, 93.2 and 91.1 $mVdec^{-1}$, respectively and is consistent with the literature [12]. The decrease in value of '***b***' from MoC to pure (Mo_2C) phase formation reveals the faster reaction kinetics at the surface of product phase. The values '***b***' for R-3 is lower than both (R-10 and R-13). However, for R-10 and R-13 it is nearly same, which signifies that discharge reaction is fast in R-3 compared to R-10 and R-13. The rate reaction step is tending more towards Hevyrosky step in R-3 and rate of reaction is determined by Volmer step in R-10 and R-13 [58]. The lower '***b***' values samples synthesized at 800 C (Fig. 4.21c) represented in Table 4.4 attributes to the higher conducting nature of carbon over Mo_2C. A little low value of '***b***' for R-13 compared to R-10 might be a result of the higher surface area, which provides more active sites and improves the rate of reaction. The as prepared samples show enhanced HER results, having the lower value of '***b***' as compared to previously reported results as given in Table 4.5. The comparison of the overpotential, onset potential and the exchange current density calculated for the synthesized samples are given in Table 4.5. Among the synthesized β–Mo_2C@C samples, R-3 exhibits lower overpotential and onset potential as compared to R-10 and R-13. This might be the result of conducting graphitic surface carbon which enhanced the charge transfer rate at lower potentials. However, the lower onset and overpotential and higher exchange current density of MoC phase (R-12) corresponds to lower crystallite size.

Table 4.5: Comparison of present HER analysis with the reported results.

Sample Id	**Over potential (mV) at $10 mAcm^{-2}$**	**Catalyst loading ($mgcm^{-2}$)**	**Tafel Slope ($mVdec^{-1}$)**	**Reference**
MoC_x-2	160	0.354	93	66
Mo_2C@NPC	260	0.14	126.4	31
C-Mo_2C	293	0.102	98	67
alpha-Mo_2C	198	0.102	56	
Ni-Mo_2C@C	169	0.15	127	68
MC-G50	283	0.357	101	69
P-Mo_2C	160	-	128	70
Mo_2C/CC	140	1.5	124	
C-Mo_2C	260	-	168	
Mo_2C/CNT	250	8.2	251	71
Mo_2C/CXG	170	6.3	264	
Mo_2C/GR	242	1.4	82	72
Mo_2C/CNT-GR	130	0.65	58	

4.3.6.2 Electrochemical double layer capacitance (EDLC, C_{dl})

The electrochemical surface area (ECSA)/ EDLC measurements were done via CV analysis performed in voltage range 0.2 to 0.4 V at different scan rates (20-230 mVS^{-1}) is shown in Fig. 4.22 a-h. The CV plot of the samples synthesized at relatively higher temperature shows more rectangular behavior of CV curve, while the lower temperature phases depict the quasi rectangular curve as shown in Fig. 4.22. However, the pure phase (β–Mo_2C@C) samples, R-3 (Fig. 4.23a) and R-10 (Fig. 4.23b) samples exhibit better rectangular shape compared to R-13 (Fig. 4.23c). This corresponds to good capacitance behavior exhibited by pure phase β–Mo_2C@C samples and more reversibility during charging and discharging. It also correspond to non-faradic character exhibited by the synthesized samples. The plot of scan rate (mVs^{-1}) on the x-axis and current density $\Delta j_{0.3}$ ($mAcm^{-2}$) on the y-axis for the synthesized samples are shown in Fig. 4.24 a-c. Figure 4.24a shows the EDLC estimation of the pure phase β–Mo_2C@C samples. The corresponding EDLC values are tabulated in Table 4.4.

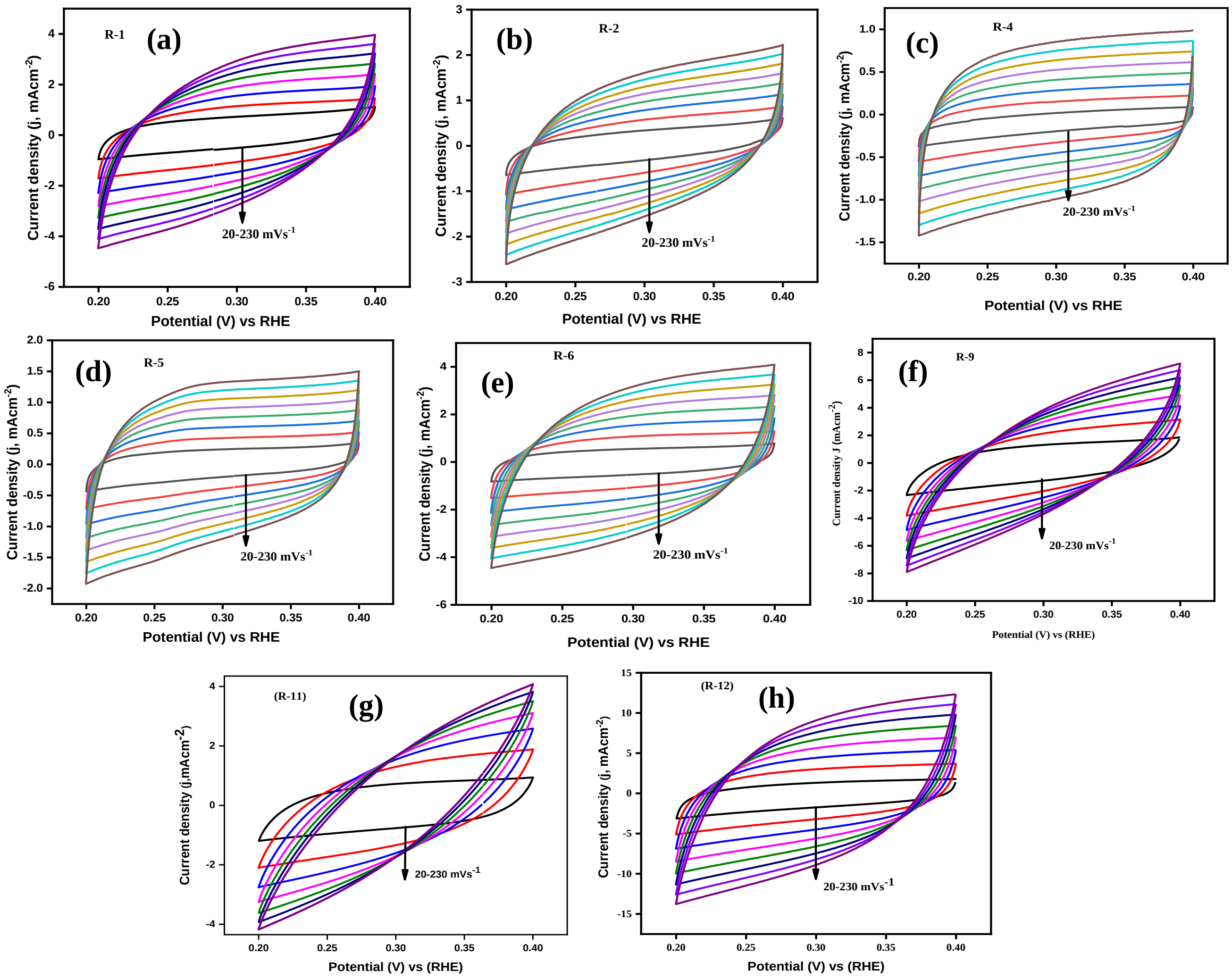

Figure 4.22: CV plots of the synthesized samples (a) R-1, (b) R-2, (c) R-4, (d) R-5, (e) R-6, (f) R-9, (g) R-11 and (h) R-12.

.

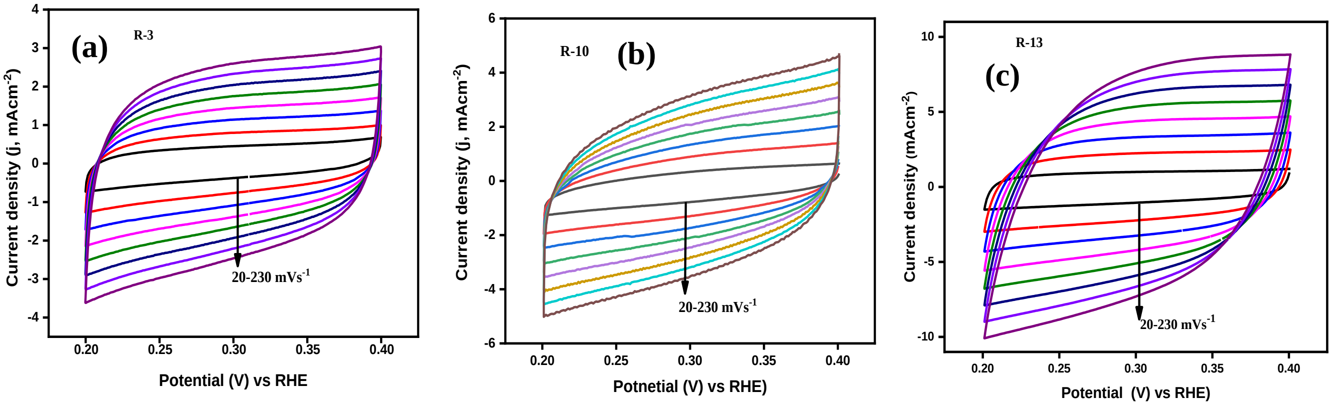

Figure 4.23: CV plot of pure phase β–Mo_2C@C samples (a) R-3 (800 °C for 10 h), (b) R-10 (700 °C for 14 h) and (c) R-13 (600 °C for 20 h).

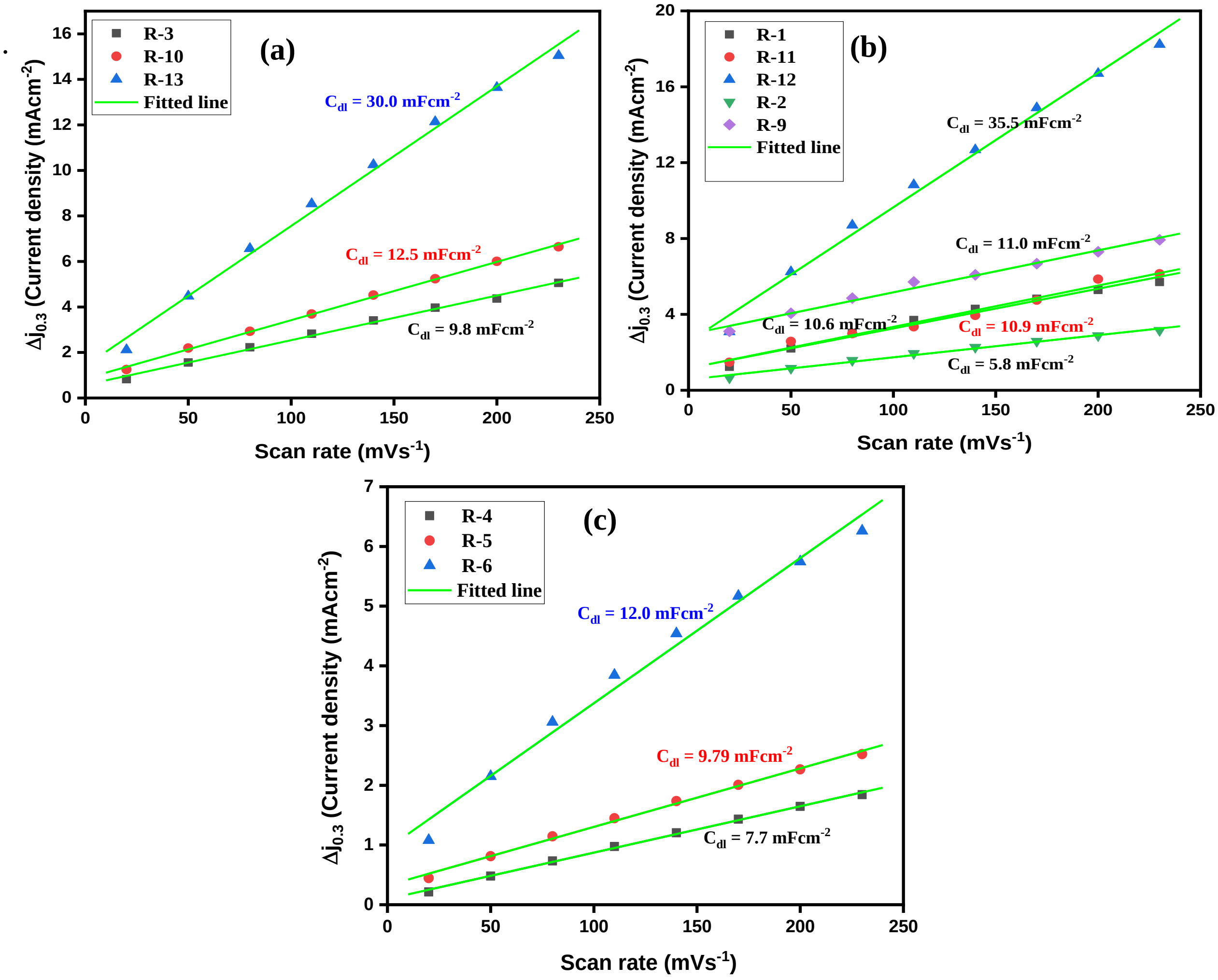

Figure 4.24: EDLC of (a) R-3, R-10 & R-13, (b) R-1, R-11, R-12, R-2 & R-9, (c) R-4, R-5 & R-6.

The β–Mo_2C@C samples (Fig. 4.24a) exhibit EDLC values of 9.8, 12.5 and 30.0 mFcm^{-2} for R-3, R-10 and R-13, respectively. R-13 has about 2.5 and 3 times C_{dl} value as that of R-10 and R-3, which is in agreement with the high BET specific surface area. However, in the relatively lower temperature (700 °C) synthesized phase R-2, R-9 and R-10 (Fig. 4.24b), the EDLC performance is enhanced with carburization of Mo and MoO_x species to get final product (Mo_2C). The EDLC value of R-1 (Table 4.4 and Fig. 4.24b) mostly corresponds to the carbon species, which have not diffused within the MoO_x phase at lower temperature. The MoC phases (R-11 and R-12) have higher ELDC values because of their lower crystallite size (Fig. 4.24b). The lower value of R-3, R-4 (Fig. 4.24c), R-5 (Fig. 4.24c) might be associated with the sintering of surface pores at relatively higher temperature (800 °C). The little higher value of R-6 (Fig. 4.24c) might correspond to surface oxidation of R-3, which exhibits new active site to enhance charge storage capacity. The

BET surface area was not the sole reason affecting EDLC/ESCA β–Mo_2C@C. However, the morphological features, composition, and environment of active sites affect the same [73]. The lower value of the current density of R-13 although having the higher value of EDLC might also be a consequence of excess carbon and high oxygen content in the material. The higher ECSA of R-12 is responsible for higher current density and low value of Tafel slope as observed in LSV measurements and Tafel plots, respectively. The decrement in the value of ESCA with the rise in synthesis temperature might be because of surface sintering and thus inhibiting the active sites.

4.3.6.3 Electrochemical impedance spectroscopy (EIS)

The EIS of β–Mo_2C@C (R-3, R-10 and R-13) samples were done to gain further insight about HER activity of synthesized Mo_2C nano powders encapsulated in carbon matrix. Figure 4.25a-c shows the Nyquist plot of R-3, R-10 and R-13 at different applied potentials (20-300 mV vs RHE). The near semi-circular curves observed at different potentials estimates the lower charge transfer resistance of the synthesized samples. The semicircular curve of smaller diameter formed at higher potentials shows that charge transfer resistance (R_{ct}) reduces with increase in applied potential [31,59]. This reflects the kinetics of HER process and depicts superior hydrogen evolution with applied potential. Deviation from the semicircular fit corresponding to an equivalent circuit to calculate the value of resistance (R_{ct}) and other parameters may be attributed to surface inhomogeneity, roughness (variable capacitance across surface), electrode porosity (wide/uneven pore size) and surface reactivity [74,75] . In case of R-3 and R-10, the graphitic carbon layer enclosing the particle acts as the electronic bridge and enhances the electron transfer on the surface and electronic conductivity of electrocatalyst [59]. The interconnection between Mo_2C and graphitic surface carbon decreases the contact electrical resistance, which leads to enhancement in electron transfer along each microstructure. The Bode plots of R-3, R-10 and R-13are shown in Fig. 4.25d-f. The phase angle and the total impedance becomes smaller at higher frequencies and shows similar impedance properties with regard to the HER potentials. However, the semicircular curve observed in both the cases shows potential dependency at higher values. The decrease and the shifting of phase angle towards higher frequencies indicates the lower resistance and superior HER kinetics.

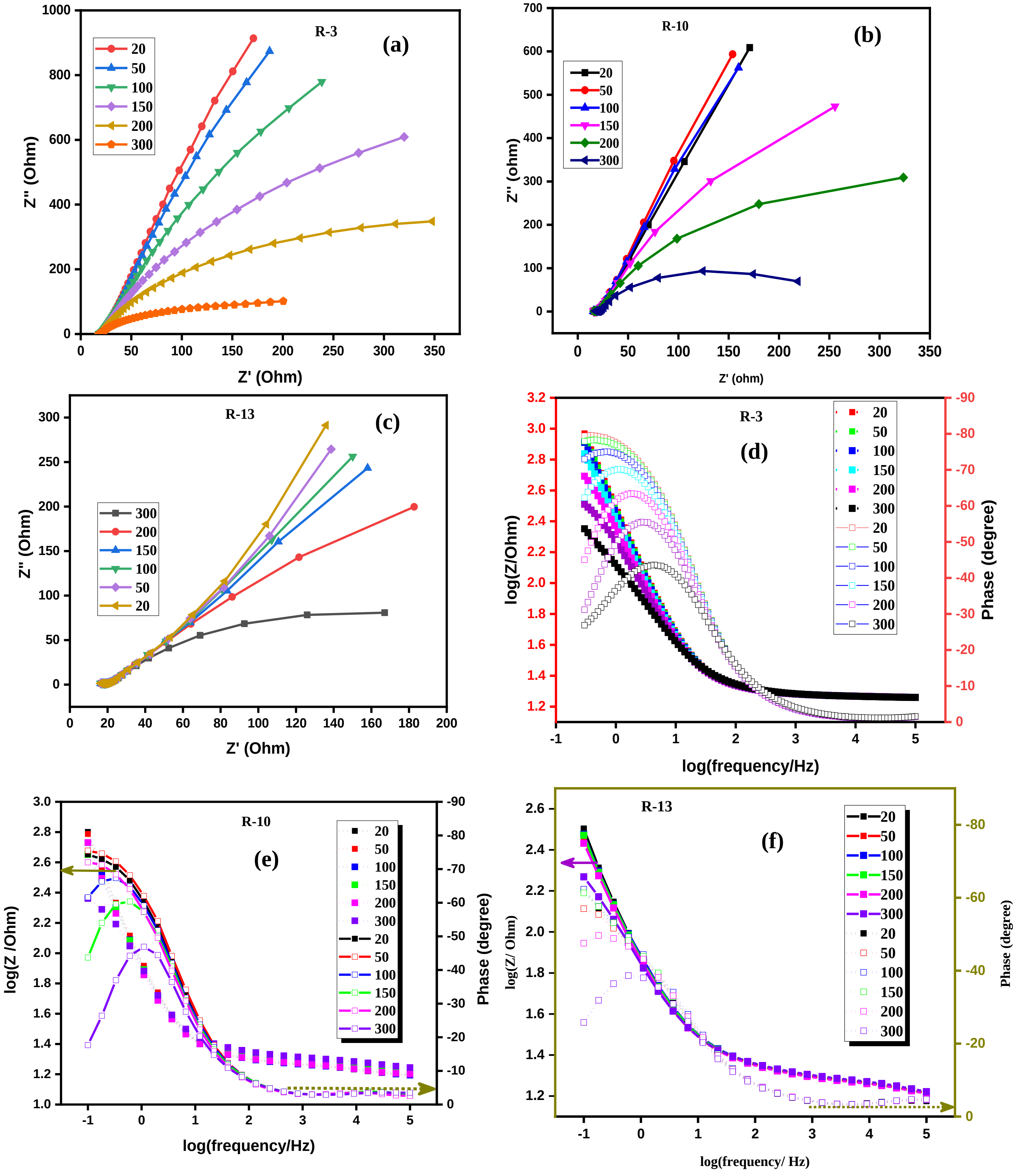

Figure 4.25: EIS of pure phase Mo_2C samples, Nyquist plots (a) R-3 (800 °C for 10 h), (b) R-10 (700 °C for 14 h) and (c) R-13 (600 °C for 20 h).

References

1 G. Kaur, D. Homa, K. Singh, O. P. Pandey, B. Scott and G. Pickrell, *Journal of Power Sources*, 2013, **242**, 305–313.

2 Y. N. Regmi, G. R. Waetzig, K. D. Duffee, S. M. Schmuecker, J. M. Thode and B. M. Leonard, *Journal of Materials Chemistry A*, 2015, **3**, 10085–10091.

3 X. Zou and Y. Zhang, *Chemical Society reviews*, 2015, **44**, 5148–80.

4 D. Wang, Z. Pan, Z. Wu, Z. Wang and Z. Liu, *Journal of Power Sources*, 2014, **264**, 229–234.

5 N. N. Chen, Q. Mo, L. He, X. Huang, L. Yang, J. Zeng and Q. Gao, *Electrochimica Acta*, 2019, **299**, 708–716.

6 R. A. Rather, S. Singh and B. Pal, *Journal of Catalysis*, 2017, **346**, 1–9.

7 M. M. O. Thotiyl and S. Sampath, *Electrochimica Acta*, 2011, **56**, 3549–3554.

8 D. Mukherjee, P. Muthu Austeria and S. Sampath, *ACS Applied Energy Materials*, 2018, **1**, 220–231.

9 G. García, M. Roca-Ayats, O. Guillén-Villafuerte, J. L. Rodríguez, M. C. Arévalo and E. Pastor, *Journal of Electroanalytical Chemistry*, 2017, 793, 235–241.

10 F. Yang, K. Sliozberg, H. Antoni, W. Xia and M. Muhler, *Electroanalysis*, 2016, **28**, 2293–2296.

11 K. Ojha, S. Saha, H. Kolev, B. Kumar and A. K. Ganguli, *Electrochimica Acta*, 2016, **193**, 268–274.

12 K. Zhang, Y. Zhao, D. Fu and Y. Chen, *Journal of Materials Chemistry A*, 2015, **3**, 5783–5788.

13 Z. Y. Yu, Y. Duan, M. R. Gao, C. C. Lang, Y. R. Zheng and S. H. Yu, *Chemical Science*, 2017, **8**, 968–973.

14 A. Samsuri, T. Shafazila, T. Saharuddin, F. Salleh, R. Othaman, M. Wahab, M. Hisham and A. Yarmo, *Materials Science Forum*, 2016, **840**, 299–304.

15 J. Dang, G. H. Zhang, L. Wang and K. C. Chou, *International Journal of Refractory Metals and Hard Materials*, 2015, **51**, 275–281.

16 J. Dang, G. H. Zhang, K. C. Chou, R. G. Reddy, Y. He and Y. Sun, *International Journal of Refractory Metals and Hard Materials*, 2013, **41**, 216–223.

17 S. Chaudhury, S. K. Mukerjee, V. N. Vaidya and V. Venugopal, *Journal of Alloys and Compounds*, 1997, **261**, 105–113.

18 J. Dang, G. Zhang, L. Wang, K. Chou and P. C. Pistorius, *Journal of the American Ceramic Society*, 2016, **99**, 819–824.

19 A. Gupta, G. Singla and O. P. Pandey, *Ceramics International*, 2016, **42**, 13024–13034.

20 H. Kwon, W. Kim and J. Kim, *Journal of the American Ceramic Society*, 2015, **98**, 315–319.

21 J. Sun, Tawei; Gary R. Pickrell and Jeese J. Brown, *Journal of American Ceramic Society*, 1994, **77**, 3209–3214.

22 G. R. Pickrell, T. Sun and J. J. Brown, *Fuel Processing Technology*, 1995, **44**, 213–236.

23 F. E. Frey and D. F. Smith, *Industrial and Engineering Chemistry Research*, 1928, **20**, 948–951.

24 G. Singla, K. Singh and O. P. Pandey, *International Journal of Hydrogen Energy*, 2015, **40**, 5628–5637.

25 B. Edenhofer, D. Joritz, M. Rink and K. Voges, *Carburizing of steels*, Woodhead Publishing Limited, 2014.

26 J.-D. Lee, D. H. Lee, N. K. Park, S. O. Ryu, W. C. Chang and T. J. Lee, *The Preparation of metallic tungsten and flower-like structure tungsten materials with Using CO/CO2 Mixtures*, Studies in Surface Science and Catalysis, 2007, vol. 153.

27 Y. Zhao, Z. Yao, Y. Shi, X. Qiao, G. Wang, H. Wang, J. Yin and F. Peng, *New Journal of Chemistry*, 2015, **39**, 4901–4908.

28 A. Kumar, K. Singh and O. P. Pandey, *Physica E: Low-Dimensional Systems and Nanostructures*, 2010, **42**, 2477–2483.

29 L. K. Brar, G. Singla and O. P. Pandey, *RSC Advances*, 2015, **5**, 1406–1416.

30 G. Singla, K. Singh and O. P. Pandey, *Particulate Science and Technology*, 2015, **33**, 47–52.

31 J. Sen Li, Y. Wang, C. H. Liu, S. L. Li, Y. G. Wang, L. Z. Dong, Z. H. Dai, Y. F. Li and Y. Q. Lan, *Nature Communications*, 2016, **7**, 11204.

32 L. K. Brar, G. Singla and O. P. Pandey, *RSC Advances*, 2016, **6**, 109174–109184.

33 E. Parthé and V. Sadogopan, *Acta Crystallographica*, 1963, **16**, 202–205.

34 K. Huang, K. Bi, C. Liang, S. Lin, W. J. Wang, T. Z. Yang, J. Liu and R. Zhang, 2015, 1–11.

35 A. C. Ferrari, *Solid State Communications*, 2007, **143**, 47–57.

36 E. Amoros, M. Chiron, B. Thelot, A. Ndiaye and B. Laumon, *Injury Prevention*, 2011, **16**, A205–A205.

37 L. Ji, J. Wang, L. Guo and Z. Chen, *Journal of Materials Chemistry A*, 2017, **5**, 5178–5186.

38 S. lijima, T. Ichihashi and Y. Ando, *Nature*, 1992, **356**, 776–778.

39 N. S. Alhajri, D. H. Anjum and K. Takanabe, *Journal of Materials Chemistry A*, 2014, **2**, 10548–10556.

40 Y. Luo, Z. Wang, Y. Fu, C. Jin, Q. Wei and R. Yang, *Journal of Materials Chemistry A*, 2016, **4**, 12583–12590.

41 K. Zhang, C. Li, Y. Zhao, X. Yu and Y. Chen, *Physical chemistry chemical physics*, 2015, **17**, 16609–14.

42 Q. Gao, X. Zhao, Y. Xiao, D. Zhao and M. Cao, *Nanoscale*, 2014, **6**, 6151–6157.

43 Y. Zhu, S. Wang, Y. Zhong, R. Cai, L. Li and Z. Shao, *Journal of Power Sources*, 2016, **307**, 552–560.

44 A. Mehta, A. Mishra, M. Sharma, S. Singh and S. Basu, *Journal of Nanoparticle Research*, 2016, **18**, 1–9.

45 Y. J. Lee, S. H. Kim, T. H. Lee, H. H. Nersisyan, K. H. Lee, M. H. Han, S. U. Jeong, K. S. Kang, K. K. Bae and J. H. Lee, *Chemical Engineering Science*, 2014, **107**, 227–234.

46 W. Wang, P. Liu, M. Zhang, J. Hu and F. Xing, *Open Journal of Composite Materials*, 2012, **2**, 104–112.

47 M. Thommes, *Chemie-Ingenieur-Technik*, 2010, **82**, 1059–1073.

48 N. S. Alhajri, H. Yoshida, D. H. Anjum, A. T. Garcia-Esparza, J. Kubota, K. Domen and K. Takanabe, *Journal of Materials Chemistry A*, 2013, **1**, 12606.

49 A. Gaber, M. A. Abdel- Rahim, A. Y. Abdel-Latief and M. N. Abdel-Salam, *International Journal of Electrochemical Science*, 2014, **9**, 81–95.

50 H. Wu, X. Wang, Y. Bai, L. Jiang, C. Wu, B. Hu, Q. Wei, X. Liu and N. Li, *Journal of Solid State Electrochemistry*, 2013, **17**, 2453–2460.

51 R. A. Mir, P. Sharma and O. P. Pandey, *Scientific Reports*, 2017, **7**, 3518.

52 P. Ping, J. Bergeron and R. Apweiler, *Thermochemical Data of Elements and Compounds*, 2008, vol. 8.

53 H. yu ZHU, Z. bang LI, H. sen YANG and L. gen LUO, *Journal of Iron and Steel Research International*, 2013, **20**, 51–56.
54 I. Istadi and N. A. S. Amin, *Journal of Natural Gas Chemistry*, 2005, **14**, 140–150.
55 S. V. Aydinyan, Z. Gumruyan, K. V. Manukyan and S. L. Kharatyan, *Materials Science and Engineering B*, 2010, **172**, 267–271.
56 D. Voiry, H. Yamaguchi, J. Li, R. Silva, D. C. B. Alves, T. Fujita, M. Chen, T. Asefa, V. B. Shenoy, G. Eda and M. Chhowalla, *Nature Materials*, 2013, **12**, 850–855.
57 C. H. Kuo, L. K. Lamontagne, C. N. Brodsky, L. Y. Chou, J. Zhuang, B. T. Sneed, M. K. Sheehan and C. K. Tsung, *ChemSusChem*, 2013, **6**, 1993–2000.
58 Y. P. Mu, Y. Zhang, L. Fang, L. Liu, H. J. Zhang and Y. Wang, *Electrochimica Acta*, 2016, **215**, 357–365.
59 N. S. Alhajri, D. H. Anjum and K. Takanabe, *Journal of Materials Chemistry A*, 2014, **2**, 10548–10556.
60 H. Bin Wu, B. Y. Xia, L. Yu, X. Y. Yu and X. W. Lou, *Nature Communications*, 2015, **6**, 1–12.
61 C. He and J. Tao, *Chemical Communications*, 2015, **51**, 8323–8325.
62 B. Avasarala and P. Haldar, *Electrochimica Acta*, 2010, **55**, 9024–9034.
63 D. J. Li, U. N. Maiti, J. Lim, D. S. Choi, W. J. Lee, Y. Oh, G. Y. Lee and S. O. Kim, *Nano Letters*, 2014, **14**, 1228–1233.
64 B. E. Conway and B. V. Tilak, *Electrochimica Acta*, 2002, **47**, 3571–3594.
65 N. Kaur, R. A. Mir and O. P. Pandey, *Journal of Alloys and Compounds*, 2019, **782**, 119–131.
66 X. Yang, X. Feng, H. Tan, H. Zang, X. Wang, Y. Wang, E. Wang and Y. Li, *Journal of Materials Chemistry A*, 2016, **4**, 3947–3954.
67 L. Ma, R. Lin and V. Molinari, *Journal of Materials Chemistry A: Materials for energy and sustainability*, 2015, **3**, 8361–8368.
68 X. Li, L. Yang, T. Su, X. Wang, C.-Y. Sun and Z.-M. Su, *J. Mater. Chem. A*, 2017, **5**, 5000–5006.
69 K. Ojha, S. Saha, H. Kolev, B. Kumar and A. K. Ganguli, *Electrochimica Acta*, 2016, **193**, 268–274.
70 M. Fan, H. Chen, Y. Wu, L. L. Feng, Y. Liu, G. D. Li and X. Zou, *Journal of Materials Chemistry A*, 2015, **3**, 16320–16326.
71 B. Šljukić, M. Vujković, L. Amaral, D. M. F. Santos, R. P. Rocha, C. A. C. Sequeira and J. L. Figueiredo, *Journal of Materials Chemistry A*, 2015, **3**, 15505–15512.
72 D. H. Youn, S. Han, J. Y. Kim, J. Y. Kim, H. Park, S. H. Choi and J. S. Lee, *ACS Nano*, 2014, **8**, 5164–5173.
73 Z. Shi, Y. Wang, H. Lin, H. Zhang, M. Shen, S. Xie, Y. Zhang, Q. Gao and Y. Tang, *J. Mater. Chem. A*, 2016, **4**, 6006–6013.
74 K. Ojha, M. Sharma, H. Kolev and A. K. Ganguli, *Catalysis Science and Technology*, 2017, **7**, 668–676.
75 J. B. Jorcin, M. E. Orazem, N. Pébère and B. Tribollet, *Electrochimica Acta*, 2006, **51**, 1473–1479.

Chapter 5

Synthesis of nano Mo_2C using plastic waste

Overview

Considering the fact that pipette tip is mainly manufactured from polypropylene polymer, the present work is undertaken to synthesize the Mo_2C/C composite utilizing used pipette tip (waste plastic) as carbon source. This pipette tip is discarded after its use. The environmental issues caused by the disposal of these plastic wastes and the limitations of recycling/reuse has been addressed. In this chapter, reaction parameters have been optimized to obtain pure phase Mo_2C encapsulated in carbon matrix (Mo_2C/C). More emphasis is given to study the effect of initial amount of carbon content on pure phase formation and the amount of residual surface carbon present in the synthesized product. The pure phase (Mo_2C/C) synthesized under different experimental conditions has been characterized for structural, morphological and surface characteristic by XRD, Raman spectroscopy, FESEM, TEM/HRTEM, XPS, BET and TGA. The surface characteristics (specific surface area) show strong dependence on amount of carbon source along with the reaction temperature. The amount of carbon present in Mo_2C/C determined by TGA varying with respect to initial amount of carbon source plays imperative role in protecting the carbide particles from oxidation and firmly contributes to the electrochemical activity. The effect of carbon content and nature of residual surface carbon over Mo_2C on HER activity and EDLC has been elaborated.

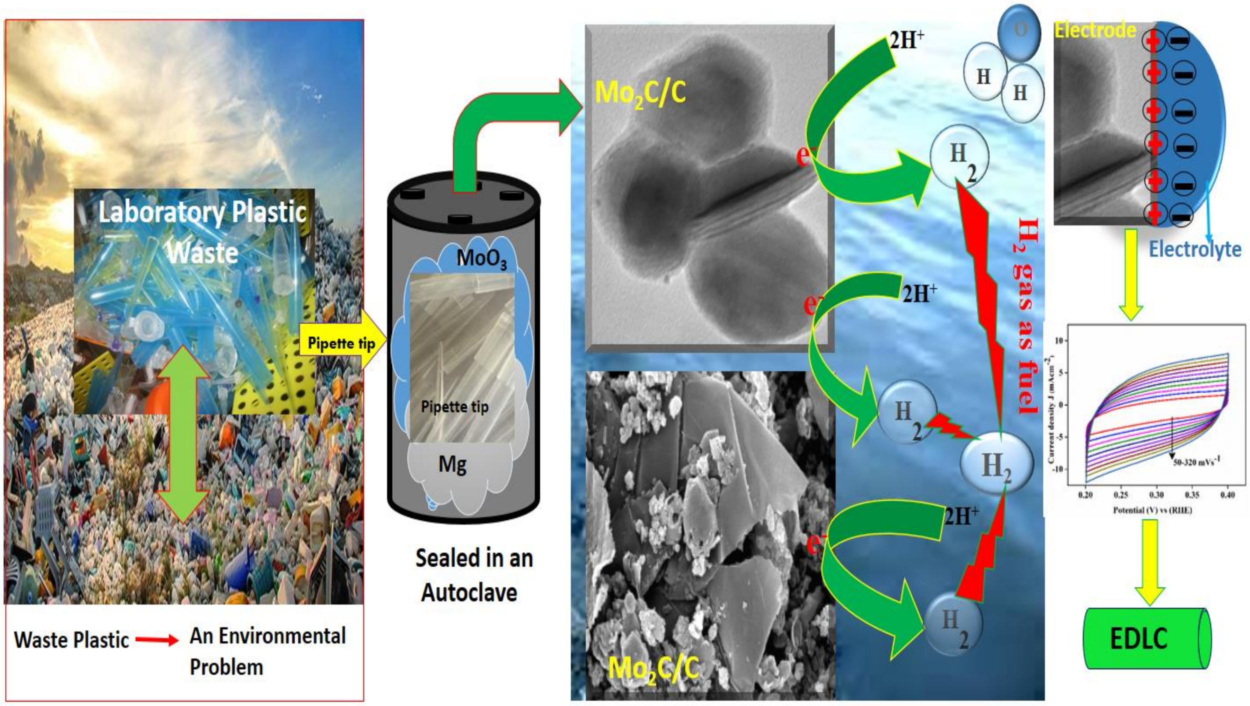

Schematic representation of synthesis of Mo_2C/C and its electrochemical activity.

5.1 Introduction

Hydrogen is contemplated as the efficient, sustainable and zero carbon emission energy source. The most suitable promising energy substitution to diminishing fossil fuels is hydrogen [1,2]. However, hydrogen production is still challenging problem in the present era. One of the irresistible methods for producing hydrogen (H_2) by hydrogen evolution reaction (HER) through electrochemical water splitting is indispensable owing to its high efficiency [3–6]. Presently the key issue of this method is the requirement of the highly active electrocatalyst to promote HER performance. Till date, platinum (Pt.) is considered as the suitable and efficient eletrocatalyst for HER, but its practical use is limited due to its higher cost and low profusion [3,7,8]. Molybdenum carbide (Mo_2C/MoC) an interesting candidate among transition metal carbides (TMCs) has attained special level as catalyst due to variation in its electronic features, which resembles to Pt [9,10]. The HER activity of Mo_2C gets enhanced when synthesized in nanoscale with different morphological structures. To achieve high surface area for eletrocatalytic activity, the surface carbide carbon plays a vital role [11,12]. The crystallite size, morphology and nature of carbon coating encapsulating the carbide particles depend on synthesis method/parameters and amount of carbon source [13]. Carbon support on Mo_2C in different forms also enhances the charge storage capacity of the nano-composites in supercapacitors and EDLCs [2,14–17].

The key parameter of the present work is the utilization of laboratory waste plastics as the source of carbon for the synthesis of carbon supported molybdenum carbide (Mo_2C) in an autoclave. The carbonaceous gases produced by waste plastics inside the autoclave helps in reduction of MoO_3 and carburize to Mo_xC (x=1,2). The current developed process is environment friendly, inexpensive and easy to scale up.

In this work carburization temperature and amount of initial carbon has been varied to obtain single phase Mo_2C with different morphological features. Herein, the influence of residual carbon content and nature of carbon for HER activity and charge storage capacity over Mo_2C has been studied. The synthesized products MoC/Mo_2C incorporated in the carbon matrix exhibits superior stability and enhanced HER performance than the supported non-precious metal and bulk materials in the acidic medium [18]. The EDLC measurements of high temperature synthesized Mo_2C particles with graphitic carbon support have shown improved storage efficiency [2]. The present work demonstrates the influence of carbon content for the synthesis of pure phase Mo_2C and its effect on HER performance and the charge storage capacity. The present facile method is the promising approach to synthesize low cost and non-noble metal electrocatalysts for the water splitting.

5.2 Synthesis of nano Mo_2C

The synthesis of pure phase Mo_2C was carried out in autoclave using plastic waste (pipette tip) as carbon source, MoO_3 and Mg as molybdenum (Mo) source and reducing agent, respectively. The pipette tip used in micropipette is ‘use and through’ and becomes a waste material. The experiments were performed as described in section 3.1 (Chapter 3). The other synthesis parameters are given in Table 5.1.

Table 5.1: Sample labelling and synthesis parameters of Mo_2C

Sample Id	Reaction Temperature (°C)	Reaction Time (h)	Rate of heating (°C/min)	MoO_3 (g)	Mg (g)	Pipette tip (g)
PT1	600	10	5	1.4394	3.5	1
PT2	700	10	5	1.4394	3.5	1
PT3	800	10	5	1.4394	3.5	1
PT4	800	10	5	1.4394	3.5	0.25
PT5	800	10	5	1.4394	3.5	0.5
PT6	800	10	5	1.4394	3.5	0.75
PT7	600	12	5	1.4394	3.5	1
PT8	600	15	5	1.4394	3.5	1

5.3 Results and discussion

5.3.1 X-ray Diffraction (XRD)

The XRD plot for samples synthesized at various temperatures (600, 700 and 800 ºC) for reaction time of 10 hours is shown in Fig 5.1. The PT1 shows the formation of molybdenum carbide (MoC) cubic phase, ICDD pattern (065-0280). The results reveal the formation of carburized product MoC at a relatively low temperature (600 ºC). The typical XRD pattern of PT1 having broad diffraction peaks confirm the less crystallinity of the product phase. The results reveal the rapid reduction/carburization of MoO_3 in presence of Mg and carbon source (pipette tip) inside the autoclave. The obtained reaction products indicate that reaction temperature is not sufficient enough to form the crystalline Mo_2C phase. Increasing the temperature to 700 ºC for 10 hours (PT2) leads to the formation of Mo_2C phase (ICDD reference 035-0787) as shown in Fig. 5.1. The X-ray diffraction peaks correspond to the (100), (002), (101), (102), (110), (103), (200), (112) and (201) planes at positions 34.4, 37.9, 39.4, 52.1, 61.6, 69.5, 74.5 and 75.5°, respectively. The extra peak at 26.6 corresponds to carbon (hexagonal, ICDD pattern 026-1076) as shown in (Fig. 5.1a), which attributes to crystalline carbon formed inside the autoclave and deposited over Mo_2C surface at relatively higher temperatures. Further increasing the temperature to 800 ºC (PT3), highly intense peaks of Mo_2C phase (Fig. 5.1a), as a result of enhanced carburization at higher temperatures was observed. Moreover, the intensity of carbon peak also increased showing more crystallization of carbon at higher temperatures [19]. In order to optimize the initial carbon content for Mo_2C phase formation at 800 ºC for 10 hours, the variation in the amount of initial carbon content was done as given in Table 5.1. Figure 5.1b depicts the typical XRD pattern for samples prepared at 800 ºC for fixed reaction time of 10 hours with variation in carbon content. The PT4 in which the carbon source was 0.25g, shows the formation of Mo_2C along with impure phase Mo (ICDD reference 089-5023) as shown in (Fig. 5.1b). It reveals that the reduction has accomplished at this stage. However, the amount of carbon or the carbonaceous gases so generated are not optimum for carburization of MoO_3/Mo to Mo_2C phase. Increasing the carbon content to 0.5g (PT5) shows the formation of Mo_2C phase (Fig. 5.1b) along with the diffraction peaks of Mo and an intermediate $Mo_{0.42}C_{0.58}$ (ICDD pattern 036-0863), which also shows that the reduction of MoO_3 has accomplished. However, the amount of carbon is not enough to convert reduced Mo and the intermediate phase ($Mo_{0.42}C_{0.58}$) to Mo_2C. The amount of carbon source although higher than the stoichiometric value does not favor the complete carburization of MoO_3 [20,21].

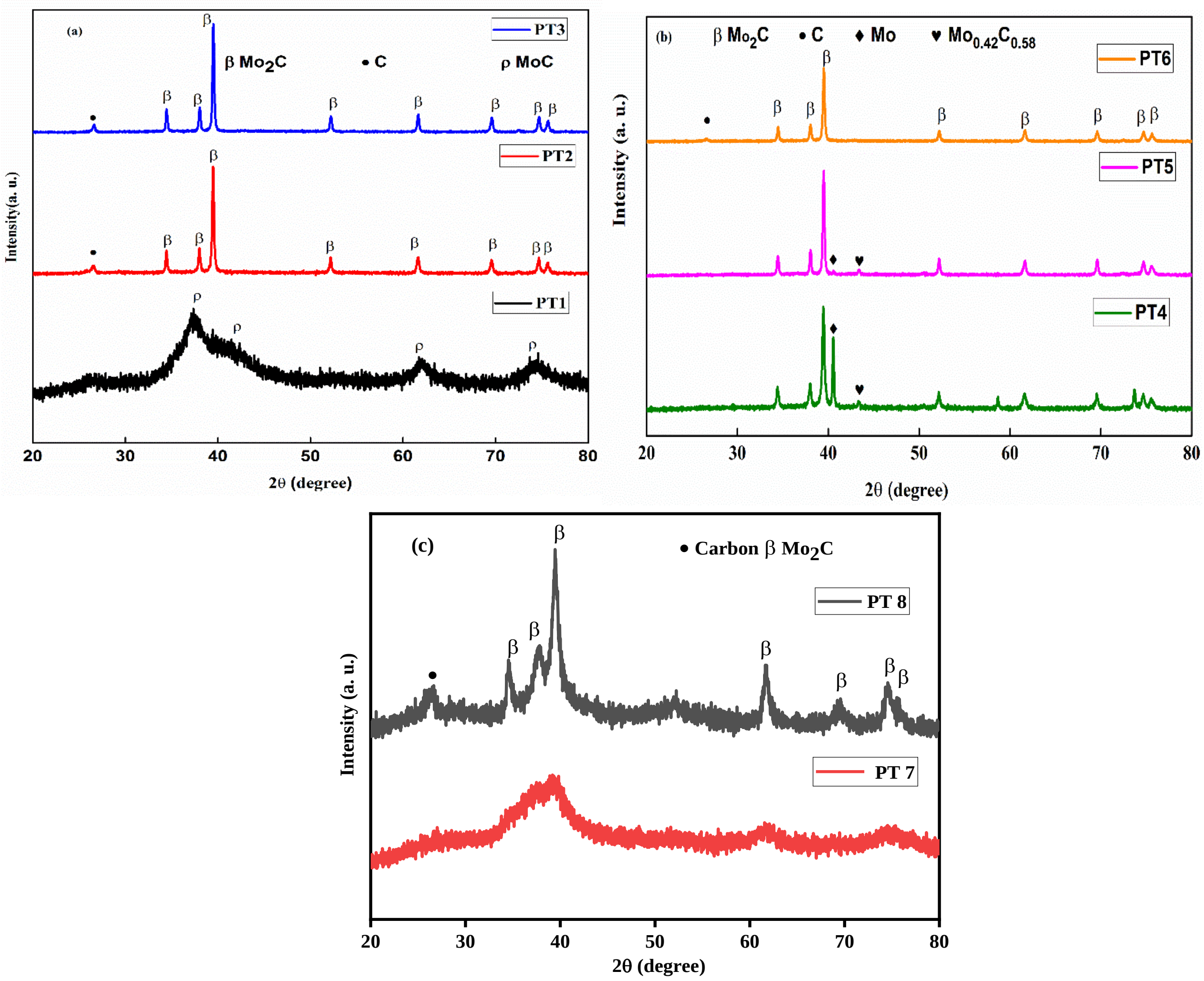

Figure 5.1: XRD pattern of the synthesized samples (a) variation in temperature and (b) variation in carbon content and (c) variation in time at 600 °C.

The sample PT6 (0.75g of carbon) shows the formation of single phase Mo_2C (035-0787) as depicted in (Fig. 5.1b). The peak intensity for the diffraction pattern is little lower as compared to the sample synthesized at same temperature and time with 1g of initial carbon content (PT3). Moreover, no diffraction peak corresponding to carbon shows the accomplishment of carbon content for formation of the product phase. The results predict that the 0.75g of carbon concentration is optimum for formation of Mo_2C phase. Whereas the 1g of carbon at the same synthesis conditions shows the formation of Mo_2C and residual free carbon. Higher the amount of carbon concentration in Mo lattice, more is the platinum like behavior of the product [22].

In another set of experiments the reaction time was optimized to obtain single phase Mo_2C at relatively lower temperature 600 °C as shown in Fig. 5.1c. The PT7 shows the formation of less crystalline phase having pattern nearly similar to Mo_2C, but the phase formation is not clear as depicted by the XRD pattern. This also shows the enhancement in carburization with increase in reaction temperature. Pure phase Mo_2C was obtained at reaction time of 15 h at 600 °C (PT8) as shown in Fig. 5.1c. The peak broadening observed in XRD pattern of PT8 reveals the formation of smaller size Mo_2C at relatively lower temperature. The XRD results of (PT2, PT3, PT6 and PT8) reveal the formation of pure Mo_2C phase having hexagonal structure (ICDD-035-0787).

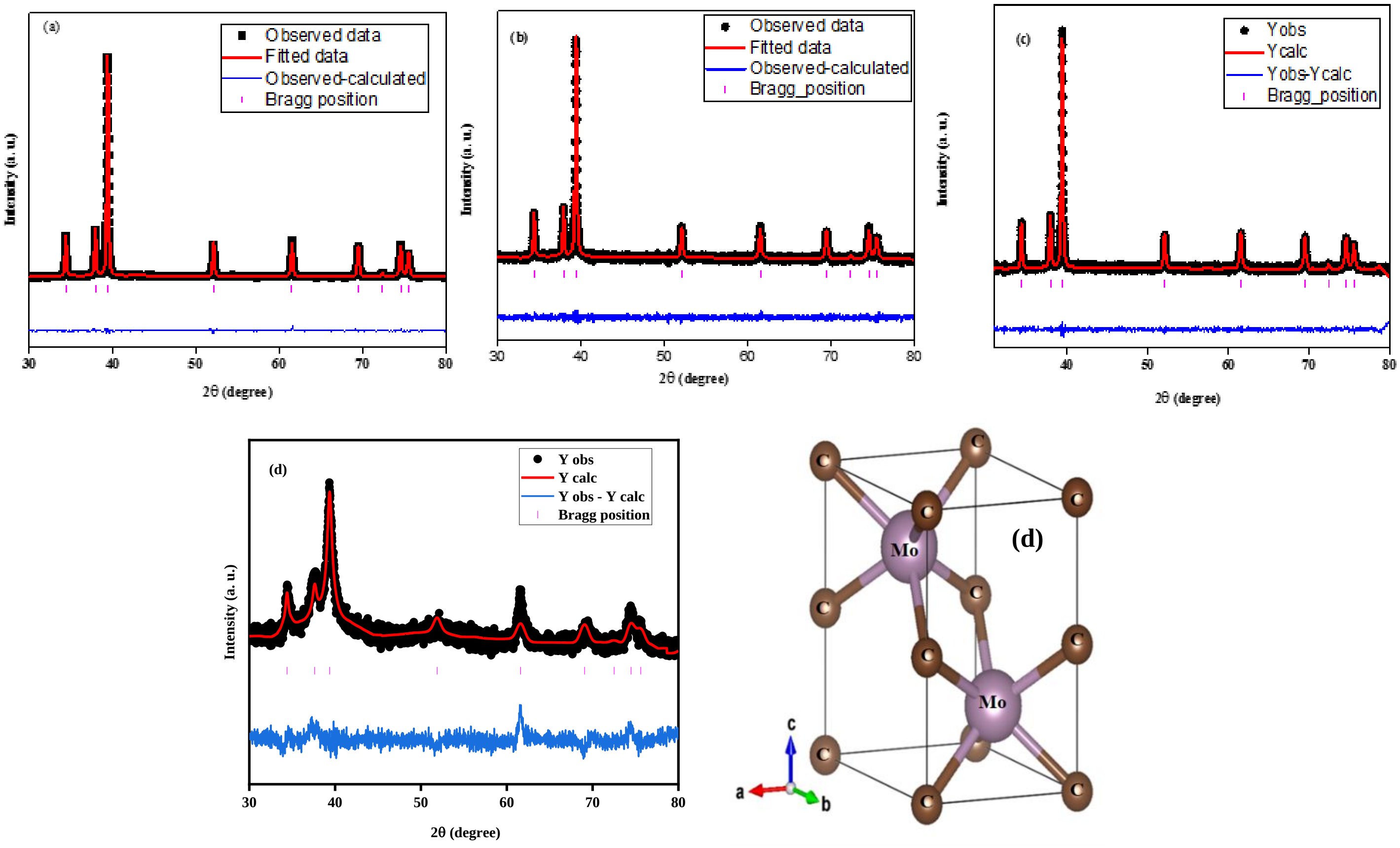

Figure 5.2: Fitted Rietvield refinement plots (a) PT2 , (b) PT3, (c) PT6, (d) PT8 and (e) hexagonal structure of PT3.

To verify the crystal structure of the pure phase Mo_2C, the XRD data has been fitted via Rietveld refinement for hexagonal space group (P63/mmc) with Wyckoff positions for Mo and C as given in literature [23]. The fitted Rietveld refinement plots of the synthesized products (PT2, PT3, PT6 & PT8) are depicted in Fig. 5.2a-d, respectively. The χ^2 values, lattice parameters of the analyzed samples and the site occupancy of Mo and C so estimated is given in Table 5.2. The deviation from the fitting pattern of PT8 correspond to the growth of (110) than the regular pattern. The crystal structures generated from Rietveld fit for the hexagonal system of PT3 is shown in Fig.

5.2e. The PT2 and PT3 shows nearly stoichiometry of Mo and C.The amount of carbon in Mo_2C lattice is a function of carbon content. It generates the higher carbon gradient to favor diffusion of C in Mo lattice through surface diffusion. In this process carbon network forms on the surface of particle, which further hinder the diffusion of carbon in Mo lattice.

5.3.2 Crystallite size and strain

The crystallite size estimated from Scherrer criterion is given in Table 5.2. The estimated crystallite size of PT1 is very small, which is attributed to peak broadening. For Mo_2C phase it shows a decreasing pattern with temperature as evidenced in Table 5.2. It enhances with increase in carbon content followed by decrease as mentioned in Table 5.2. The relatively lower temperature synthesized phase shows smaller crystallite size, attributed to its low crystallinity which shows a broad peak pattern. The strain induced in the synthesized samples as a result of carburization affects the peak broadening. Williamson-Hall (W-H) study estimates the strain induced in the synthesized samples. The detailed mathematical formulas of different W-H models, for hexagonal systems are given in equations 3.4-3.7 (Chapter 3). For cubic systems the calculations were done with the help of expression given in literature [24]. The MoC (PT1) phase shows lower crystallite size and more strain. It might be because of the intermediate phase formation at low temperature. The quality of the fit for (100) of PT2 is depicted in Fig. 5.3a. The crystallite size has shown decreasing trend with increase in the temperature given in (Table 5.2) for PT3 and PT2, respectively.

Table 5.2: Rietveld refienemnt and Williamson-Hall parameters

Sample Id	**Rietveld refinement parameters**		**USM**		**USDM**			**USEDM**				**Scherrer criterion**
	χ^2	**Lattice Parameters**	**D (nm)**	**$\varepsilon\times10^{-3}$**	**D (nm)**	**$\varepsilon\times10^{-3}$**	**σ (GPa)**	**D (nm)**	**$\varepsilon\times10^{-3}$**	**σ (GPa)**	**$U\times10^2$ (KJm^{-3})**	**D (nm)**
PT1	**-**	-	2.31	8.21	2.31	8.2	2.7	2.31	5.8	1.9	110	3.46
PT2	2.0	a=b= 3.0123 c=4.7423	45.76	0.86	46.4	0.74	0.29	47.65	0.56	0.22	1.27	81.0
PT3	1.0	a=b= 3.0130 c=4.7422	46.65	0.55	49.2	0.58	0.23	49.51	0.41	0.16	0.66	75.36
PT4	-	-	35.10	1.36	31.9	1.1	0.44	33.33	0.84	0.33	2.9	61.08
PT5	-	-	42.02	0.90	43.3	0.8	0.31	44.44	0.59	0.23	1.14	78.78
PT6	1.9	a=b= 3.0127 c=4.7416	50.79	0.98	55.0	1.07	0.42	56.82	0.79	0.31	2.5	84.33
PT7	-	-	5.42	9.31	6.60	12.3	4.84	6.60	8.73	3.4	300	10.2
PT8	2.7	a=b= 3.008 c=4.778	20.42	2.35	22.51	2.95	0.7	22.51	1.71	0.66	17.1	30.74

The results are in agreement with full width at half maxima (FWHM), which shows an increase with rise in temperature as presented in Fig. 5.3a-b. The Scherrer plot for PT2 with (1/β) on x-axis and cosθ on y-axis is shown in Fig. 5.3c. These models were fitted and the uniform strain energy density model (USEDM) seems to be more appropriate having better quality of fit (R^2=0.99) than uniform strain deformation model (USDM, R^2=0.98) and uniform strain model (USM) (R^2=0.96) as depicted in (Fig. 5.3d-f), respectively. The estimated results are tabulated in (Table 5.2).

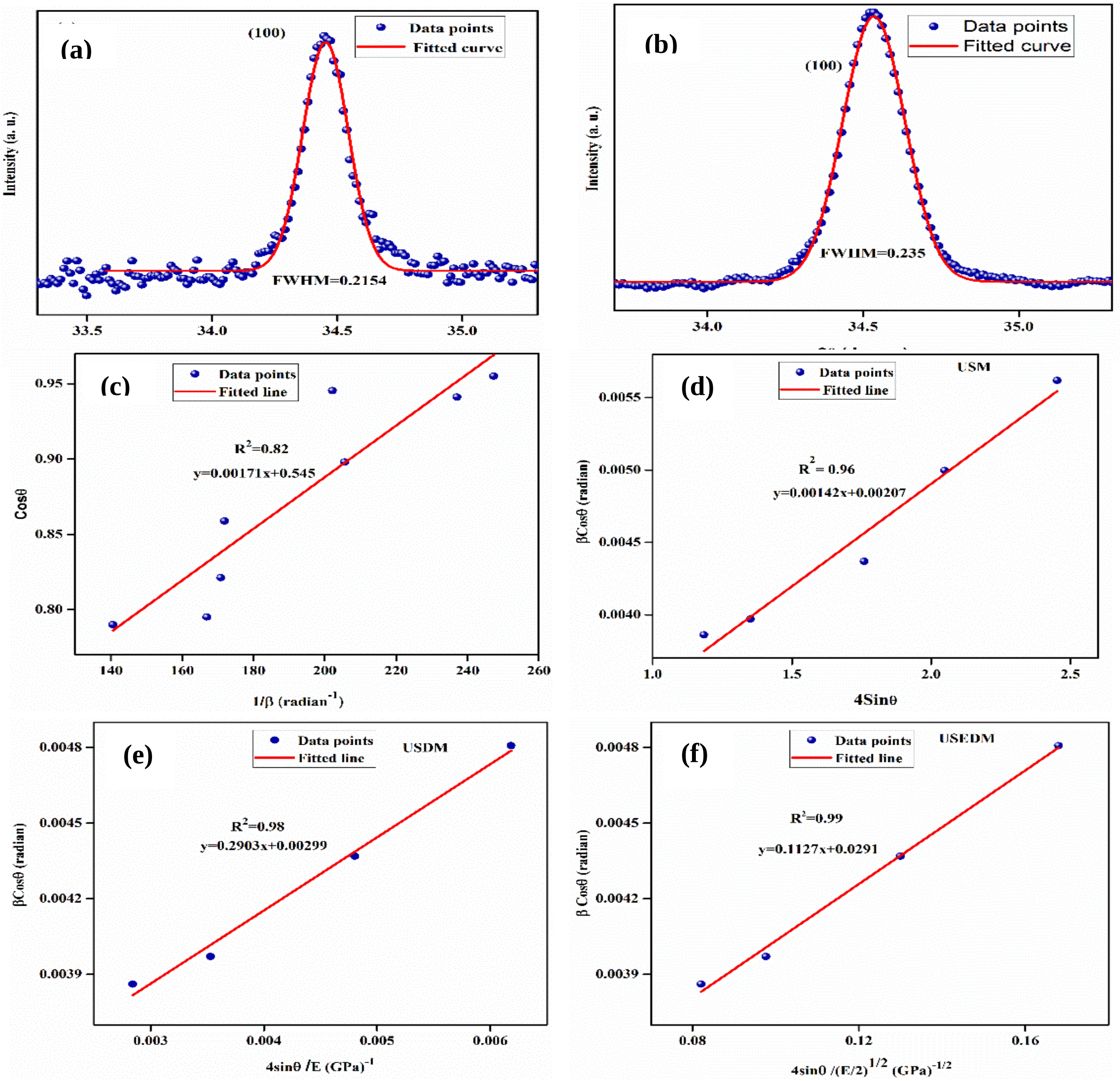

Figure 5.3: Williamson- Hall analysis analysis (a) Fitted curve for (100) of PT2, (b)) Fitted curve for (100) of PT3, (c) Scherrer plot of PT2 (d) USM, (e) USDM and (f) USEDM.

The crystallite size calculated from the USM, USDM and USEDM are consistent. The strain estimated from W-H analysis shows decreasing trend with rise in temperature. The prominent peak of carbon in PT3 compared to PT2 indicates that the diffusion of carbon at higher temperature got saturation value and lattice carbon gets relaxed leading to low strain value. However, the higher strain value in PT4 might be due to the presence of more Mo intermediate phase, which has not attained equilibrium because the amount of carbon is not sufficient enough for the formation of pure Mo_2C phase. The gradient of carbon diffusion might be a reason for strain induction in the product phase. However, further increasing the carbon content, PT5 shows a different pattern of strain. The strain generated in PT5 is less as compared to PT4, because of the higher carbon content gradient than PT4, which favors the diffusion of C in Mo lattice and lowers the strain. Brar *et al.* [25] also observed a different pattern in strain analysis below 5.5 (molar ratio) carbon concentration. Increasing the initial carbon content (PT6) shows the increase in strain value because of pure phase formation of Mo_2C with no extra carbon peak in XRD pattern (Fig. 5.1b). The results predict that carbon in PT6 is accomplished to form Mo_2C. Due to strong interaction between Mo and carbon on the surface, the product phase in PT6 remains in the higher strained state, because of the low carbon on the surface. However, strain induced in PT3 is lower as compared to PT6 where the extra carbon formed on surface of Mo_2C helps in retaining the stable state of the product phase with lower strain [25]. The higher stain observed in PT7 and PT8 is in accordance with lower crystallinity. In comparison PT2, PT3 and PT6, the higher strain and lower crystallite size of PT8 justifies the breaking of Mo oxide particles and get simultaneously carburize to form Mo_2C. These carburized particles do not attain the equilibrium state of carbon diffusion and hence retain the high strained state.

5.3.3 Morphological Studies

The FESEM micrographs of the synthesized samples (PT1, PT2, PT3, PT6 and PT8) are shown in Fig. 5.4a-f. Structural analysis reveal that the particles are agglomerated having tubular to faceted morphology for PT1 and PT2 (Fig. 5.4a-b), respectively. However, PT3 shows the different morphological features where presence of graphene sheet and agglomerated particles can be seen (Fig. 5.4c). Higher magnified image (Fig. 5.4d) shows the stacked thick sheet like structures. In sample PT6 (Fig. 5.4e) agglomerated particles are observed. The PT8 (Fig. 5.4f) shows the highly agglomerated particles but of uniform size. Certain structures exhibit hollow like shape as shown in Fig. 5.4f. The structural variation is observed because of different in synthesis conditions.

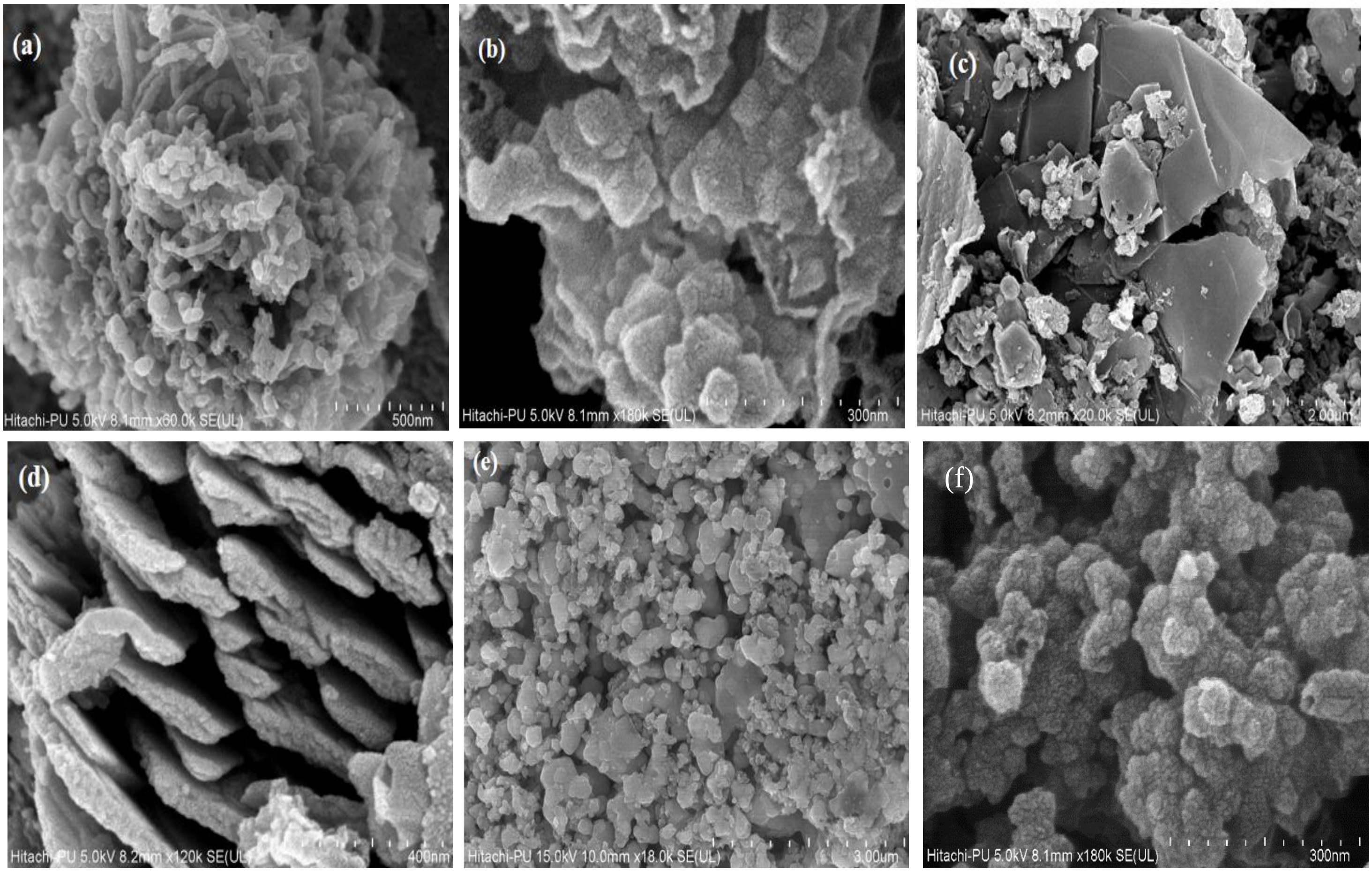

Figure 5.4: FESEM micrographs of (a) PT1, (b) PT2, (c) & (d) PT3, (e) PT6 and (f) PT8.

The EDS elemental analysis shown in Fig. 5.5a-e, reveals the presence of C, Mo and O elements, where carbon content is higher for PT3 as given in Table 5.3. The presence of higher amount of elemental carbon in the synthesized sample contribute positively for better performance and stability during application.

Table 5.3: Elemental composition as estimated from FESEM-EDS analysis

Sample Id	**Atomic (%)**		
	Mo	**C**	**O**
PT1	6.03	81.82	12.15
PT2	8.71	80.13	11.16
PT3	3.21	90.29	6.49
PT6	6.00	82.81	11.19
PT8	13.44	73.06	13.50

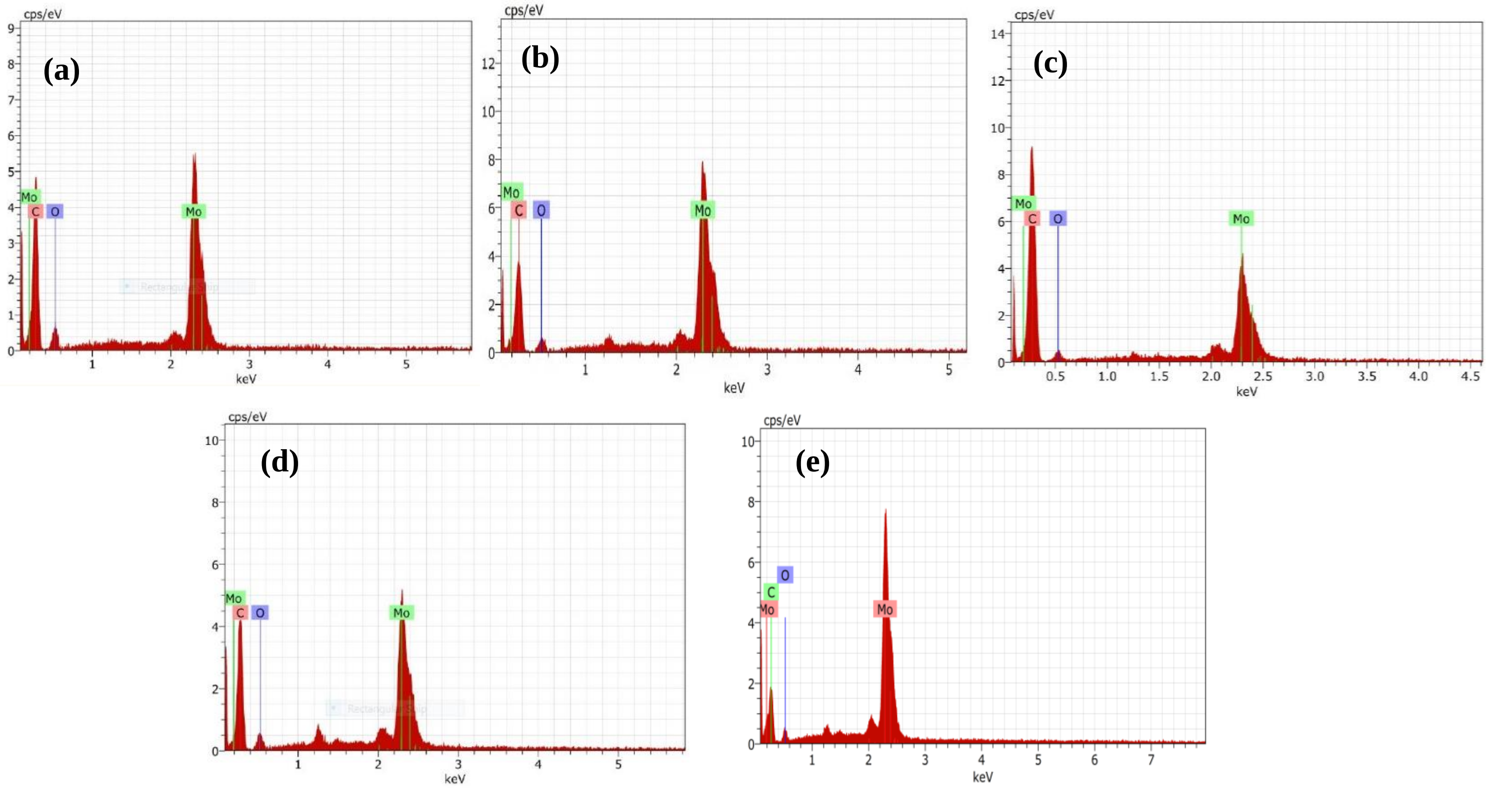

Figure 5.5: FESEM- EDS pattern of (a) PT1, (b) PT2, (c) PT3, (d) PT6 and PT8.

The TEM analysis of PT2 sample (Fig. 5.6) exhibits spherical to faceted morphology of particles encapsulated in carbon matrix as shown in Fig. 5.6a. The HRTEM micrograph (Fig. 5.6b) and SAED pattern (Fig. 5.6c) confirmed the incorporation of the Mo_2C in carbon cloth. These results are consistent with XRD reference (ICDD pattern -035-0787) for Mo_2C and carbon (ICCDD pattern-026-1076). The SAED pattern (Fig. 5.6c) also confirm the formation of Mo_2C particles in accordance with d-spacing of (002), (102) and (201) planes.

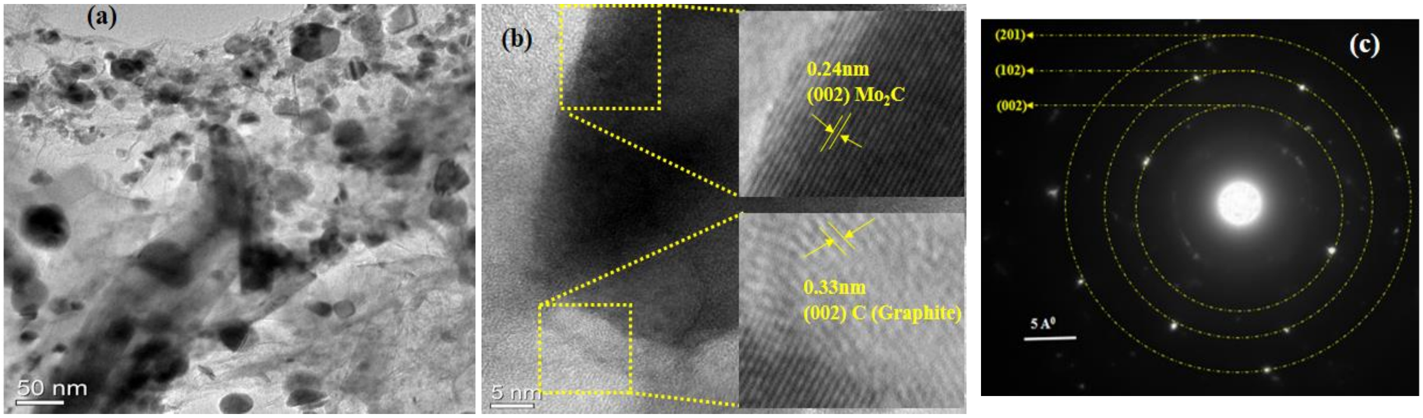

Figure 5.6: TEM micrographs of PT2 (a) showing particles embedded in carbon cloth, (b) HRTEM and (c) SAED pattern.

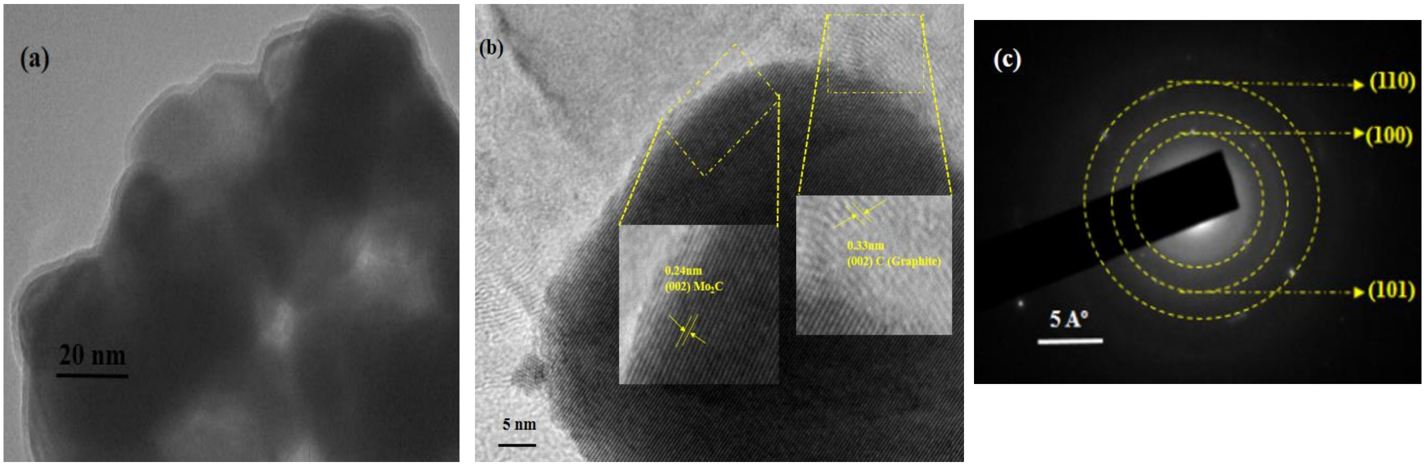

Figure 5.7: TEM microstructures of PT6 (a) showing connected particles (b) HRTEM and (c) SAED pattern of Mo_2C.

Thee coating in TEM image of PT6 (Fig. 5.7a) is little thinner, which is in agreement with experimental parameters. The HRTEM and SAED pattern confirms the Mo_2C phase formation enclosed in the graphitic carbon layer as shown in Fig. 5.7b and 5.7c, consistent with XRD pattern.

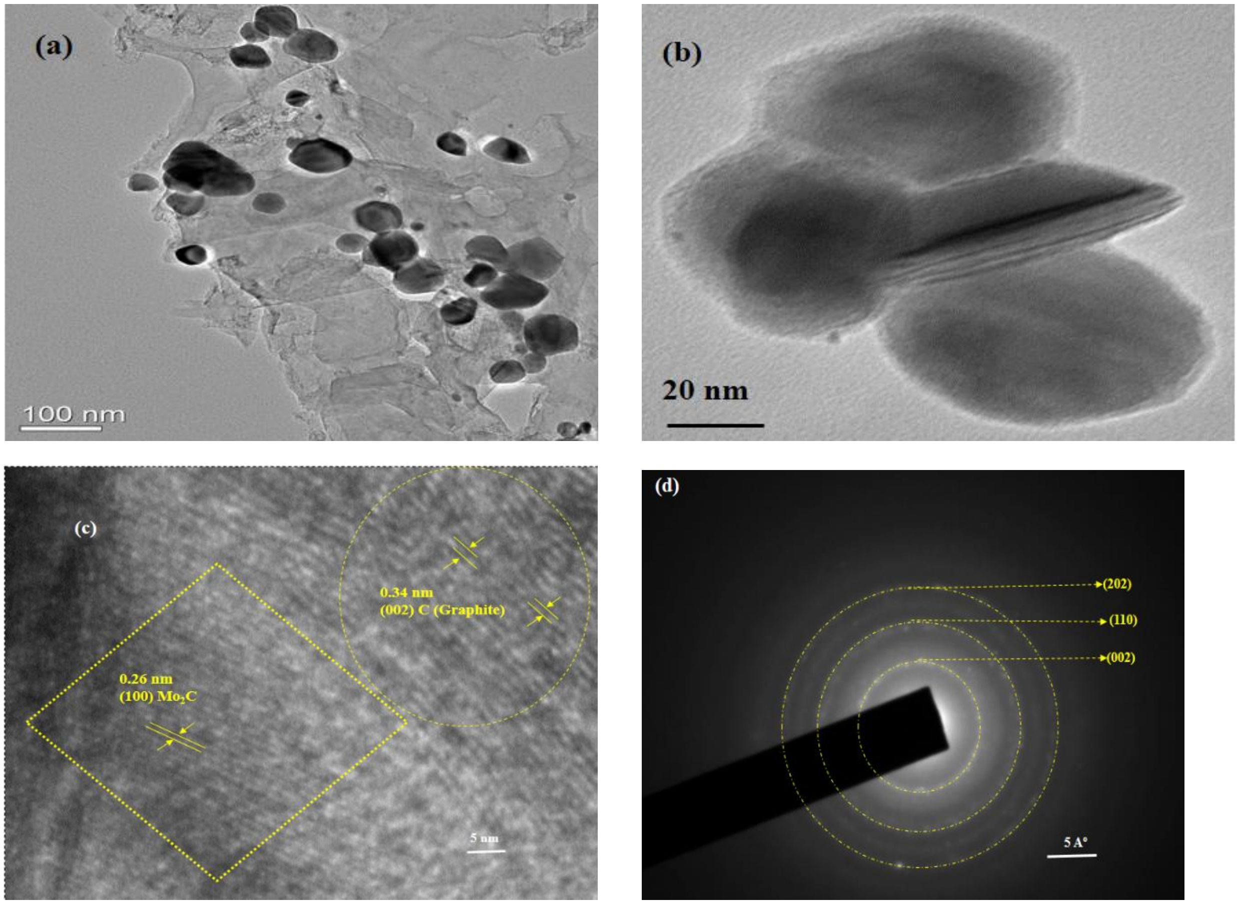

Figure 5.8: TEM micrographs of PT3 (Mo_2C) (a) TEM, (b) stacked layers, (c) HRTEM and (d) SAED pattern of Mo_2C.

In PT3 faceted Mo_2C particles embedded in graphene sheet can be seen in Fig. 5.8a. These faceted structure having thick carbon coating form the layered structure (Fig. 5.8b). The HRTEM (Fig. 5.8c) and SAED pattern (Fig. 5.8d) confirms the graphitic carbon coated Mo_2C as the final carburized product consistent with ICDD reference pattern of carbon and Mo_2C, respectively. The results are also in accordance with FESEM micrographs showing formation of graphene sheets (Fig. 5.4c) and stacking of layered structures (Fig. 5.4d). The TEM micrographs of PT8 show highly dense, smaller size particles encapsulated in carbon cloth (Fig. 5.9a). The growth of the sheet like structure encapsulating Mo_2C particles is observed (Fig. 5.9b). This sheet formation increases with increase in temperature as observed in PT2, PT6 and PT3, respectively. The HRTEM (Fig. 5.9c) and SAED pattern (Fig. 5.9d) shows formation of Mo_2C consistent with XRD pattern (ICDD reference 035-0787). The HRTEM (Fig. 5.8c) shows the Mo_2C particles encapsulated in amorphous carbon. This attributes to lower synthesis temperature and lower crystallinity as observed in XRD pattern.

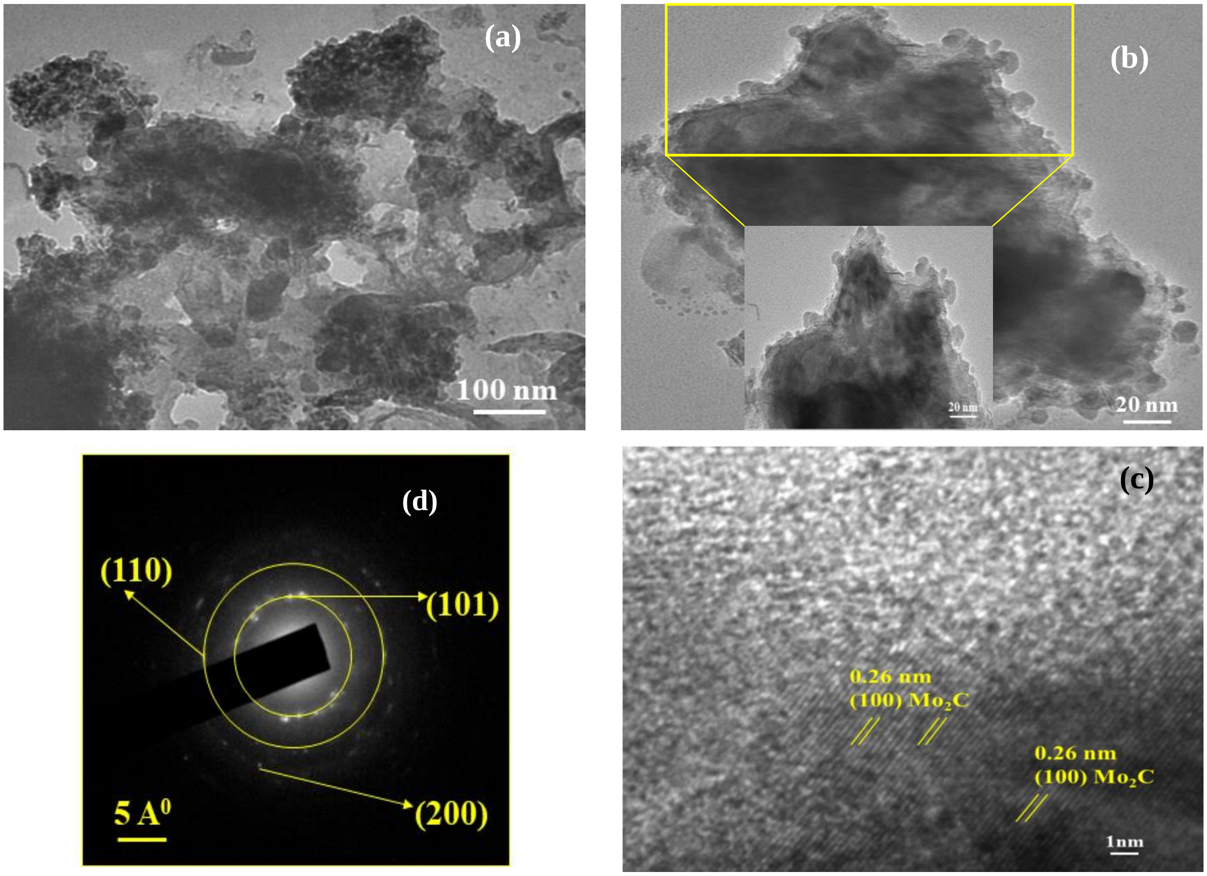

Figure 5.9: TEM micrographs of PT8 (Mo_2C) (a) and (b) TEM, (c) HRTEM and (d) SAED pattern of Mo_2C.

5.3.4 X-ray photoelectron spectroscopy (XPS)

The surface chemistry analysis and the chemical composition of the pure phase synthesized samples (PT3 and PT6) were determined by XPS. The overall survey spectrum of the PT3 and PT6 are given in (Fig. 5.10a&b), respectively. It precisely shows the presence of Mo, O and C, respectively. The peak positions at binding energy (BE) 231.4, 284.5, 396.8, 412.9 and 531.4 eV correspond to Mo3d, C1s, $Mo3p_{5/2}$, $Mo3p_{3/2}$ and O1s, respectively [26].

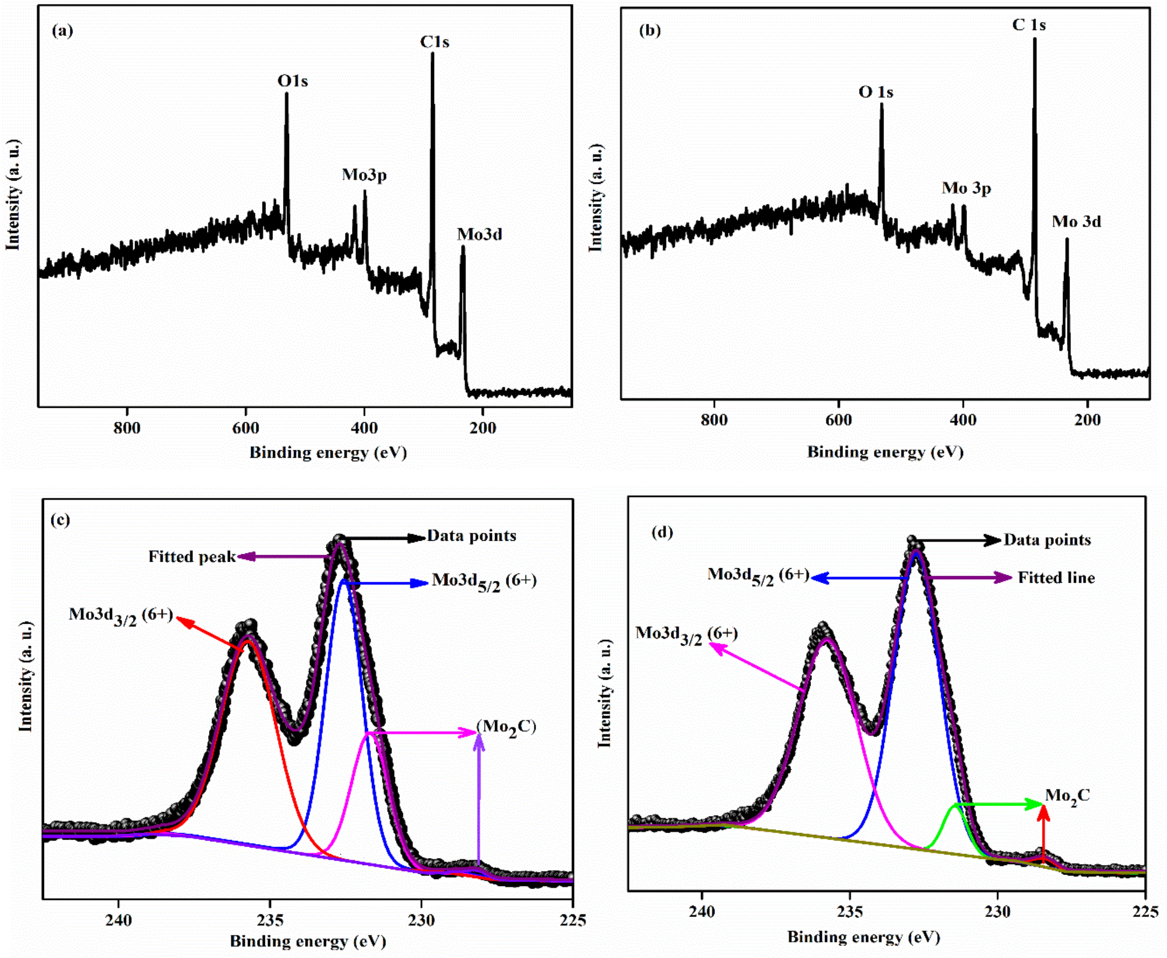

Figure 5.10: XPS spectra of (a) Survey spectra of PT3, (b) Survey spectra of PT6, (c) HR spectra of Mo3d of PT3 and (d) HR spectra of Mo3d of PT6.

The high resolution spectra of PT3, Mo3d (Fig. 5.10c) depicts the presence of $Mo3d_{5/2}$ (2+) and $Mo3d_{3/2}$ (2+) bonded to Mo_2C at positions 228.3 and 231.6 eV, respectively [1]. The peaks having BE 232.5 and 235.7 eV correspond to $Mo3d_{5/2}$ (6+) and $Mo3d_{3/2}$ (6+), respectively, which is attributed to oxidation of Mo_2C surface in air or prolonged duration during XPS analysis[19]. The spectra of PT6 Mo3d shown in (Fig. 5.10d) reveal the formation of product phase Mo_2C due to presence of $Mo3d_{5/2}$ (2+) and $Mo3d_{3/2}$ (2+) species at BE positions 228.5 and 231.3 eV. The indication of enriched electron around Mo in Mo_2C was confirmed by shift in BE of Mo^{2+} towards lower side [1]. The peaks having BE of 232.5 and 235.7 eV correspond to $Mo3d_{5/2}$ (6+) and $Mo3d_{3/2}$ (6+), respectively as a result of oxidation of Mo_2C to form MoO_3[19]. The C1s spectra of PT3 and PT6 are given in (Fig. 5.11a&c), the peaks ~284.4 and ~285.2 attribute to C-C (graphitic), respectively[27]. In C1s spectra, the Mo-C (carbide) peak is inhibited by the carbon peak due the excess surface carbon having similar BE region of C-C and Mo-C [28]. Moreover, the O1s spectra of PT3 and PT6 in (Fig. 5.11b&d) shows the presence of surface molybdenum oxide species having BE 530.5, 531.2, 532.3 and 529.2, 530.2 and 530.7, respectively corresponding to Mo-O and C-O [29].

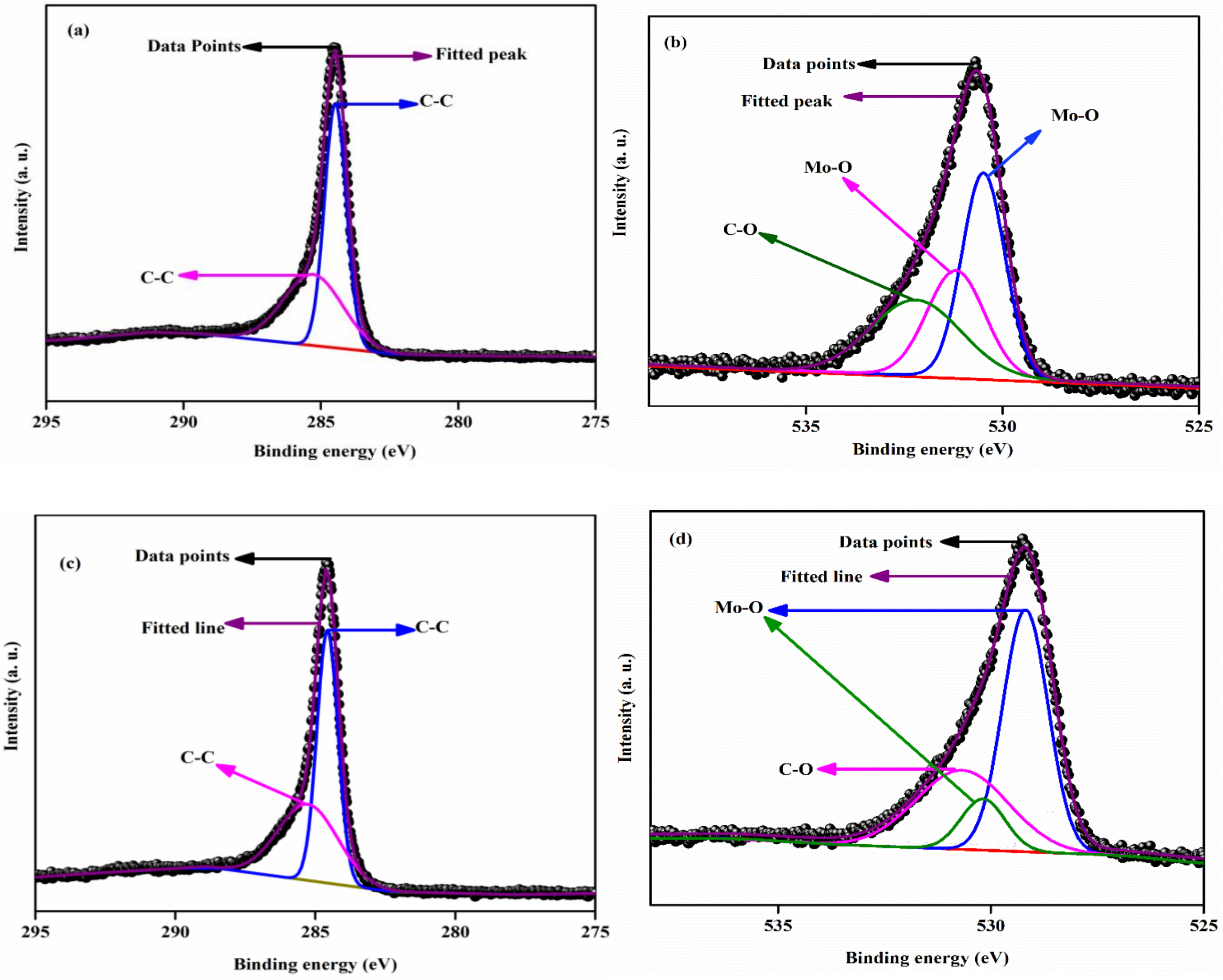

Figure 5.11: High resolution (HR) XPS spectra of (a) C1s of PT3, (b) O1s of PT3, (c) C1s of PT6 and (d) O1s of PT6.

5.3.5 Raman spectroscopy

The Raman spectroscopy studies were done to estimate the graphitization of the synthesized products. The Raman spectrum of synthesized samples (PT1, PT2 and PT3) shown in Fig. 5.12a, exhibits the Raman peaks at positions given in Table 5.4. These correspond to the disorder induced D-band, G-band and 2D-band for the crystalline graphite, respectively [30,31]. The ID/IG ratio (Table 5.4) of PT1, PT2 and PT3 is nearly same, which confirms the similar order of the carbon. The presence of the 2D peak in PT2 and PT3 confirms the formation of graphite/graphene with increase in temperature [32]. The increase in I2D/IG ratio (Table 5.4) confirms the increase in graphitization of carbon with temperature. The shifting of the 2D band towards (2690 cm^{-1}) attributes to the transformation of highly pyrolytic graphitic carbon to graphene. The shift of G band peak about (10 cm^{-1}) attributes to the self-doping defects of in-situ carbon coated Mo_2C phase [32]. The increase in I2D/IG correspond to increase in graphene layers with temperature. The Raman spectra for the synthesized samples PT4, PT5 and PT6 with variation in initial carbon content is shown in Fig. 5.12b and the corresponding bands so obtained are given in Table 5.4. Low intensity peak at ~658.2 corresponds to (Mo-O-Mo stretch) of molybdenum oxide species [13]. The presence of highly intense peak at position 817.2 cm^{-1} is (Mo=O stretch) and the peak at ~987 cm^{-1} belongs to MoO_3 species.

Table 5.4: Raman spectroscopy parameters.

Sample Id	D band		G band		2D band		ID/IG	I2D/IG
	Peak position (cm^{-1})	Intensity (a. u)	Peak position (cm^{-1})	Intensity (a. u)	Peak position (cm^{-1})	Intensity (a. u)		
PT1	1334.3	8779.2	1590.3	12468.1	-	-	0.7	-
PT2	1344.9	3735.4	1579.6	5452.8	2693.1	2738.7	0.69	0.5
PT3	1350.7	6116.3	1590.3	8582.7	2691.6	5779.2	0.71	0.67
PT4	-	-	-	-	-	-	-	-
PT5	1339.1	2306.7	1569.7	6942.2	2684.7	4764.2	0.33	0.68
PT6	1346.6	1584.6	1571.3	3331.1	2701.5	1889.2	0.48	0.57
PT7	1342.9	4189.4	1589.9	3819.1	-	-	1.1	-
PT8	1342.2	7361.2	1582.4	7410.0	-	-	0.99	-

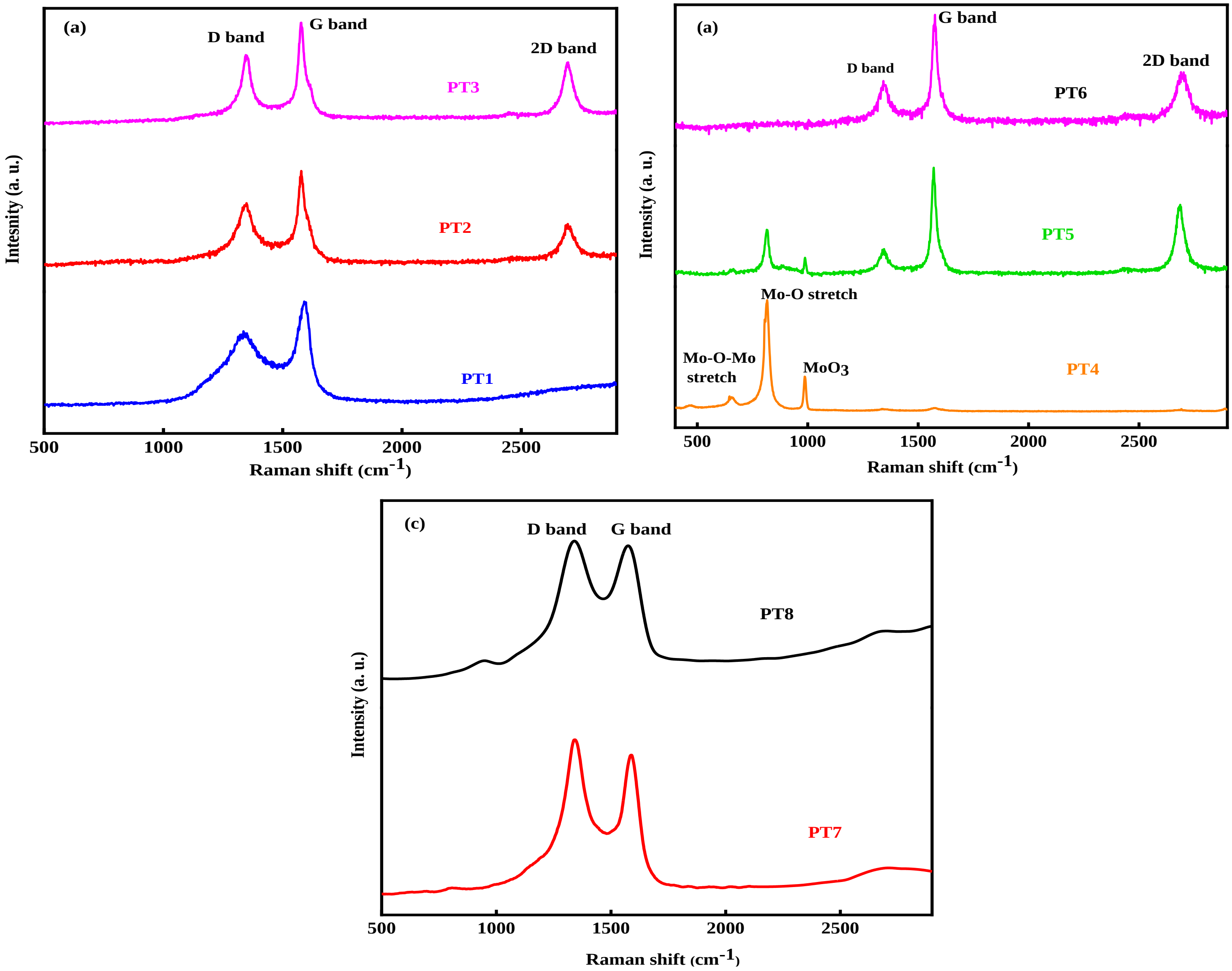

Figure 5.12: Raman spectra of (a) PT1, PT2 & PT3, (b) PT4, PT5 & PT6 and (c) PT7 and PT8.

Moreover, the PT4 (Fig. 5.12b) shows no sign of D and G bands confirming that 0.25 g carbon source is not sufficient to have surface carbon. The oxide species so obtained in Raman spectra of PT4 may be due to some oxide content present in the sample as the phase transformation from oxide to carbide has not occurred completely and is beyond the determination limit of XRD. The Raman spectra of the PT5 sample follows the same trend with decreasing intensity of molybdenum oxide species peaks and shows the presence of D, highly intense G and 2D band at positions (Table 5.4) shown in Fig. 5.12b. The molybdenum oxide species may correspond to inherently retained oxide within the carbon matrix. The surface carbon prevents the oxidation of the Mo_2C surface, which results in a decreased intensity of Mo oxide species as compared to PT4. However, the PT6 (Fig. 5.12b) sample only shows the presence of D, G and 2D band in Raman spectra at positions given in Table 5.4. The peak positions shifted towards higher wave number as compared to PT5. The decrease of peak intensity for D and G bands in PT6 as compared to PT5 may be due to utilization of more carbon to accomplish the phase formation of Mo_2C. The shifting of the 2D peak from 2684.7 to 2701.5 reveals the formation of graphene in carbon support. The ID/IG and I2D/IG of PT6 is lower than PT3, which shows the presence of higher disorder and graphitized carbon species, respectively [31]. The Raman spectra of lower temperature synthesized phases PT7 and PT8 (Fig. 12c) reveal the presence of D-band and G-band only at positions given in Table 5.4. The higher ratio of ID/IG (PT7) confirms the lower crystallinity of surface carbon. The lower graphitization of surface carbon over Mo_2C at 600 °C (PT8) is also in accordance with XRD results exhibiting broad XRD peaks. The results are in well agreement with the formation of more carbon support over Mo_2C surface with increase in initial carbon content as observed in XRD and microstructural analysis. The results also confirm the enhancement in graphitization of carbon with increase in temperature as has been observed in Raman spectra of pure phase Mo_2C samples PT8, PT2 and PT3, respectively.

5.3.6 Thermogravimetric analysis

Thermogravimetric analysis (TGA) for the synthesized powders (Fig. 5.13) have been performed from room temperature to 1000 ºC under flowing air to estimate the thermal stability and chemical composition. The expected mass loss may attribute to the oxidation of carbon residue, whereas the oxidation of Mo_xC (x=1, 2) species lead to mass gain. The TGA analysis of the synthesized samples (PT1, PT2 and PT3) is depicted in Fig. 5.13a. The initial mass loss of about 1 % is observed for all the synthesized samples that correspond to the absorbed water on the surface. The mass gain of about 7 % in PT1confirm the oxygen incorporation in MoC to form MoO_xC_y. The weight loss about 10 % in between 376 to 467 ºC corresponds to the combustion of carbon releasing CO and CO_2. The slight mass gain thereafter till 535 ºC attributes to the oxidation of remaining MoC and MoOxCy to form MoO_3 [33]. The straight line till 715 ºC determines the stability of the formed product. The weight decreases gradually thereafter, but the decrease is slow till 800 ºC. The rapid mass loss thereafter is in accordance with the evaporation of MoO_3 [34]. The straight line TGA curve of carbon coated Mo_2C (PT2 and PT3) in Fig. 5.13a, shows higher thermal stability as compared to MoC (PT1) in temperature range 308 ºC and 315 ºC, respectively. The slow mass gain till 438 and 363 ºC in case of the PT2 and PT3 designate the oxidation of Mo_2C species, respectively[35]. Both the mass gain and loss occur simultaneously because of oxidation of carbide and carbon species. The mass gain till 128 and 130 % at peak points 572 ºC and 555 ºC attributes oxidation of Mo_2C to MoO_3· The result shows almost straight line till 444 ºC in PT3, indicating a thicker graphitic carbon layer, which inhibits rapid oxidation of Mo_2C. The formation of oxide layer in temperature range (363 to 444 ºC) also enhances stability of the product phase. The samples show mass loss as a result of oxidation/combustion of carbon residue up to temperature range of 720 ºC [33]. The sudden and rapid mass loss thereafter is attributed to the evaporation of molybdenum oxide phase [36].

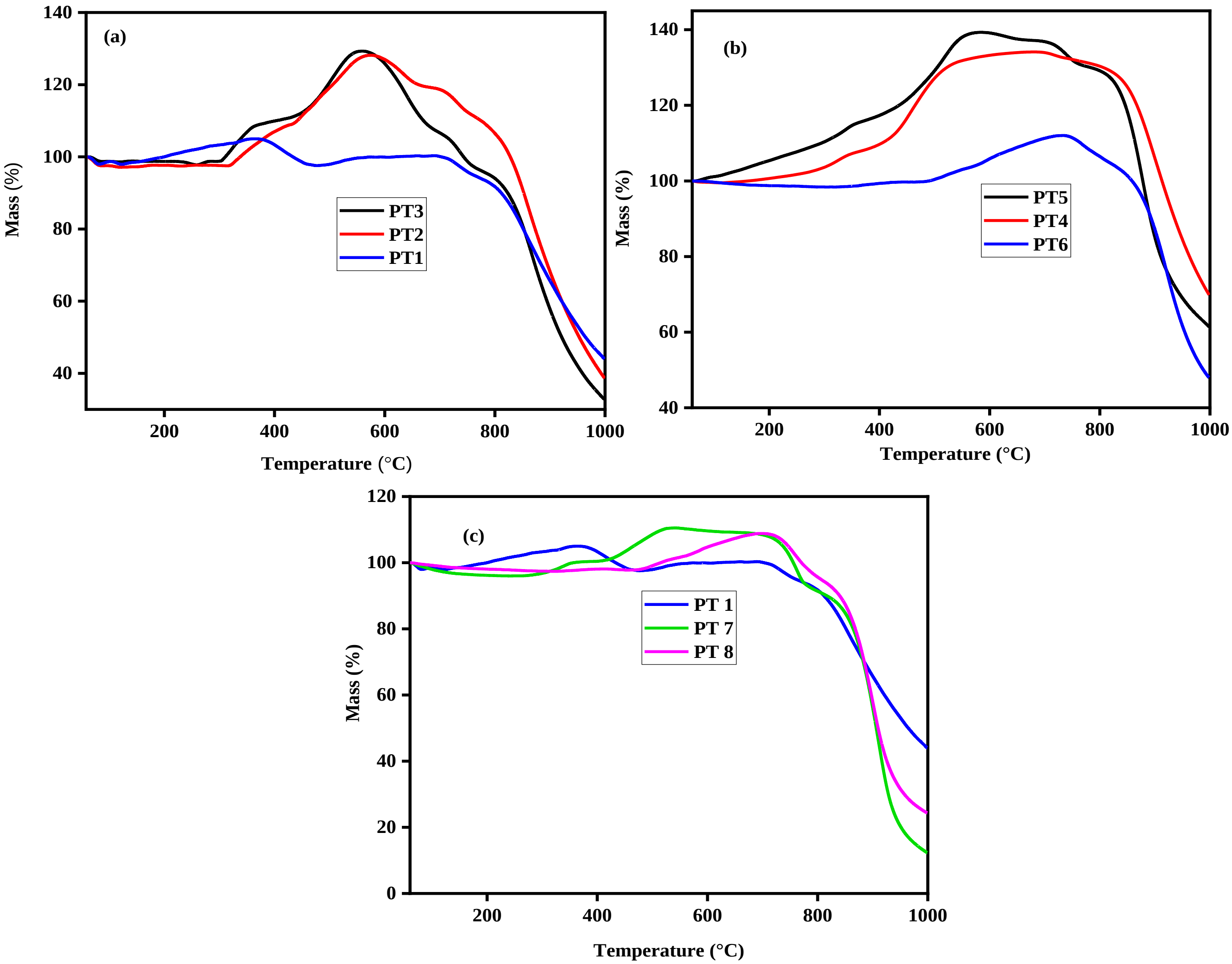

Figure 5.13: Thermogrvemtric analysis (TGA) of (a) PT1, PT2 and PT3 and (b) PT4, PT5 and PT6.

The TGA for samples (PT4, PT5 and PT6) is shown in Fig. 5.13b. The mass gain trend in TGA curve of PT4 and PT5 (till 350 ºC) shows the oxidation of Mo species in the synthesized product. The sudden increase in mass may be the result of less extra carbon in the sample to inhibit the oxidation process. The rapid mass gain till 530 and 565 ºC for PT4 and PT5 (139 %) results from oxidation of Mo and Mo_2C species, respectively. The TGA curve remains constant for PT4 from 530 to 810 ºC, which reveals the stability of the MoO_3 and intermediate molybdenum oxide. The sudden increase in mass may be the result of less extra carbon in the sample to inhibit the oxidation process. The slight variation in mass gain trend (PT5) might be a reason of complex oxidation of Mo_2C and carbon residue present in the system. The slight decrease in mass variation may be the result of combustion of carbon residue because of the higher initial carbon content in PT5 compared to PT4 that shows change in TGA pattern till 715 ºC. The mass loss from 715 to 750 ºC is attributed to the evaporation of formed MoO_3 [37]. However, the stable curve till 810 ºC may due to comproportion of intermediate molybdenum oxide species stable within this temperature range. The rapid mass loss after 810 ºC reveals the evaporation of the formed MoO_3 phase. The PT6 sample shows the trend comparable to PT3 and PT2 showing stability till 482 ºC after releasing the absorbed water. The slight change from (350-482 ºC) in TGA curve (Fig. 5.13b) may be due to the oxidation of residual surface carbon fallowed by the formation of oxide layer. The mass increases sharply up to 736 ºC as a result of oxidation of Mo_2C to MoO_3. The sample shows higher thermal stability as compared to PT3, PT4 and PT6, respectively. The mass decrease till 840ºC may be the result of oxidation of carbon residue as discussed and then shows a decreasing trend corresponding to evaporation of MoO_3. The PT6 results suggest higher amount of Mo_2C phase as observed by mass gain above 550 ºC [19]. The oxidation of molybdenum carbide (Mo_xC x=1,2) and incorporated carbon species is a complex process as determined by the TGA analysis. The relatively lower temperature synthesized phase PT7 shows a continuous mass loss (4.8 %) up to 300 °C corresponding to adsorbed water on surface and combustion of low crystalline surface carbon (Fig. 5.13c). The sample then exhibits a mass gain (5%) till 350 °C attributed to oxidation of some intermediate Mo carbide species leading to formation of MoO_3, which remains stable till 420 °C as shown in Fig. 5.13c. The oxide layer formed on the surface and some carbon present in the sample inhibits further oxidation of the Mo_2C phase. This mass gain of 10 % till 520 °C (Fig. 5.13c) shows the transformation of Mo_2C and other intermediate carbides present in the sample to form MoO_3. There after the TGA curve remains straight till 710 °C showing stability of the MoO_3

in the said temperature range. The mass decreases rapidly after 710 °C is attributed to sublimation of MoO_3. The more rapid mass loss after 850 °C correspond to evaporation of the MoO_3. However, the sample (PT8) pure phase Mo_2C exhibits a different trend in comparison to PT7, which reveals the presence of some intermediate species in PT7. The mass loss of nearly 3% up to 475 °C (Fig. 5.13c) is attributed to water adsorbed on surface and combustion of some residual carbon. The mass gain of nearly 13 % from 475 to 720 °C corresponds to oxidation of formed Mo_2C to MoO_3 (Fig. 5.12c). The sample synthesized at lower temperature is thermally less stable because no straight line is present in the TGA curve, which might be the result of less crystalline nature of the synthesized sample. The mass loss shows the same trend as that of PT7 after 720 °C as shown in Fig. 5.13c. This again reveals the sublimation and evaporation of the formed MoO_3 phase. The composition of sample was estimated from mass change analysis, assuming only carbon coated Mo_2C in samples and MoO_3 as solid combustion product. The free carbon in all the synthesized samples is calculated by the equation 5.1 and 5.2, respectively [25,38].

$$\%\, free\ carbon = \left[1 - \frac{m_i Molecular\ mass\ of\ (MoC)}{m_f Molecualr\ mass\ of\ MoO_3}\right] \times 100 \qquad (5.1)$$

$$\%\, of\ free\ carbon = [1 - \frac{M_i Molecualr\ mass\ of\ Mo_2C}{M_f \times 2 \times molecular\ mass\ of\ MoO_3}] \times 100 \qquad (5.2)$$

Where M_i: initial mass; and M_f: final mass.

The results so obtained are given in Table 5.5. The estimated free carbon content is higher in PT3 and lowest in PT4 and PT8, which is in accordance with the experimental parameters. Though the initial carbon content in PT1, PT2 and PT3 is same, however, in the final product the free carbon content varies with synthesis temperature. It might be due to less graphitization of hydrocarbon gases in low temperature range, which is in accordance with microstructural and Raman analysis.

5.3.7 Brunauer–Emmett–Teller (BET) analysis

The BET specific surface area (SSA) for the synthesized samples was estimated by nitrogen (N_2) adsorption/desorption studies. The adsorption-desorption isotherms presented in (Fig. 5.14a) demonstrate type II isotherm due to porous nature of carbon coated Mo_2C composites [39]. The estimated values of BET SSA of the synthesized powders are mentioned in Table 5.5. The PT1 sample reveals the higher BET SSA, which is in correlation with the lower crystallite size estimated from XRD analysis. However, the surface area has shown decreasing trend with the increase in temperature tabulated in Table 5.5.

Table 5.5: Carbon content estimation from TGA, BET estimated parameters and electrochemical results of the synthesized samples.

Sample Id	% Free carbon (TGA)	BET SSA (m^2g^{-1})	Pore volume cm^3g^{-1}	Pore diameter (nm)	Tafel slope (b) $mvdec^{-1}$	EDLC (C_{dl}) $mFcm^{-2}$
PT1	67.0	40.7	22.2	4.0	122.4	1.2
PT2	72.0	11.0	38.5	14.0	93.9	3.5
PT3	76.6	6.6	27.3	16.7	82.6	19.45
PT4	50.0	9.3	39.5	17.0	101.5	0.3
PT5	56.6	37.1	74.8	8.0	122.2	1.75
PT6	65.9	7.9	10.2	5.2	80.1	12.2
PT7	78.6	17.0	35.2	8.9	151.1	7.5
PT8	77.8	36.4	88.9	12.8	130.3	23.4

The pore size estimated from BET analysis increases, while the pore volume depicted decreasing trend with the increase in temperature (Table 5.5). The BET SSA has decreased with the increase in temperature, which corresponds to sintering of the powder surfaces at higher temperatures [40]. The increase in SSA from PT4 to PT5 might be the result of more porous nature of PT5 having a mean pore size of 8 nm as revealed in (Fig. 5.14b). The SSA decreases from PT5 to PT6 with increase in carbon content. The highly dense crystalline nature of carbon around Mo_2C may result in lowering of BET SSA [40]. The pore size distribution of PT6 (Fig. 5.14c) shows wider pore size distribution and lower pore volume as given in Table 5.5. The decrease in pore volume and with increase in carbon content (PT5 to PT6) might be because of the pore strain and pore rapture at higher temperatures [41]. The agglomeration of the pure phase Mo_2C particles encapsulated in dense carbon matrix in PT3 and PT6 results in lower surface area [42]. The desorption isotherms of relatively lower temperature synthesized phases (PT7 and PT8) are shown in Fig 5.14d exhibit a type II isotherm curve. The pure phase Mo_2C (PT8) shows a higher specific surface area (SSA) than PT7 as given in Table 5.5. This might be because of higher porous nature of surface carbon over Mo_2C. The higher pore volume also supports the porous structure of the synthesized sample, which also attributes to the **hollow** structures exhibited in FESEM micrographs. Moreover, the higher SSA of PT8 is in accordance with the lower crystallite size.

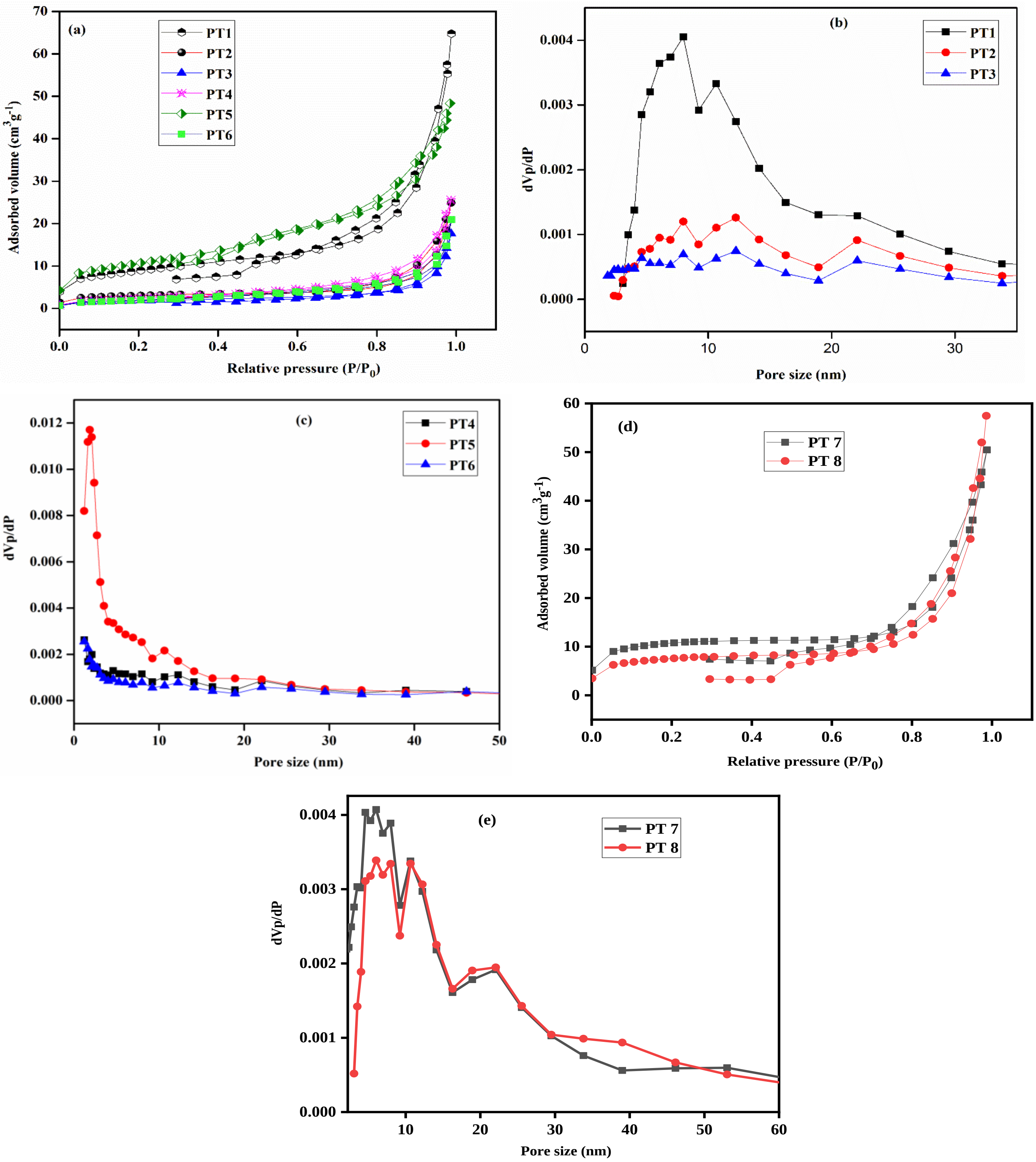

Figure 5.14: (a) Adsorption-desorption isotherms of (PT1 to PT6), (b) pore size distribution of PT1, PT2 and PT3, (c) pore size distribution of PT4, PT5 and PT6, (d) adsorption-desorption isotherms of PT7 & PT8 and (e) pore size distribution of PT7 and PT8.

5.3.8 Electrochemical studies

5.3.8.1 HER activity

The HER activity of prepared samples of carbon coated MoC (PT1) and Mo_2C (PT2 & PT3) were analyzed by linear sweep voltammetry (LSV) measurements at a scan rate of 2 mVs^{-1}. The polarization curves of PT1, PT2 and PT3 are shown in Fig. 5.15a. The current density of PT1 is 34 $mAcm^{-2}$ and those of PT2 and PT3 are 15.4 and 27.2 $mAcm^{-2}$, respectively. The higher value of current density in MoC (PT1) is attributed to small crystallite size as calculated from XRD analysis and higher BET specific surface area [43]. The transport path ways of electrolyte ions is enhanced by the smaller size of the particles. The current density is less in PT2 as compared to the PT1, which may be the result of larger crystallite size, less BET specific surface area and incorporation of the agglomerated Mo_2C particles in the carbon matrix. The PT3 shows enhanced current density values (Fig. 5.15a) as compared to PT2. This may be due to the decrement in crystallite size and surface carbon graphitization, which improves the charge transfer kinetics on Mo_2C surface [2]. The increase in synthesis temperature (PT2 to PT3) results in improvement of current density. The synthesis conditions leading to variation in nature of surface carbon affects the charge kinetics of Mo_2C surface, which influences the current density values [43]. The temperature dependent strain generated in the lattice shows variation in d-band structure and thus affects HER activity [44]. The PT4 having Mo_2C as major phase and Mo as impurity phase and the PT5 having Mo_2C as major, Mo and $Mo_{0.42}C_{0.58}$ as minor impurity phases shows the current density of 16 and 27.5 $mAcm^{-2}$, respectively as given in Fig. 5.15b. The lower current density value obtained in PT4, although having low value of crystallite size as compared to PT5 might be the result of low carbon content in the sample. The PT5 having higher value of extra carbon as compared to PT4 as evidenced from Raman and TGA, shows higher surface area and thus enhances the current density values as depicted in Fig. 5.15b. The presence of molybdenum oxide species as evidenced from the Raman analysis being less electrochemically active candidates also decreases the current density values. The results also predict increase in the current density with more Mo_2C content in the prepared samples. The result of PT4 and PT5 confirms that Mo is not an active electrocatalyst. However, the incorporation of C in Mo lattice makes it active because of resemblance of d-band structure with Pt [45,46]. The pure phase Mo_2C (PT6) shows current density of 25.0 $mAcm^{-2}$ (Fig. 5.15b). The higher value of current density might be because of the pure phase formation of Mo_2C and presence of extra carbon content in product. The conductive carbon layer as confirmed by Raman spectroscopy and TEM in between the particles facilitate the electron transfer and enhances the conductivity between the Mo_2C particles. The molybdenum carbide particles embedded in carbon matrix also inhibit them from agglomeration and activates more exposed sites [2]. The low crystalline sample (PT7) although having lower crystalline size, shows only current density of 23.2 $mAcm^{-2}$, which is lower than pure phase MoC and Mo_2C. This might be because of intermediate phase formation at lower temperature. Moreover, the pure phase Mo_2C synthesized at same reaction temperature PT8 (Fig. 5.15c) shows enhanced current density of 44.8 $mAcm^{-2}$. This correspond to the lower crystallite size and higher surface area of the synthesized phase. The lower temperature synthesized phase enhances the number of active sites and increases the current density, which improves the HER activity.

For HER performance, the stability of the synthesized samples is an imperative parameter. The stability of the product phases has been determined by cyclic voltammetry (CV) analysis in acidic medium for 2000 cycles in voltage window (0.2 to -0.3 V) at a scan rate of 100 mVs^{-1}. The LSV performed after 2000 CV cycles for PT1 shows negligible loss of current density as depicted in Fig. 5.15a. The higher stability may be due to surface carbon, which inhibits the degradation of the synthesized product during HER activity. The LSV measurements of PT3 as compared to PT2 shows similar polarization curve with loss of current by 23%, respectively (Fig. 5.15a). This shows that PT2 is more stable as compared to PT3. The stability of PT2 and PT3 is influenced by the nature of surface carbon. The less graphitic carbon in PT2 as compared to PT3 enhances the stability of the product although the current density is low [47]. The higher free carbon as estimated from TGA enhances the current density in PT3, but during testing the catalyst destabilizes because the higher amount surface carbon hinders certain active sites and decreases the stability. The larger pore size in PT3 might be the reason for lesser stability, which hiders the electron movement on the surface and block the ion movement within the site. The excessive carbon in the carburized product may also cover some of the active sites and deteriorate the HER activity. The PT4 and PT5 sample lose their efficiency with maximum loss of current in the given range as implied in Fig. 5.15b.

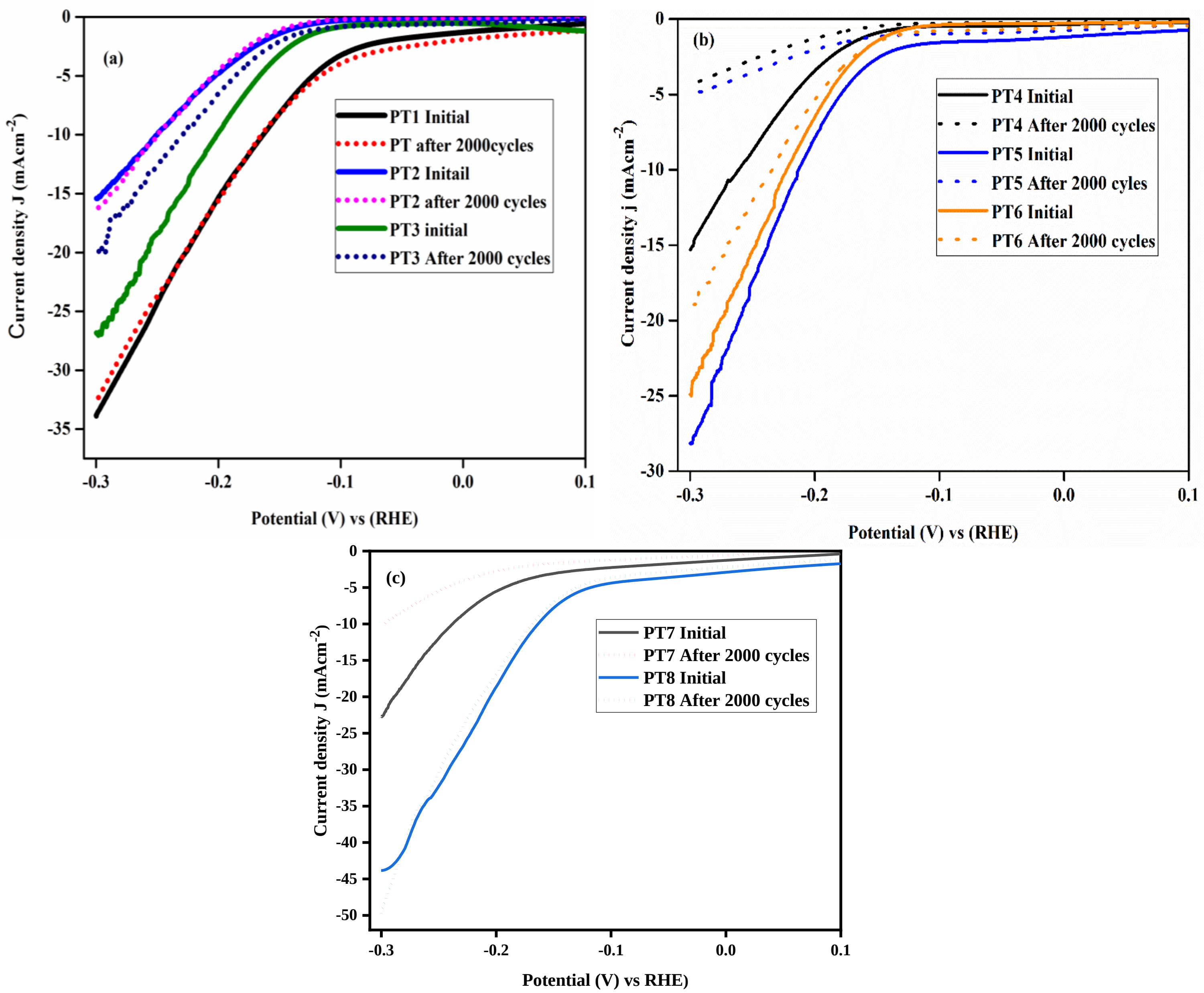

Figure 5.15: Linear voltammetry plots (a) PT1, PT2 & PT3, (b) PT4, PT5 & PT6 and (c) PT7 & PT8.

The presence of more Mo phase in PT4 could lead to oxidation/corrosion of the product surface to form a less electroactive species and diminishes its efficiency. The PT5 shows higher initial current density, but its stability is comparable to PT4 after 2000 CV cycles as depicted in Fig. 5.15b. The destabilization of PT4 and PT5 could be a result of oxidation/corrosion of Mo_2C and Mo species in acidic medium because of the low surface carbon content. However, PT6 sample shows the loss of current by 23 % as shown in Fig. 5.15b, which is more stable than PT4 and PT5 but the results are comparable to PT3. The results predict that the amount of initial carbon content 0.75 and 1.0g for its synthesis shows the similar results for HER activity. The results also reveal that most stoichiometric phase of Mo$_2$C as calculated from the Rietveld refinement (PT2) shows low current density and higher stability as compared to carbon vacant phase (PT3 and PT6), having enhanced current density and relatively low stability. The results reveal that the vacancy of carbon within the synthesized species enhances the charge transfer rate. The lower temperature intermediate phase (PT7) deteriorates the performance (Fig. 5.15c), because of the lower resistance to acidic corrosion. This might also correspond to more pore volume and pore size compared to PT1. However, the synthesized pure phase (PT8/Mo$_2$C) at the same reaction temperature (600 °C) shows higher stability in accordance with lower crystalline surface carbon and higher carbon content [47]. However, the nature of in-situ developed surface carbon and its thickness needs to be optimized at lower temperatures to enhance the efficiency and activity of electrocatalyst.

To discern the mechanism responsible for HER activity, the Tafel slope '***b***' an immanent characteristics of the electrocatalyst was estimated from Tafel plot shown in (Fig. 5.16a-c) and the values are designated in (Table 5.5). The HER mechanism follows the following steps:

$$S + H_3O^+ + e^- \leftrightarrow SH_{ads} + H_2O \qquad (Volmer\ step) \qquad (5.3)$$

$$SH_{ads} + H_3O^+ + e^- \leftrightarrow H_2 + S + H_2O \qquad (Heyrovsky\ step) \qquad (5.4)$$

$$SH_{ads} + SH_{ads} \leftrightarrow H_2 + 2S \qquad (Tafel\ step) \qquad (5.5)$$

Where 'S' is an active site and SH_{ads} is the hydrogen adsorbed on that particular site.

The Volmer reaction (5.3) is rate determining step, if the value of '***b***' is up to 120 mVdec^{-1}.The Heyrovsky (5.4) and Tafel (5.5) reactions are the rate determining steps, if the value of '***b***' is about 40 and 30 mVdec^{-1}, respectively. The Tafel slope '***b***' of PT1 is 122.4 mVdec^{-1} (Fig. 5.16a), which is comparable to 120 mVdec^{-1}. The results predict the rate determining step for HER activity is Volmer reaction. The value of '***b***' for PT2 and PT3 (Fig. 5.16a) are 93.9 and 82.6 mVdec^{-1}, respectively and also predicts that Volmer-Heyrovsky step is rate determining for HER. The hydrogen bubble produced on the surface of the working electrode shown in (Fig. 3.1, Chapter 3) reveals the production of hydrogen on the electrode surface. The low value of '***b***' compared to PT1 might be the result of pure phase formation of Mo$_2$C, which is more efficient electrocatalyst for HER and exhibit similar electronic structure as that of Pt. The transformation of the residual free carbon to graphitic carbon with rise in synthesis temperature enhances the electrical conductivity, hydrogen adsorption and improves the HER activity. The Tafel slope '***b***' for PT4, PT5 and PT6 are 101.5, 122.2 and 80.11 mVdec^{-1}, respectively (Fig. 5.16b). The obtained values are tabulated in Table 5.5.

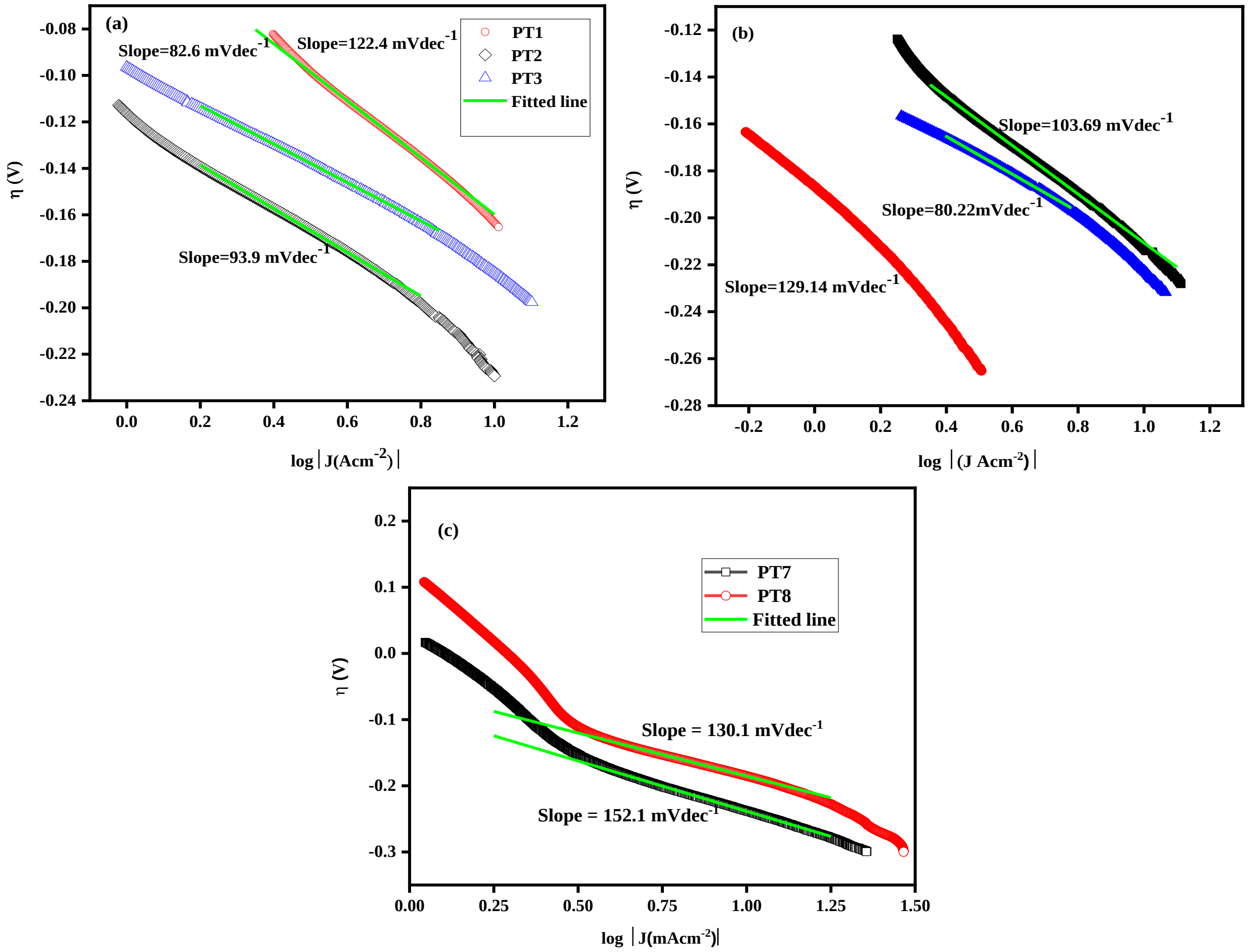

Figure 5.16: Tafel plots of (a) PT1, PT2 & PT3, (b) PT4, PT5 & PT6 and (c) PT7 & PT8.

The higher value of '***b***' for PT4 determines weak adsorption on electrocatalyst surface, because of low initial carbon content and negligible surface carbon as estimated from Raman analysis. The higher value of '***b***' for PT5 as compared to PT4 might correspond to lattice distortion calculated from W-H analysis, which affects covalent properties, surface atomic arrangements and electron occupation states [48,49]. The Tafel slope '***b***' for PT6 shows that reaction (5) proceeds faster as compared to PT4, PT5 and PT2. The results of PT3 and PT6 are comparable and depends on the graphitization of the surface carbon content that enhances the charge transfer kinetics. The Tafel slope '***b***' of intermediate phase (PT7) shown in Fig. 5.16c is higher than PT1, which shows adsorption of H^+ ion on the surface is very slow and only Volmer step is the rate determining step. This corresponds to higher crystallite size and lower surface area compared to PT1, which does not provide active sites for adsorption and frequent desorption to enhance the charge transfer rate. However, the Tafel slope '***b***' shows smaller value compared to PT8 (Fig. 5.16c), which correspond to pure phase formation of Mo_2C. The PT8 although exhibits higher SSA, crystallite size than pure phase samples (PT2, PT3 and PT6), but shows higher Tafel slope '***b***' and reveal Volmer reaction as slow and rate determining step. The obtained values are better than reported results in literature as given in Table 5.6. This attributes to lower crystallinity of the synthesized sample and amorphous nature of surface carbon. The results confirm the higher current density is attributed to higher SSA and low crystallite size, but the lower Tafel slope '***b***' depends on the crystallinity and surface characteristics.

5.3.8.2 Electrochemical double layer capacitance (EDLC, C_{dl})

The EDLC (C_{dl}) analysis have been performed via CV at different scan rates (50-320 mVs^{-1}) in a voltage range of 0.2 to 0.4V as has been depicted in (Fig. 5.17a-h). Only the pure phase Mo_2C samples incorporated in carbon matrix show good pattern of CV cycles as shown in Fig. 5.17 b, c, and h for PT2, PT3 and PT8, respectively. Little distorted rectangular curve is obtained in PT6, which might be due to lower surface carbon over Mo_2C. The CV plots for the synthesized samples at a fix scan rate (320 mVs^{-1}) are shown in Fig. 5.18. The pure Mo_2C phase (PT3) incorporated in carbon matrix exhibit regular and sharp rectangular shape (Fig.5.18). This indicates enhanced electrochemical reversibility even at higher scan rates during the charge/discharge processes. The plots of scan rate (mVs^{-1}) with current density $\Delta j_{0.3}$ ($mAcm^{-2}$) is shown in Fig. 5.19a-c and the results are depicted in Table 5.5. The MoC (PT1) incorporated in carbon matrix shows the C_{dl} value of 1.2 $mFcm^{-2}$ (Table 5.5). However, the Mo_2C (PT2, PT3) encapsulated in carbon shows the C_{dl} of 3.5 and 19.46 $mFcm^{-2}$, respectively. The results are in correlation with the shape of CV cycles towards rectangular pattern exhibiting enhanced charge storage capacity. The C_{dl} results estimated for PT3 are higher as compared to results obtained by Li *et al.*[2]. However, the CV of PT4 and PT5 also deviate from rectangular pattern. The higher value of C_{dl} for pure phase Mo_2C could be the result of fast charge separation of non-faradic process between the interface of electrode and electrolyte. The C_{dl} values obtained for PT4 and PT5 are 0.29 and 1.8 $mFcm^{-2}$, respectively. The decrement in value of C_{dl} for these samples is due to presence of lesser amount of residual carbon. Moreover, the C_{dl} value of PT6 as estimated is 12.2 $mFcm^{-2}$. The results predict that the incorporation of Mo_2C in the graphitic carbon residue enhances the charge storage capacity.

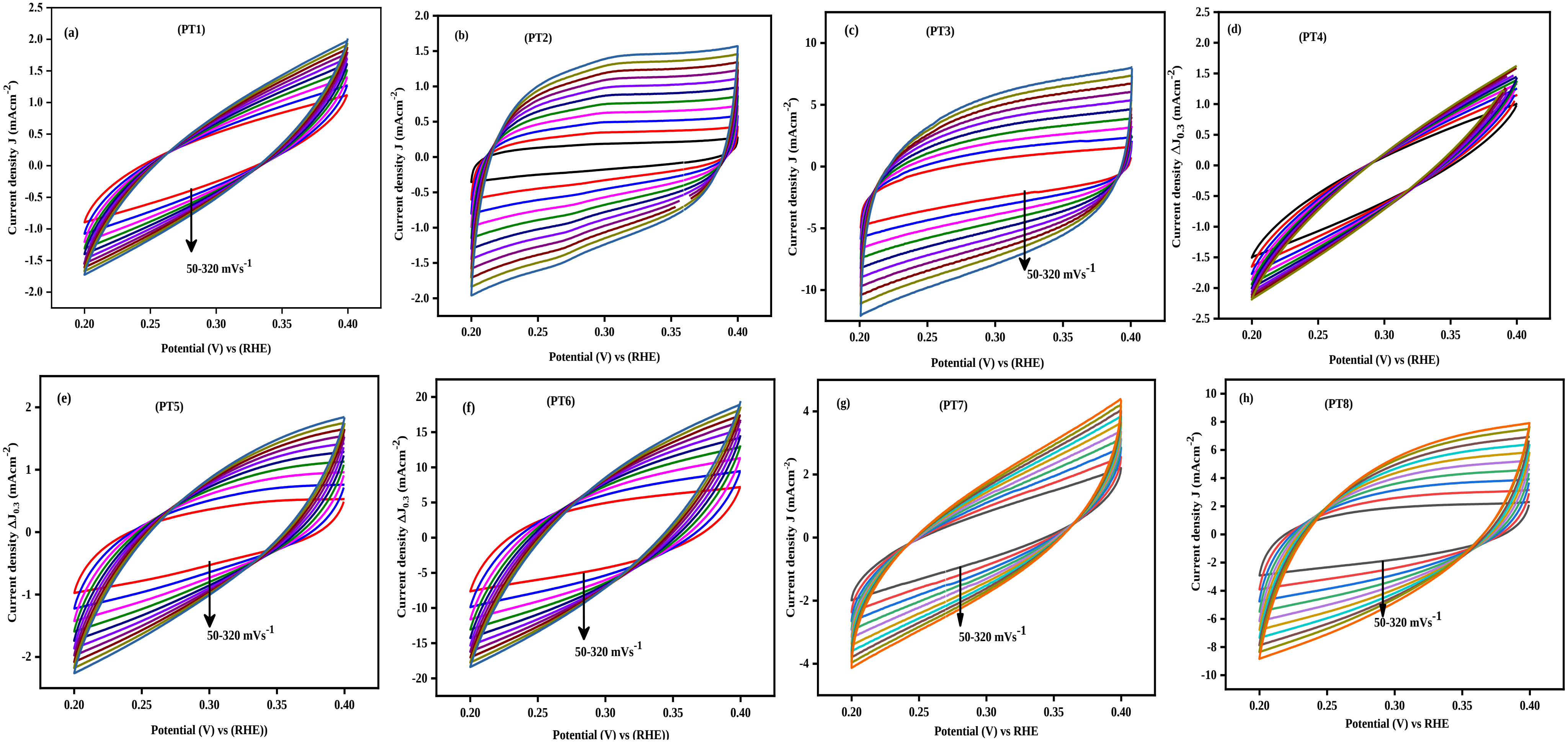

Figure 5.17: Cyclic voltammtery (CV) plots at various scan rates (a) PT1, (b) PT2, (c) PT3, (d) PT4, (e) PT5, (f) PT6, (g) PT7 and (h) PT8.

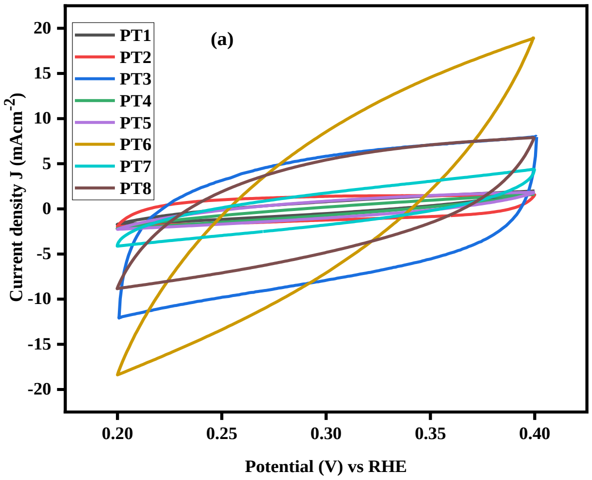

Figure 5.18: Cyclic voltammetry (CV) plots at 320 mVs^{-1}.

The C_{dl} measurements reveal that high temperature synthesized Mo_2C nanostructures encapsulated in conductive carbon layers obtained from waste plastics during in-situ synthesis are novel materials for energy storage applications. The PT8 shows higher C_{dl} value as compared to PT1 and PT7 as shown in Fig. 5.19c. Among the pure phase Mo_2C samples PT3 and PT8 exhibit higher C_{dl} values corresponding higher graphitic carbon and higher surface area, respectively. The C_{dl} results estimated for PT3 and PT8 are higher as compared to results obtained by Li *et al.*[2]. The C_{dl} measurements also predict the higher electrochemical surface area (ECSA) of Mo_2C particles in PT3 and PT8 and contributes efficiently to their HER activity [50]. The TEM and FESEM micrographs of PT3 showing faceted stacking makes the exterior sheet surface available for electrolyte ions, which improves the C_{dl} value. The higher pore volume SSA, lower crystallite size contributes to EDLC performance of PT8. The specific capacitance (SC) of the synthesized samples is shown in Fig. 5.19d. It reveals the increase in SC with increase in pure phase formation with respect to temperature and shows a strong dependence on the amount of initial as well as final carbon residue over Mo_2C. The higher SSA contributes to SC at fixed temperature along with pure phase formation of Mo_2C. The enhanced charge storage capacity apart from BET surface area may be attributed to variation in pore size, shape and surface functionalization. The meso and micro pores interconnected in the supported carbon nanostructures improve the charge transfer, accommodation and distribution, which utilize all the surface of the electrode material. The HER performance of PT1 although having low C_{dl} value is due to lower particle size and higher specific surface area. The higher current density and HER performance of PT8 attributes to its higher ECSA.

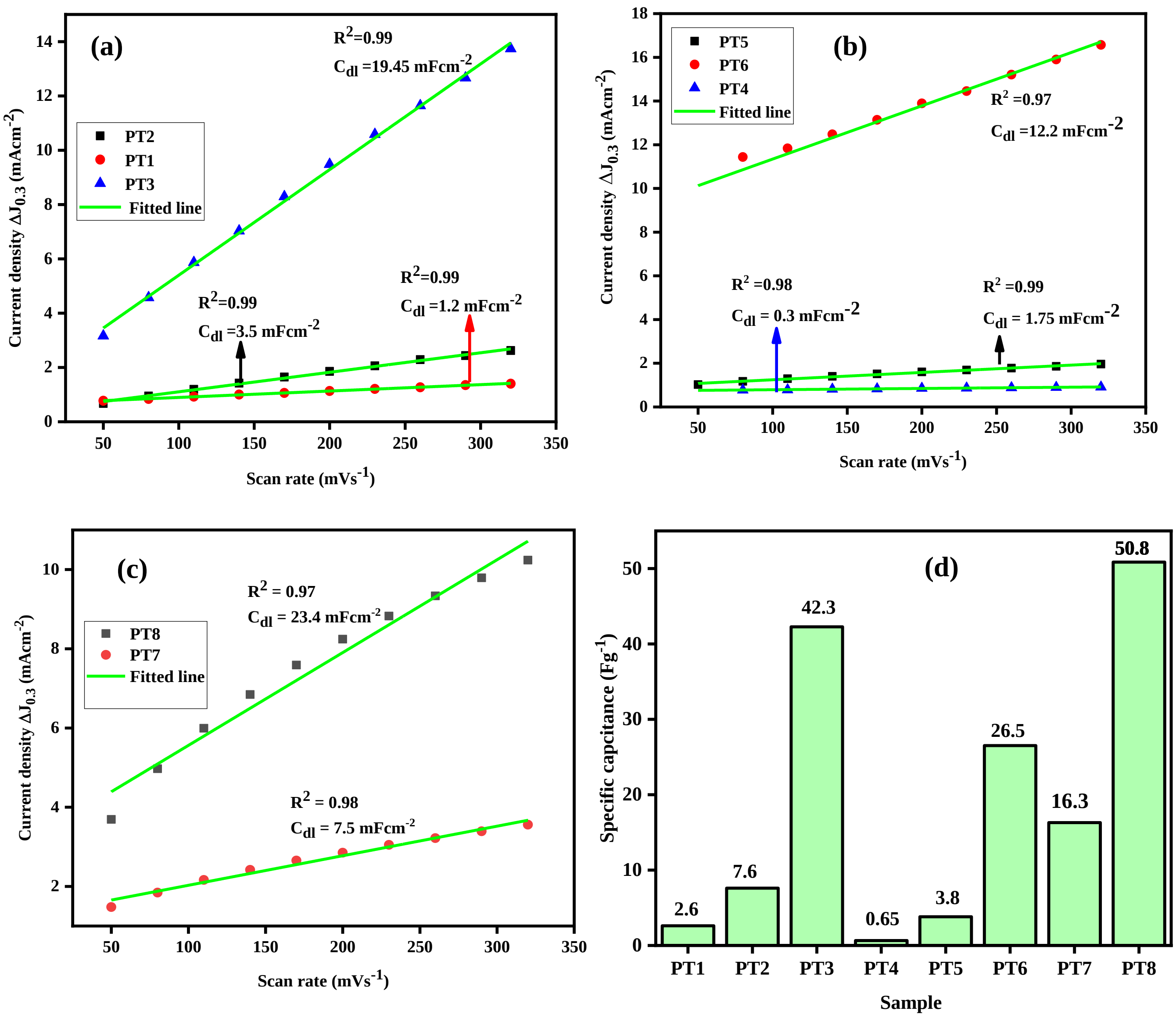

Figure 5.19: (a) Electric double layer capacitance (EDLC) of PT1, PT2 & PT3, (b) EDLC of PT4, PT5 & PT6, (c) PT7 & PT8 and (d) Specific capacitance (SC) of the synthesized samples.

Table 5.6: Comparison table of electrochemical results with the reported results.

Sample	**Catalyst loading mgcm^{-2}**	**Tafel slope '*b*' mVdec^{-1}**	**Onset potential (mV)**	**Over potential (mV)**	**Exchange current density (J_0) mAcm^{-2}**	**Reference**
PT1	**0.57**	**122.4**	**99.7**	**160**	**0.495**	This work
PT2	**0.57**	**93.9**	**120.1**	**213.7**	**0.075**	
PT3	**0.57**	**82.6**	**114.5**	**179.1**	**0.067**	
PT4	**0.57**	**101.5**	**158.0**	**209.8**	**0.085**	
PT5	**0.57**	**122.2**	**140.5**	**309.34**	**0.0334**	
PT6	**0.57**	**80.11**	**137.6**	**213.35**	**0.022**	
PT7	**0.57**	**152.1**	**151.1**	**237.6**	**0.270**	
PT8	**0.57**	**131.1**	**130.3**	**185.4**	**0.377**	
Mo_2C@NPC		126.4	137	260	0.00316	2
Mo_2Cx-2	0.354	93	35	160	-	51
Mo_2C.com	-	89	-	242	0.00195	52
Mo_2C-C	-	74	-	187	0.0326	
Mo_2C/GR	1.4	82	150	242	-	53
Mo_2C/CNT	8.2	251	-	250	1.43	54
Mo_2C/CXG	6.3	264	-	170	1.69	
Mo_2C@NC-2-950	-	83	-	290	-	
MoC	-	56	101	221	0.00058	55
Mo_2C	-	45	51	164	0.00012	
3DHP-Mo2C		75	-	166	0.287	56
MoDCA-2	-	68	62	205	0.017	57
Mo_2C/GCSs	0.36	62.6	120	200	0.0125	58
MoN nanosheets`	0.28	-	-	278	-	59
Mo_2C@C	-	64	133	197	0.01	60
MoC-G	0.8	88	15	221	-	61
PANI-MoCN	0.4	50	120	230	-	62

C-Mo_2C	-	168	-	260	-	63
MC-G50	0.33-0.357	101	-	283	-	64
MC-G100	0.33-0.357	93	-	259	-	
MC-G350	0.33-0.357	67	-	206	-	
MC-G500	0.33-0.357	71	-	216	-	
MoS_2		101		300		65
Fe-MoS_2		148		300		
Co-MoS_2		144		300		

References

1 Z. Shi, K. Nie, Z. J. Shao, B. Gao, H. Lin, H. Zhang, B. Liu, Y. Wang, Y. Zhang, X. Sun, X. M. Cao, P. Hu, Q. Gao and Y. Tang, *Energy and Environmental Science*, 2017, **10**, 1262–1271.

2 J. Sen Li, Y. Wang, C. H. Liu, S. L. Li, Y. G. Wang, L. Z. Dong, Z. H. Dai, Y. F. Li and Y. Q. Lan, *Nature Communications*, 2016, **7**, 11204.

3 X. J. Yang, X. J. Feng, H. Q. Tan, H. Y. Zang, X. L. Wang, Y. H. Wang, E. B. Wang and Y. G. Li, *Journal of Materials Chemistry A*, 2016, **4**, 3947–3954.

4 Y. Mu, Y. Zhang, L. Fang, L. Liu, H. Zhang and Y. Wang, *Electrochimica Acta*, 2016, **215**, 357–365.

5 L. Liao, S. Wang, J. Xiao, X. Bian, Y. Zhang, M. D. Scanlon, X. Hu, Y. Tang, B. Liu and H. H. Girault, *Energy and Environmental Science*, 2014, **7**, 387–392.

6 Y. Zheng, Y. Jiao, M. Jaroniec and S. Z. Qiao, *Angewandte Chemie - International Edition*, 2015, **54**, 52–65.

7 D. H. Youn, S. Han, J. Y. Kim, J. Y. Kim, H. Park, S. H. Choi and J. S. Lee, *ACS Nano*, 2014, **8**, 5164–5173.

8 K. M. Naik and S. Sampath, *Electrochimica Acta*, 2017, **252**, 408–415.

9 C. Wan, Y. N. Regmi and B. M. Leonard, *Angewandte Chemie - International Edition*, 2014, **53**, 6407–6410.

10 H. Bin Wu, B. Y. Xia, L. Yu, X. Y. Yu and X. W. Lou, *Nature Communications*, 2015, **6**, 1–17.

11 C. Tang, Z. Wu and D. Wang, *ChemCatChem*, 2016, **8**, 1961–1967.

12 V. Kiran, K. L. Nagashree and S. Sampath, *RSC Advances*, 2014, **4**, 12057–12064.

13 T. Mo, J. Xu, Y. Yang and Y. Li, *Catalysis Today*, 2016, **261**, 101–115.

14 J. Leis, M. Arulepp, M. Käärik and A. Perkson, *Carbon*, 2010, **48**, 4001–4008.

15 J. Li, Q. M. Yang and I. Zhitomirsky, *Nanoscale Research Letters*, 2010, **5**, 512–517.

16 C. Wallar, D. Luo, R. Poon and I. Zhitomirsky, *Journal of Materials Science*, 2017, **52**, 3687–3696.

17 Y. Su and I. Zhitomirsky, *Journal of Power Sources*, 2014, **267**, 235–242.

18 X. Zou and Y. Zhang, *Chem. Soc. Rev.*, 2015, **44**, 5148–5180.

19 N. S. Alhajri, D. H. Anjum and K. Takanabe, *Journal of Materials Chemistry A*, 2014, **2**, 10548–10556.

20 Y. Zhao, Z. Yao, Y. Shi, X. Qiao, G. Wang, H. Wang, J. Yin and F. Peng, *New Journal of Chemistry*, 2015, **39**, 4901–4908.

21 J. Dang, G. Zhang, L. Wang, K. Chou and P. C. Pistorius, *Journal of the American Ceramic Society*, 2016, **99**, 819–824.

22 J.-S. Choi, G. Bugli and D. Ega-Mariadassou, *Journal of Catalysis*, 2000, **193**, 238–247.

23 E. Parthé and V. Sadogopan, *Acta Crystallographica*, 1963, **16**, 202–205.

24 V. Krasnenko and M. G. Brik, *Solid State Sciences*, 2012, **14**, 1431–1444.

25 L. K. Brar, G. Singla and O. P. Pandey, *RSC Advances*, 2016, **6**, 109174–109184.

26 Q. Gao, X. Zhao, Y. Xiao, D. Zhao and M. Cao, *Nanoscale*, 2014, **6**, 6151–6157.

27 Y. Liu, M. Zhu and D. Chen, *Journal of Materials Chemistry A*, 2015, **3**, 11857–11862.

28 P. Xiao, X. Ge, H. Wang, Z. Liu, A. Fisher and X. Wang, *Advanced Functional Materials*, 2015, **25**, 1520–1526.

29 R. Ding, Y. Wu, Y. Chen, H. Chen, J. Wang, Y. Shi and M. Yang, *Catalysis Science and Technology*, 2016, **6**, 2065–2076.

30 A. C. Ferrari, *Solid State Communications*, 2007, **143**, 47–57.
31 J. Ferrari, A. C., and Robertson, *Physical Review B*, 2000, **61**, 14095–14107.
32 A. Das, B. Chakraborty and A. K. Sood, *Bulletin of Materials Science*, 2008, **31**, 579–584.
33 M. Pang, C. Li, L. Ding, J. Zhang, D. Su, W. Li and C. Liang, *Industrial & Engineering Chemistry Research*, 2010, **49**, 4169–4174.
34 Y. Chen, H. Zhang, J. Zhang, J. Ma, H. Ye, G. Qian and Y. Ye, *Materials Sciences and Applications*, 2011, **2**, 1313–1316.
35 B. Wang, G. Wang and H. Wang, *Journal of Materials Chemistry A*, 2015, **3**, 17403–17411.
36 N. S. Alhajri, D. H. Anjum and K. Takanabe, *Journal of Materials Chemistry A*, 2014, **2**, 10548–10556.
37 E. U. Ikhuoria, A. U. Liyanage and M. M. Lerner, *Materials Chemistry and Physics*, 2013, **139**, 911–916.
38 A. L. Tomas-Garcia, Q. Li, J. O. Jensen and N. J. Bjerrum, *International Journal of Electrochemical Science*, 2014, **9**, 1016–1032.
39 Y. J. Lee, S. H. Kim, T. H. Lee, H. H. Nersisyan, K. H. Lee, M. H. Han, S. U. Jeong, K. S. Kang, K. K. Bae and J. H. Lee, *Chemical Engineering Science*, 2014, **107**, 227–234.
40 H. Wu, X. Wang, Y. Bai, L. Jiang, C. Wu, B. Hu, Q. Wei, X. Liu and N. Li, *Journal of Solid State Electrochemistry*, 2013, **17**, 2453–2460.
41 R. A. Rather, S. Singh and B. Pal, *Journal of Catalysis*, 2017, **346**, 1–9.
42 R. A. Rather, S. Singh and B. Pal, *Applied Catalysis B: Environmental*, 2017, **213**, 9–17.
43 Y. Zhong, X. Xia, F. Shi, J. Zhan, J. Tu and H. J. Fan, *Advanced Science*, 2016, **3**, 1500286.
44 W. Sun, Z. Wang, W. Q. Zaman, Z. Zhou, L. Cao, X.-Q. Gong and J. Yang, *Chemical Communications*, 2018, **54**, 996–999.
45 R. B. Levy and M. Boudart, *Science*, 1973, **181**, 547–549.
46 R. Michalsky, Y. J. Zhang and A. A. Peterson, *ACS Catalysis*, 2014, **4**, 1274–1278.
47 K. Zhang, C. Li, Y. Zhao, X. Yu and Y. Chen, *Physical chemistry chemical physics*, 2015, **17**, 16609–14.
48 T. Daio, A. Staykov, L. Guo, J. Liu, M. Tanaka, S. Matthew Lyth and K. Sasaki, *Scientific Reports*, 2015, **5**, 13126.
49 D. Ma, Z. Lu, Y. Tang, T. Li, Z. Tang and Z. Yang, *Physics Letters A*, 2014, **378**, 2570–2575.
50 K. Zhang, C. Li, Y. Zhao, X. Yu and Y. Chen, *Physical Chemistry Chemical Physics*, 2015, **17**, 16609–16614.
51 X. Yang, X. Feng, H. Tan, H. Zang, X. Wang, Y. Wang, E. Wang and Y. Li, *Journal of Materials Chemistry A*, 2016, **4**, 3947–3954.
52 Y. Mu, Y. Zhang, L. Fang, L. Liu, H. Zhang and Y. Wang, *Electrochimica Acta*, 2016, **215**, 357–365.
53 S. Meyer, A. V. Nikiforov, I. M. Petrushina, K. Köhler, E. Christensen, J. O. Jensen and N. J. Bjerrum, *International Journal of Hydrogen Energy*, 2015, **40**, 2905–2911.
54 B. Šljukić, M. Vujković, L. Amaral, D. M. F. Santos, R. P. Rocha, C. A. C. Sequeira and J. L. Figueiredo, *Journal of Materials Chemistry A*, 2015, **3**, 15505–15512.
55 H. Lin, Z. Shi, S. He, X. Yu, S. Wang, Q. Gao and Y. Tang, *Chemical Science*, 2016, **7**, 3399–3405.
56 T. Meng, L. Zheng, J. Qin, D. Zhao and M. Cao, *Journal of Materials Chemistry A*, 2017,

5, 20228–20238.
57 R. Ma, Y. Zhou, Y. Chen, P. Li, Q. Liu and J. Wang, *Angewandte Chemie - International Edition*, 2015, **54**, 14723–14727.
58 W. Cui, N. Cheng, Q. Liu, C. Ge, A. M. Asiri and X. Sun, *ACS Catalysis*, 2014, **4**, 2658–2661.
59 J. Xie, S. Li, X. Zhang, J. Zhang, R. Wang, H. Zhang, B. Pan and Y. Xie, *Chemical Science*, 2014, **5**, 4615–4620.
60 Z. Shi, K. Nie, Z. J. Shao, B. Gao, H. Lin, H. Zhang, B. Liu, Y. Wang, Y. Zhang, X. Sun, X. M. Cao, P. Hu, Q. Gao and Y. Tang, *Energy and Environmental Science*, 2017, **10**, 1262–1271.
61 C. He and J. Tao, *Chemical Communications*, 2015, **51**, 8323–8325.
62 Y. Zhao, K. Kamiya, K. Hashimoto and S. Nakanishi, *Journal of the American Chemical Society*, 2015, **137**, 110–113.
63 M. Fan, H. Chen, Y. Wu, L. Feng, Y. Liu and G. Li, *Journal of Materials Chemistry A*, 2015, **3**, 16320–16326.
64 K. Ojha, S. Saha, H. Kolev, B. Kumar and A. K. Ganguli, *Electrochimica Acta*, 2016, **193**, 268–274.
65 Y. Shi, Y. Zhou, D. R. Yang, W. X. Xu, C. Wang, F. Bin Wang, J. J. Xu, X. H. Xia and H. Y. Chen, *Journal of the American Chemical Society*, 2017, **139**, 15479–15485.

Chapter 6

Comparative study of C-Mo_2C and C/N-Mo_2C

Overview

The environmental issues caused globally due to the disposal of the non-biodegradable carbonaceous wastes need to be addressed. The present work emphasizes on utilization of waste ployethene as carbon source for the synthesis of C-Mo_2C and C/N-Mo_2C, respectively. In this chapter reaction temperature and time have been optimized to obtain pure phase C-Mo_2C and C/N-Mo_2C in an autoclave. The MoO_3 and ammonium heptamolybdate tetrahydrate (AHM) were used as Mo source and N/Mo source for the synthesis of C-Mo_2C and C/N-Mo_2C composites. The presence of N in the carbon matrix over Mo_2C has been confirmed by XPS and STEM. The comparative electrochemical study (HER activity and EDLC performance) of C-Mo_2C and C/N-Mo_2C has been done to highlight the role of N encapsulation in the carbon matrix supported over Mo_2C.

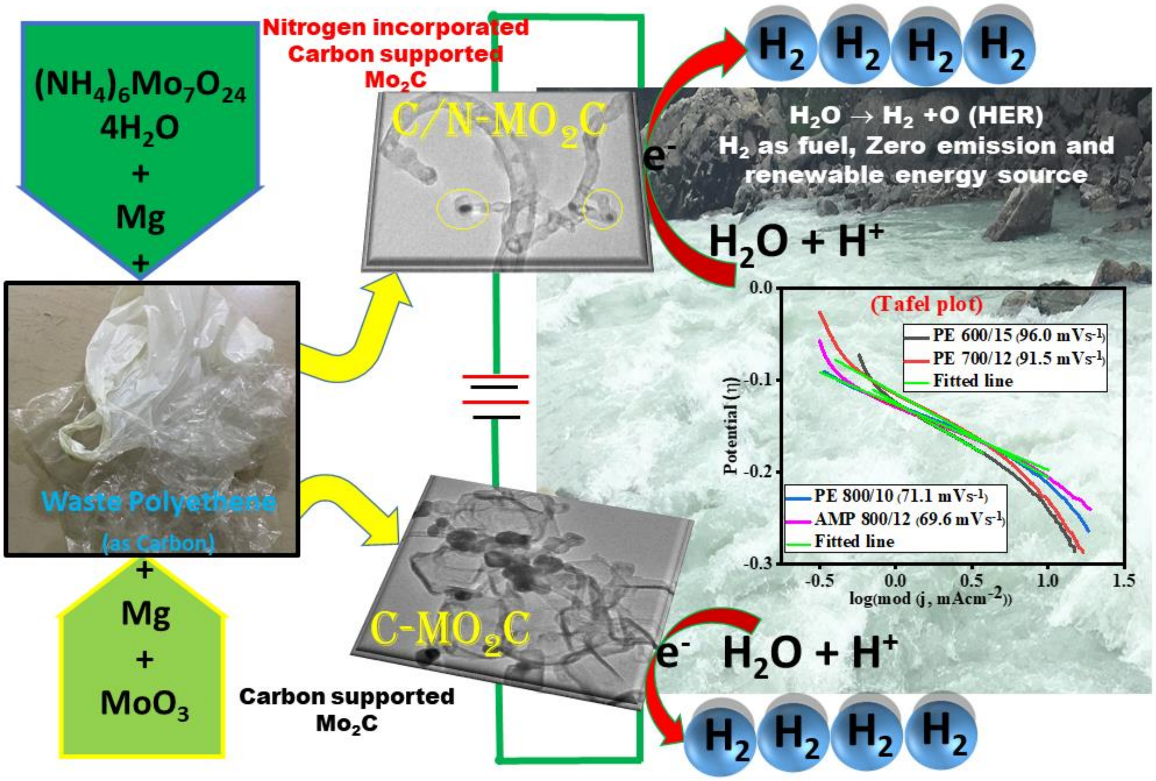

Schematic representation of utilization of waste polyethene for C-Mo_2C and C/N-Mo_2C formation for electrocatalytic applications

6.1 Introduction

Molecular hydrogen (H_2) is considered as the highly efficient, higher energy density and zero carbon emission energy source [1–3]. The production of hydrogen through electrochemical water splitting by hydrogen evolution reaction (HER) is considered as the promising approach for green, non-toxic exhaustion and renewable energy [4,5]. The need of highly efficient and durable electrocatalysts to improve the kinetics of electrochemical water splitting is still prevailing. Extensive research is going on to replace Platinum (Pt) as an efficient electrocatalyst in HER because its low abundance and high cost hinder its commercial use [6]. Worldwide researchers steadfast the efforts to develop and fabricate noble metal free electrocatalysts like transition metal carbides, selenides, sulphides, nitrides, oxides, phosphides etc., to improve HER efficiency [7–16]. Molybdenum carbide (Mo_2C) is an earth abundant and inexpensive replacement for traditional expensive noble metal ectrocatalysts, because its electronic structure near Fermi level resembles with platinum [17,18]. The HER being surface phenomena depends on the size, chemical species on surface and morphology, which depends on method of synthesis [6,19,20]. In case of molybdenum carbide, the crystal phase developed during synthesis plays an important role for electrocatalytic HER activity, β-Mo_2C being the most suitable one [21]. The support of carbon over Mo_2C in various forms like CNTs, graphene, porous carbon etc., not only protect it from corrosion, but also increases the active sites and improves the HER performance [5,22–25]. To improve the charge transfer rate and active sites, the introduction of metal–free elements like nitrogen (N), phosphor (P) and Sulphur (S) within the carbon matrix improves HER activity [26–30]. N encapsulated in carbon over Mo_2C has several advantages compared to other elements [28,31–33] (i) This include tuning of the electronic states of Mo and distribution of the active sites in the desired way, (ii) regulate the electronic structure of carbon skeleton near Fermi level, (iii) prevents unavoidable high temperature agglomeration of particles and (iv) enhance H^+ adsorption/desorption property to improve HER. The synergistic effect of N incorporation in the less resistance network of C encapsulating Mo_2C further shortens the electronic path and enhances the electrochemical activity. The improved electrochemical HER activity of the carbon (C) or nitrogen doped carbon (C/N) support over Mo_2C has broaden the application for energy storage devices like electric double layer, pseudo and super capacitors depending on the interaction of the material surface with electrolyte ions [16,34,35].

The C and C/N supported Mo_2C when synthesized using waste carbon source like polyethene will further reduce the cost of the synthesized product. It will also address the issues related to disposal of these wastes. At present different methods have been adopted to utilize these ployethene wastes into fuel [36,37]. Mostly it include recycling, but the large amount of hazardous gases and requirement of high energy to process it further may cause the environmental and human health issues. Apart from this about 30 % of these carbonaceous wastes are landfilled, which disturb the ecological balance and affect natural species especially waterbodies.

Here in the present work, carbon and nitrogen doped carbon supported Mo_2C (C and C/N supported Mo_2C) have been synthesized in an autoclave at different processing conditions. For the synthesis of C and C/N supported Mo_2C, molybdenum trioxide (MoO_3) and AHM $(NH_4)_6Mo_7O_{24}4H_2O$) has been used as molybdenum and nitrogen incorporated molybdenum source, respectively. Waste polyethene a non-biodegradable waste has been used as carbon source. The present synthesis method is cost effective and eco-friendly because no gas is discharged in atmosphere rather it participate in reaction during synthesis. The synthesized products revealed efficient electrochemical HER performance and suitable promising candidates for fabrication of low cost and durable capacitors.

6.2 Synthesis of C-Mo_2C and C/N-Mo_2C

The synthesis was carried out in the similar way as described in experimental section (Chapter 3). For synthesis of C-Mo_2C and C/N-Mo_2C, MoO_3 and AHM were used as Mo and N/Mo sources, respectively. Waste polyethene was used as carbon source in both the conditions. The synthesis parameters, sample labelling and the phases obtained are given in Table 6.1. The sample labelling in Table 6.1, has been done based on starting materials like (PE temperature/time) for C-Mo_2C and (AMP temperature/time) for C/N-Mo_2C, respectively.

Table 6.1: Sample labelling, synthesis parameters and phase formation.

	Sample Id	**MoO_3 (g)**	**Mg/ Polyethene (g)**	**Temperature (°C)**	**Time (hours)**	**Phases**
C-Mo_2C	**PE 600/10**	1.4394	3.5/1	600	10	Mo, MoO_2, Mo_2C
	PE 700/10	1.4394	3.5/1	700	10	Mo, Mo_2C
	PE 800/10	1.4394	3.5/1	800	10	Mo_2C
	PE 600/12	1.4394	3.5/1	600	12	Mo, Mo_2C
	PE 600/15	1.4394	3.5/1	600	15	Mo_2C
	PE 700/12	1.4394	3.5/1	700	12	Mo_2C
	PE 800/8	1.4394	3.5/1	800	8	Mo, $Mo_{0.42}C_{0.58}$, Mo_2C
C/N-Mo_2C	**Sample id**	**AHM (g)**	**Mg/ Polyethene (g)**	**Temperature (°C)**	**Time (hours)**	**Phases**
	AMP 600/10	1.258	3.5/1	600	10	MoO_2, MoC
	AMP 700/10	1.258	3.5/1	700	10	MoO_2, MoC, Mo_2C
	AMP 800/10	1.258	3.5/1	800	10	MoO_2, $Mo_{0.42}C_{0.58}$, Mo_2C
	AMP 800/12	1.258	3.5/1	800	12	Mo_2C
	AMP 800/8	1.258	3.5/1	800	8	MoO_2, $Mo_{0.42}C_{0.58}$, Mo_2C

6.3 Results and discussion

6.3.1 X-ray diffraction (XRD)

The carbon supported Mo_2C (C-Mo_2C) has been synthesized at 600, 700 and 800 °C for the reaction duration of 15, 12 and 10 hours, respectively as shown in XRD pattern (Fig. 6.1). The reaction time and temperature affects the phase formation of Mo_2C inside the autoclave in presence of Mg and carbon [38,39]. The effect of reaction temperature at a fixed reaction time of 10 hours on phase formation is shown in Fig. 6.2a. The reaction time also plays vital role for phase formation. The effect of reaction time at particular temperature is depicted in Fig. 6.2b-d, respectively. The hydro-carbon chain of polyethene induces fast carburization due to production of more carburizing gases and enhances the reduction-carburization of MoO_3 to Mo_2C at relatively lower temperature. Moreover, the phase formation at lower reaction temperature takes more time to accomplish carburation. The lower chain hydro-carbon species (polyethene) enhances the carburization even at low temperatures as compared to higher chain substituents [40].

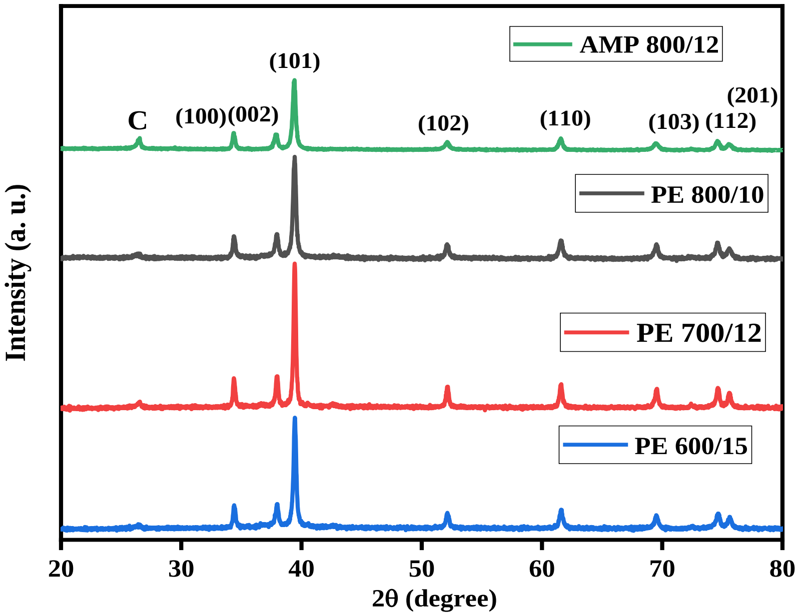

Figure 6.1: XRD pattern of pure phase Mo_2C syntheizesed at different temperatures and time.

The results reveal that the diffusion of C in Mo lattice is slow at lower temperature, whereas at higher temperatures due to higher kinetic energy of molecules and high pressure, the diffusion is very rapid and favors the carburization less time. Using the same polyethene as carbon source, C/N-Mo_2C was synthesized at 800 °C (AMP 800/12) for a reaction time of 12 hours. The XRD pattern of the synthesized pure phase C/N supported Mo_2C is shown in Fig. 6.1.

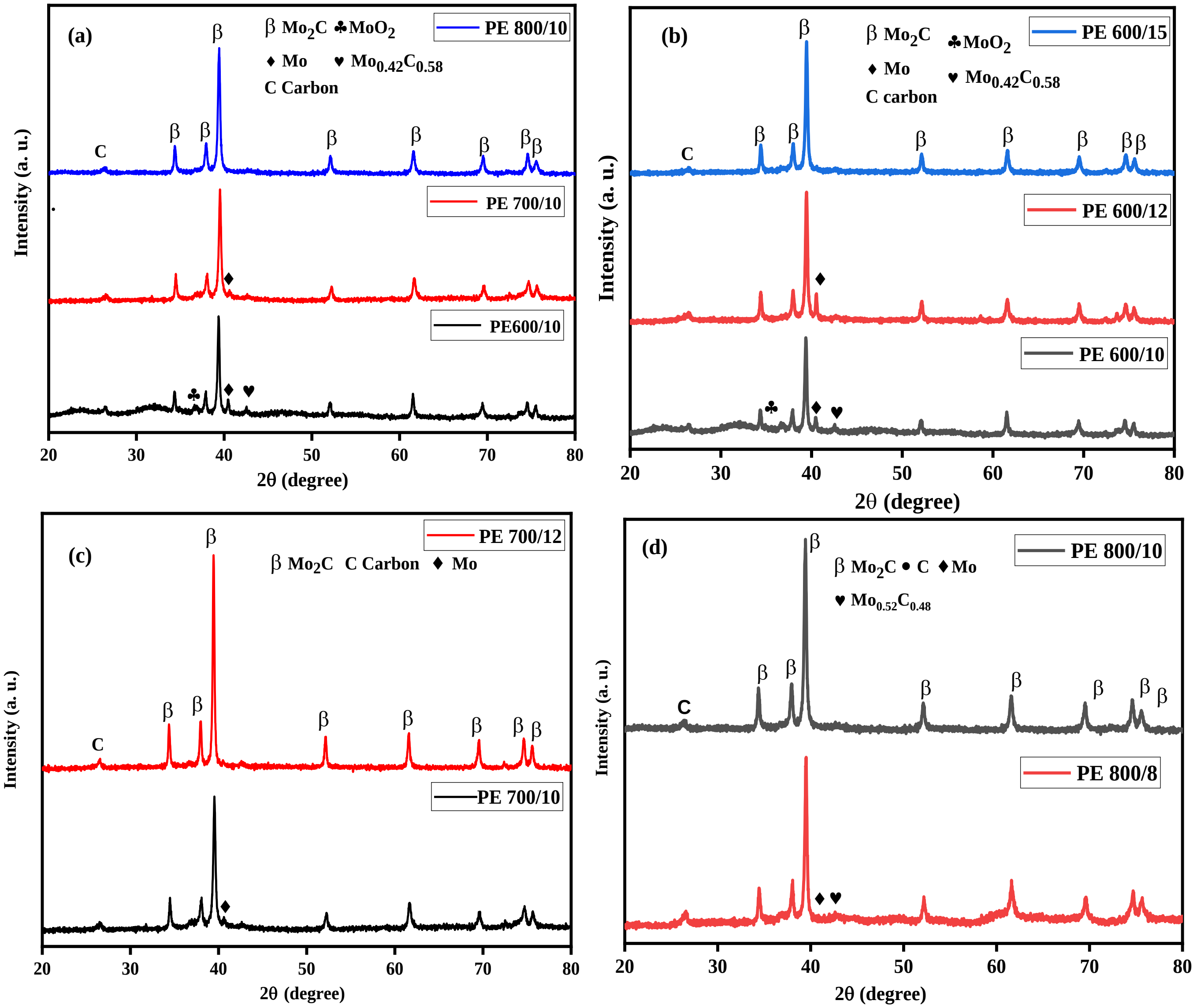

Figure 6.2: XRD pattern of C-Mo_2C (a) variation in temperature at fixed time, (b) variation in time at 600 °C, (c) 700 °C and (d) 800 °C.

The reaction temperature and time also facilitate the reduction and carburization of AHM to C/N-Mo_2C in presence of Mg in an autoclave. The effect of reaction temperature and time again shows prominent role on pure phase formation (Fig. 6.3a-b). The relatively lower temperature 600 and 700 °C could not lead to pure phase formation of Mo_2C. This could be the reason of complex reduction reactions occurring during decomposition of AHM. Sidana *et al.* [41] predicted the formation of MoO_x (x=2-3) as a resultant compound during heating AHM in presence of reducing agent. Due to different reaction byproducts produced during decomposition of AHM and simultaneous carburization, the reaction accomplished even at 800 °C for the longer duration as compared to those prepared using MoO_3 as molybdenum source. The insufficient carburization attained at relatively lower temperature (600 and 700 °C) might be the result of insufficient amount of carburizing gases, which helps in reduction of MoO_x species to get it simultaneously carburized to form Mo_2C. The crystallite size calculated from XRD analysis using Scherer criterion [42,43] for pure phase Mo_2C is 75.35, 80.59, 62.2 and 50.0 nm for PE 600/15, PE 700/12, PE 800/10 and AMP 800/12, respectively. The results show a decrease in crystallite size with increase in temperature. The presence of H_2O in AHM further helps to reduce the size as compared to those prepared from MoO_3.

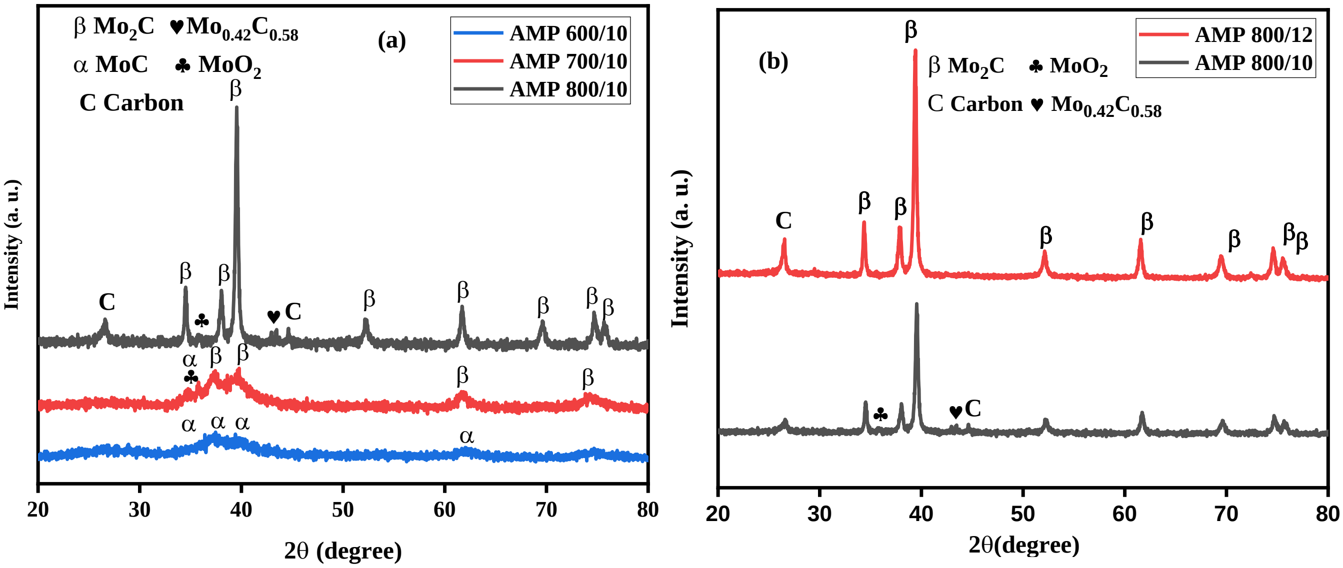

Figure 6.3: XRD pattern of variation of temperature and time using AHM ($(NH_4)_6Mo_7O_{24}4H_2O$) as molybdenum source (C/N-Mo_2C), (a) variation of temperature at fixed time and (b) variation of time at 800 °C.

6.3.2 Morphological Features

The morphological features of the synthesized samples are characterized by TEM/HRTEM shown in Fig 6.4-6.7. The TEM micrograph of sample (C-Mo_2C) PE 600/15 (Fig. 6.4a) exhibits the presence of nano Mo_2C particles embedded in carbon cloth. Fig. 6.4b confirms the phase formation of Mo_2C and surface graphitic carbon in agreement with ICDD pattern (035-0787) and (001-0640), respectively. The synthesized sample (PE 600/15) shows stacking of layered structures as depicted in Fig 6.4c-d. Figure 6.5a reveals the presence of stacked carbon flakes encapsulating the Mo_2C particles. The HRTEM (Fig. 6.5b) confirm the pure phase formation of Mo_2C and the carbon flakes resemble to that of graphene [44,45]. The transparency of the graphitic layer in PE 700/12 reveals that the layer number decreases with increase in temperature [46].

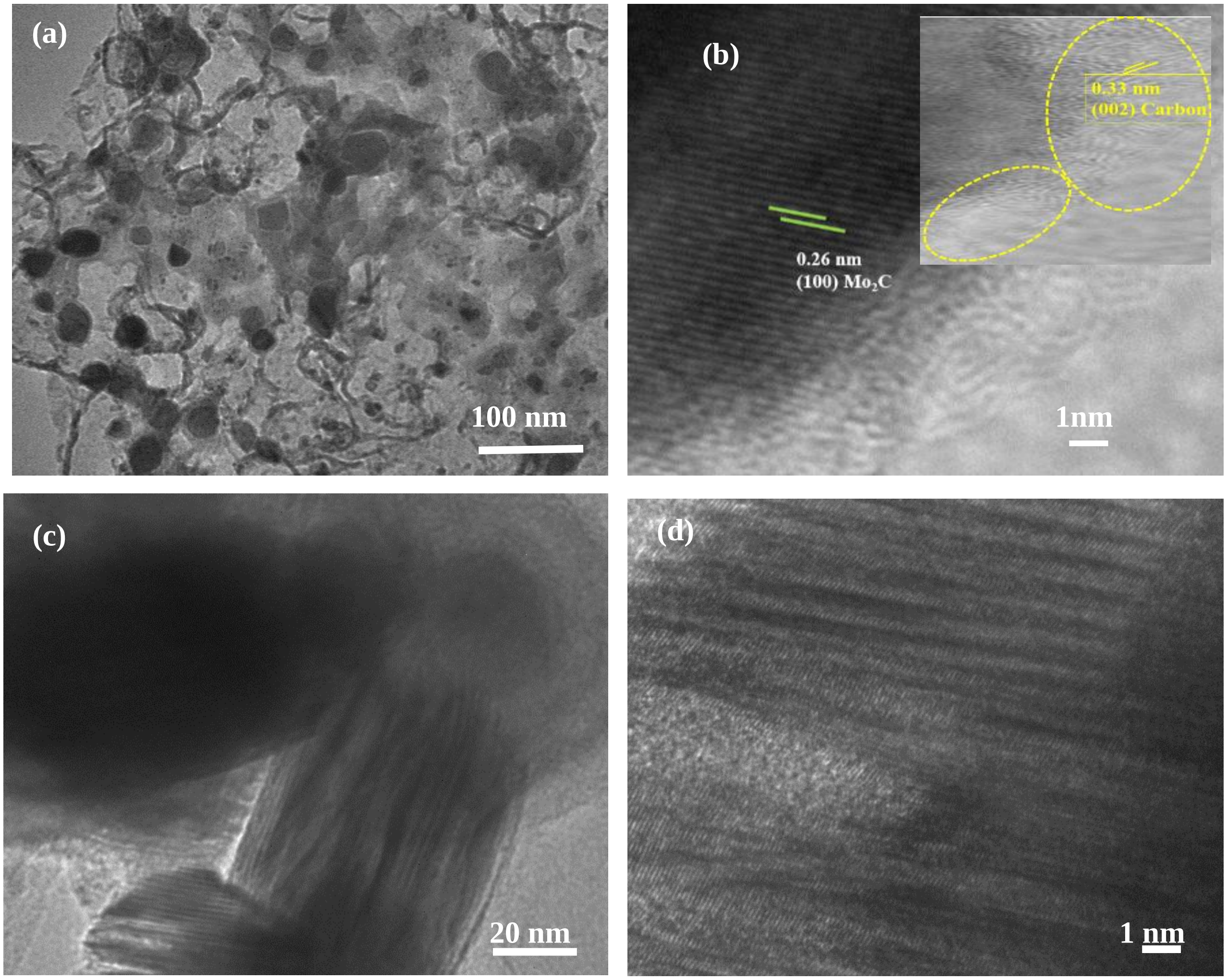

Figure 6.4: TEM micrograph of PE 600/15 (a) showing particle agglomeration in carbon cloth, and (b) HRTEM lattice fringing of Mo_2C and carbon (ICDD pattern -035-0787 and -001-0640), (c) stacking of layers and (d) HR TEM showing layered structures.

The TEM micrographs of Mo_2C phase synthesized at 700 °C (PE 700/12) is shown in Fig. 6.5a-b. The stacking of these layers is less dense and more transparent in PE 700/12 as compared to that of PE 600/15. The TEM micrographs of sample PE 800/10 are shown in Fig. 6.6a-d. The TEM image (Fig. 6.6a-b) reveals the formation of faceted Mo_2C structures embedded in the graphite/graphene flakes. The formation of Mo_2C (Fig. 6.6c) and conductive graphitic nature of carbon (Fig. 6.6d) has been confirmed by HRTEM. The in-situ developed graphene support over Mo_2C helps in achieving better electrochemical properties [47]. The TEM/ HRTEM micrographs of N/C-Mo_2C (AMP 800/12) are shown in Fig. 6.7a-d. The N/C supported Mo_2C (Fig. 6.7a) shows formation of curved graphene encapsulating the agglomerated structures.

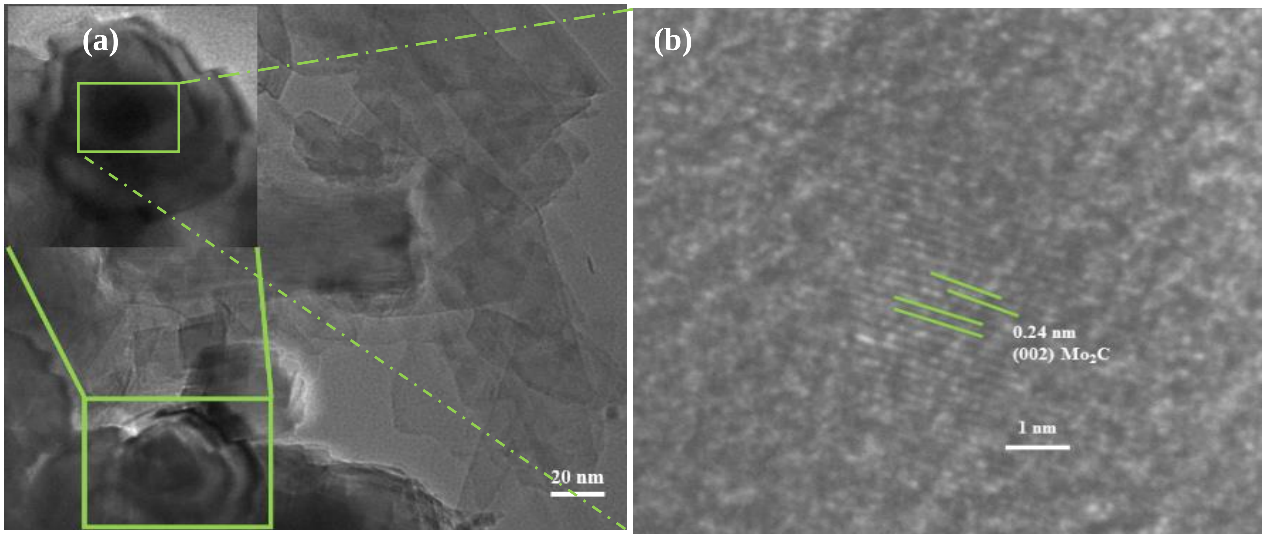

Figure 6.5: TEM micrograph of PE 700/12 (a) faceted structure of carbon have caged Mo_2C particles and (b) HRTEM lattice fringes of Mo_2C (ICDD pattern-035-0787)

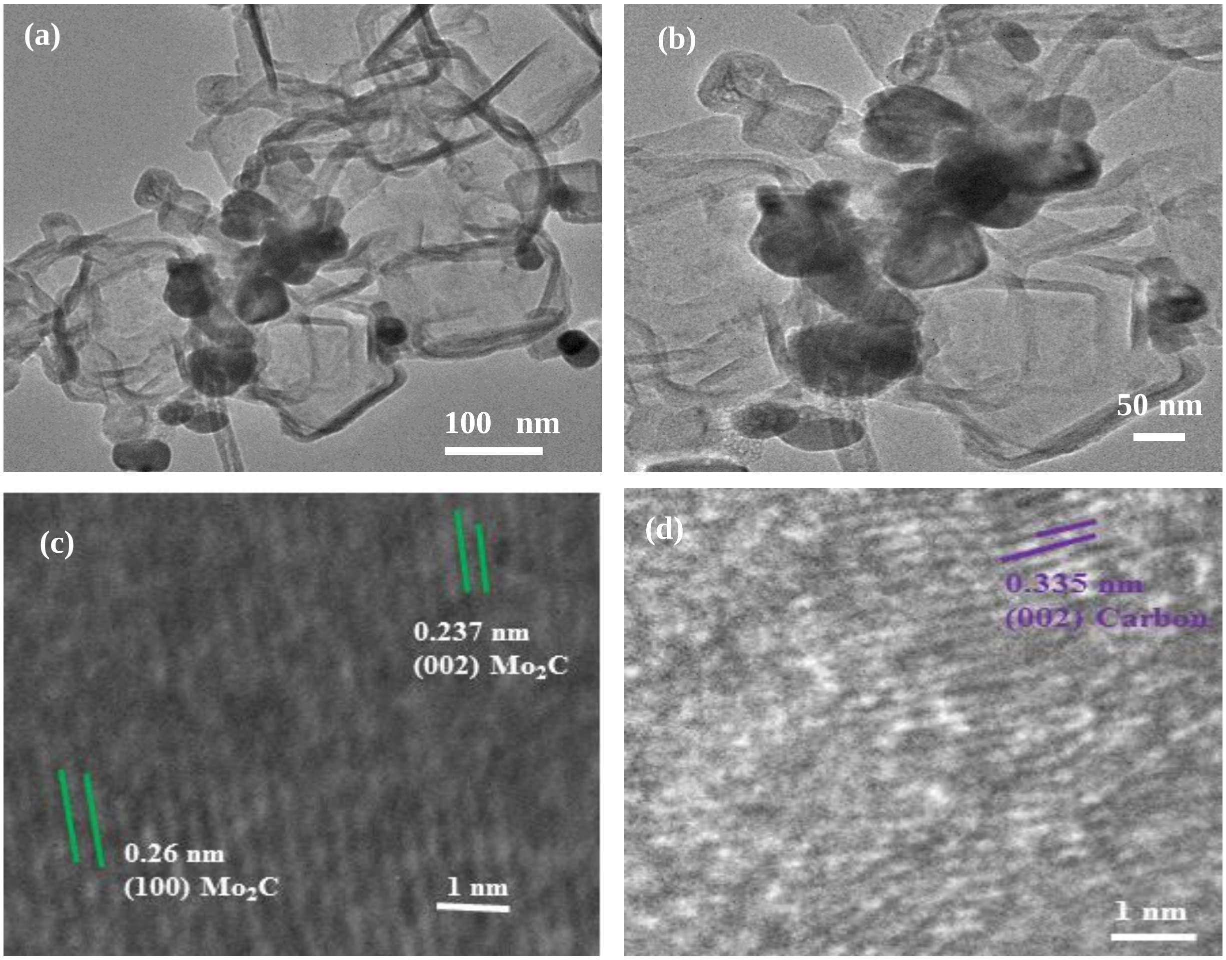

Figure 6.6: TEM micrograph of PE 800/10 (a) and (b) showing faceted morphology of Mo_2C particles interlinked in graphite/graphene flakes, (c) and (d) HRTEM lattice fringing of Mo_2C and graphitic carbon consistent with ICDD pattern-035-0787 and -001-0640, respectively.

The particles are highly agglomerated and are embedded in the connected mesh of carbon as depicted in Fig. 6.7b. However, the Fig. 6.7c, shows the formation of bamboo like tubular structures incorporating the Mo_2C particle. The tube like structure might have formed because of rolling and bending of graphene sheets at relatively higher temperatures. The HRTEM (Fig. 6.7d) and magnified image is (Fig. 6.8) attributes to the formation of Mo_2C and graphitic carbon. The results reveal that with increase in temperature, the formation of graphitic and graphene formation increases. The low temperature synthesized phase shows less agglomeration compared to those synthesized at relatively higher temperatures. To confirm the incorporation of N in the synthesized structures, the scanning tunneling electron microscopy (STEM) was done as shown in Fig. 6.9a-f. The STEM micrographs show uniform elemental distribution N in C matric encapsulating the Mo particles. The presence N in the carbon matrix coated over Mo_2C contributes efficiently for electrochemical applications.

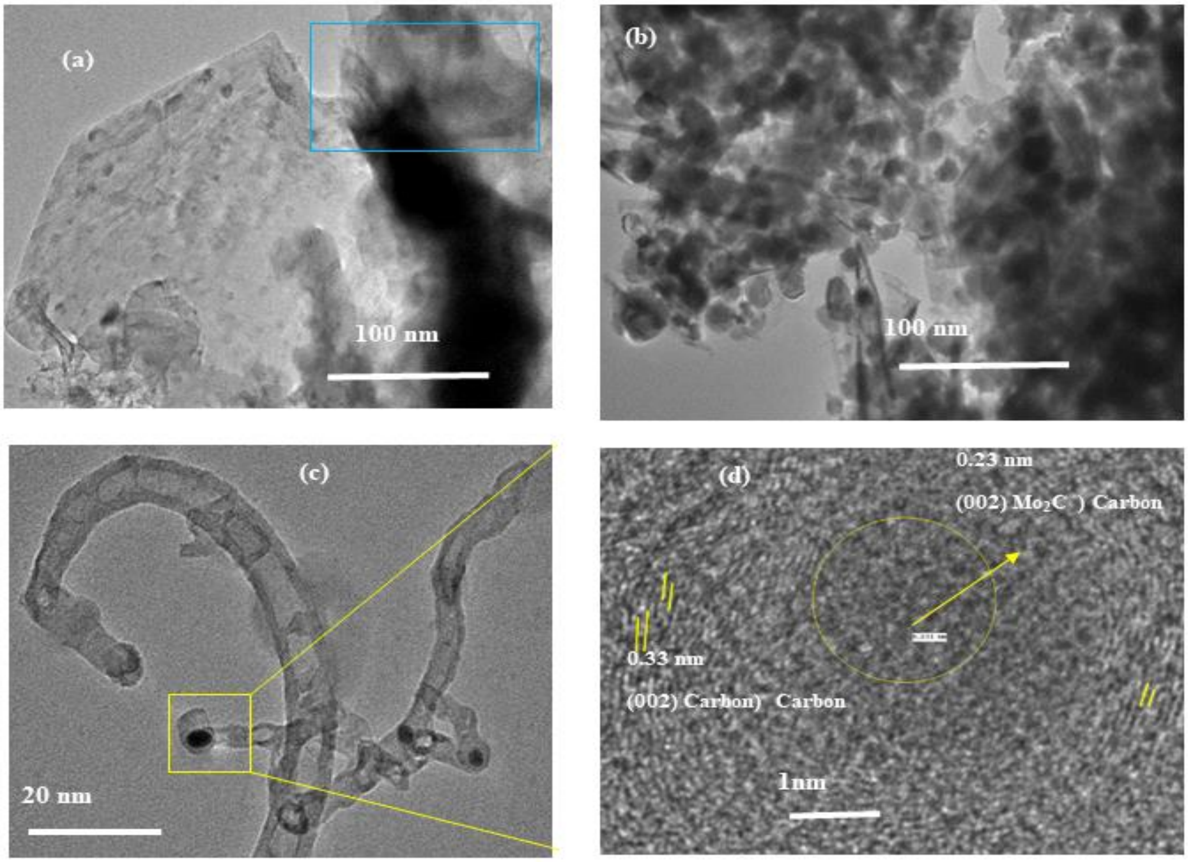

Figure 6.7: TEM micrograph of AMP 800/12 (a) showing particle high agglomeration of particles and formation of curved graphene sheet incorporating particles (b) carbon coated interlinked Mo_2C particles, (c) Mo_2C particle encapsulated in tubular bamboo like carbon structure and (d) HRTEM confirming lattice fringes of Mo_2C (ICDD pattern -035-0787 and graphitic carbon (ICDD pattern -001-0640).

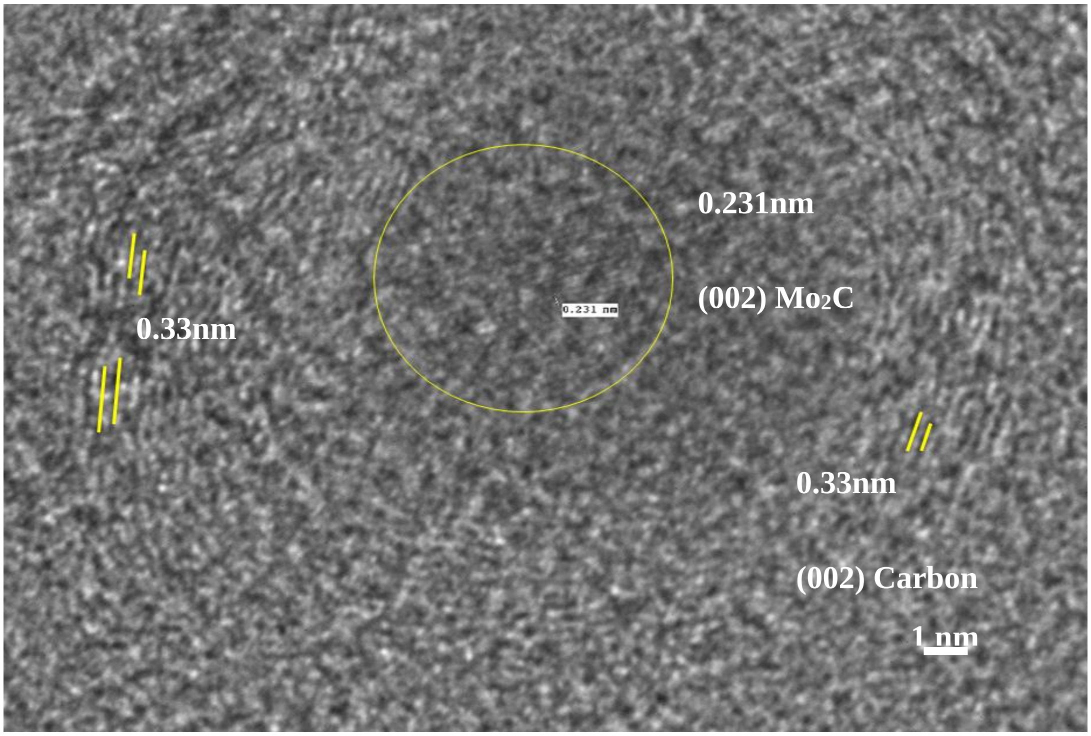

Figure 6.8: Magnified view of HRTEM of AMP 800/12**.**

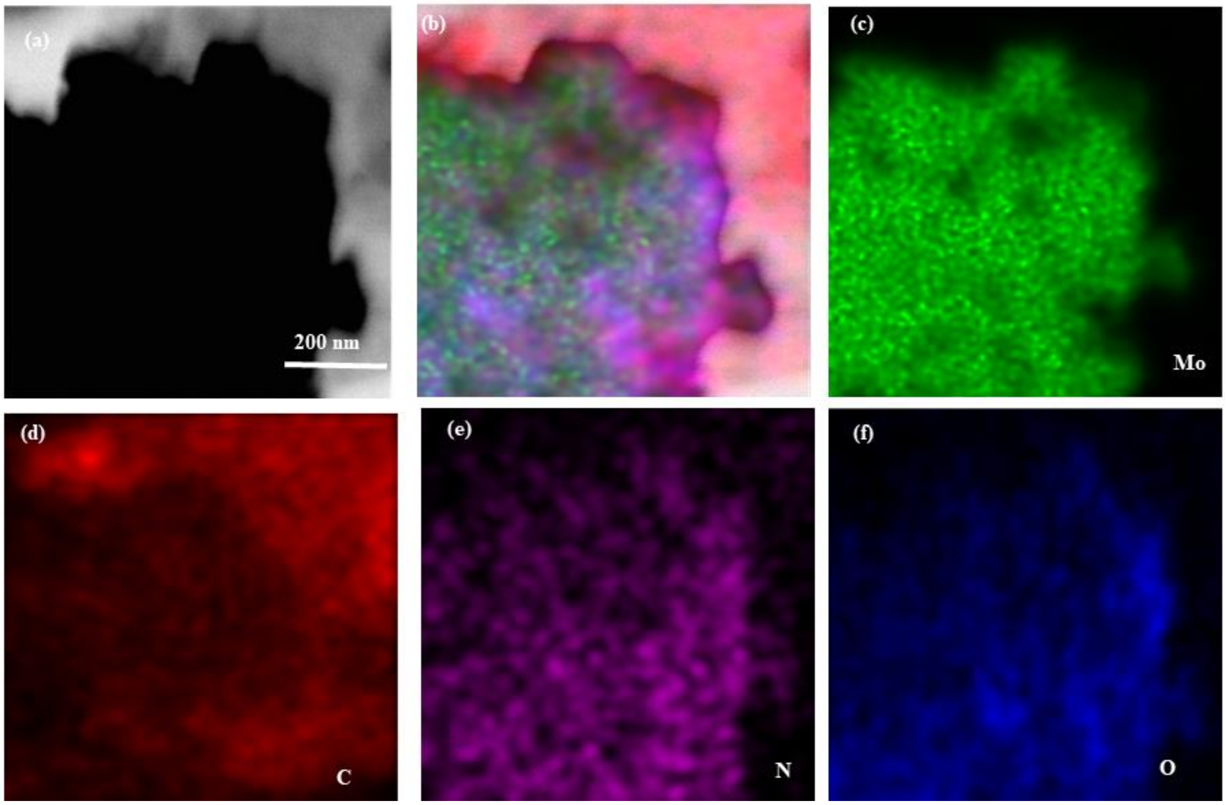

Figure 6.9: STEM micrograph of AMP 800/12 confirming the presence of nitrogen (N): (a) TEM micrograph, (b) survey mapping, (c) elemental molybdenum (Mo), (d) carbon (C), (e) nitrogen (N) and (f) oxygen (O).

6.3.3 Raman Spectroscopy

Raman spectroscopy is the sensitive tool used to get valuable information about the carbon structures. The Raman spectroscopy results of the synthesized samples are shown in Fig. 6.10-6.12, respectively. The Raman spectra of pure phase C-Mo_2C (Fig. 6.10 and Fig. 6.11a-d) signifies D, G and 2D bands at positions given in Table 6.2. The D band corresponds to disorder, G band attributes to graphitization and 2D band indicates the distinct order in the sample structures [48]. The lower value of I_D/I_G (Table 6.2) for carbon supported pure phase Mo_2C PE 800/10 compared to PE 700/12 and PE 600/15 attributes to the growth of graphitized carbon structures with temperature (Fig. 6.10). The increase in I_D/I_G value with time at a particular temperature is given in Table 6.2.

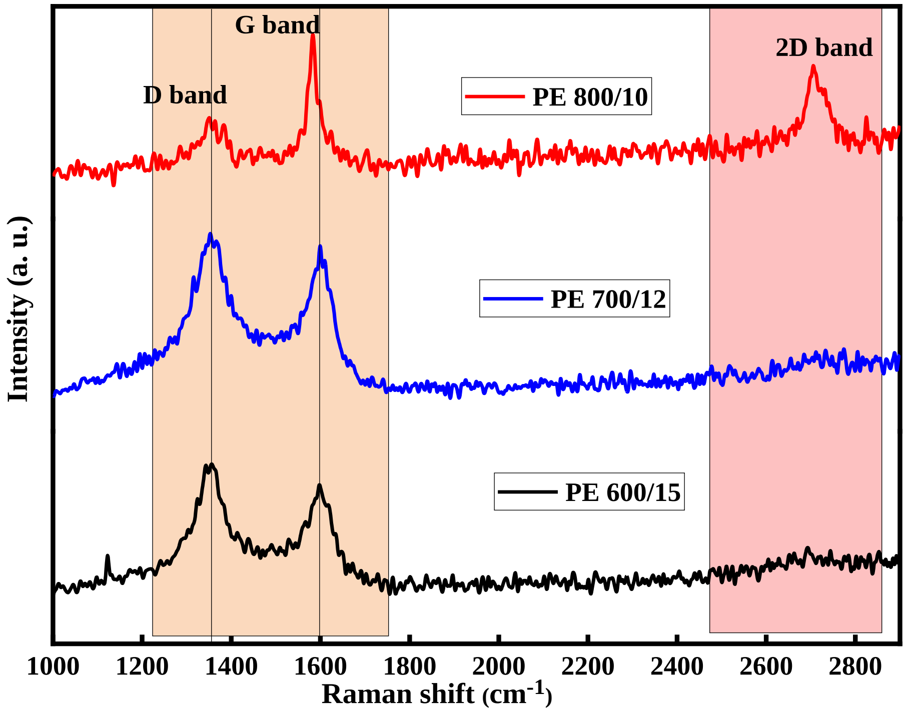

Figure 6.10: Raman spectra of pure phase C-Mo_2C samples.

The crystallinity of carbon layer is more prone to synthesis temperature than time as shown in Fig 6.11a-d and tabulated in Table 6.2. The graphitization increases with reaction temperature at a fixed reaction time (Fig. 6.11a). Lower graphitization was obtained at relatively lower temperature 600 °C although the reaction time varied from 12-15 h (Fig. 11b). However, the graphitization of carbon at 700 and 800 °C represented in Fig. 11c and d, enhances with phase formations as compared to that obtained at 600 °C. The corresponding peak positions and degree of graphitization is tabulated in Table 6.2.

Table 6.2: Raman analysis parameters of the synthesized samples.

Sample Id	D-band (cm^{-1})	G-band (cm^{-1})	2D-band (cm^{-1})	I_D/I_G
PE 800/10	1359.57	1587.19	2705.17	0.65
PE 700/12	1355.57	1605.59	--	1.13
PE 600/15	1348.03	1598.34	--	1.12
PE 600/10	1359.49	1594.73	--	0.82
PE 600/12	1355.26	1594.73	--	0.82
PE 700/10	1366.73	1601.96	--	0.90
PE 800/1	1359.249	1591.11	--	1.06
PE 800/5	1355.57	1598.3	--	1.04
PE 800/8	1351.95	1598.34	2712.4	0.96
AMP 600/10	1352.25	1594.73	--	0.95
AMP 700/10	1355.57	1591.11	--	0.86
AMP 800/10	1363.11	1583.57	2723.57	0.59
AMP 800/12	1363.11	1579.95	2741.97	0.50
AMP 800/8	1364.72	1581.74	2717.64	0.91

The shift of G-band from lower frequency to higher frequency and again to lower frequency with temperature attributes to the transformation of distorted carbon to nano crystalline graphite to perfectly graphitic carbon respectively [49]. Moreover, the presence of 2D peak in PE 800/10 confirms the formation of layered structures (graphene/graphene) at relatively higher temperature [50]. The formation of more graphite/graphene for the same is also been confirmed by TEM. The broad and splitting in 2D peak (Fig. 6.10a) reveals the formation of multilayer graphitic carbon structure. The relative intensity of 2D band with respect to G-band and the shape of 2D reveals transformation of multi-layer graphene to graphite. The formation of graphite enhanced with reaction time (≥ 8 hours) at 800 °C (Fig. 6.11d). The Raman spectra of synthesized samples (C/N-Mo_2C), reveals the increase in crystallinity of graphitic carbon with respect to temperature evidenced by I_D/I_G values summarized in (Table 6.2) and the corresponding Raman pattern is shown in Fig. 6.12.

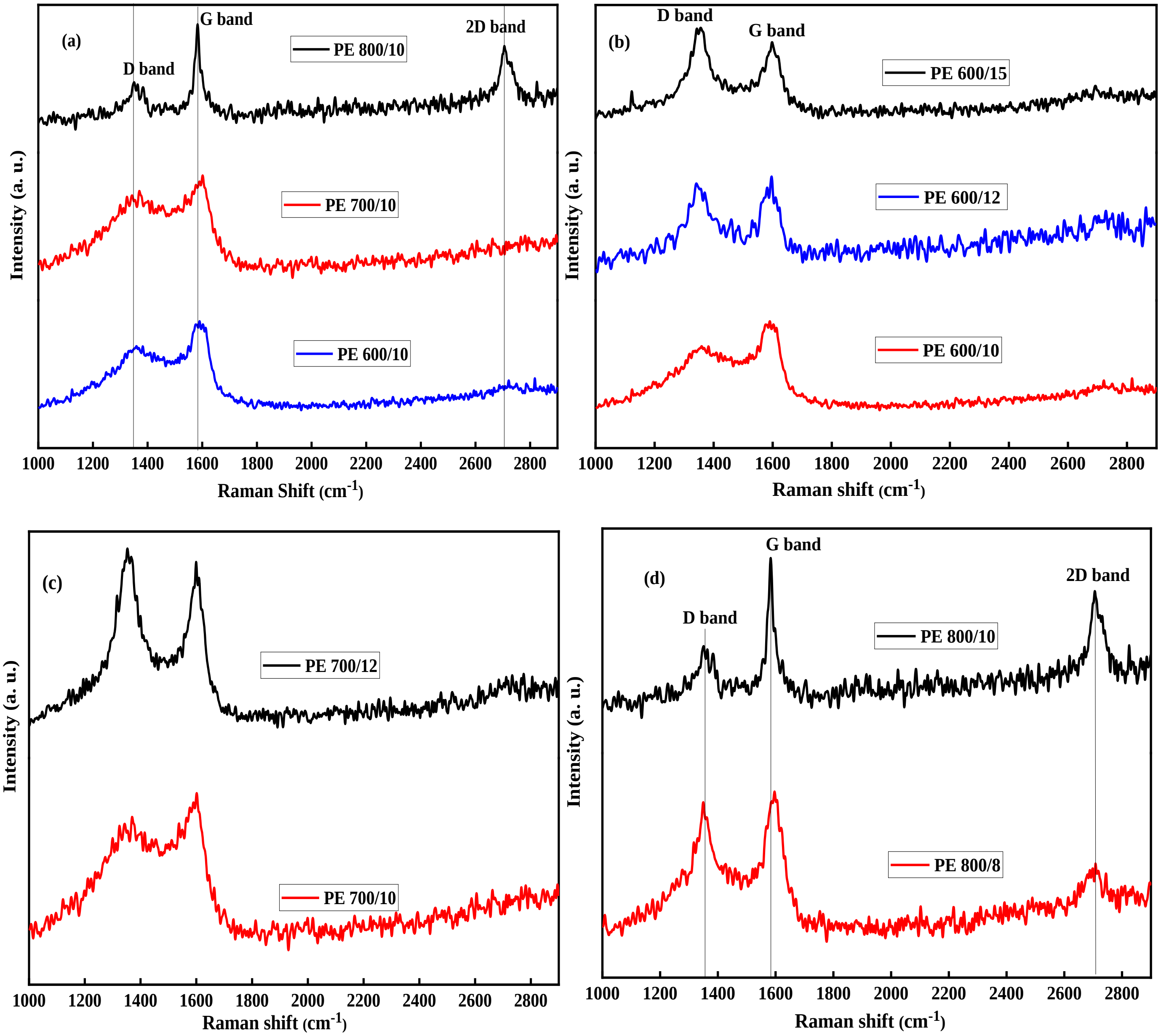

Figure 6.11: Raman spectroscopy results of C-Mo_2C with variation in temperature and time using MoO_3 as molybdenum source (a) Variation of temperature at fixed time, (b) variation of time at 600 °C, (c) 700 °C and (d) 800 °C.

The higher amount of graphitic carbon has been observed in pure phase C/N-Mo_2C, which has been also confirmed by very narrow Raman peaks as depicted in Fig. 6.12. The existence of broad 2D band at 800 °C for samples (AMP 800/8, 10 and 12) reveals the formation of multilayer graphite structures [48]. The formation of graphitic/graphene nature of carbon improved with the incorporation of nitrogen and higher water content in the surface carbon [49,51]. The number of graphene layer increases with time at 800 °C as is confirmed by widening and splitting of 2D peak as shown in Fig. 6.12. The redshift of 2D band reveals the formation of highly oriented pyrolytic graphite (HOPG) [52].

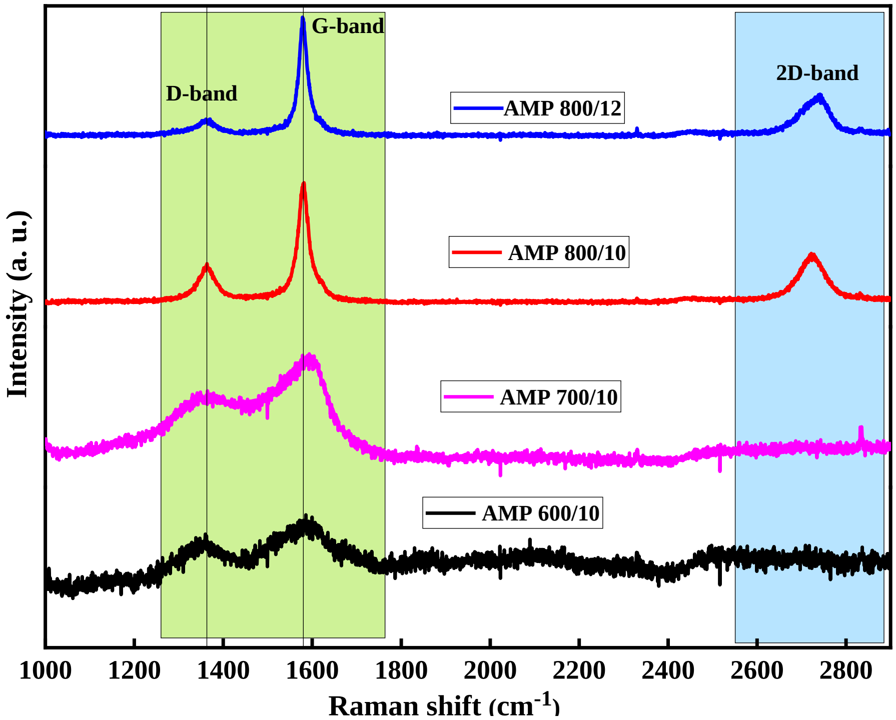

Figure 6.12: Raman spectra of C/N-Mo_2C samples.

The strain analysis of pure phase C-Mo_2C samples (PE 800/10, PE 700/12 and PE 600/15) was done by the shift in Raman peak positions. The shifting of the disordered Raman band determines that the strain is not uniaxial [53]. The lower side shift of D-band for relatively lower temperature 600 °C as given in Table 6.2 corresponds to more tensile strain defects in comparison to those synthesized at higher temperatures. The blue shift of G-band in PE 800/10 with respect to PE 700/12 and PE 600/15 reveals the lowering of distance between C-C and strengthening of the C-C bond [54] . The higher stretching in PE 700/12 and PE 600/15 has been confirmed by presence of G-band near to 1600 cm^{-1}. The shift in G-band might also correspond to the pressure generated inside the autoclave introducing the disordered state of the synthesized samples. The narrowing of Raman peaks also correspond to decrease in strain with increase in temperature as shown in Fig. 6.10 and 6.12, respectively. The presence of D band at lower frequency with respect to AMP 800/12 shows the more tensile strain in the samples synthesized at 700 and 600 °C, respectively. The peak pattern of D-band in AMP 800/12 compared to AMP 800/10 reveals lower strained state of C/N-Mo_2C.

6.3.4 X-ray photoelectron spectroscopy (XPS)

In the pure phase PE 800/10 and AMP 800/12, C and C/N supported Mo_2C were further selected to analyze the surface composition and electronic structure via X-ray photoelectron spectroscopy (XPS). The survey spectrum of PE 800/10 and AMP 800/12 as shown in Fig. 6.13 implies that the as-prepared product consists of Mo, C, O and Mo, C, N, O, respectively. The survey spectrum of XPS represents the presence of Mo3d, C1s, Mo3p and O1s at positions (231.2 & 530.7), (284 & 283.7), (397.1 & 414.5), (529.4 & 529.5) eV for PE 800/10 and AMP 800/12, respectively. The Mo3p and N1s peak overlap at the same positions. For the nitrogen incorporated samples AMP 800/12, the N1s peak is designated at 397.6 and Mo3p, which can be bonding of Mo-N also at 414.6 eV.

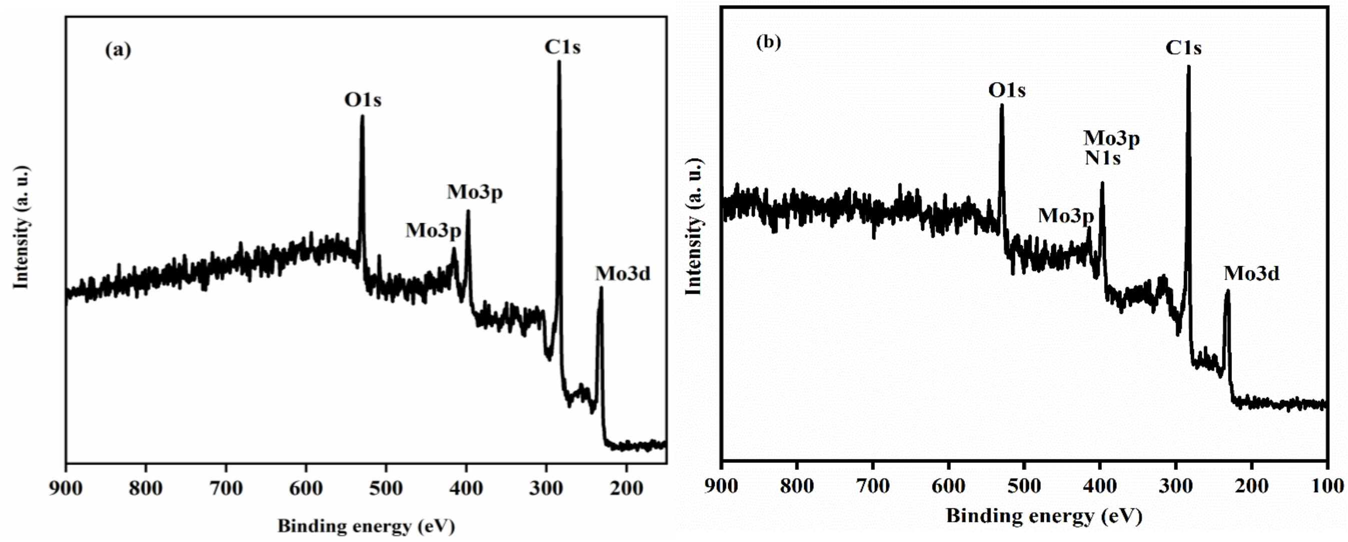

Figure 6.13: XPS Survey spectra of (a) PE 800/10 (C-Mo_2C) and (b) AMP 800/12 (C/N-Mo_2C).

The peak position of Mo3p and N1s spectra usually overlap due to same binding energies. The Mo3d spectrum (Fig. 6.14a and b) can be divided to four and six peaks for PE 800/10 and AMP 800/12 respectively. The peaks at (228.3 & 231.1 eV) in case of PE 800/10 and (227.8 & 231.1 eV) for AMP 800/12 correspond to Mo_2C (Fig. 6.14a-b). The peaks at (232.7 & 235.7 eV) in PE 800/10 and (232.0 & 235.2 eV) in case of AMP 800/12 attributes to Mo3p5/2 and Mo3p3/2 for Mo (VI) state of molybdenum oxide formed due to inevitable oxidation during XPS process exposing in air [55]. The additional peaks at 233.1 and 236.1 eV can be assigned to Mo (IV) and Mo (VI) state of molybdenum oxide is also in accordance with oxidation during XPS analysis (Fig. 6.14b) [5,56].

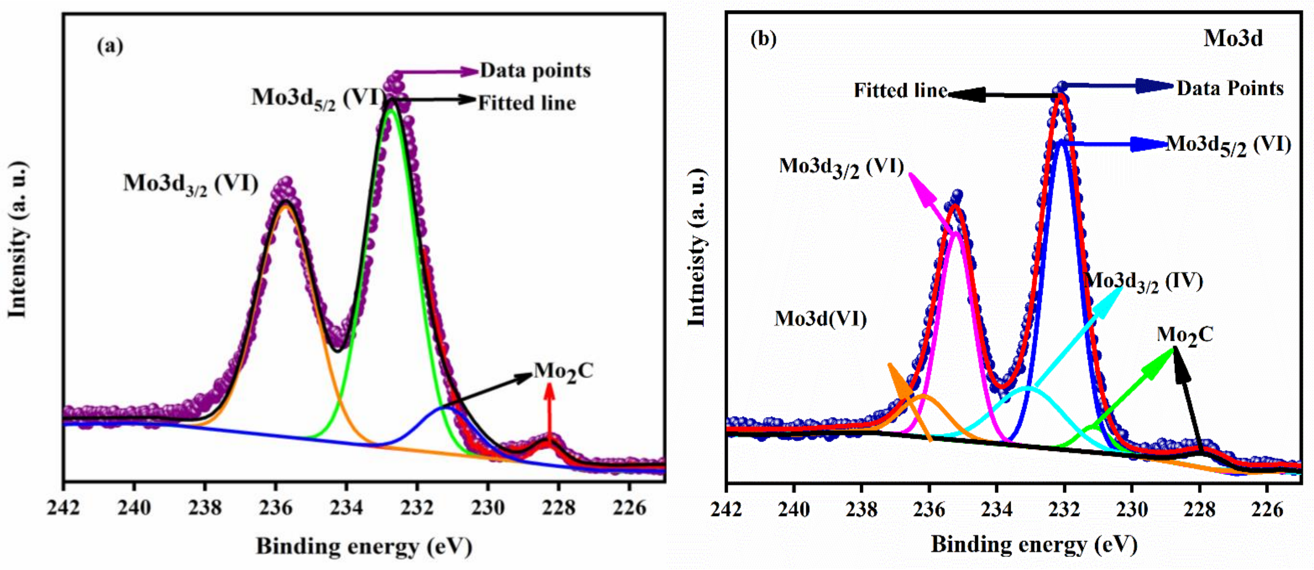

Figure 6.14: XPS pattern of (a) Mo3d of C-Mo_2C (PE 800/10) and (b) Mo3d pattern of C/N-Mo_2C (AMP 800/12).

From fitted pattern of C1s (Fig. 6.15a) three peaks located at positions 283.5, 284.3, and 285.1 eV) suggest the successful formation of Mo_2C, presence of free carbon and oxygen containing functional groups on the surface [28,57]. The main peak of carbon at 284.0 eV in AMP 800/12 (Fig. 6.15b) inhibits the peak corresponding to Mo_2C because of similar binding energies [58]. The other two peaks (284.5 and 287.2 eV) again show the presence of oxide species on the surface [28]. The clarification of nitrogen content in different forms within the synthesized sample (AMP 800/12) was also confirmed as shown in Fig. 6.15c. The N1s spectrum was fitted to five peaks at positions 395.9, 397.8, 399.3, and (400.6 & 401.5 eV) assigned to Mo3p state (may be Mo-N), pyridinic N, pyrolic N and Quaternary N (graphitic-N), respectively [21,31]. The high ratio of pyridinic N has been considered to be useful for the electrocatalytic activity C/N-Mo_2C. Consequently, the HRTEM, XRD and XPS results confirm the phase formation of Mo_2C. The O1s spectrum for both PE 800/10 and AMP 800/12 is shown in Fig. 6.16a-b, respectively. The spectrum confirms the presence of Mo-O and C-O, C=O species formed due to surface oxidation. The peak at positions (530.3 & 529.9 eV), (530.7 eV) and (532.3 and 532.2 eV) in both PE 800/10 (Fig. 6.16a) and AMP 800/12 (6.16b) correspond to Mo-O and C-O, respectively. The additional peaks in PE 800/10 at 533.4 and 534.2 eV attributed to C=O, as shown in Fig. 6.16a.

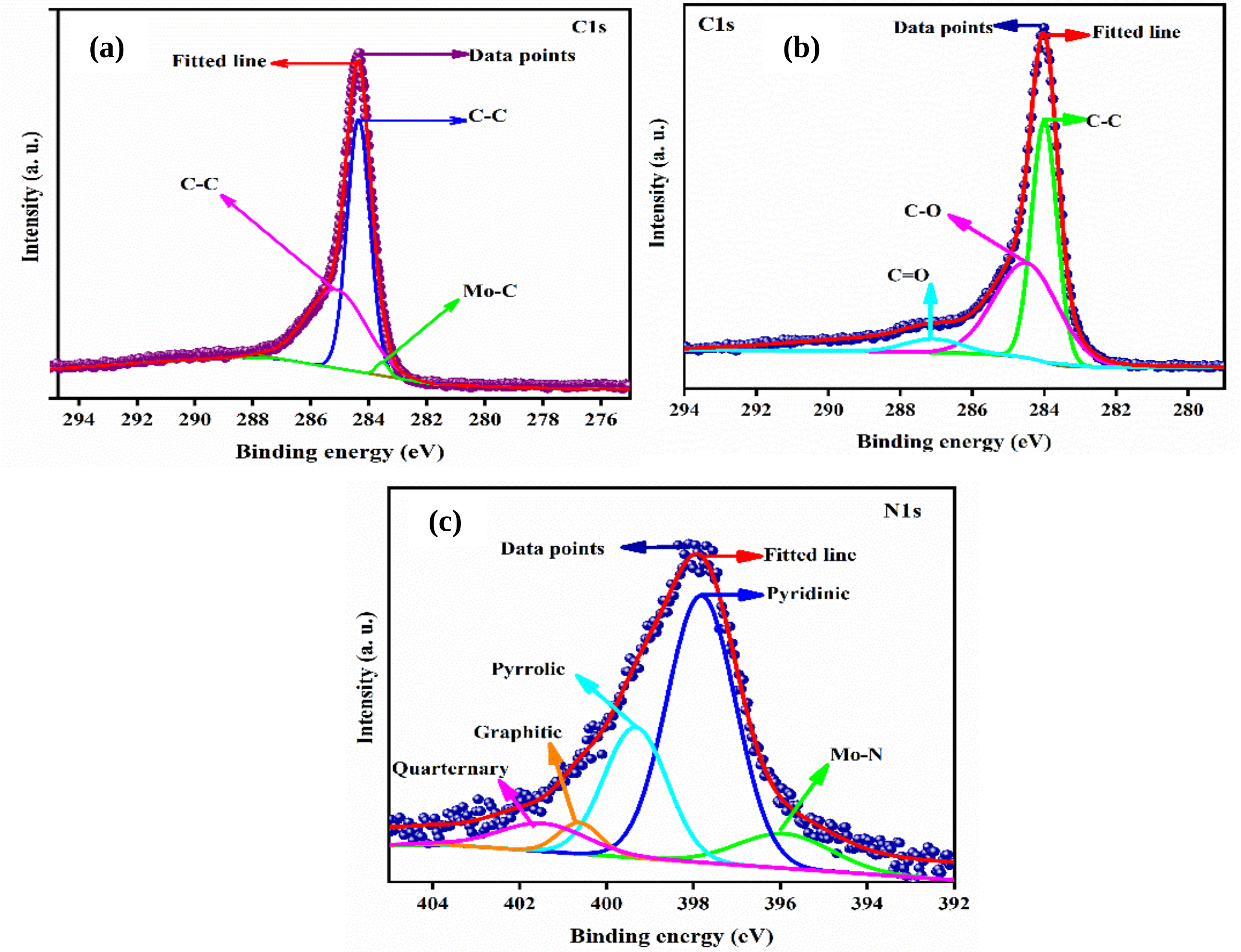

Figure 6.15: XPS pattern of (a) C1s (C-Mo_2C), (b) C1s (C/N-Mo_2C) and (c) N1s of C/N-Mo_2C.

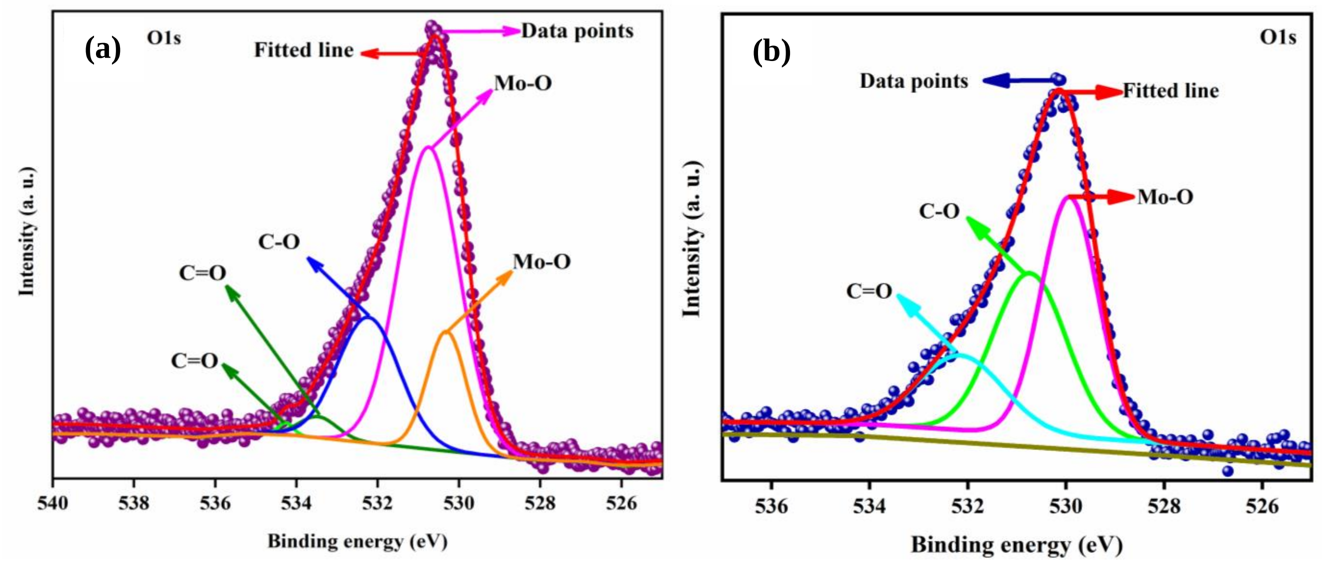

Figure 6.16: High resolution (HR) XPS spectra of (c) O1s (PE 800/10) and (d) O1s (AMP 800/12).

6.4. Electrochemical studies

6.4.1 HER activity

The elctrocatalytic HER activity of the pure phase synthesized samples (C-Mo_2C) and (C/N-Mo_2C) have been studied to compare the effect of N incorporation in carbon matrix over Mo_2C. The linear sweep voltammetry (LSV) polarization curves of the synthesized samples are shown in Fig. 6.17. The polarization curves of pure phase C-Mo_2C and C/N-Mo_2C as depicted in Fig. 6.17 revealed the higher current response for a low potential as compared to reported literature [55,59]. The higher current density value was observed for Mo_2C incorporated in C/N network (AMP 800/12) as compared to carbon encapsulated Mo_2C (C-Mo_2C). The higher current density corresponds to nitrogen doping in the carbon network, which enhances the active sites for electron transfer [28]. This also attributes to higher graphitic/ graphene carbon network, which provides higher conducting surface for electron transfer [5]. The current density C-Mo_2C (Fig. 6.17) increases with increase in synthesis temperature. This corresponds to more crystallization of the product and carbon (graphite/graphene) observed by Raman analysis and faceted morphological features observed in TEM. The higher current density of PE 800/10 and AMP 800/12 also correspond to their lower crystallite size compared to PE 700/12 and PE 600/15, respectively.

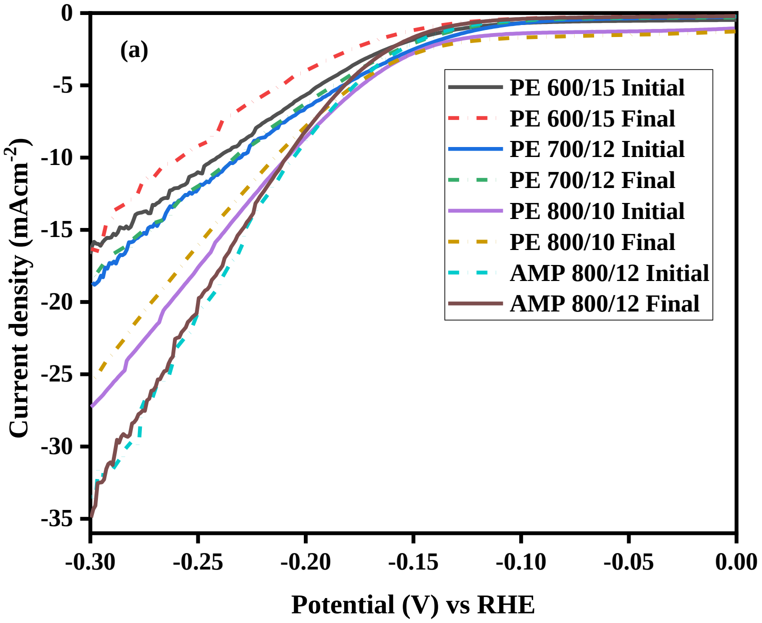

Figure 6.17: LSV plot of pure phase C-Mo_2C and C/N-Mo_2C.

The increase in current density with respect to synthesis temperature for samples (PE 600/10, PE 700/10 and PE 800/10) was also observed as shown in Fig. 6.18a. This attributes to pure phase formation with increase in temperature, which incorporates carbon within molybdenum (Mo) lattice to produce the higher electron density near Fermi level resembling with platinum [55]. Similar effects were also observed for reaction time variation as shown in Fig. 6.18 b-d. Only ambiguity observed was in PE 600/12, which shows higher current density than pure phase C-Mo_2C synthesized at 600 °C. The reason is not clear but might be due to the fragmented and un-carburized (Mo) particles (Fig. 6.2b, XRD pattern), which provide more electron sites along with Mo_2C [60].

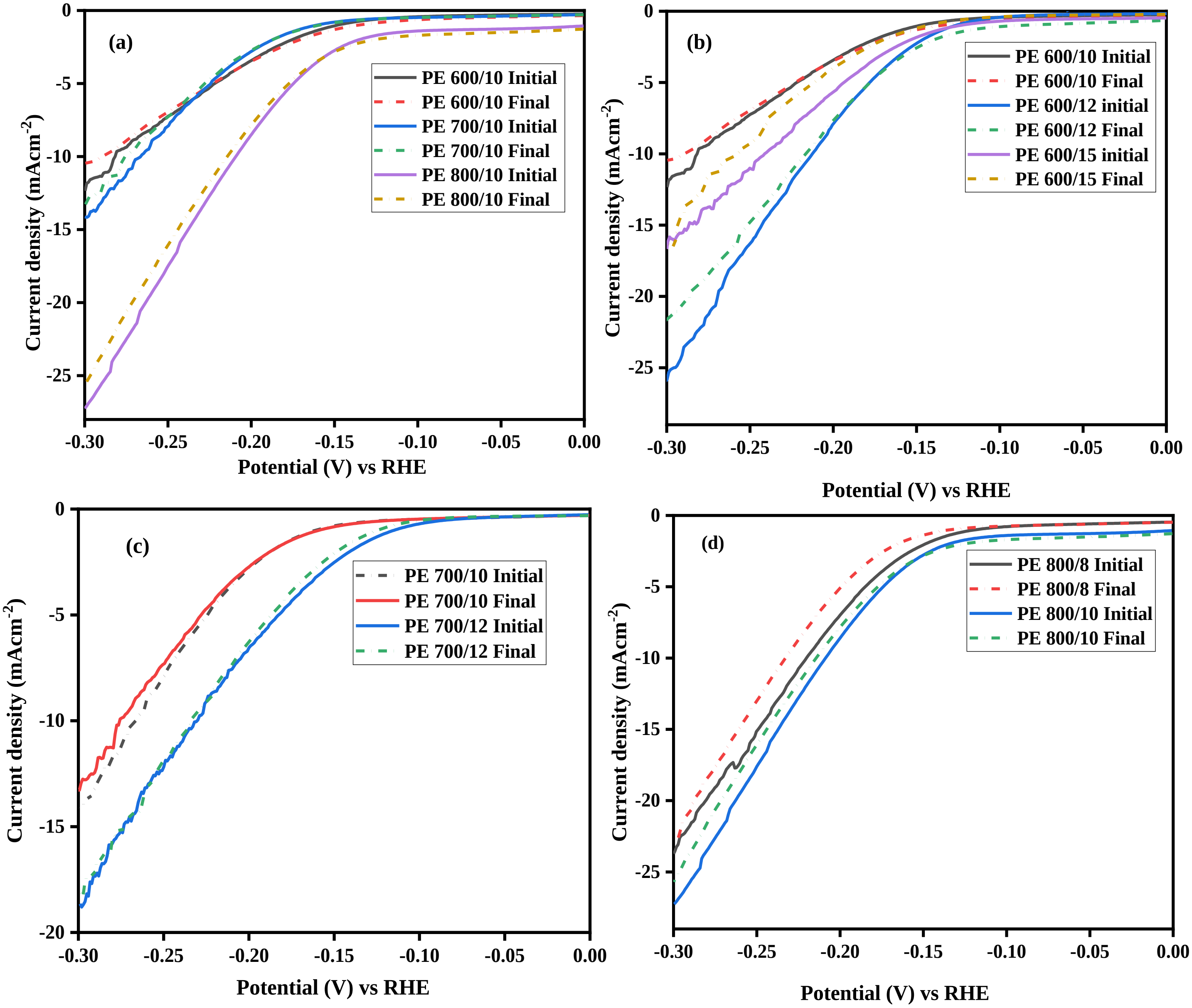

Figure 6.18: LSV plots of C-Mo_2C samples with respect to (a) change in temperature, and variation in reaction time at fixed temperatures at (b) 600 °C, (c) 700 °C & (d) 800 °C.

The current density trend also increases with temperature and time in N-doped samples synthesized (C/N-Mo_2C), as depicted in Fig. 6.19a-b. This also predict that only the pure phase Mo_2C samples encapsulated in N incorporated carbon matrix as active species for efficient HER activity. In this case both the graphite and pure phase formation enhances the current density. The observed higher portion of pyridinic N determined by XPS (Fig. 7e), increases the active sites and improves the electrocatalytic performance [21,28].

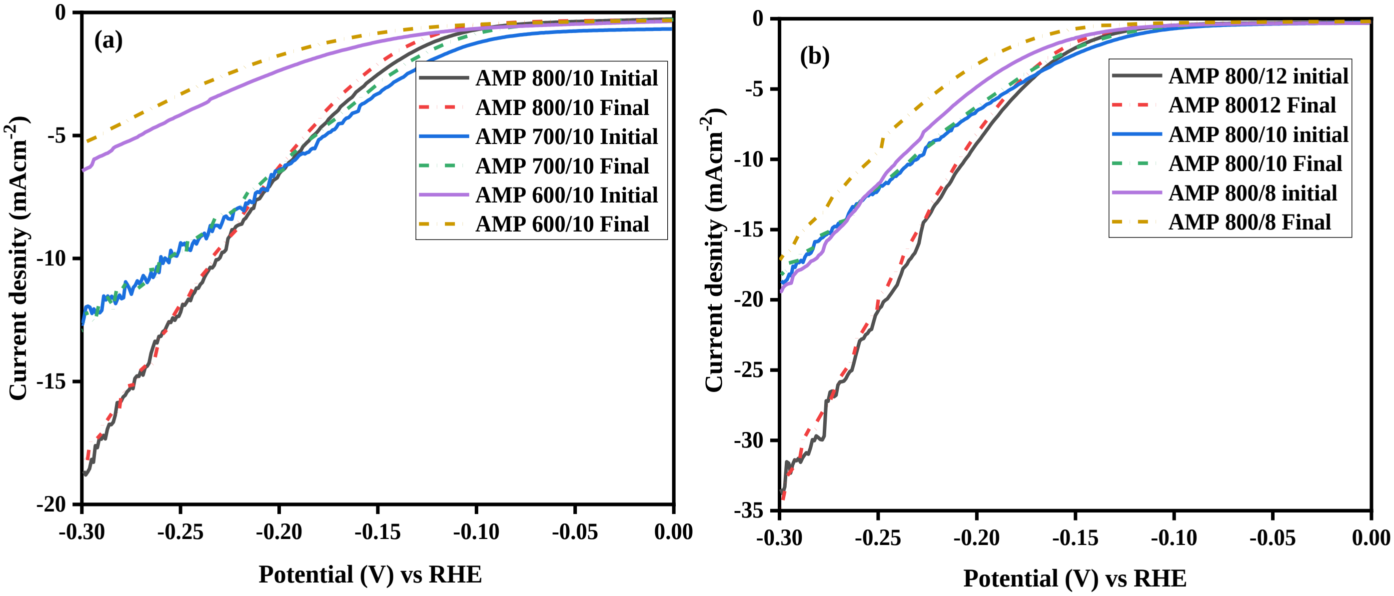

Figure 6.19: LSV plots of C/N-Mo_2C samples with respect to (a) change in temperature, and variation in reaction time at fixed temperatures at (b) 800 °C.

The stability is the key parameter for the commercial use of any electrocatalyst. The stability of the synthesized samples was tested by CV analysis performed for 2000 cycles. The final LSV plot (Fig. 6.17) after 2000 CV cycles for pure phase C and C/N-Mo_2C shows negligible loss of current. The higher stability with similar initial and final LSV curve having higher current density was exhibited by C/N-Mo_2C (AMP 800/12). The nitrogen doped carbon inhibit the acidic corrosion of Mo_2C particles and provide more conducting contact surface to enhance the stability with higher charge transfer rate. The enhanced stability of PE 600/15, PE 700/12 and PE 800/10 could be due the carbon network encapsulating the Mo_2C structure which renders the corrosion protection in acidic medium. The higher stability of PE 600/15 and PE 700/12 compared to PE 800/10 corresponds to their lower graphitic nature, which provide more protection as observed in reported results [61]. The impure phase incorporated samples shown in Fig. 6.18a-d and 6.19a-b get destabilized during CV analysis because of the presence of metallic (impurity) species which corrode easily in acidic medium and deteriorate their performance. The results reveal that the pure Mo_2C phase act as the active and stable species for HER activity in acidic medium. The stability of the pure phase C and C/N supported Mo_2C samples has also been tested by chronoamperometry as shown in Fig. 6.20. The time vs current density plot at fixed potential of (-120.0 mV) shows the negligible loss of the current density for PE 800/10 and AMP 800/12 in 10 hours, respectively. The higher stability attributes to encapsulation of Mo_2C particles in higher crystalline carbon network and special dispersion of Mo, C and N in and AMP 800/12, respectively as observed in TEM elemental mapping.

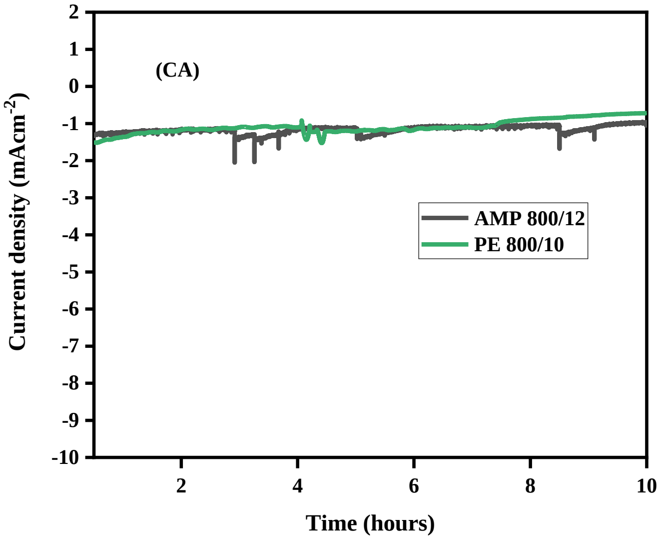

Figure 6.20: Chronoamperometry (CA) plot of PE 800/10 and AMP 800/12.

Tafel analysis was done to investigate the reaction kinetics and mechanism involved in HER [62,63]. The HER has been considered to three elementary reactions as [63,64]:

$$\boldsymbol{A + (H^+)H_2O + e^- \leftrightarrow AH_{ads} + H_2O} \qquad (6.1)$$

$$\boldsymbol{AH_{ads} + (H^+)H_2O + e^- \leftrightarrow H_2 + A + H_2O} \qquad (6.2)$$

$$\boldsymbol{AH_{ads} + AH_{ads} \leftrightarrow H_2 + 2A} \qquad (6.3)$$

Where, $\boldsymbol{A}$ is active site of the elctrocatalyst and $\boldsymbol{AH_{ads}}$ is hydrogen absorbed at that active site. The equation (6.1) is Volmer reaction, where hydrated proton attaches on surface of the catalyst and the produced H_2 leaves the active surface via (equation 6.2 and 6.3) as Heyrovsky and Tafel reactions, respectively. The Tafel slope '$\boldsymbol{b}$' is an important parameter to determine the reaction mechanism for HER. The value of Tafel slope '$\boldsymbol{b}$' for the above reaction (equation 6.1, 6.2 and

6.3) are 120, 40 and 30 mV dec^{-1}, respectively [21,65]. The Tafel plot (Fig.6.21) of the synthesized samples and the corresponding values of Tafel slope '***b***' are summarized in Table 6.3. The lowest value Tafel slope '***b***' exhibited by AMP 800/12 (Fig. 6.21) is 69.2 mV dec^{-1}, shows faster charge kinetics than the reported results [29,31,55,59,66,67]. It also predict that the HER mechanism is governed by Volmer-Heyrovsky reactions, because of the presence of more active sites and enhanced mass transfer rate due to presence of N in carbon coating over Mo_2C. The presence of pyridinic N causes C vacancies in the system and it behaves like p-doped semiconductor. The presence of graphitic-N acts as electron donor and also regulate the electronic structure near Fermi level without causing any effect on C species. In other sample containing impure phases along with Mo_2C (Fig. 6.22a), Volmer step is rate determining step excluding PE 600/12 (Fig.6.22a), which shows lower Tafel slope '***b***'. This ambiguity could be because of the intermediate fragmented particles with unaccomplished carburized species. Similar trend was also observed in nitrogen incorporated samples as shown in Fig. 6.22b. The Tafel slope '***b***' as depicted in Fig. 6.22b, decreases with pure phase formation of Mo_2C corresponding to reaction temperature and time.

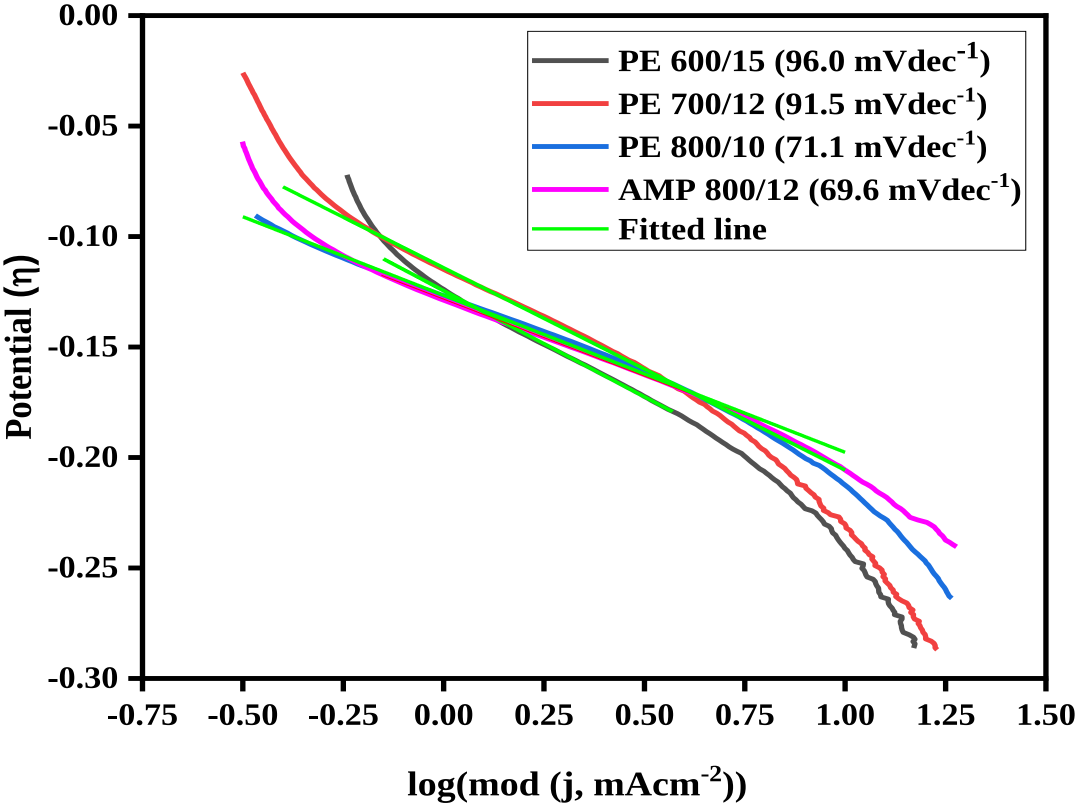

Figure 6.21: Tafel plot of pure phase C-Mo_2C and C/N Mo_2C phases.

Table 6.3: HER activity parameters, C_{dl} and SC of synthesized samples.

Sample	Tafel slope (mVdec^{-1})	Over potential (mV)	C_{dl} (mFcm^{-2})	Specific capacitance (SC) Fg^{-1}
PE 600/15	96.0	220.5	10.1	21.9
PE 700/12	91.5	206.0	8.7	18.8
PE 800/10	71.1	197.7	21.3	46.2
AMP 800/12	69.2	197.9	16.3	35.4
PE 700/10	90.7	250.57	7.7	16.7
PE 600/10	97.6	244.71	13.0	28.2
PE 600/12	77.6	205.22	5.7	12.4
PE 800/8	91.5	212.67	3.5	7.6
AMP 800/10	88.8	203.3	11.7	25.4
AMP 700/10	118.5	208.2	5.2	11.3
AMP 600/10	171.1	307.46	6.3	13.6
AMP 800/8	89.0	226.67	1.9	4.1

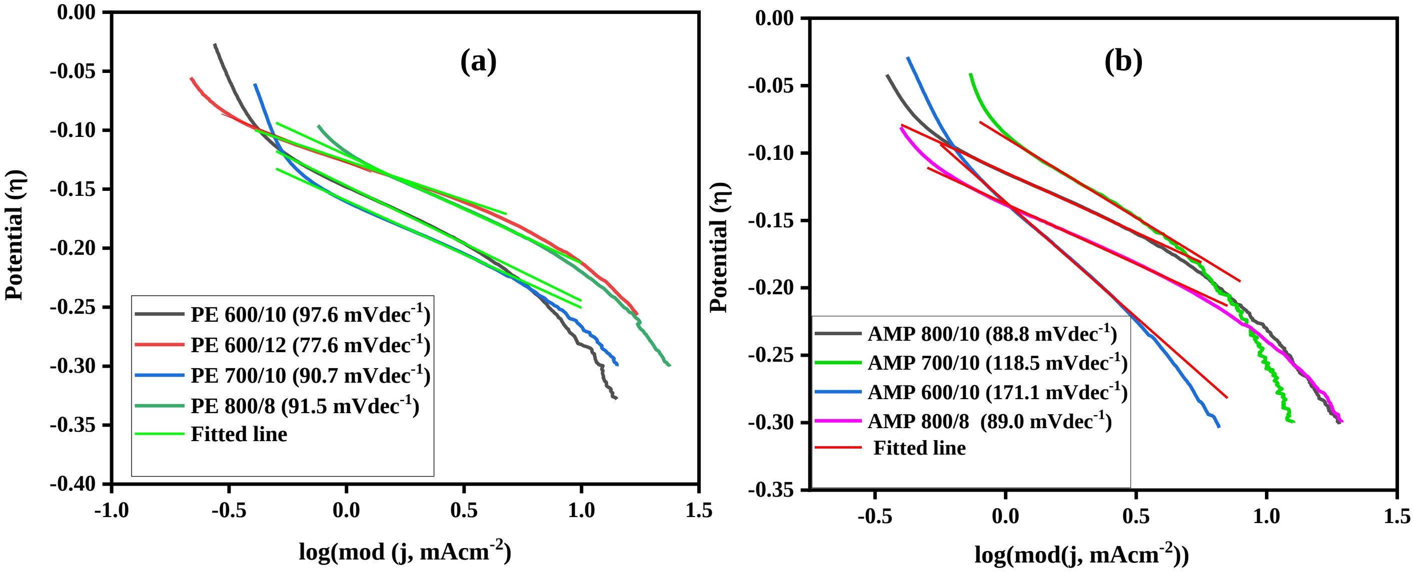

Figure 6.22: Tafel plots of (a) C-Mo_2C (PE 600/10, PE 600/12, PE 700/10 and PE 800/8) and (b) C/N-Mo_2C (AMP 600/10, AMP 700/10, AMP 800/10 and AMP 800/8).

Along with Tafel slope '***b***' the over potential of the electrocatalyst is also an important factor which, determine its commercial applicability. The over potential is calculated according to equation 3.11 (Chapter 3). The over potential of the synthesized samples to obtain current density of 10 mAcm^{-2} is mentioned in Table 6.3. The lower over potential exhibited by AMP 800/12 compared to other synthesized samples show better performance than the reported results [20,31].

The more the Mo_2C phase in the synthesized sample, the lower is the over potential, which again justifies the excellent electrocatalytic behavior of Mo_2C phase. The lower over potential was also estimated for PE 800/10 having higher amount of graphitic/graphene content, lower crystallite size compared to PE 600/15 and PE 700/12, respectively. The performance comparison in terms of Tafel slope '***b***' and over-potential of the synthesized samples along with fabricated and reported literature is given in Table 6.4. The compared results reveal the enhancement in performance of the low cost synthesized C and C/N supported Mo_2C because of the higher graphitic/graphene formation. The incorporation of N in carbon support over Mo_2C has greatly influenced HER activity in electron, mass transfer and has provided more active sites for adsorption/desorption.

Table 6.4: Comparison of HER activity of synthesized samples with reported literature.

Sample ID	Over potential (mV) at 10mAcm^{-2}	Catalyst loading (mgcm^{-2})	Exchange Current density J_0 (mAcm^{-2})	Tafel Slope (mVdec^{-1})	Reference
PE600/15	**220.5**	**0.461**	**0.054**	**96.0**	**This work**
PE 700/12	**206.0**	**0.461**	**0.060**	**91.5**	
PE 800/10	**197.7**	**0.461**	**0.139**	**71.1**	
AMP 800/12	**197.9**	**0.461**	**0.014**	**69.2**	
C-Mo_2C	293	0.102	-	98	68
Mo_2C/C	340			110	31
Mo_2C/NCNT-10	213			86	
Mo_2C/NCNT-20	200			82	
Mo_2C/NCNT-30	195			75	
Mo_2C/NCNT-40	212			81	
NCNT	497				
CNT	596				
Mo_2C-nanocomposites		0.25		110-235	63
Graphite				206	59
P-Graphene	490			113	
N-Graphene	533			116	

N,P-Graphene	422			91	
Mo$_2$C@NC-1	306		-	99	69
Mo$_2$C@NC-2	240		-	83	
Mo$_2$C@NC-3	270		-	90	
Mo$_2$C@NC-4	301		-	145	
Mo$_2$C@NC-2-650	310		-	99	
Mo$_2$C/CNT	251	8.2		251	70
Mo$_2$C/CNG	264	6.3		264	
Mo$_2$C	410		0.011	124	71
Fe- Mo$_2$C	377		0.014	132	
Co- Mo$_2$C	243		0.020	89	
Ni- Mo$_2$C	205		0.028	81	
Cu- Mo$_2$C	227		0.017	84	
Ag- Mo$_2$C	210		0.030	83	

6.4.2 Electric double layer capacitance (EDLC, C_{dl})

The energy storage performance of pure phase C and C/N supported Mo$_2$C was studied by CV analysis performed at various scan rates as shown in Fig.6.23a-d. The rectangular and quasi rectangular CV curve exhibited by PE 800/10, PE 700/12 and PE 600/15, AMP 800/12 reveal their good capacitive behavior. The nearly rectangular shape and absence of any redox peak in CV curve exhibited by these synthesized samples reveal their non-Faradic character. The retention of rectangular shape even at higher scan rate reveal their excellent stability during charging and discharging. The EDLC, C_{dl} value extracted from the plot of scan rate (mVs^{-1}) on x-axis and current density at fixed potential ($\Delta j_{0.3}$, mAcm^{-2}) on y-axis is summarized in (Table 6.3). The C_{dl} measurements revealed from (Fig. 6.24) is higher than the earlier for Mo$_2$C and Mo$_2$C supported species [5,9].

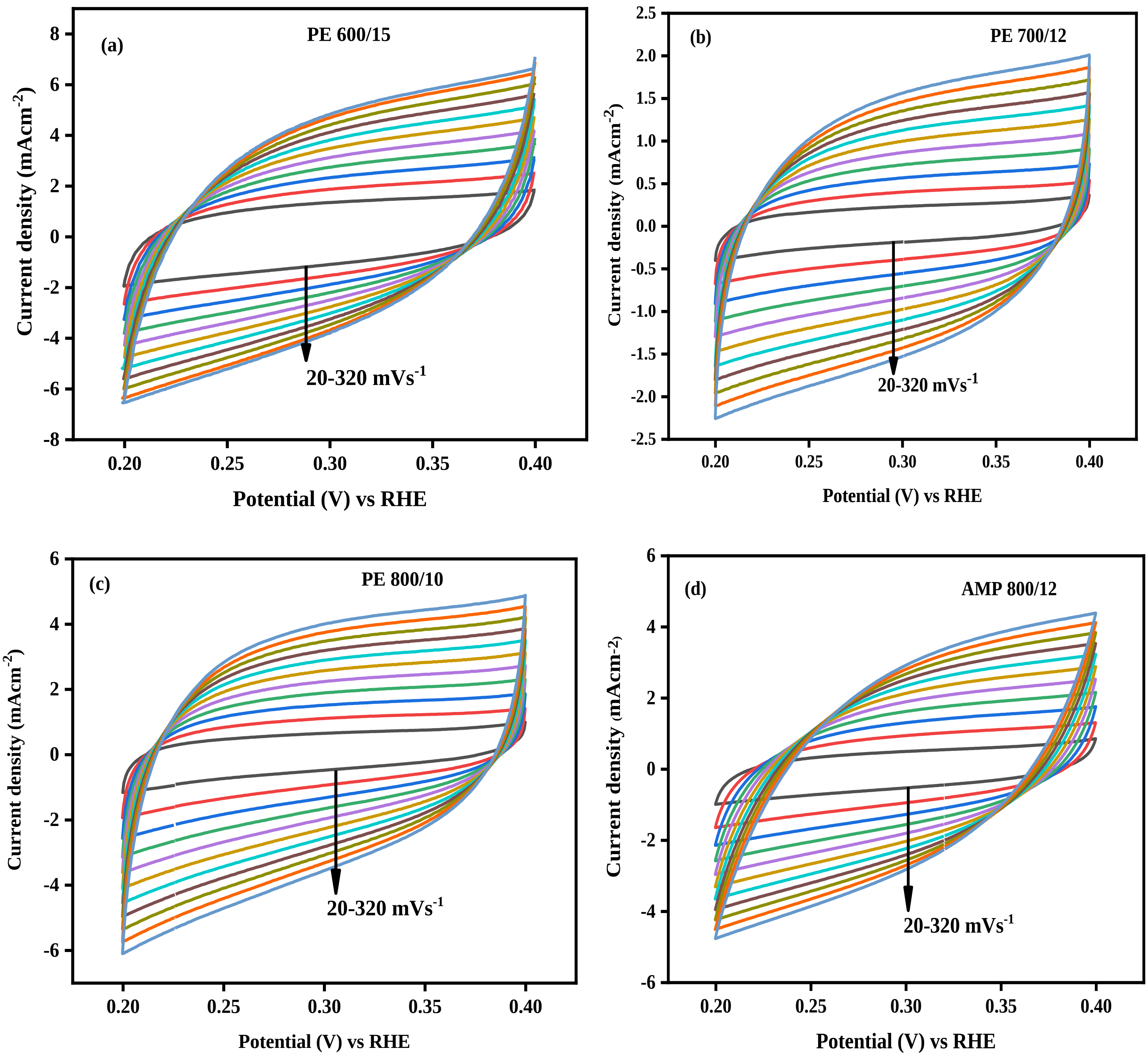

Figure 6.23: Cyclic voltammetry (CV) at different scan rates (a) PE 600/15, (b) PE 700/12 & (c) PE 800/10 for C-Mo_2C and (d) AMP 800/12 for C/N-Mo_2C.

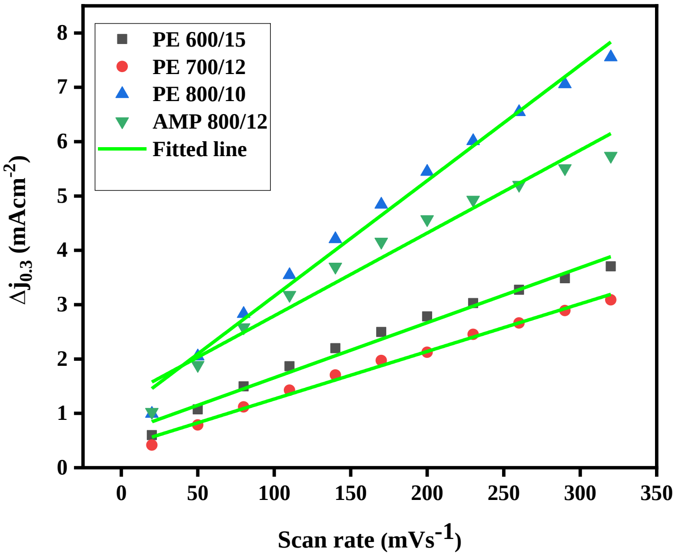

Figure 6.24: EDLC plot of scan rate (mVs^{-1}) vs current density (mAcm^{-2}) at a fixed potential.

The higher C_{dl} exhibited by PE 800/10 corresponds to higher graphitic carbon network surrounding the Mo_2C particles. The presence of different nitrogen species (pyridinic and graphitic N) as per XPS analysis helps to enhance the charge transfer kinetics along with its higher graphitic carbon nature exhibited in Raman analysis. The enhancement in C_{dl} of PE 800/10 compared to PE 700/12 and PE 600/15 is mainly due to the higher graphitic nature of carbon at higher synthesis temperatures and lower crystallite size. The formation of graphene flakes observed in TEM also provide more active site available for electron transfer and enhance the charge storage rate. The little lower value of PE 700/12 compared to PE 600/15 might be due to the agglomerated particles although it is supported by graphitic carbon. Another advantage of PE 600/15 is that the stacking of particles as observed in TEM provide active surfaces for charge transfer. However, the synergetic effects of N incorporation in carbon improves the active sites and lowers the electron path to enhance the charge storage capacity [34]. The presence of bamboo like carbon tubes encapsulating Mo_2C structures also enhances the charge storage capacity due to their higher surface area and flexible nature. The N incorporation in the carbon matrix over Mo_2C improves the charge distribution and enhances the surface wettability, which in turn increases the capacitance of the product. The multiple scan rate CV cycles of C-Mo_2C and C/N-Mo_2C samples, having impure phases are shown in Fig. 6.25 and 6.26a-d, respectively. The C_{dl} values so obtained from the Fig. 6.27a-b and tabulated in Table 6.3. The results also reveal the presence of pure Mo_2C within the C or C/N matrix, which helps to enhance the charge storage capacity. It shows that the Mo_2C is a promising candidate for capacitor applications. The specific capacitance (SC) obtained for pure phase Mo_2C and other synthesized samples encapsulated in C and C/N matrix is given in Table 6.3. The higher EDLC or electrochemical surface area (ECSA) of PE 800/10 shows increased active sites as compared to AMP 800/12. The lower '***b***' and overpotential of AMP 800/12 although having little lower EDLC than PE 800/10, shows the enhanced HER activity due to synergistic effect of N incorporation in C matrix over Mo_2C.

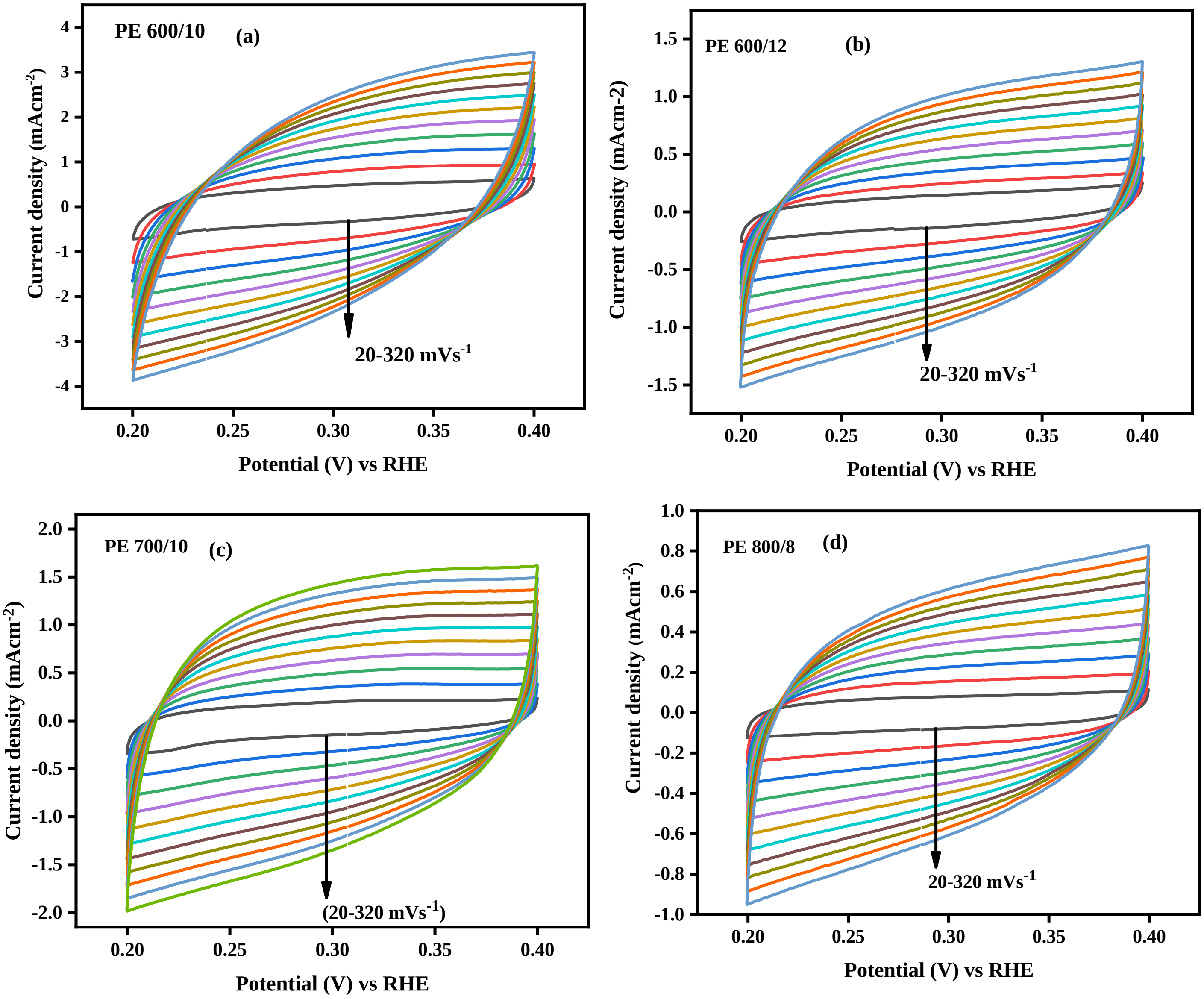

Figure 6.25: CV with different scan rates (a) PE 600/10, (b) PE 600/12, (c) PE 700/10 and PE 800/8.

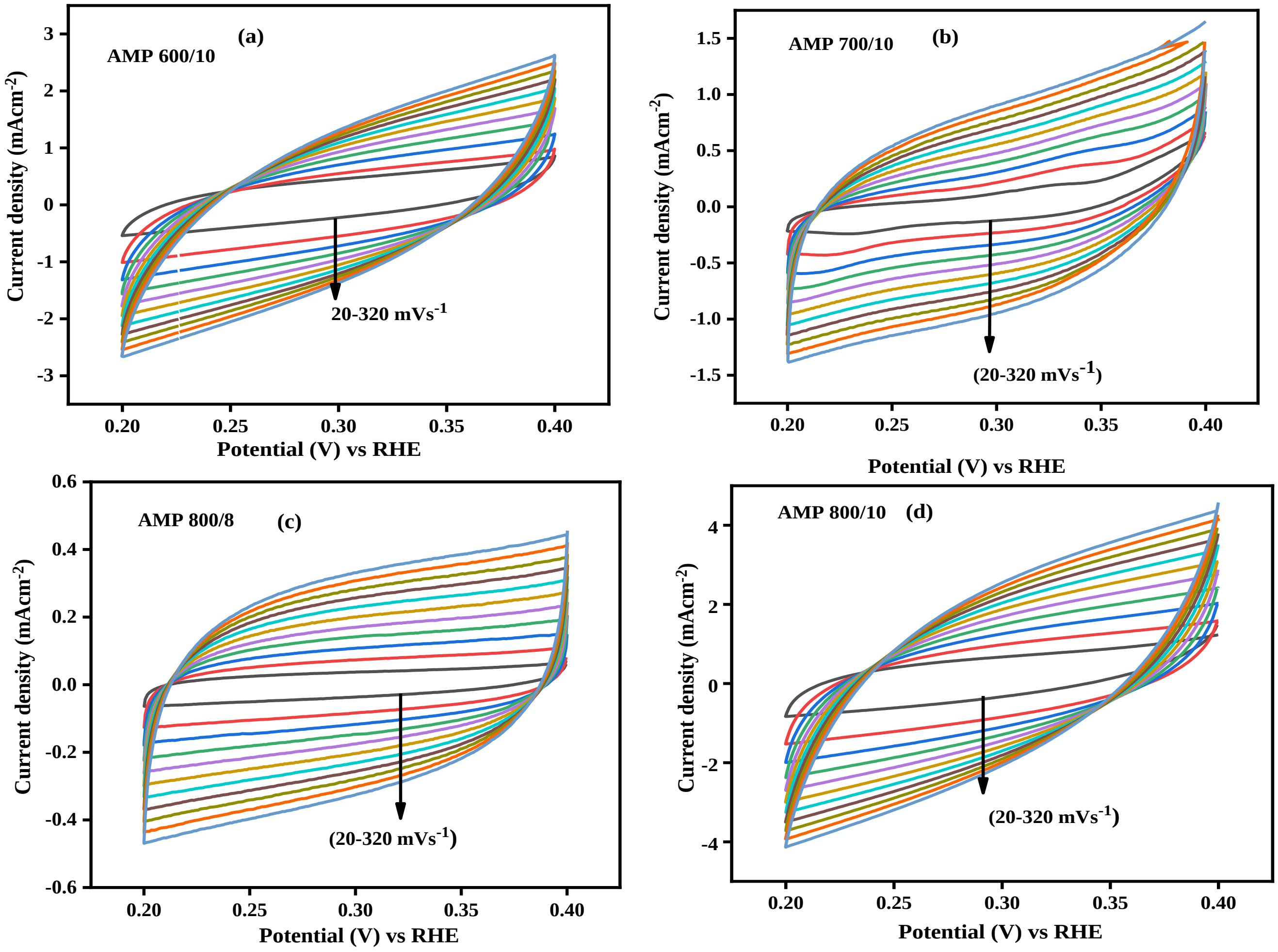

Figure 6.26: CV with different scan rates (a) AMP 600/10, (b) AMP 700/10, (c) AMP 800/8 and AMP 800/10.

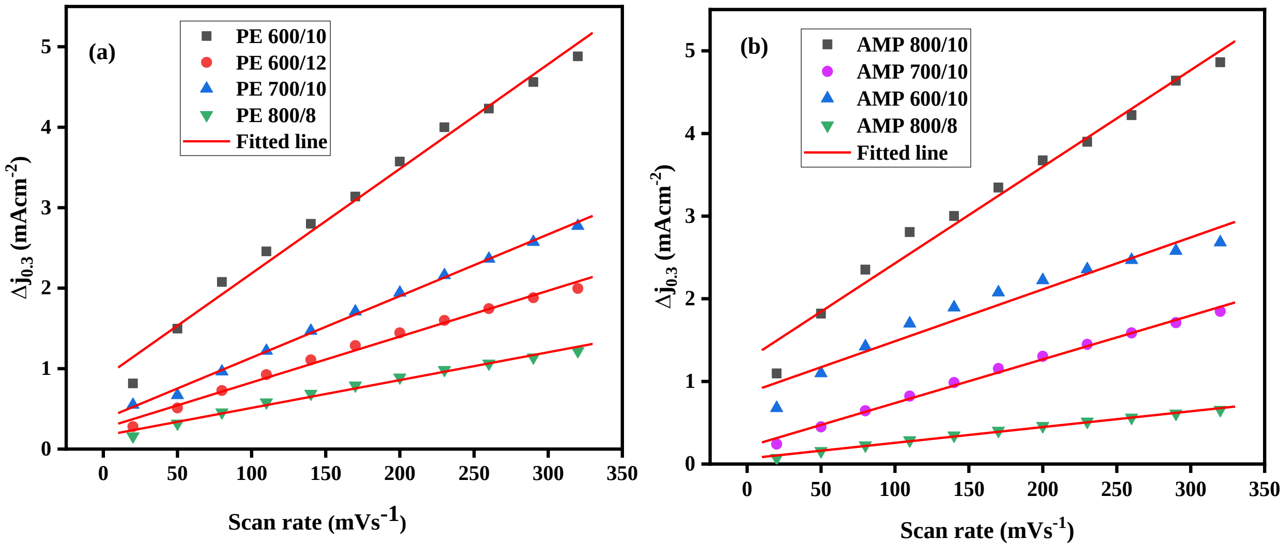

Figure 6.27: EDLC measurements of samples synthesized samples (a) C-Mo$_2$C (PE 600/10, PE 600/12, PE 700/10 and PE 800/8) and (b) C/N-Mo$_2$C (AMP 600/10, AMP 700/10, AMP 800/8 and AMP 800/10).

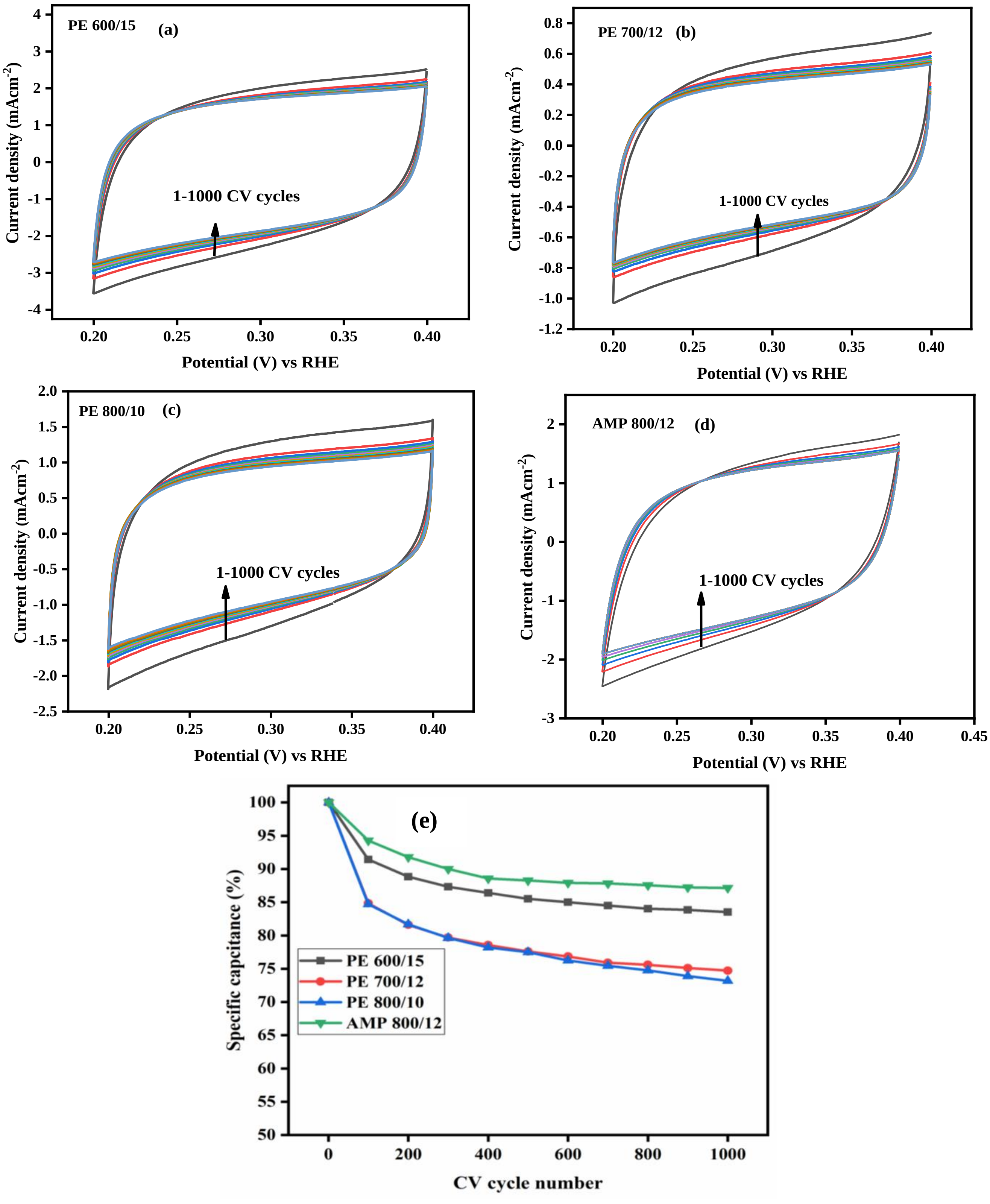

Figure 6.28: CV verssus cycle number (a) PE 600/15, (b) PE 700/12, (c) PE 800/10 for C-Mo_2C, (d) AMP 800/12 and (e) EDLC plot for C & C/N-Mo_2C.

The long time durability of the capacitors was tested by CV analysis performed in the same voltage window for 1000 CV cycles at fix scan rate. The CV plot C-Mo_2C and C/N-Mo_2C is shown in Fig. 6.28a-d. The plot of specific capacitance retention (%) and CV cycle number is shown in Fig. 6.28e. Only distortion of first CV cycle has been observed, which could be due the chemical activation during analysis. The AMP 800/12 shows the higher retention rate with respect to carbon supported Mo_2C, which again shows the high corrosion resistance due to nitrogen incorporation in graphitic carbon matrix over Mo_2C. The results reveal the promising potential application of synthesized materials for fabrication of low cost and durable capacitors.

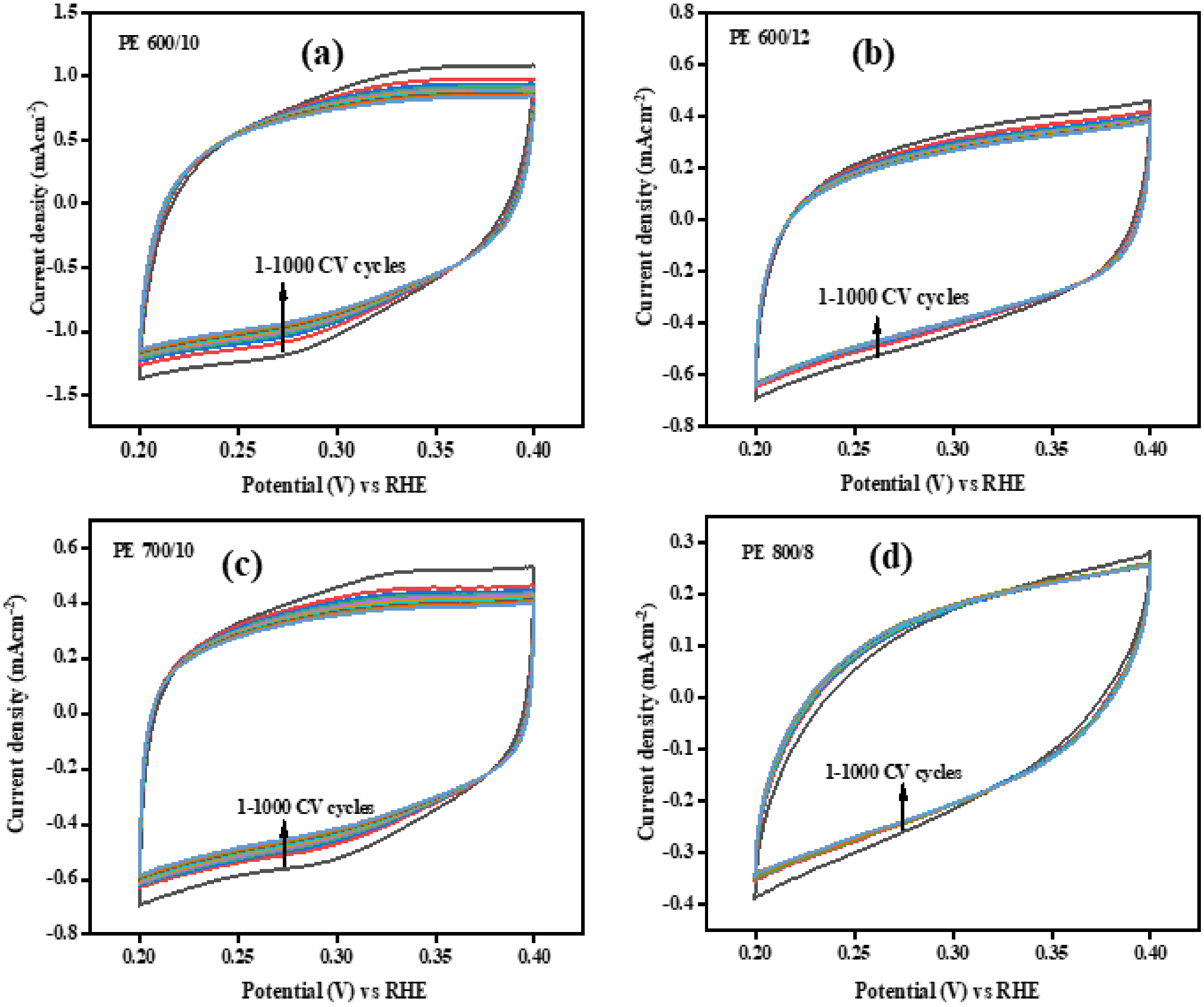

Figure 6.29: CV at fix scan rate for 1000 cycles (a) PE 600/10, (b) PE 600/12, (c) PE 700/10 and PE 800/8.

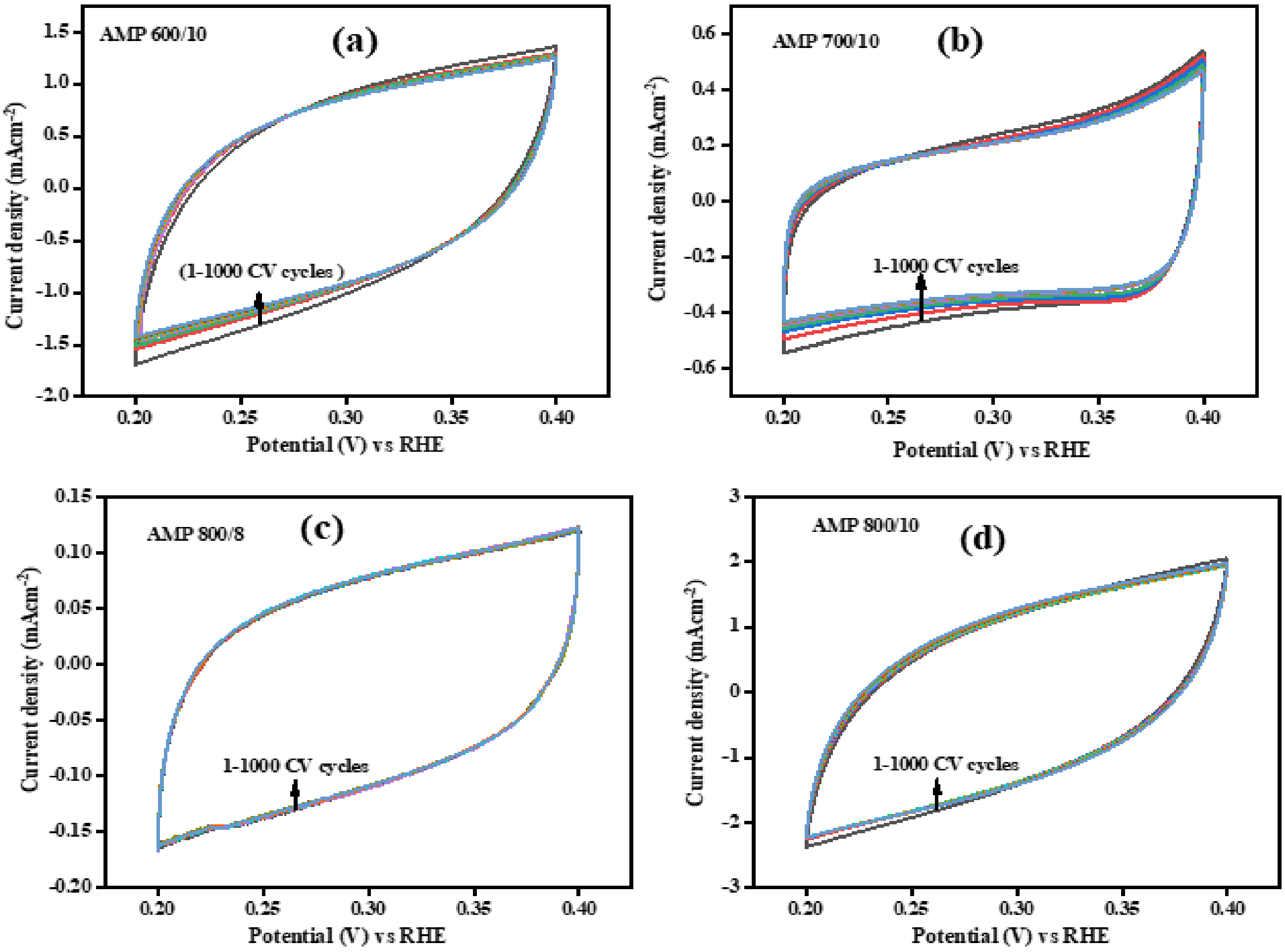

Figure 6.30: CV at fix scan rate for 1000 cycles (a) AMP 600/10, (b) AMP 700/10, (c) AMP 800/8 and AMP 800/10.

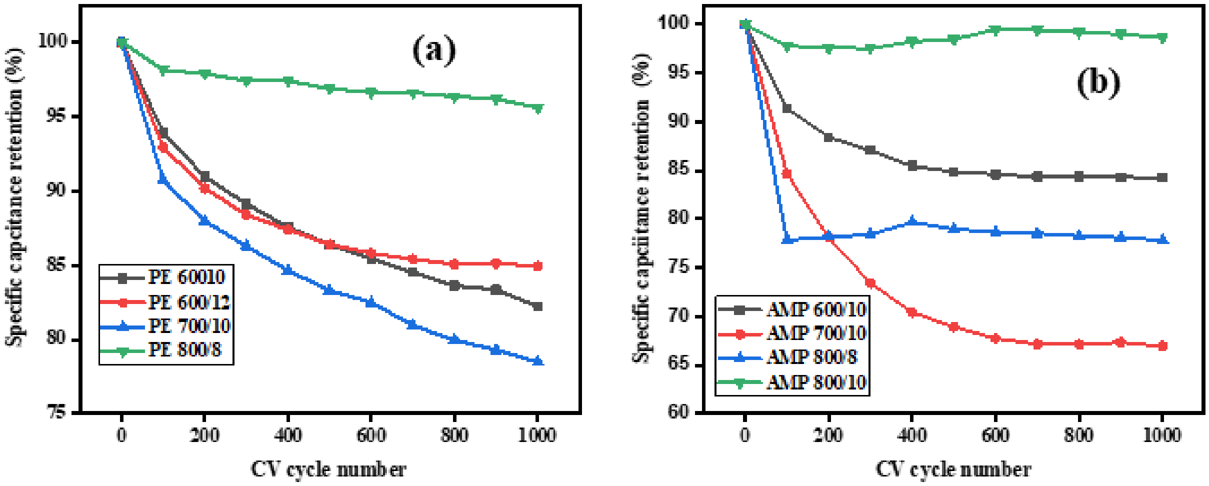

Figure 6.31: Specific capaciytance retention (%) for samples synthesized by (a) scheme 1 (PE 600/10, PE 600/12, PE 700/10 and PE 800/8) and (b) scheme 2 (AMP 600/10, AMP 700/10, AMP 800/8 and AMP 800/10).

The cyclic durability of impure phase containing samples C-Mo_2C and C/N-Mo_2C are shown in Fig.6.29 and 6.30a-d, respectively. The respective SC retention plot is depicted in Fig. 6.31a-b. The more Mo_2C phase formation enhances the stability of the synthesized samples as evidenced from the CV shape retention in Fig. 6.30a-d. The CV shape of C/N-Mo_2C (Fig. 6.30a-d) is quasi rectangular in comparison to C-Mo_2C, which also shows enhancement in CV pattern retention with increase in pure phase formation. The results predict that the pure phase Mo_2C encapsulated in C/N network as the possible potential candidate for EDLC and supercapacitor applications.

6.4.3 Electrochemical impedance spectroscopy (EIS)

To gain further information regarding the reaction kinetics of HER of the pure phase Mo_2C samples, EIS tests were performed. The Nyquist plot of the synthesized samples is shown in Fig. 6.32a-d. The pattern shows the voltage dependency of the curves, which tend to form semicircular curves with increase in applied potential [72]. PE 600/15 and AMP 800/12 show the higher kinetic control as compared to PE 700/12 and PE 800/10, respectively. It also confirms the decrease in charge transfer resistance with applied voltage. The tendency to form smaller semicircle in higher frequency region and nearly linear pattern upwards in lower frequency region reveals the kinetic control and mass control characteristics of the synthesized samples (Fig 6.32 a & d). Due to surface inhomogeneity, variable capacitors across the surface, and uneven potential surfaces, the corresponding circuit fitting was not observed. This could be due to the presence of constant phase element present in the synthesized samples due inhomogeneous surface characteristics. The linear pattern tilted upwards in lower frequency region also supports the good EDLC behavior of the synthesized samples. However, the Nyquist plot reveals the smaller series resistance (R_s) (resistance between electrode material and electrolyte) in PE 800/10 as compared to other samples and the corresponding estimated values are given in Fig.6.32. The mass transfer control dependency on applied potential is less in AMP 800/12 compared to others. The presence of all kinetic, mixed and mass transfer control regions in PE 600/15 and AMP 800/12, predicts some redox reactions occurring deep within the pores of the prepared material. Here again the results confirm the strong bridge of graphitic/conductive carbon over Mo_2C hence decreases the Rs and charge transfer resistance (R_{ct}) of PE 800/10 and PE 700/12. Moreover, the higher kinetics in PE 600/15 and AMP 800/12 attributes to its smaller size and the presence of N in carbon matrix, which enhances the active sites and also shorten the path for electron transfer.

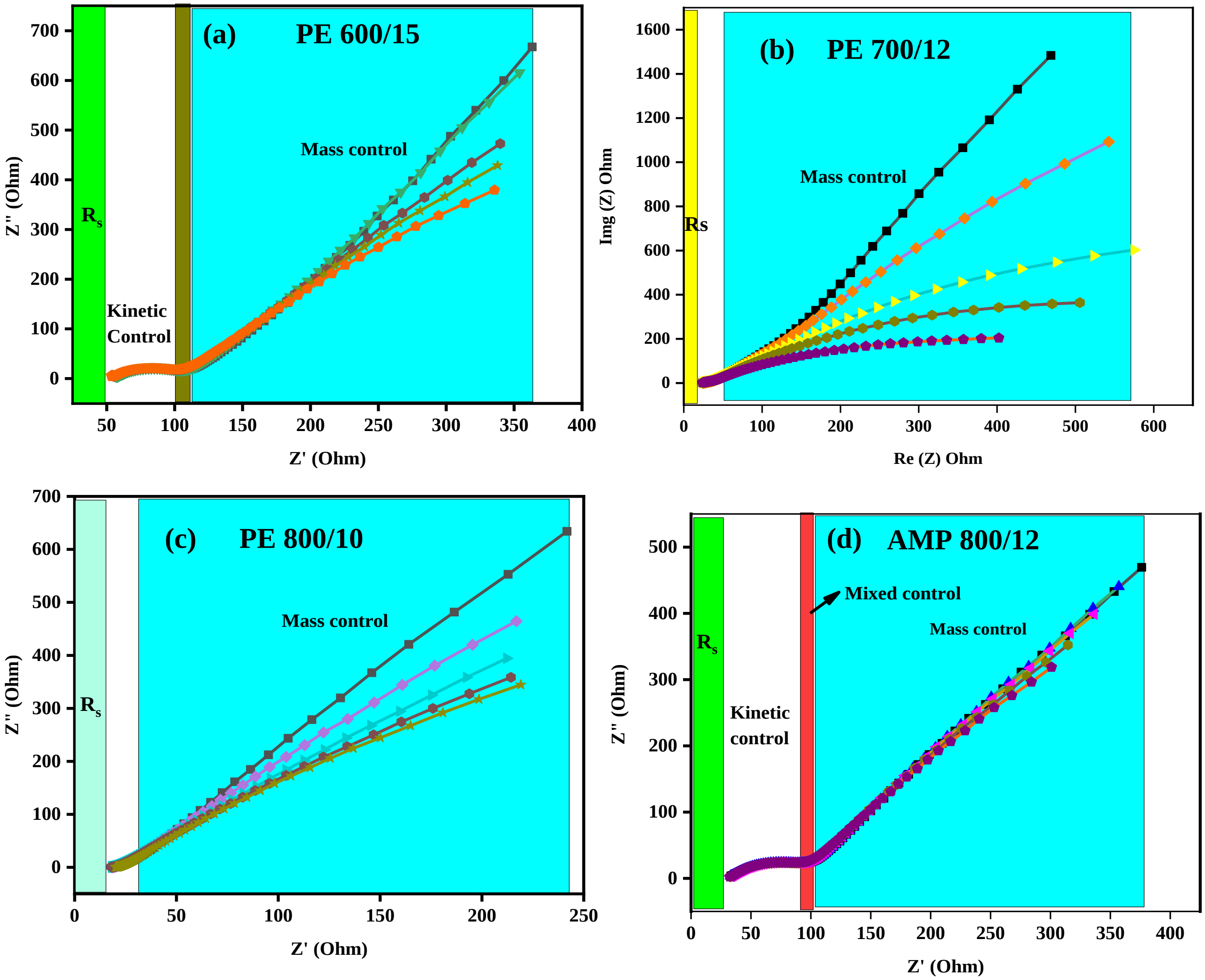

Figure 6.32: Nyquist plots of (a) PE 600/15 (R_s = 53.4 Ω), (b) PE 700/12 (R_s = 23.7 Ω), (c) PE 800/10 (R_s = 17.5 Ω)and (d) AMP 800/12 (R_s = 32.2 Ω).

References

1 X. Zou and Y. Zhang, *Chemical Society reviews*, 2015, **44**, 5148–80.
2 R. A. Rather, D. Pooja, P. Kumar, S. Singh and B. Pal, *Journal of Cleaner Production*, 2018, **175**, 394–401.
3 I. P. Jain, *International Journal of Hydrogen Energy*, 2009, **34**, 7368–7378.
4 J. A. Turner, *Science (New York, N.Y.)*, 2004, **305**, 972–974.
5 J. Sen Li, Y. Wang, C. H. Liu, S. L. Li, Y. G. Wang, L. Z. Dong, Z. H. Dai, Y. F. Li and Y. Q. Lan, *Nature Communications*, 2016, **7**, 11204.
6 Y. Luo, L. Tang, U. Khan, Q. Yu, H. M. Cheng, X. Zou and B. Liu, *Nature Communications*, 2019, **10**, 1–9.
7 J. Li, C. Zhou, J. Mu, E. Yang and X. Zhao, *RSC Advances*, 2018, **8**, 17202–17208.
8 J. D. Wiensch, J. John, J. M. Velazquez, D. A. Torelli, A. P. Pieterick, M. T. McDowell, K. Sun, X. Zhao, B. S. Brunschwig and N. S. Lewis, *ACS Energy Letters*, 2017, **2**, 2234–2238.
9 N. Kaur, R. A. Mir and O. P. Pandey, *Journal of Alloys and Compounds*, 2019, **782**, 119–131.
10 K. Ojha, S. Saha, S. Banerjee and A. K. Ganguli, *ACS Applied Materials and Interfaces*, 2017, **9**, 19455–19461.
11 Z. Xing, Q. Liu, A. M. Asiri and X. Sun, *Advanced Materials*, 2014, **26**, 5702–5707.
12 C. Giordano, C. Erpen, W. Yao and M. Antonietti, *Nano Letters*, 2008, **8**, 4659–4663.
13 D. Mukherjee, P. Muthu Austeria and S. Sampath, *ACS Applied Energy Materials*, 2018, **1**, 220–231.
14 K. M. Naik and S. Sampath, *Electrochimica Acta*, 2017, **252**, 408–415.
15 R. Chen, I. K. Puri and I. Zhitomirsky, *Ceramics International*, 2018, **44**, 18007–18015.
16 Y. Su and I. Zhitomirsky, *Journal of Power Sources*, 2014, **267**, 235–242.
17 L. Liao, S. Wang, J. Xiao, X. Bian, Y. Zhang, M. D. Scanlon, X. Hu, Y. Tang, B. Liu and H. H. Girault, *Energy and Environmental Science*, 2014, **7**, 387–392.
18 W.-F. Chen, C.-H. Wang, K. Sasaki, N. Marinkovic, W. Xu, J. T. Muckerman, Y. Zhu and R. R. Adzic, *Energy & Environmental Science*, 2013, **6**, 943–951.
19 T. Mo, J. Xu, Y. Yang and Y. Li, *Catalysis Today*, 2016, **261**, 101–115.
20 L. K. Brar, A. Gupta and O. P. Pandey, *Catalysis Today*, 2019, **325**, 98–108.
21 S. Jing, L. Zhang, L. Luo, J. Lu, S. Yin, P. K. Shen and P. Tsiakaras, *Applied Catalysis B: Environmental*, 2018, **224**, 533–540.
22 M. Pang, L. Ding, C. Li and C. Liang, *Studies in Surface Science and Catalysis*, 2010, **175**, 275–278.
23 H. Bin Wu, B. Y. Xia, L. Yu, X. Y. Yu and X. W. Lou, *Nature Communications*, 2015, **6**, 1–17.
24 C. Wallar, D. Luo, R. Poon and I. Zhitomirsky, *Journal of Materials Science*, 2017, **52**, 3687–3696.
25 R. Chen, I. K. Puri and I. Zhitomirsky, *Journal of The Electrochemical Society*, 2019, **166**, A935–A940.
26 X. J. Yang, X. J. Feng, H. Q. Tan, H. Y. Zang, X. L. Wang, Y. H. Wang, E. B. Wang and Y. G. Li, *Journal of Materials Chemistry A*, 2016, **4**, 3947–3954.
27 Z. Shi, K. Nie, Z. J. Shao, B. Gao, H. Lin, H. Zhang, B. Liu, Y. Wang, Y. Zhang, X. Sun, X. M. Cao, P. Hu, Q. Gao and Y. Tang, *Energy and Environmental Science*, 2017, **10**, 1262–1271.
28 Y. Liu, B. Huang, X. Hu and Z. Xie, *International Journal of Hydrogen Energy*, 2019, **44**,

3702–3710.
29 Z. Wu, M. Song, Z. Zhang, J. Wang and X. Liu, *Journal of Colloid and Interface Science*, 2019, **536**, 638–645.
30 D. K. Singh, R. N. Jenjeti, S. Sampath and M. Eswaramoorthy, *Journal of Materials Chemistry A*, 2017, **5**, 6025–6031.
31 Y. Song, J. Ren, G. Yuan, Y. Yao, X. Liu and Z. Yuan, *Journal of Energy Chemistry*, 2019, **38**, 68–77.
32 Z. Wu, B. Hu, P. Wu, H. Liang, Z. Yu, Y. Lin, Y. Zheng, Z. Li and S. Yu, *NPG Asia Materials*, 2016, **8**, 1–8.
33 Y. Su and I. Zhitomirsky, *Journal of The Electrochemical Society*, 2015, **162**, A5013–A5019.
34 C. Zhan, Y. Zhang, P. T. Cummings and D. E. Jiang, *Physical Chemistry Chemical Physics*, 2016, **18**, 4668–4674.
35 R. R. Li, S. G. Wang, W. Wang and M. H. Cao, *Physical Chemistry Chemical Physics*, 2015, **17**, 24803–24809.
36 A. Ramos, E. Monteiro, V. Silva and A. Rouboa, *Renewable and Sustainable Energy Reviews*, 2018, **81**, 380–398.
37 I. Barbarias, G. Lopez, M. Artetxe, A. Arregi, J. Bilbao and M. Olazar, *Energy Conversion and Management*, 2018, **156**, 575–584.
38 L. K. Brar, G. Singla and O. P. Pandey, *RSC Advances*, 2016, **6**, 109174–109184.
39 A. Gupta, G. Singla and O. P. Pandey, *Ceramics International*, 2016, **42**, 13024–13034.
40 T. Xiao, A. P. E. York, V. C. Williams, H. Al-megren, A. Hanif, X. Zhou and M. L. H. Green, 2000, 3896–3905.
41 H. K. Sidana, R. A. Mir and O. P. Pandey, *Journal of Alloys and Compounds*, 2018, **736**, 255–265.
42 G. Singla, K. Singh and O. P. Pandey, *Applied Physics A: Materials Science and Processing*, 2013, **113**, 237–242.
43 R. Priya and O. P. Pandey, *Vacuum*, 2018, **156**, 283–290.
44 C. Wu, G. Dong and L. Guan, *Physica E:*, 2010, **42**, 1267–1271.
45 H. M. A. Hassan, V. Abdelsayed, E. Rahman, M. Abouzeid, J. Terner, R. S. Khder and J. Terner, *Journal of Materials Chemistry*, 2009, **19**, 3832–3837.
46 P. K. Srivastava, P. Yadav and S. Ghosh, *Nanoscale*, 2016, **8**, 15702–15711.
47 C. Wu, G. Dong and L. Guan, *Physica E: Low-dimensional Systems and Nanostructures*, 2010, **42**, 1267–1271.
48 A. C. Ferrari, *Solid State Communications*, 2007, **143**, 47–57.
49 Y. V Fedoseeva, A. V Okotrub, V. O. Koroteev, Y. M. Borzdov, Y. N. Palyanov, Y. V Shubin, E. A. Maksimovskiy, A. A. Makarova, W. Münchgesang, L. G. Bulusheva and A. Vyalikh, *Carbon*, 2019, **141**, 323–330.
50 L. Peng, J. Shen, L. Zhang, Y. Wang, R. Xiang, J. Li, L. Li and Z. Wei, *Journal of Materials Chemistry A*, 2017, **5**, 23028–23034.
51 S. H. Yang, W. H. Shin and J. K. Kang, *Small*, 2008, **4**, 437–441.
52 A. Das, B. Chakraborty and A. K. Sood, *Bulletin of Materials Science*, 2008, **31**, 579–584.
53 N. Ferralis, *Journal of Materials Science*, 2010, **45**, 5135–5149.
54 M. Nazhipkyzy, B. T. Lesbaev, N. G. Prikhodko, Z. A. Mansurov and R. R. Nemkaeva, 2015, **3**, 17–20.
55 N. S. Alhajri, D. H. Anjum and K. Takanabe, *Journal of Materials Chemistry A*, 2014, **2**,

10548–10556.
56 K. Ojha, S. Saha, H. Kolev, B. Kumar and A. K. Ganguli, *Electrochimica Acta*, 2016, **193**, 268–274.
57 Y. Liu, M. Zhu and D. Chen, *Journal of Materials Chemistry A*, 2015, **3**, 11857–11862.
58 P. Xiao, X. Ge, H. Wang, Z. Liu, A. Fisher and X. Wang, *Advanced Functional Materials*, 2015, **25**, 1520–1526.
59 Y. Zheng, Y. Jiao, L. H. Li, T. Xing, Y. Chen, M. Jaroniec and S. Z. Qiao, *ACS Nano*, 2014, **8**, 5290–5296.
60 J. Dong, Y. Shi, C. Huang, Q. Wu, T. Zeng and W. Yao, *Applied Catalysis B: Environmental*, 2019, **243**, 27–35.
61 K. Zhang, C. Li, Y. Zhao, X. Yu and Y. Chen, *Physical Chemistry Chemical Physics*, 2015, **17**, 16609–16614.
62 K. Rajrana, A. Gupta, R. A. Mir and O. P. Pandey, *Physica B: Condensed Matter*, 2019, **564**, 179–185.
63 N. S. Alhajri, D. H. Anjum and K. Takanabe, *Journal of Materials Chemistry A*, 2014, **2**, 10548–10556.
64 T. Shinagawa, A. T. Garcia-Esparza and K. Takanabe, *Scientific reports*, 2015, **5**, 13801.
65 L. Chai, W. Yuan, X. Cui, H. Jiang, J. Tang and X. Guo, *RSC Advances*, 2018, **8**, 26871–26879.
66 T. Ouyang, Y. Q. Ye, C. Y. Wu, K. Xiao and Z. Q. Liu, *Angewandte Chemie - International Edition*, 2019, **58**, 1–7.
67 J. Xing, Y. Li, S. Guo, T. Jin, H. Li, Y. Wang and L. Jiao, *Electrochimica Acta*, 2019, **298**, 305–312.
68 L. Ma, R. Lin and V. Molinari, *Journal of Materials Chemistry A: Materials for energy and sustainability*, 2015, **3**, 8361–8368.
69 Y. Hu, G. Jia, S. Ma, J. Hu, P. Zhu, T. Cui, Z. Li and Z. Zou, *Catalysts*, 2016, **6**, 208.
70 B. Šljukic, D. M. F. Santos, M. Vujkovic, L. Amaral, R. P. Rocha, C. A. C. Sequeira and J. L. Figueiredo, *ChemSusChem*, 2016, **9**, 1200–1208.
71 M. Chen, Y. Ma, Y. Zhou, C. Liu, Y. Qin, Y. Fang, G. Guan, X. Li, Z. Zhang and T. Wang, *Catalysts*, 2018, **8**, 294.
72 K. Ojha, M. Sharma, H. Kolev and A. K. Ganguli, *Catalysis Science and Technology*, 2017, **7**, 668–676.

Chapter 7

Synthesis of Mo_2C@C/N using plastic waste

Overview

The present work is undertaken to utilize carbonaceous wastes for the synthesis of low cost electrocatalysts for HER and EDLC applications. Here in this chapter the synthesis of nitrogen incorporated carbon supported molybdenum carbide (Mo_2C@C/N) using waste pipette tip as carbon source has been described. The number of hydrocarbons present in the carbon source affects the pure phase formation of Mo_2C (Mo_2C@C/N). The role of processing parameters (temperature, time and carbon source) on pure phase formation has been described in detail. The HER activity and EDLC performance of Mo_2C@C/N synthesized under different synthesis conditions has been described.

7.1 Introduction

The rapid development in the industrial sector and increase in the global population leads to the higher energy demand. The traditional fossil fuels are limited. At the same time these produce toxic gases, which cause environmental pollution. The production of electric energy from different renewable energy resources has its own limitations. Hydrogen being most promising substitute for extinguishing fossil fuels having zero-carbon emission and high energy efficiency is being worked out [1]. To do so electrochemical water splitting is the most preferred pathway to produce hydrogen. The hydrogen evolution reaction (HER) through electrochemical water splitting requires active and durable electrocatalysts to promote hydrogen production at a higher with low over potential [1–3]. As discussed in previous chapters Platinum (Pt) is the most efficient electrocatalyst for this purpose but its low abundance and high cost, limits its usage for the large scale hydrogen production [4–6]. The transition metal-based compounds especially the molybdenum (Mo)-based chalcogenides, oxides, carbides, nitrides, and other alloys got attention due to their special surface features and activities [7–15]. Among all these compounds, molybdenum carbides have attained special significance as a highly efficient electrocatalyst due to their high conductivity and analogous d-band structure resembling Platinum (Pt) [8,16]. The pure phase crystalline molybdenum carbide (Mo_2C) is regarded as an efficient electrocatalyst for the HER in alkaline and acidic medium with higher stability and corrosion resistance [17].

Intensive attempts have been made to enhance the catalytic performance of the Mo_2C towards HER by tailoring the structure, constructing proper morphologies, alloying and doping etc. [18,19]. The encapsulation of Mo_2C particles in the supported carbon (in different forms) matrix enhances both efficiency and stability [2,20–23]. Carbon based materials have shown efficient results for the electrochemical double layer capacitors (EDLC, C_{dl}), a special class of supercapacitors [23–27]. The incorporation of different metal and non-metal elements in the carbon coating along with Mo_2C enhances the HER performance [28–31]. The synergistic effect due to the presence of nitrogen in carbon coated matrix over Mo_2C provide high specific surface area, improved electronic conductivity, improved electron/mass transport property and large number of active sites hence performance of Mo_2C improves [2,32,33].

In the present work, nitrogen incorporated carbon coated Mo_2C (Mo_2C@C/N) has been synthesized in an autoclave using waste plastic as the carbon source. The use of these wastes reduces the cost of the product and also addresses the environmental issues caused by these wastes.

The disposalof these wastes is affecting the entire world and is posing serious threat to the human health and water species. The present synthesis route is eco-friendly because no gases are evolved in the environment during the synthesis. This method will also address the issue faced during pyrolysis and recycling of these wastes. The nitrogen incorporated molybdenum precursor was used both as molybdenum/ nitrogen source and waste plastic as carbon source, respectively. The in-situ carbon coating incorporated with nitrogen over pure phase Mo_2C ($Mo_2C@C/N$) enhances the HER activity and stability. It also improves the charge storage ability of the synthesized material.

7.2 Synthesis of $Mo_2C@C/N$

The synthesis was carried out in the similar way as described in experimental section (Chapter 3). For synthesis of nitrogen incorporated carbon supported molybdenum carbide ($Mo_2C@C/N$), ammonium heptamolybdate tetrahydrate (AHM) were used as both N and Mo source, respectively. Waste plastic (used laboratory pipette tip) was used as carbon source. The synthesis parameters, sample labelling and the phases obtained are given in Table 7.1.

Table 7.1: Sample labelling, synthesis parameters and phase formation.

Sample Id	Temperature (°C)	Time (hours)	AHM (g)	Mg (g)	Pipette tip (g)	Phases
AM 1	800	10	1.235	3.5	1	Mo_2C
AM 2	700	10	1.235	3.5	1	Mo_2C
AM 3	600	10	1.235	3.5	1	MoO_2, Mo_2C
AM 4	800	8	1.235	3.5	1	MoO_2, Mo_2C
AM 5	700	8	1.235	3.5	1	MoO_2, MoC, Mo_2C
AM 6	800	10	1.235	3.5	0.5	Mo, Mo_2C
AM 7	800	10	1.235	3.5	0.75	MoO_2, Mo_2C

The synthesis conditions has been optimized to obtain pure phase $Mo_2C@C/N$. In this regard first reaction temperature has been varied from 600-800 °C with a fix reaction time. The effect of reaction time at 700 and 800 °C favoring the carburization of AHM to Mo_2C has been studied. The results reveal the reaction time of 10 h optimum for phase formation of Mo_2C. The role of initial carbon content on pure phase formation has also been optimized, which shows lower carbon content <1 g is not optimum to accomplish the carburization even at 800 °C. The effect of synthesis parameters on phase formation is discussed below:

7.3 Results and discussion

7.3.1 X-ray diffraction (XRD)

The typical XRD pattern of the synthesized samples is shown in Fig. 7.1. The data reveals the formation of pure phase Mo_2C at 800 °C for the reaction time of 10 h (AM 1). However, the sample synthesized at 700 °C (AM 2) for the same reaction time also favors the formation of Mo_2C and the results are in accordance with standard peak positions of Mo_2C (ICDD pattern 035-0787). The relatively higher temperature synthesized phase (AM 1) is more crystalline as compared to AM 2 (Fig. 7.1). The reaction temperature of 600 °C (AM 3) shows the formation of mixed molybdenum di-oxide (MoO_2) ICDD pattern (002-0422) and Mo_2C phases (Fig. 7.1). This shows the favorable reduction of AHM to MoO_2 and simultaneous carburization to Mo_2C in the presence of Mg and plastic waste [34]. However, the reaction conditions are not optimum to accomplish the carburization of MoO_2 at this stage. The reduction of AHM to MoO_2 inside the autoclave in the presence of Mg and carbon/hydrogen are in well agreement with those reported in the literature [35,36] . This also indicates that the carburization takes place after the reduction of AHM to MoO_2 and then it transforms into Mo_2C. The more crystalline nature of synthesized Mo_2C phase (AM 1) affects the properties, especially the electrochemical activity.

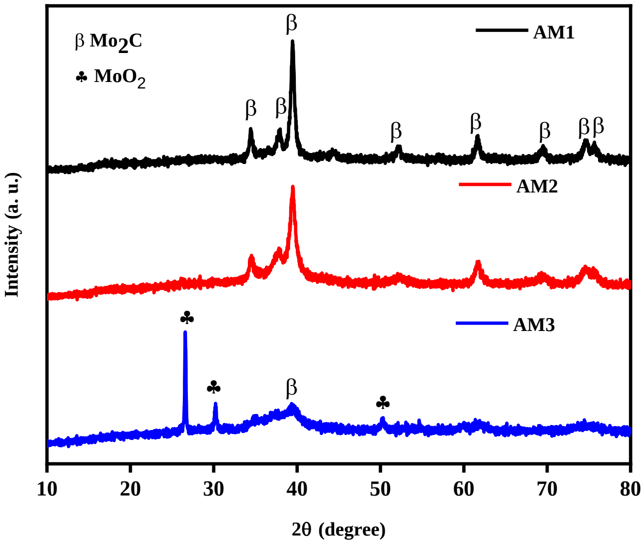

Figure 7.1: XRD pattern of AM 1 (800 °C), AM 2 (700 °C) and AM3 (600 °C).

Decreasing the reaction time to 8 h at 700 and 800 °C lead to formation of Mo_2C incorporated with the impure phase as shown in Fig. 7.2. It reveals the carburization accomplished for the reaction time of 10 h. The phase formation at 700 °C, reveals that the longer hydrocarbon chain in pipette tip favors the carburization even at relatively lower temperature.

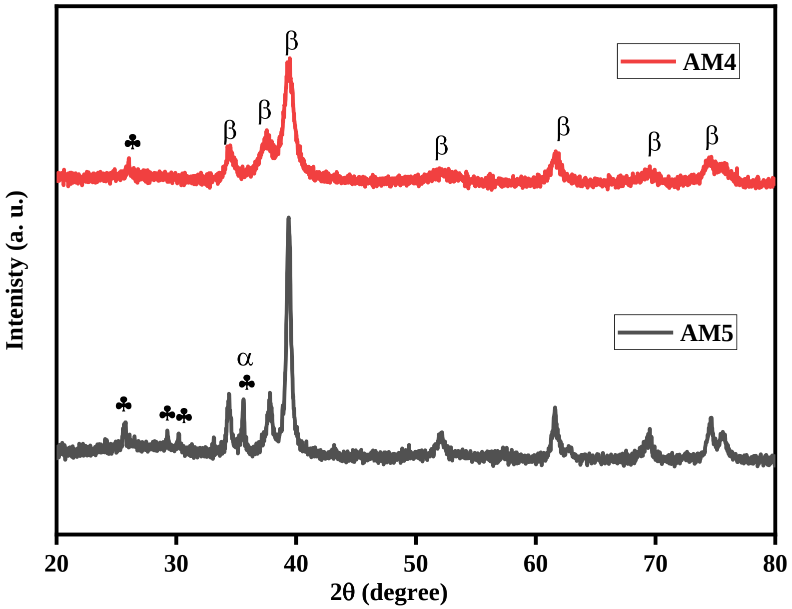

Figure 7.2: XRD pattern of AM 4 (800 °C for 8 h) and AM 5 (700 °C for 8 h).

The optimization of amount of initial carbon content at 800 °C for 10 h was also done as shown in Fig. 7.3. The results reveal that initial amount carbon content plays a vital role in phase formation.

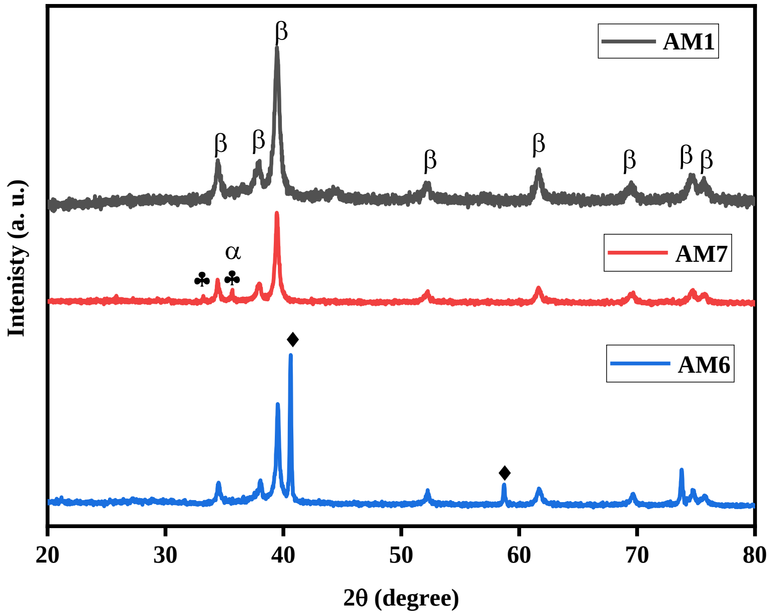

Figure 7.3: XRD pattern of AM 6 (0.5 g), AM 7 (0.75 g) and AM 1 (1 g).

Figure 7.3 reveals the initial amount of carbon content 0.5 g (AM 6) is not sufficient to carburize AHM to Mo_2C. The presence of more Mo content in AM 6 shows that the reduction is favorable because of less carbon content helps to diffuse inside the Mo lattice. Increasing the carbon content in AM 7 shows the formation of Mo_2C with some amount of MoO_2, which signifies that the carburization enhances with the increase in initial carbon content compared to AM 6 (Fig. 7.3). The amount of initial carbon content of (1 g/ AM 1) accomplishes the reduction of AHM and its carburization to form Mo_2C.

7.3.2 Morphological features

The morphological features of the synthesized samples ($Mo_2C@C/N$) were characterized by FESEM as shown in Fig. 7.4a-b. AM 1 sample shows more agglomerated particles due to higher synthesis temperature as shown in Fig. 7.4a. The particles show interconnected deformed faceted morphology. However, AM 2 (Fig. 7.4b) shows the agglomeration of flaky structures having more size uniformity as compared to the AM 1 (Fig 7.4a).

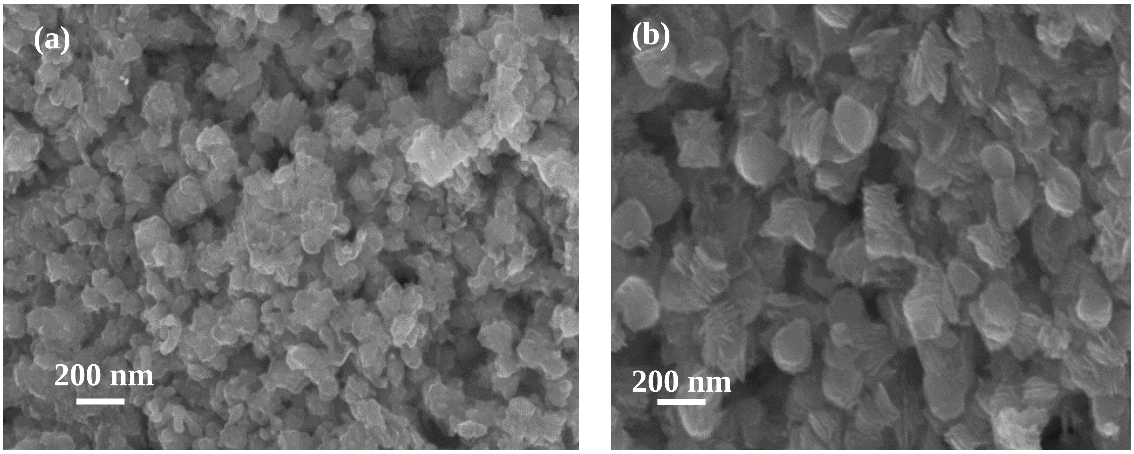

Figure 7.4: FESEM micrographs of (a) AM 1 (800 °C/ 10h) and (b) AM 2 (700 °C/ 10h).

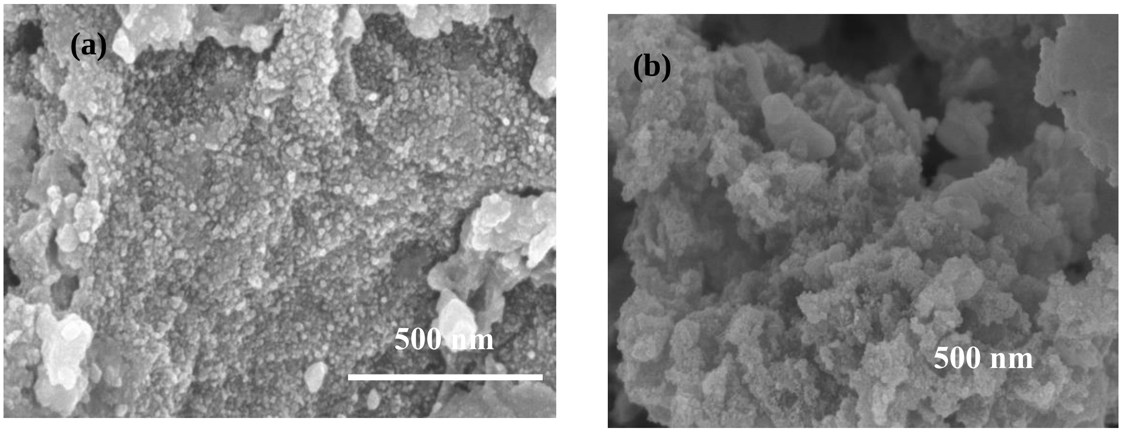

Figure 7.5: FESEM micrographs of (a-b) AM 3 (600 °C/10 h).

AM 3 does not form any well-defined morphology and shows high agglomeration of particles compared to the AM 1 and 2 as shown in Fig. 7.5a-b . Figure 7.5b clarifies the presence of multiple phases in the samples because of the different morphological characteristics. The EDS of AM 1, AM 2 and AM 3 reveals the presence of nitrogen in the synthesized samples as shown in Fig. 7.6 a-c. The elemental composition for the same is given in Table 7.2, where the presence of higher oxygen content in AM 3 is in agreement with the XRD results. The elemental mapping of elements (AM 1) is shown in Fig 7.7a-e. It also confirms the presence of N in the supported carbon matrix.

Table 7.2: Elemental composition of synthesized samples in weight (wt.) and atomic (at.) %.

Sample Id	**Mo**		**C**		**N**		**O**	
	wt. %	**at. %**	**wt. %**	**at. %**	**wt. %**	**at. %**	**wt. %**	**at. %**
AM 1	42.61	9.11	39.85	68.02	2.20	3.21	15.35	19..67
AM 2	45.05	9.98	37.73	66.74	2.22	3.37	15.00	19.91
AM 3	11.78	1.78	58.70	70.78	5.58	5.76	23.95	21.68

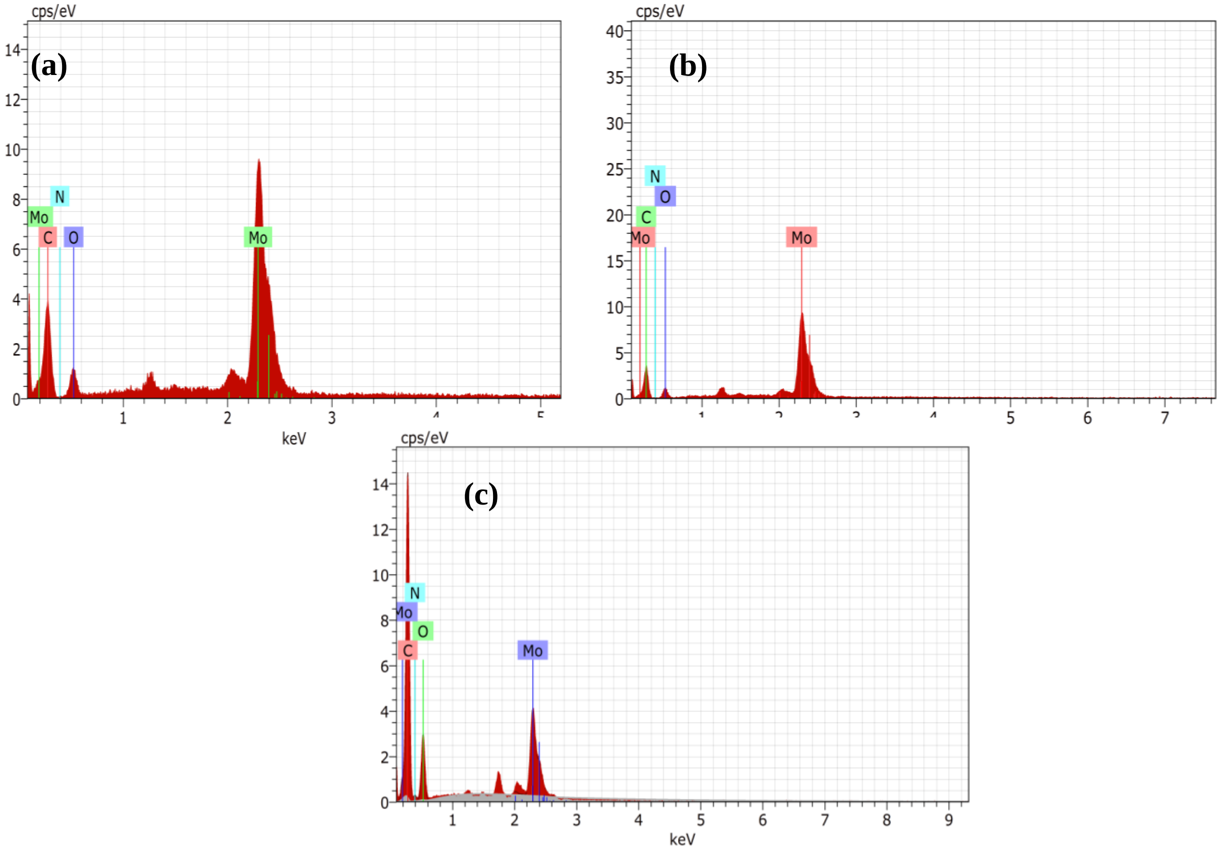

Figure 7.6: EDS pattern of (a) AM 1 (800 °C/ 10h), (b) AM 2 (700 °C/ 10h) and (c) AM 3 (600 °C/ 10h).

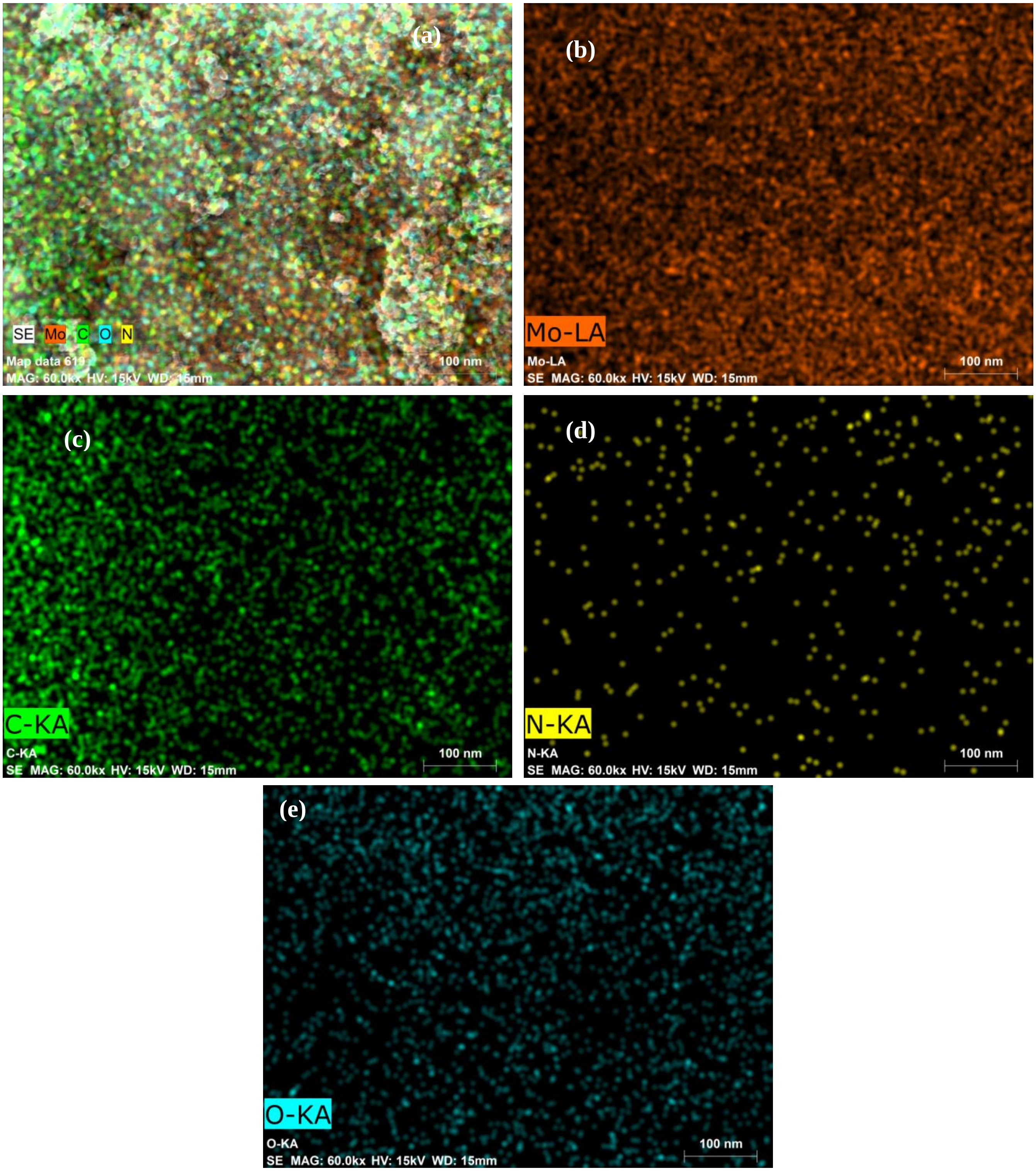

Figure 7.7: EDS elemental mapping of AM 1 (800 °C/ 10h) (a) survey , (b) Mo, (c) C, (d) N and (e) O.

TEM and HRTEM micrographs of the pure phase (Mo_2C@C/N) AM 1 and AM 2 samples are shown in Fig. 7.8 and 7.9, respectively. The TEM micrograph (Fig. 7.8a) of AM 1 reveals the agglomeration of the particles in carbon cloth. Figure 7.8b depicts the laminar growth of the carbon cloth encapsulating the aggregated Mo_2C particles. The HRTEM (Fig. 7.8c) confirm the Mo_2C phase formation. The corresponding lattice fringing matches with d-spacing of (002) and (101) planes of Mo_2C (ICDD pattern -035-0787).

The sheet like nature of carbon (Fig.7.8d) also confirm the transformation of carbon to graphite or graphene. The stacking of these sheets is also evident from the Fig. 7.8e. The dark pattern of stacked layers in Fig. 7.8d shows stacking of the multiple layers. The resemblance of d-spacing as shown in Fig. 7.8f with the (100) plane of ICDD pattern (001-0640) confirms the formation of layered graphitic carbon structures. The TEM micrograph of AM 2 in Fig. 7.9a shows the presence of particles in the linearly grown carbon. The phase formation of Mo_2C was confirmed by the HRTEM (Fig.7.9b) and the lattice fringes corresponds to the ICDD pattern -035-0787. However, certain flaky type structures were also observed in Fig.7.9c, which shows the incorporation of the Mo_2C particles in the faceted carbon structures. The presence of these stacked flaky structures is in accordance with the FESEM results. The flaky structures (Fig. 7.9d) with certain dark and transparent structures reveals the presence of multi-layer carbon structures. The HRTEM pattern shown in Fig. 7.9e is in accordance with d-spacing of graphitic carbon (ICDD pattern 001-0640). The results reveal that upon increasing the reaction temperatures (AM 2 to AM 1), linear growth of carbon structures gets enhanced. It also improves the stacking of multiple graphitic carbon layers, as supported by Raman spectroscopy (discussed below).

7.3.3 Raman spectroscopy

Raman spectroscopy is an efficient and extensive tool used to determine the nature of supported carbon species. The Raman spectroscopy pattern for all the synthesized samples is given in Fig. 7.10. The results reveal the presence of a small intense D-band at 1354.5 cm^{-1}, more intense G-band at 1580.5 at cm^{-1} and another band (2D-band) at 2714.9 cm^{-1} in AM 1. The D-band, G-band and 2D-band corresponds to distorted carbon, graphitic carbon and more ordered carbon species, respectively [37]. The higher intensity of G-band in AM 1 in comparison to D-band attributes to more graphitization of carbon species at relatively higher temperature. The more graphitization of the supported carbon is in accordance with the sharpness of the G-band peak.

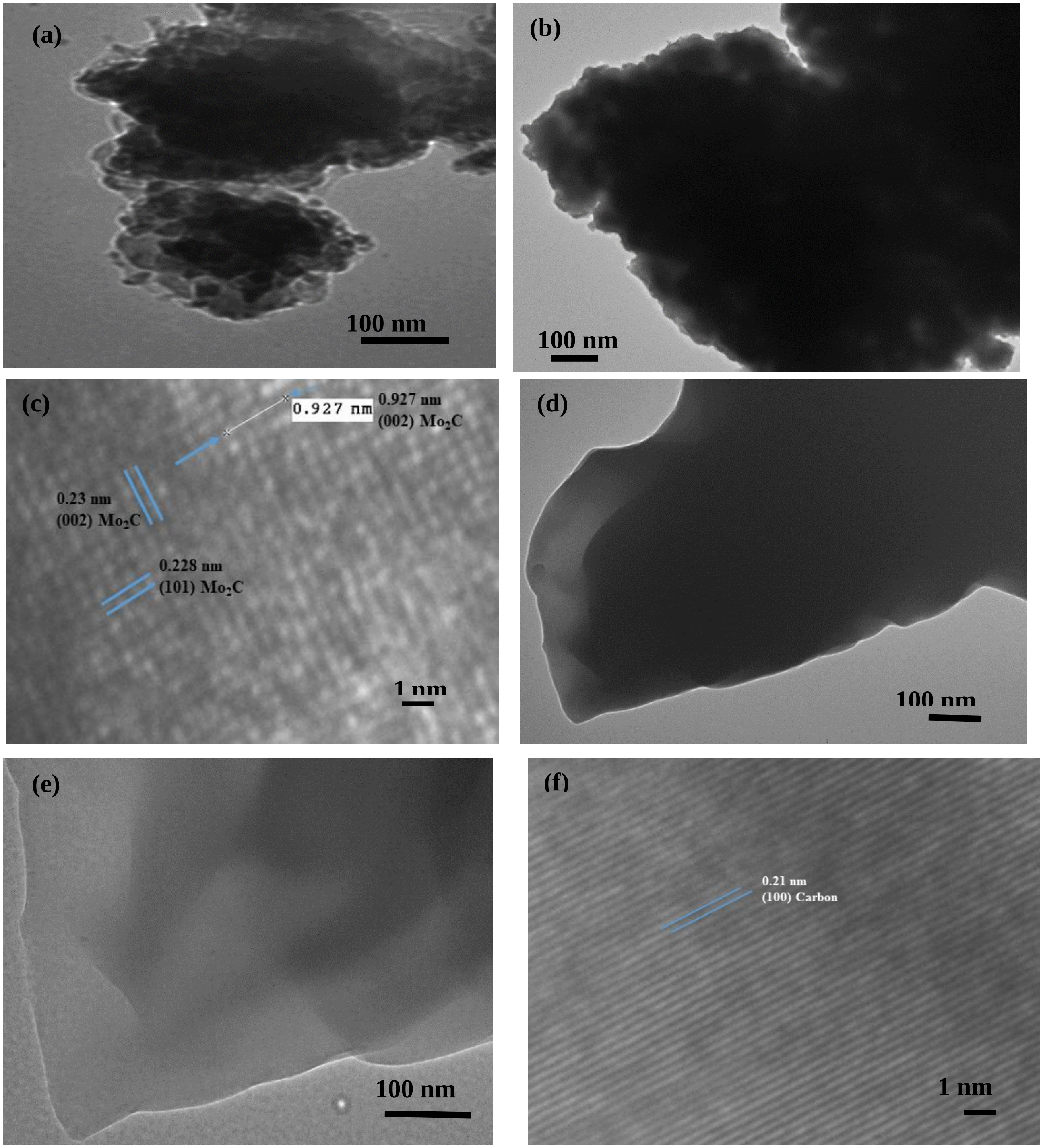

Figure 7.8: TEM micrograph of AM 1 (800 °C/ 10h) (a) showing agglomeration of particles, (b) particles embedded in carbon cloth, (c) HRTEM micrograph resembling d-spacing of Mo_2C, (d) sheet like shape of carbon, (e) stacking of carbon sheets and (f) HRTEM confirming formation of graphitic carbon.

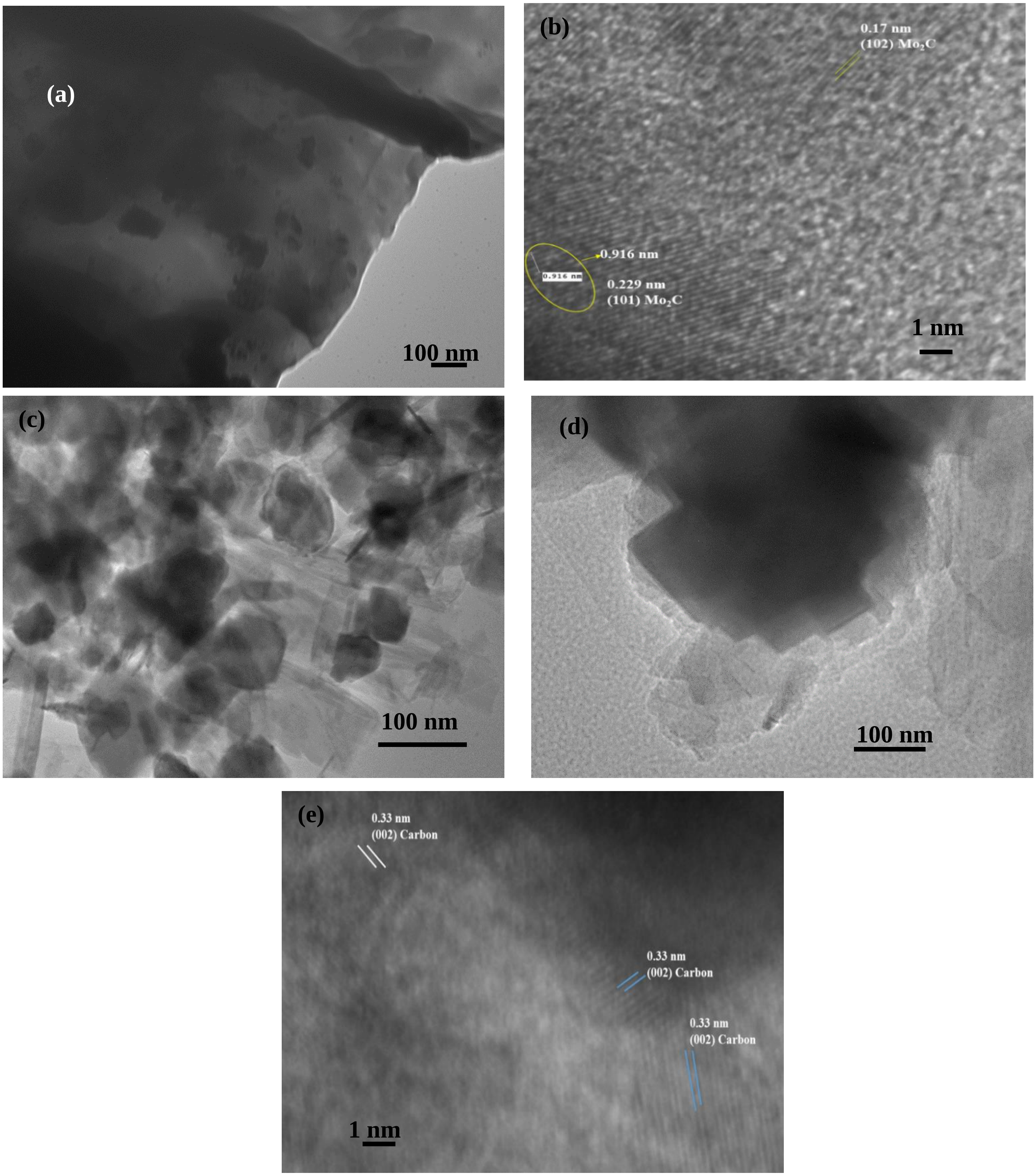

Figure 7.9: TEM micrograph of AM 2 (700 °C/ 10h) (a) showing particles embedded in carbon cloth, (b) HRTEM micrograph resembling d-spacing of Mo_2C, (c) flake like shape of carbon, (d) stacking of carbon flakes and (e) HRTEM confirming formation of graphitic carbon.

The sign of splitting and red shift in comparison to the peak position of graphene reveals the formation of layered graphitic carbon, which is also in accordance with the TEM results (Fig.7.8 and 7.9) [38]. The Raman pattern of AM 2 reveals the presence of D-band (1346.3cm^{-1}), G-band (1506.4 cm^{-1}) and 2D-band (2683.4 cm^{-1}), respectively. The I_D/I_G ratio of AM 2 (0.89) is higher compared to AM 1 (0.77), which shows more graphitization of carbon with the increase in temperature. The small sharp 2D-peak in AM 2 (Fig. 7.10) signifies the lower stacking of layers. These results are supported by the TEM results having higher transparency of flaky carbon structures as shown in Fig. 7.8. Sample AM 3 shows the peaks at positions 822.3 and 996.9 cm^{-1} corresponding to Mo-O-Mo and M=O stretching, respectively [39]. This also confirms the presence of the oxide species in the AM 3. The higher intense D-band (1333.3 cm^{-1}) compared to G-band (1597.6 cm^{-1}) for AM 3 indicates the presence of more distorted carbon at relatively lower temperature. The low intense 2D-band at 2662.1 cm^{-1} having higher value I_D/I_G (1.1), depicts the presence of more distorted carbon as compared to the AM 1 and AM 2, respectively.

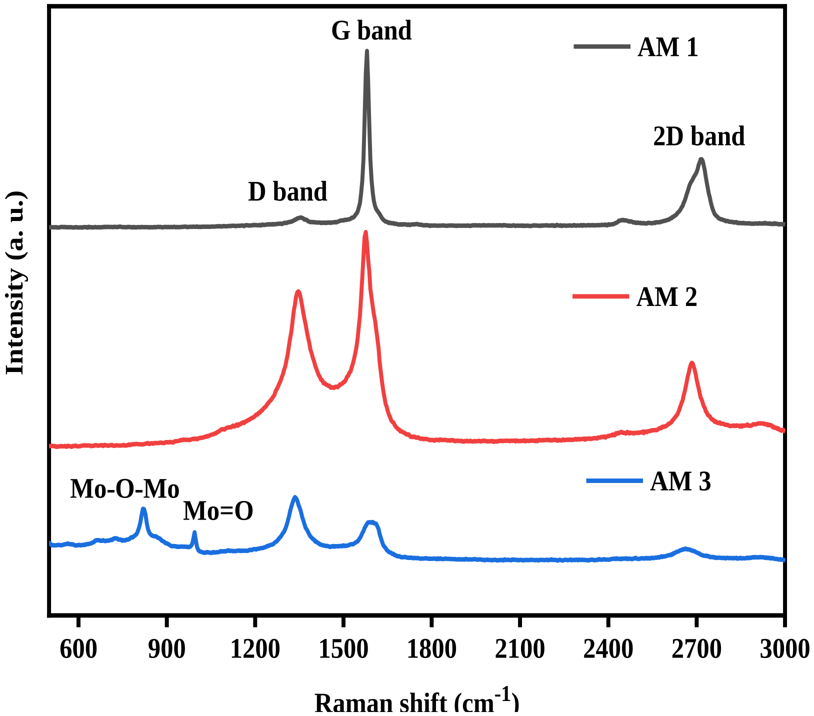

Figure 7.10: Raman Spectroscopy pattern of the synthesized samples AM 1 (800 °C/ 10h), AM 2 (700 °C/ 10h) and AM 3 (600 °C/ 10h).

7.3.4 X-ray photoelectron spectroscopy (XPS)

The presence of nitrogen in the synthesized sample was confirmed by XPS (Fig. 7.11) and it also reveals the surface chemistry as well as oxidation states of the product phase. The XPS survey spectra of the synthesized sample is given in Fig. 7.11a, which shows the presence of molybdenum (Mo), carbon (C), nitrogen (N) and oxygen (O).

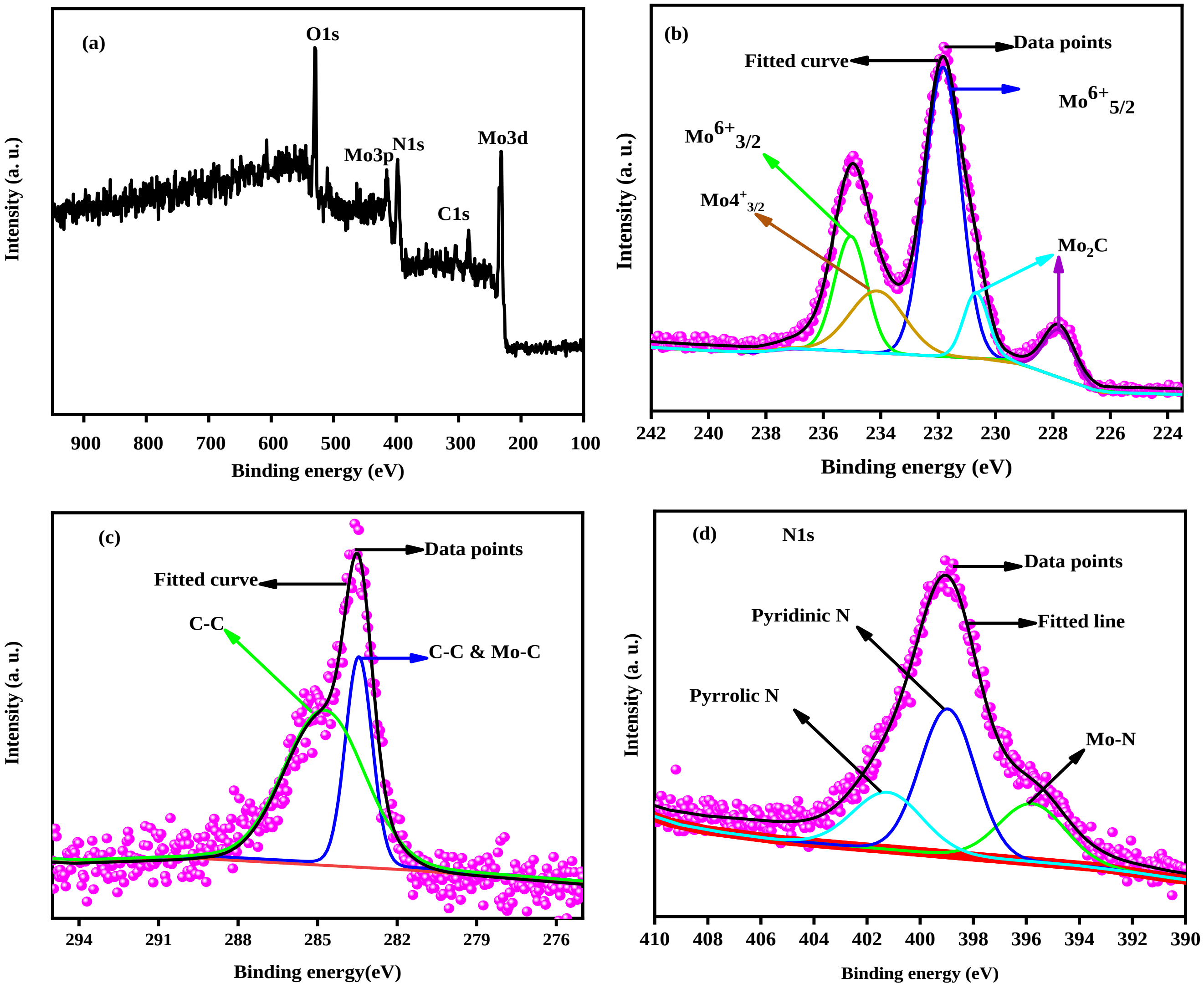

Figure 7.11: XPS of AM 1 (800 °C/ 10h) (a) Survey spectrum, (b) Mo3d, (c) C1s and (d) N1s.

The high resolution (HR) spectra of Mo3d deconvoluted into six peaks is shown in Fig. 7.11b. The peaks at lower binding energy (BE) 227.9 and 230.7 eV correspond to Mo_2C [40]. The results confirm the formation of Mo_2C phase in the synthesized sample. The peaks at 231.7 and 235.1 eV, respectively attribute to the doublet of the MoO_3 having oxidation state of 6^+. The extra peak at 234.2 eV correspond to the 4^+ oxidation state of MoO_2. The presence of these oxide phases may be because of the surface oxidation during the XPS analysis. The C1s spectra of carbon is given in Fig. 7.10c yielding two deconvoluted peak at 283.1 eV correspond to Mo-C and C-C (SP^3 C-C), respectively. The additional peak at 284.8 eV is attributed to C-C (SP^2 C-C) [41]. The Mo-C and C-

C have almost similar BE and usually overlap in the spectra of C1s [12]. The presence of N in the synthesized sample has different bonding nature as is evident from the peak deconvolution of N1s (Fig. 7.11d). The peak at positions 395.8, 398.9 and 401.3 eV corresponds to the Mo-N bonding, pyridinic N and pyrrolic N, respectively [30]. XPS analysis predicted the successful incorporation of N in the carbon matrix over Mo_2C. The N incorporation in the carbon matrix over Mo_2C enhances the HER performance by withdrawing active hydrogen and the lone pairs of electrons in the carbon matrix [42].

7.4. Electrochemical activity

7.4.1 HER performance

The electrocatalytic HER activity of Mo_2C@C/N was studied in acidic electrolyte and the polarization curves of the synthesized samples are shown in Fig. 7.12a. Among the synthesized samples, the pure phase Mo_2C (AM 1 and AM 2) displayed a maximum current density of nearly 60 and 37 mAcm^{-2}. The relatively lower temperature synthesized samples shows a lower current density value of about 10 mAcm^{-2}, respectively. The results reveal that the carburization to form (Mo_2C) enhances the charge transfer rate due to its similar electronic and catalytic behavior as that of the platinum. The higher current density yielded by AM 1 (800 °C/ 10h) compared to AM 2 (700 °C/ 10h) might be attributed to the crystallization of the product phase and higher graphitic carbon content with respect to the synthesis temperature. The presence on N in the supported carbon matrix enhances the conductivity of the carbon matrix and also elevates the current density as compared to the commercial Mo_2C.

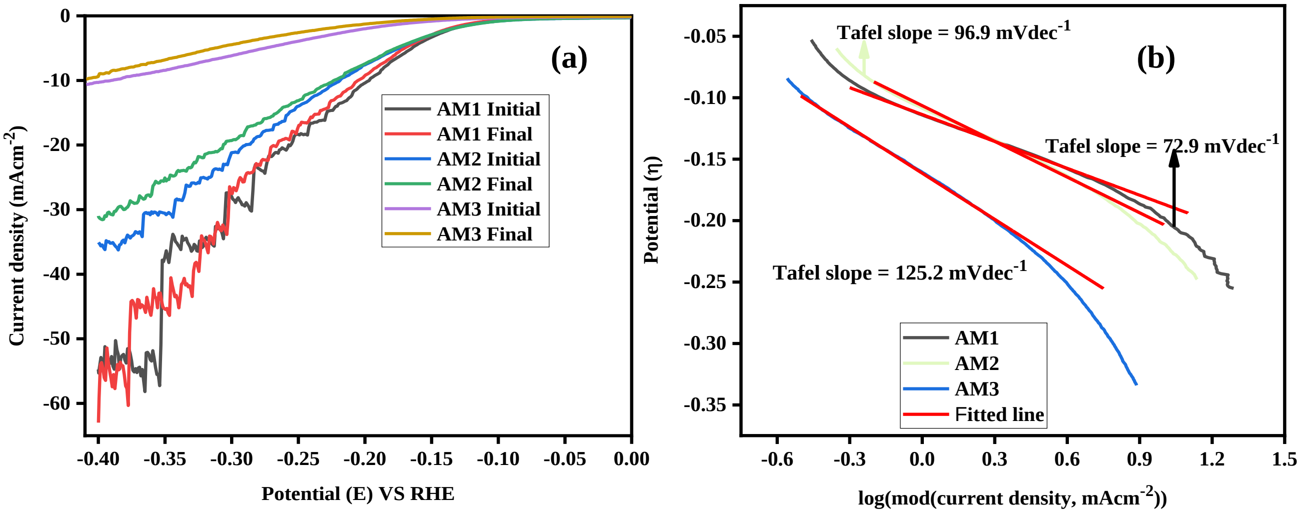

Figure 7.12: (a) LSV plot before and after 2000 CV cycles, and (b) Tafel plot of the synthesized samples.

To elucidate the mechanism responsible for the HER, Tafel analysis was done (Fig. 7.12b). The HER activity on the catalyst surface proceeds by the following three steps Volmer, Heyrovsky and Tafel reactions [23,43]. The value of the Tafel slope determines the rate determining step for the HER. The value of Tefel slope ~120 mVdec^{-1} demonstrates low desorption kinetics of the electro catalyst and supports Volmer reaction as the rate determining step. However, the Tafel slope of 30 and 40 mVdec^{-1} determines the fast adsorption and desorption kinetics and H^+ ion on the surface of the electrocatalyst and attributes to Tafel and Heyrovsky reaction as the rate determining step. The Tafel slope (Fig. 7.12b) of the synthesized Mo_2C (AM 1 and AM 2) is 72.9 and 96.9 mVdec^{-1}, respectively. The results reveal the Volmer-Heyrovsky as the rate determining step for the sample synthesized at relatively higher temperature. The Tafel slope of the AM 3 (Table 7.3) elucidates Volmer reaction as the rate determining step and corresponds to the low desorption of H^+ ion absorbed on the surface. This might correspond to the lower synthesis temperature and presence of less content of carburized product, which enhances the charge transfer rate. The Tafel slope of AM 1 is better as compared to some reported results of carbon supported Mo_2C, which indicates enhanced kinetics exhibited by the synthesized product [10,11,28,30,44]. Along with the Tafel slope, the over potential to attain a current density of 10 mAcm^{-2} is an important parameter to determine the efficiency of elctrocatalyst, because most solar equipment operates with the said amount of current density. AM 1 reveals the lower over potential of 186.6 mV, lower than AM 2 and AM 3, respectively. The obtained values are given in Table 7.3. The over potential exhibited by the AM 1 also shows better performance than reported results [11,30,45]. This result validates that the nitrogen incorporation within the carbon matrix over the Mo_2C enhances the charge transfer rate and provides more active sites for the HER. The comparison of the synthesized products in terms of (Tafel slope and overpotential) with the reported data is given in Table 7.4 (given at the end of chapter).

Table 7.3: Electrochemical parameters of the synthesized samples.

Sample Id	Tafel slope (mVdec^{-1})	Over potential (mV)	EDLC (mFcm^{-2})	SC (Fg^{-1})
AM 1	72.9	186.6	24.9	55.3
AM 2	96.9	203.3	15.3	34.0
AM 3	125.2	286.6	2.9	6.4

The stability is essential for the practical application of any electrocatalyst. The stability of the synthesized samples was studied by performing LSV (polarization curve) after 2000 cycles (Fig.

7.11a). The LSV curves show negligible loss of current for the AM 1 as compared to AM 2 and AM 3. The higher stability exhibited by AM 1 attributes to its higher crystalline nature and formation of layer of C/N coating over Mo_2C, which inhibits the acidic corrosion during continuous CV cycling. The stability of pure phase AM 1 and AM 2 was also analyzed by chronoamperomtry (CA), which plots the current density ($mAcm^{-2}$) on the x-axis with respect to time (hours) on the y-axis as shown in Fig. 7.13. Almost negligible loss of current at a given potential for 10 h could be observed. The results indicate that the synthesized samples can be regarded as the stable catalyst for the continuous performance. The fluctuation in the curve might correspond to the continuous release of hydrogen bubbles from the surface. The fluctuation in polarization curve before and after 2000 CV cycles was also observed for AM 1 and AM 2 (Fig. 7.11a). However, the polarization and CA curve of AM 3 almost remains smooth, which attributes to the strong adsorption of H^+ on the surface and facilitates the Volmer reaction and hinders the desorption of H^+ (Heyrovsky reaction). The incorporation of N in the supportive carbon matrix over Mo_2C and formation of this heterojunction enhances the fast release and electron regulation on the surface of the electrocatalyst.

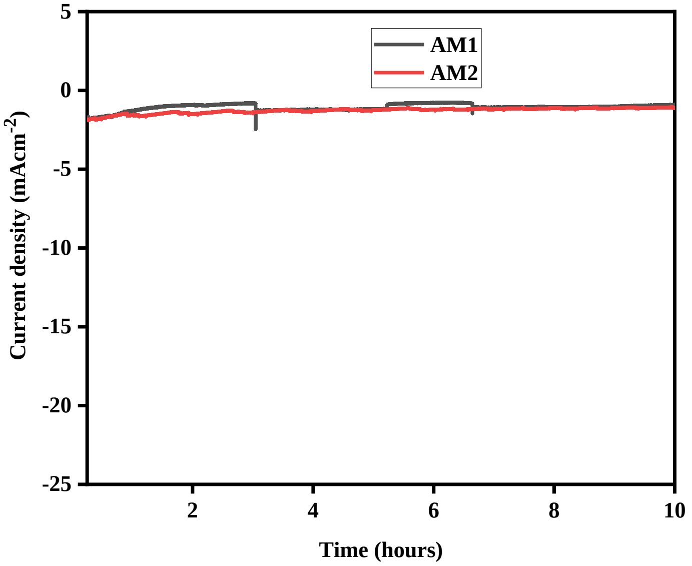

Figure 7.13: Chronoamperometry (CA) plot of AM 1 (800 °C/ 10h) and AM 2 (700 °C/ 10h).

7.4.2 Electrochemical double layer capacitance (EDLC, C_{dl})

The energy storage ability of the synthesized material was tested via cyclic voltammetry (CV) analysis (Fig. 7.14). The EDLC (C_{dl}) measurements was done by CV analysis performed at various scan rates 20-320 mVs^{-1} at a difference of 30 mVs^{-1}as shown in Fig.7.14a-c. No redox peaks are observed in the CV curve, which shows the non-Faradic behavior of the synthesized samples. The retention of the rectangular shape, even at higher scan rates reveals the good capacitance capability during the charging/discharging processes. The rectangular curves yielded by AM 1 (Fig. 7.14a) and AM 2 (Fig. 7.14b) are nearly perfect and have broader area as compared to the AM 3, which exhibits a quasi-rectangular curve (Fig.7.14c). The C_{dl} estimated from the plot of scan rate (mVs^{-1}) with current density ($\Delta J_{0.3}$, $mAcm^{-2}$) depicted in Fig. 7.14d signifies that the results are in order of AM 1> AM 2> AM 3 and the estimated values are tabulated in Table 7.3. The corresponding specific capacitance (CS, Fg^{-1}) obtained using the criterion given in equation 3.12 and the obtained values are tabulated in Table 7.3.

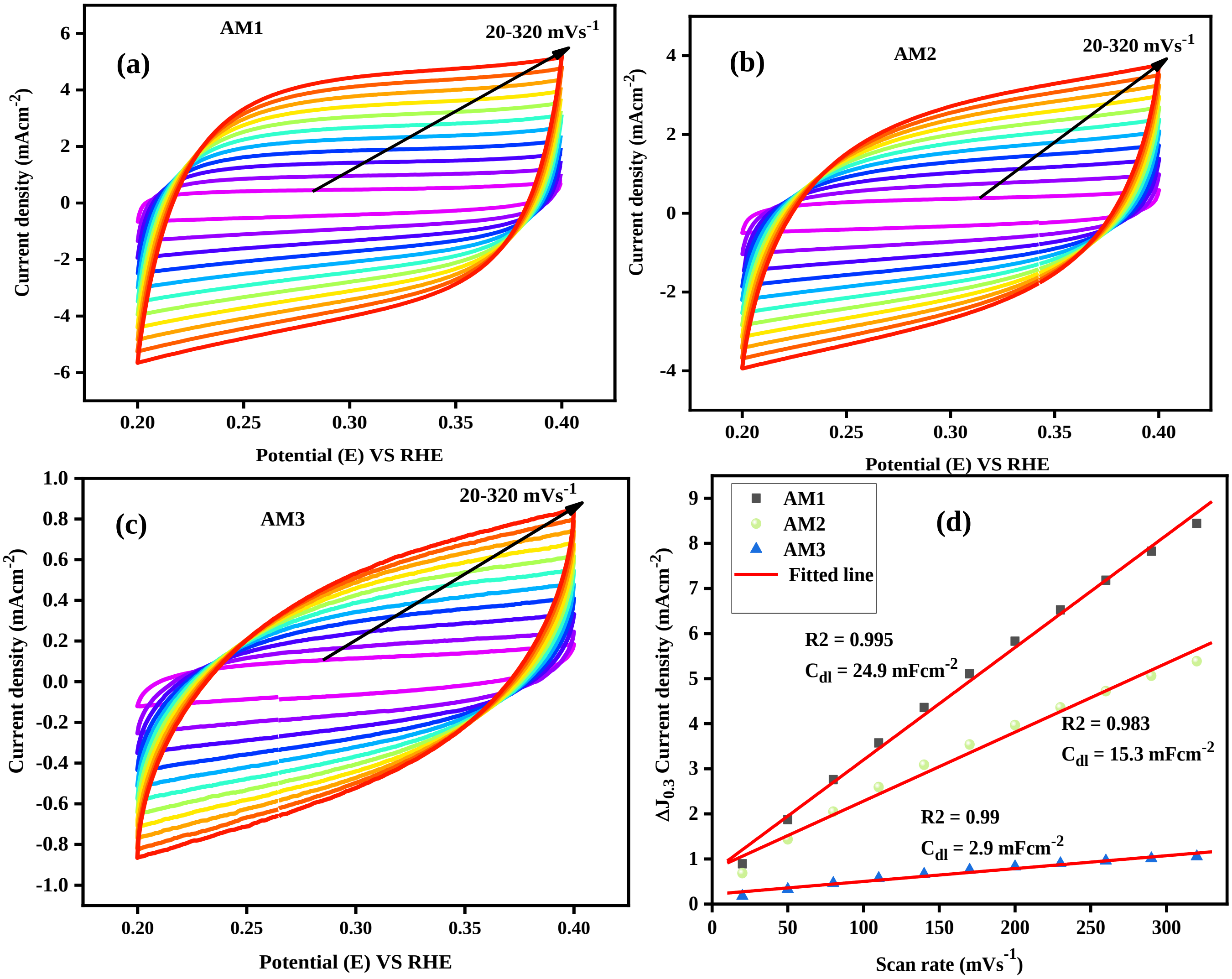

Figure 7.14: Cyclic voltammetry (CV) (a) AM 1 (800 °C/ 10h), (b) AM 2 (700 °C/ 10h), (c) AM 3 (600 °C/ 10h) at multiple scan rates, (d) EDLC (C_{dl}) plot of scan rate vs current density.

The pure phase Mo_2C with more crystalline nature and higher graphitic carbon content enhances the charge storage capacity. The charge storage capacity exhibited by pure phase samples is considerably higher [23,46–48] . It also indicates that AM 1 possess higher electrochemical active surface area (ECSA) as compared to AM 2 and AM 3, respectively. The higher ECSA of AM 1 predicts more active sites available in the product phase, which is in accordance with the LSV data, Tafel slope and EDLC measurements. The higher ECSA of AM 1 corresponds to the higher amount of graphitic and graphene carbon content, which is porous in nature. The stacking of sheet like structure of graphite enhances the electrochemical active sites and hence increases the ECSA, EDLC and HER activity.

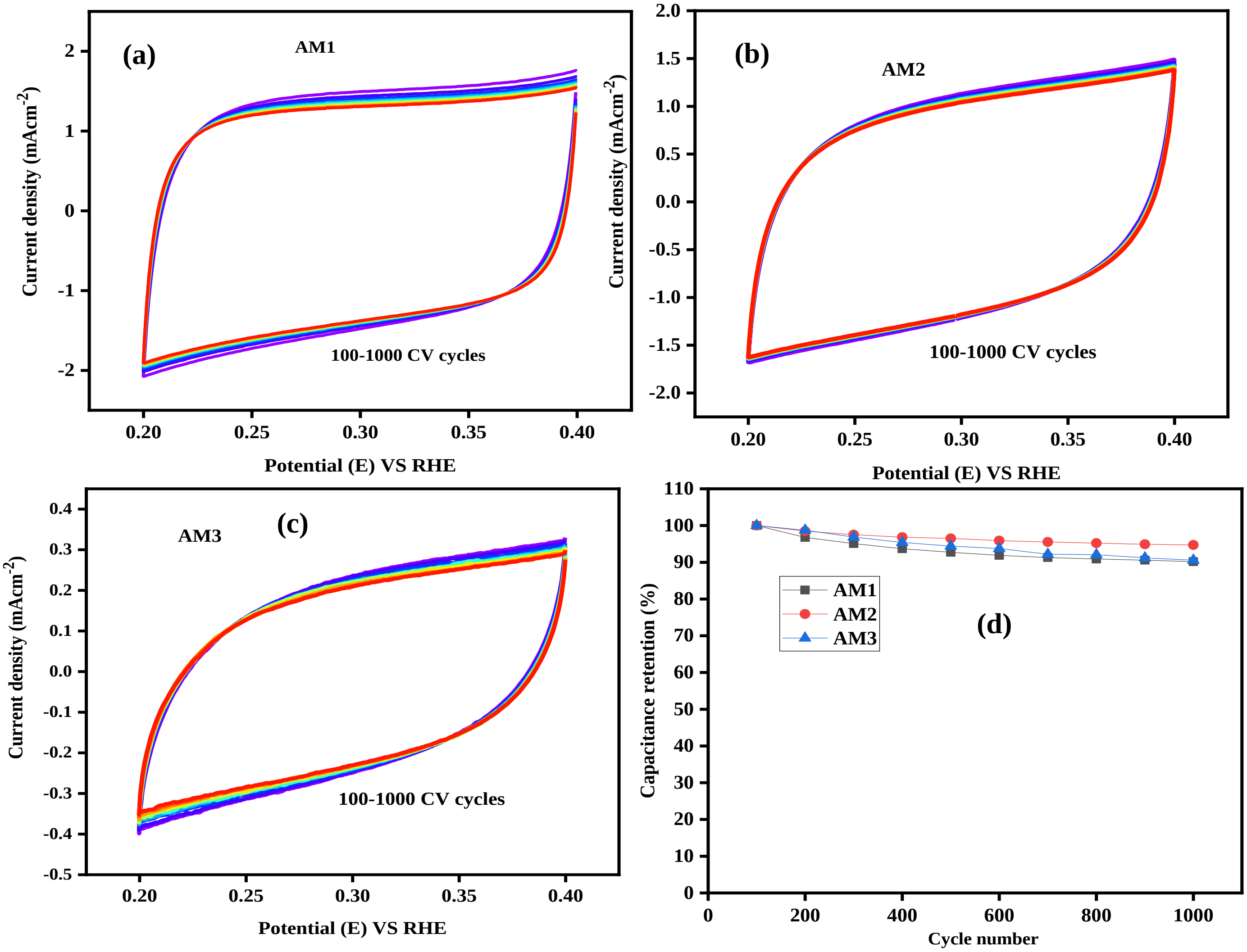

Figure 7.15: CV at fixed scan rate for 1000 cycles (a) AM 1, (b) AM 2, (c) AM 3 and (d) Capacitance retention (%) versus cycle number for 1000 CV cycles.

The stability of the material for longer duration is essential for the commercial applications. The stability of the synthesized samples was tested by CV analysis performed up to 1000 CV cycles in the given voltage window. The CV plots for the 1000 CV cycles for AM 1, AM 2 and AM 3 is shown in Fig. 7.15a-c. The capacitance retention (%) with CV cycle number is given in Fig. 7.15d. The AM 2 exhibits higher stability as compared to AM 1 and AM 3. The stability of the AM 2 is attributed to its lower crystalline nature [49]. The synthesized products reveal higher stability when compared to the reported result and yields more than 90 % capacitance retention after 1000 CV cycles [10]. The higher retention and maintenance of the CV curve shape corresponds to less corrosion reactions in acidic medium. The higher stability could be attributed to the nitrogen incorporated coating, which inhibits the oxidation in acidic electrolyte during continuous cycling. The presence of nitrogen maintains the active sites for electron flow and also shorten their path with a lower resistance path. Nitrogen atom along with lone pair of electrons always enhances the electron sites, improving the conductivity of the carbon matrix and elevates the charge storage ability.

7.4.3 Electrochemical impedance spectroscopy (EIS)

To reveal deep insight into the reaction kinetics of HER, the EIS measurements of pure phase Mo_2C has been done as shown in Fig 7.16a-d. The dependence of EIS curves on the given voltage has been reported in literature [50]. The Nyquist plot of AM 1 and AM 2 are given in Fig.7.16a and b, respectively. The plot reveals the lower series resistance (R_S) of AM 1 (33.0 Ohm) as compared to the AM 2 (42.02 Ohm). The ability of AM 1 to form the semicircle in high frequency region demonstrate the lower charge transfer resistance (CTR) [2]. The higher slope of AM 2 in low frequency region as compared to AM 1 demonstrates the efficient mass transfer on the electrode surface and the electrolyte. The deviation from the semicircular shape and fit of the curve attributes to electrode porosity, variable capacitance across the surface (surface roughness), non-uniform current densities or non-equipotential surfaces, respectively [11]. The deviation from the fit also corresponds to the presence of a constant phase element (CPE) originating because of surface inhomogeneity and fractal geometry. Moreover, it attributes to the adsorption on the catalyst surface. The lower phase change at higher frequency indicates lower resistance and higher reaction kinetics of AM 1 as compared to AM 2 (Fig.7.16c-d). The little semicircular shape observed in Fig. 7.16c is attributed to kinetics of HER process. The results are in accordance with the LSV and Tafel plots depicted higher current density and lower Tafel slope of AM 1 as compared to AM 2.

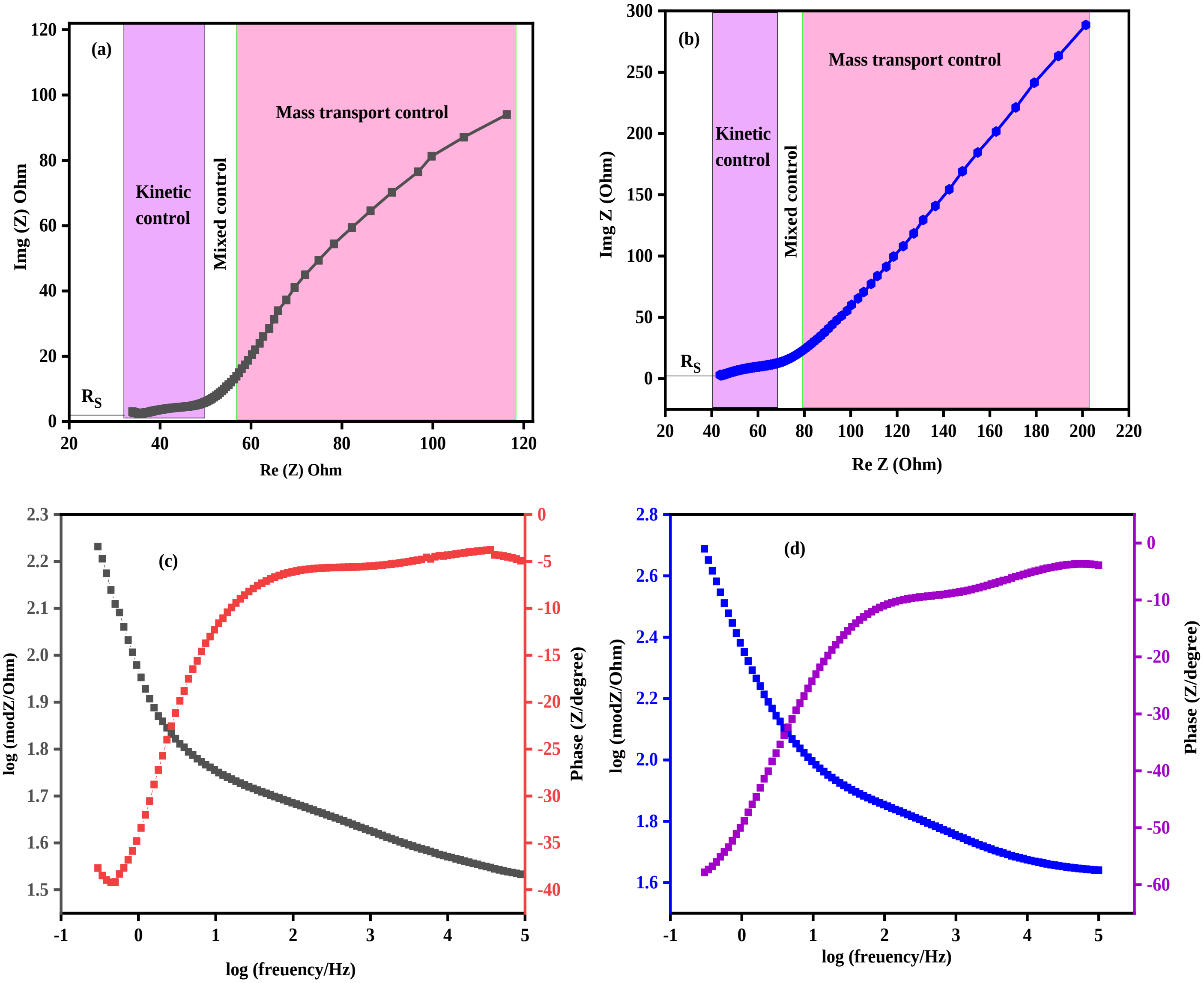

Figure 7.16: Electrochemical impedance plots Nyquist plots of (a) AM 1 (800 °C/ 10h) and (b) AM 2 (700 °C/ 10h) and Bode plots (c) AM 1 and (d) AM 2.

Table 7.4: Comparison of electrochemical HER activity with reported data in 0.5 M H_2SO_4.

Sample Id	Tafel slope (mVdec^{-1})	Overpotential (η) 10 mAcm^{-2}	Exchange curren density (j_0) mAcm^{-2}	Mass loading (mg/cm^{-2})	References
AM 1 (Mo$_2$C@C/N)	72.9	186.6	2.75×10^{-2}	0.46	**This work**
AM 2 (Mo$_2$C@C/N)	96.9	203.3	7.9×10^{-2}	0.46	
AM 3	125.2	286.6	5.1×10^{-2}	0.46	
rGO-C-MoP	111	236		1.6	11
MoO$_2$/HCSs	328	536			28
Mo$_2$C/HCSs	75	153			
MoS$_2$/HCSs	274	426			
Co/-β-Mo$_2$C@N-CNTs	92	170	0.14		29
Co@N-CNTs	115	275	0.020		
Mo$_2$C@N-CNTs	171	452	0.053		
Mo$_2$C/C	110	340			30
Mo$_2$C/NCNT-10	86	213			
Mo$_2$C/NCNT-20	82	200			
Mo$_2$C/NCNT-30	75	195			
Mo$_2$C/NCNT-40	81	212			
NCNT		497			
CNTs		596			
Mo$_2$C@N-CNFs	70	192	0.0473		51
com-Mo$_2$C	114.54	313	0.000738		

References

1 X. Zou and Y. Zhang, *Chemical Society reviews*, 2015, **44**, 5148–80.

2 Y. Liu, B. Huang, X. Hu and Z. Xie, *International Journal of Hydrogen Energy*, 2019, **44**, 3702–3710.

3 N. Xu, G. Cao, L. Gan, Z. Chen, M. Zang, H. Wu and P. Wang, *International Journal of Hydrogen Energy*, 2018, **43**, 23101–23108.

4 J. Durst, A. Siebel, C. Simon, F. Hasche´, J. Herranz and H. A. Gasteiger, *Energy & Environmental Science*, 2014, **7**, 1–9.

5 K. M. Naik and S. Sampath, *Electrochimica Acta*, 2017, **252**, 408–415.

6 V. Kiran, K. L. Nagashree and S. Sampath, *RSC Advances*, 2014, **4**, 12057–12064.

7 C. G. Morales-Guio, L. A. Stern and X. Hu, *Chemical Society Reviews*, 2014, **43**, 6555–6569.

8 P. C. K. Vesborg, B. Seger and I. Chorkendorff, *Journal of Physical Chemistry Letters*, 2015, **6**, 951–957.

9 S. K. Park, G. D. Park, D. Ko, Y. C. Kang and Y. Piao, *Chemical Engineering Journal*, 2017, **315**, 355–363.

10 N. Kaur, R. A. Mir and O. P. Pandey, *Journal of Alloys and Compounds*, 2019, **782**, 119–131.

11 K. Ojha, M. Sharma, H. Kolev and A. K. Ganguli, *Catalysis Science and Technology*, 2017, **7**, 668–676.

12 Q. Gao, X. Zhao, Y. Xiao, D. Zhao and M. Cao, *Nanoscale*, 2014, **6**, 6151–6157.

13 C. J. Wallar, R. Poon and I. Zhitomirsky, *Journal of The Electrochemical Society*, 2017, **164**, A3620–A3627.

14 Y. Su and I. Zhitomirsky, *Journal of Power Sources*, 2014, **267**, 235–242.

15 R. M. Silva, B. S. Noremberg, N. H. Marins, J. Milne, I. Zhitomirsky and N. L. V. Carreño, *Journal of Materials Research*, 2019, **34**, 592–599.

16 M. Miao, J. Pan, T. He, Y. Yan, B. Y. Xia and X. Wang, *Chemistry - A European Journal*, 2017, **23**, 10947–10961.

17 H. Vrubel and X. Hu, *Angewandte Chemie - International Edition*, 2012, **51**, 12703–12706.

18 Y. C. Chen, A. Y. Lu, P. Lu, X. Yang, C. M. Jiang, M. Mariano, B. Kaehr, O. Lin, A. Taylor, I. D. Sharp, L. J. Li, S. S. Chou and V. Tung, *Advanced Materials*, 2017, **29**, 1–11.

19 C. Giordano, C. Erpen, W. Yao and M. Antonietti, *Nano Letters*, 2008, **8**, 4659–4663.

20 J. Dang, G. H. Zhang, L. Wang and K. C. Chou, *International Journal of Refractory Metals and Hard Materials*, 2015, **51**, 275–281.

21 X. Li, L. Yang, T. Su, X. Wang, C. Sun and Z. Su, *J. Mater. Chem. A*, 2017, **5**, 5000–5006.

22 H. Yan, Y. Xie, Y. Jiao, A. Wu, C. Tian, X. Zhang, L. Wang and H. Fu, *Advanced Materials*, 2018, **30**, 1–8.

23 J. Sen Li, Y. Wang, C. H. Liu, S. L. Li, Y. G. Wang, L. Z. Dong, Z. H. Dai, Y. F. Li and Y. Q. Lan, *Nature Communications*, 2016, **7**, 11204.

24 F. Béguin, V. Presser, A. Balducci and E. Frackowiak, *Advanced Materials*, 2014, **26**, 2219–2251.

25 J. Li, Q. M. Yang and I. Zhitomirsky, *Nanoscale Research Letters*, 2010, **5**, 512–517.

26 R. Chen, I. K. Puri and I. Zhitomirsky, *Ceramics International*, 2018, **44**, 18007–18015.

27 Y. Su and I. Zhitomirsky, *Journal of The Electrochemical Society*, 2015, **162**, A5013–A5019.

28 Y. Yang, M. Luo, Y. Xing, S. Wang, W. Zhang, F. Lv, Y. Li, Y. Zhang, W. Wang and S.

Guo, *Advanced Materials*, 2018, **30**, 1–8.
29 T. Ouyang, Y. Q. Ye, C. Y. Wu, K. Xiao and Z. Q. Liu, *Angewandte Chemie - International Edition*, 2019, **58**, 1–7.
30 Y. J. Song, J. T. Ren, G. Yuan, Y. Yao, X. Liu and Z. Y. Yuan, *Journal of Energy Chemistry*, 2019, **38**, 68–77.
31 J. Chen, H. Yang, X. Xu, Z. Su, Y. Guo and Q. Wang, *Applied Surface Science*, 2018, **455**, 187–194.
32 X. J. Yang, X. J. Feng, H. Q. Tan, H. Y. Zang, X. L. Wang, Y. H. Wang, E. B. Wang and Y. G. Li, *Journal of Materials Chemistry A*, 2016, **4**, 3947–3954.
33 D. K. Singh, R. N. Jenjeti, S. Sampath and M. Eswaramoorthy, *Journal of Materials Chemistry A*, 2017, **5**, 6025–6031.
34 S. Chaudhury, S. K. Mukerjee, V. N. Vaidya and V. Venugopal, *Journal of Alloys and Compounds*, 1997, **261**, 105–113.
35 H. K. Sidana, R. A. Mir and O. P. Pandey, *Journal of Alloys and Compounds*, 2018, **736**, 255–265.
36 H. Cavus, C. Kahruman and I. Yusufoglu, *The Minerals, Metals & Materials Society*, 2012, 785–796.
37 A. C. Ferrari, *Solid State Communications*, 2007, **143**, 47–57.
38 A. Das, B. Chakraborty and A. K. Sood, *Bulletin of Materials Science*, 2008, **31**, 579–584.
39 A. Bhaskar, M. Deepa, T. N. Rao and U. V. Varadaraju, *Journal of Power Sources*, 2012, **216**, 169–178.
40 N. S. Alhajri, D. H. Anjum and K. Takanabe, *Journal of Materials Chemistry A*, 2014, **2**, 10548–10556.
41 A. Fujimoto, Y. Yamada, M. Koinuma and S. Sato, *Analytical Chemistry*, 2016, **88**, 6110–6114.
42 J. Li, C. Zhou, J. Mu, E. C. Yang and X. J. Zhao, *RSC Advances*, 2018, **8**, 17202–17208.
43 K. Rajrana, A. Gupta, R. A. Mir and O. P. Pandey, *Physica B: Condensed Matter*, 2019, **564**, 179–185.
44 L. K. Brar, A. Gupta and O. P. Pandey, *Catalysis Today*, 2019, **325**, 98–108.
45 Y. Zheng, Y. Jiao, L. H. Li, T. Xing, Y. Chen, M. Jaroniec and S. Z. Qiao, *ACS Nano*, 2014, **8**, 5290–5296.
46 T. Xiong, J. Jia, Z. Wei, L. Zeng, Y. Deng, W. Zhou and S. Chen, *Chemical Engineering Journal*, 2019, **358**, 362–368.
47 J. Tan, X. He, F. Yin, X. Liang, B. Chen, G. Li and H. Yin, *Journal of Materials Science*, 2018, **54**, 4589–4600.
48 J. Q. Chi, J. Y. Xie, W. W. Zhang, B. Dong, J. F. Qin, X. Y. Zhang, J. H. Lin, Y. M. Chai and C. G. Liu, *ACS Applied Materials and Interfaces*, 2019, **11**, 4047–4056.
49 K. Zhang, C. Li, Y. Zhao, X. Yu and Y. Chen, *Physical chemistry chemical physics*, 2015, **17**, 16609–14.
50 K. Ojha, S. Saha, S. Banerjee and A. K. Ganguli, *ACS Applied Materials and Interfaces*, 2017, **9**, 19455–19461.
51 Z.-Y. Wu, B.-C. Hu, P. Wu, H.-W. Liang, Z.-L. Yu, Y. Lin, Y.-R. Zheng, Z. Li and S.-H. Yu, *NPG Asia Materials*, 2016, **8**, 1–8.

Chapter 8

Conclusions and Future Scope

Overview

The present chapter summarizes the outcomes of the work done on nano Mo_2C using different molybdenum sources like molybdenum oxide (MoO_3) and $(NH_4)_6Mo_7O_{24}4H_2O$ (AHM). The importance of using non-biodegradable waste for synthesis of carbon coated Mo_2C has been summarized. The role of synthesis parameters (temperature/time) and carbon source (nature/amount) on pure phase formation has been described. The importance of nitrogen incorporation and role of adherent nature/amount of carbon encapsulating Mo_2C on electrocatalytic activity (HER and EDLC performance) has been concluded and summarized in this chapter. Future scope of the work is presented at the end of this chapter.

8.1 Conclusions

Molybdenum carbide (Mo_2C) is the most versatile candidate for electrocatalytic applications among transition metal carbides (TMCs). The efficiency of Mo_2C enhances in nanoscale, but the synthesis of pure phase nano Mo_2C is very crucial. The synthesis parameters play very vital role to accomplish carburization of molybdenum source to Mo_2C. The efficiency and stability is highly influenced on the adherent nature and amount of surface carbon, which depends on nature and amount of initial carbon source and synthesis temperature. Based on the work done, following conclusions are drawn:

Carbon supported molybdenum carbide (β-Mo_2C@C) has been synthesized in a specially designed autoclave at 600, 700, and 800 °C for 20, 14 and 10 hours, respectively. MoO_3 and analytical grade polypropylene has been used as molybdenum and carbon source, respectively. The presence of magnesium enhances the reduction-carburization and decomposition of polypropylene inside the autoclave. The crystallite size, surface area, nature of surface carbon over Mo_2C influence the HER activity and stability. The strain developed during the in-situ synthesis affect the electrocatalytic activity. The higher graphitic carbon content in sample synthesized at relatively higher temperature (800 °C) shows higher charge transfer kinetics with lower Tafel slope of 68.9 $mVdec^{-1}$ and overpotential of 195.3 mV to attain current density of 10 $mAcm^{-2}$ compared to those synthesized at relatively lower temperatures. The obtained results are lower than the reported data. The lower temperature (600 °C) synthesized phase having more distorted carbon content over Mo_2C exhibits higher stability and capacitance (EDLC) performance of 30$mFcm^2$, which is higher than the reported in literature. It also provides a path to utilize waste plastics for formation of such efficient and stable electrocatalyts.

The plastic waste (polypropylene based /used laboratory pipette tip) derived carbon supported molybdenum carbide (Mo_2C/C) has been synthesized at 600 for 15 h, 700 and 800 °C for 10 h, respectively. The study shows a prominent role of initial and final residual carbon content on pure phase formation, structural properties, surface characteristics and electrocatalytic applications, respectively. The optimum carbon content of 1g shows lower strain state and stable phase formation. The final residual carbon content varies with initial carbon content. The higher current density observed in lower temperature synthesized phase (MoC) is attributed to its lower crystallite size and higher surface area. In case of Mo_2C, the more graphitic and graphene formation with increase in temperature enhances the HER activity and EDLC performance due to higher conductivity and surface characteristics. The samples synthesized at 800 °C with 0.75 and 1 g of initial carbon shows lower Tafel slope of 80.11 and 82.6 $mVdec^{-1}$ exhibiting higher charge transfer kinetics. The lower crystallite size and higher surface area obtained at relatively lower temperature (600 °C) enhances the charge storage capacity exhibiting the EDLC of 23.4 $mFcm^{-2}$. The Tafel slope and EDLC values obtained is better than some of the reported results.

The pure phase carbon coated molybdenum carbide (C-Mo_2C) and nitrogen incorporated carbon coated molybdenum carbide (C/N-Mo_2C) has been synthesized in autoclave using MoO_3 and AHM as Mo and N/Mo source, respectively. Waste polyethene was used a carbon source in both the cases. Synthesis parameters affect the pure phase formation. The sheet like structure of carbon is more in this case compared to those observed using polypropylene and plastic wastes. This is attributed to the linear/laminar and 2-dimensional (2D) characteristics of waste polyethene (carbon source). The comparative study between C-Mo_2C and C/N-Mo_2C shows the higher efficiency and stability of C/N-Mo_2C for HER activity due to synergistic effects of N incorporation. C/N-Mo_2C exhibts a lower Tafel slope of 69.2 $mVdec^{-1}$, which is very low compared to C-Mo_2C and other reported elctrocatlyts. The 2D and flaky nature of relatively higher temperature synthesized phase (C-Mo_2C) shows enhanced EDLC performance and specific capacitance (SC) of 21.3 $mFcm^{-2}$ and 46.2 Fg^{-1}, respectively. This is mainly attributed to stacking of nano structurers and graphene like nature of residual carbon.

Effect of synthesis parameters on pure phase formation of nitrogen incorporated carbon supported molybdenum carbide (Mo_2C@C/N) were further studied using waste plastic (used pipette tip) as carbon source. The higher hydrocarbon chain in polypropylene based waste (pipette tip) enhances the pure phase formation at relatively lower temperature and time. The adherent nature of carbon matrix influence the electrocatalytic activity. The relatively higher temperature phase exhibits higher HER activity due to its lower Tafel slope (72.9 $mVdec^{-1}$) and higher current density (~60 $mAcm^{-2}$) in smaller voltage window. It also shows the EDLC performance (24.9 $mFcm^{-2}$) and higher stability than relatively lower temperature synthesized phase. The comparative results of electrochemical performances of the synthesized pure phase carbon supported Mo_2C samples is given in Table 8.1.

Table 8.1: Electrochemcial performance of pure phase carbon supported Mo_2C samples:

Sample Id	Carbon source	Reaction temperature/ Time	Tafel slope '*b*'	Overpotential (mV) at 10 mAcm^{-2}	EDLC (mFcm^{-2})
β-Mo_2C@C	polypropylene	600/20	91.1	211.2	30.0
		700/14	93.2	198.7	12.5
		800/10	68.9	195.3	9.8
Mo_2C/C	Waste plastic (pipette tip)	600/15	131.1	185.4	23.4
		700/10	93.9	213.7	3.5
		800/10 (1g C)	82.6	179.1	19.4
		800/10 (0.75 g C)	80.11	213.3	12.2
C-Mo_2C	Waste polyethene	600/15	96.0	220.5	10.1
		700/12	91.5	206.0	8.7
		800/10	71.1	197.7	21.3
C/N-Mo_2C	Waste polyethene	800/12	69.2	197.2	16.3
Mo_2C@C/N	Waste plastic (pipette tip)	700/12	96.9	203.3	24.9
		800/10	72.9	186.0	15.3

8.2 Summary

The results reveal the synthesis of Mo_2C nano structures at relatively lower temperature than the reported results. Different carbon sources analytical polypropylene, non-biodegredable wastes (waste plastic and polyethene) has been utilized as carbon source for formation of carbon coated Mo_2C. Moreover, it also addresses the environmental issues caused due to disposal of these wastes. The carburization shows a dependency on the length of hydrocarbon chain of the initial carbon source. The temperature dependent nature of surface carbon over Mo_2C influence the electrochemical performance in terms of stability and efficiency. Among all the synthesized samples, N incorporated carbon coated Mo_2C (C/N-Mo_2C and Mo_2C@C/N) exhibits the lower Tafel slope and overpotential compared to carbon coated Mo_2C (Mo_2C@C, Mo_2C/C and C-Mo_2C), which exhibit enhanced HER activity due to synergistic effects of N incorporation with the carbon matrix. The growth of supported carbon matrix having 2D shape shows more EDLC performance due to their graphene like characteristics. The strong binding of conductive supported carbon matrix with encapsulated Mo_2C acts as the electronic bridge to enhance the charge transfer kinetics and improves the stability. The present route described for synthesis of these nanopowders is an efficient and environmentally friendly path because no toxic gases are evolved into the atmosphere during processing. The carbonaceous gases formed inside the autoclave play a vital role to enhance the kinetics of pure phase formation of Mo_2C.

8.3 Future scope

The described path can be used for the synthesis of other materials for energy production and conversion applications. The other industrial, food and agricultural wastes can be processed in the similar way to address the environment problems and utilize these waste for wealth. The efficiency of the synthesized nanopowders shows a favorable path for the use of these materials for other applications like oxygen reduction reaction (ORR) and CO_2 reduction etc. The photoctalytic HER activity of these materials need to be further analyzed by incorporation certain metal/non-metals and semi-conductors with low band gap. The incorporation of other non-metals (Sulphur ‘S’, Fluorine ‘F’ and phosphorus ‘P’) needs to be studied to enhance the efficiency of the material. The supercapacitor performance can be further improved for higher cycles and specific capacitance by optimizing the thickness of coated carbon. The lithium (Li) incorporation through present route can widen the use these materials for battery applications with higher charging capacity for longer durations.